SEASONAL AND SPATIAL VARIABILITY

IN TEMPERATURE, SALINITY AND CIRCULATION

OF THE

MIDDLE ATLANTIC BIGHT

By

NAOMI ELISABETH FLEMING

A Dissertation submitted to the

Graduate School-New Brunswick

Rutgers, The State University of New Jersey

In partial fulfillment of the requirements

For the degree of

Doctor of Philosophy

Graduate Program in Oceanography

Written under the direction of

John L. Wilkin

And approved by

_____

_____

_____

_____

New Brunswick, New Jersey

October, 2016

ABSTRACT OF THE DISSERTATION

Seasonal and Spatial Variability in Temperature, Salinity and Circulation of

the Middle Atlantic Bight

By NAOMI ELISABETH FLEMING

Dissertation Director:

Dr. John L. Wilkin

The physical oceanography of the Middle Atlantic Bight (MAB) is investigated, with

an emphasis on identifying seasonal and alongshore variability within the region.

While many previous studies assume uniform values throughout the MAB, and

provide only a two-dimensional view of temperature, salinity and circulation, here a

fully three dimensional spatial atlas of the MAB is developed for each month of the

year. Case studies of the low-salinity coastal plumes, and glider observations near

the shelfbreak, highlight the alongshore variability that exists within the MAB.

A weighted least squares regression technique is used to map historical temperature

and salinity data onto a gridded four dimensional atlas, dubbed MOCHA (The Mid-

Atlantic Ocean Climatological and Hydrographic Atlas). MOCHA fields compare

well to the input data, to independent datasets, to other climatologies, and even to

sophisticated real-time ocean models.

well to the input data, to independent datasets, to other climatologies, and even to sophisticated real-time ocean models.

MOCHA provides a detailed four-dimensional view of the Middle Atlantic Bight "cold pool". The well-known cycles of the warming of a summer mixed layer with a strong thermocline, and the development and shrinking of the cold pool, are clearly evident in MOCHA fields. Alongshore variations in the extent of the cold pool are observed.

A coastal ocean model of circulation and transport is developed using MOCHA as input, calculating box volume budgets of water, heat and freshwater. The seasonal cycles of heat and freshwater budgets are quantified, and the alongshore variability in sea-surface slope and offshore transport is identified. MAB waters, heat and freshwater are both lost and gained across the 85-m isobath along the entire length of the MAB, with the majority of MAB water turning offshore north of Cape Hatteras. Little, if any, of the MAB water volume enters the South Atlantic Bight (SAB), however the location of the offshore turn, and the amount entering and leaving the SAB vary seasonally.

Overall, MOCHA provides a much more detailed view of the MAB than previously published, and indicates that there is strong seasonality in temperature, salinity and circulation, along with considerable along-shore variation in properties that should be taken into consideration during future studies.

Acknowledgements

I would like to express my appreciation for the help and guidance of my thesis advisor, Dr. John Wilkin, and I would like to thank Dr. Glen Gawarkiewicz, Dr. Scott Glenn and Dr. Javier Zavala for serving on my thesis committee and for their many helpful suggestions.

I would like to thank Dr. Robert Chant for suggesting I work on the LEO-15 project (that became Chapter 3 of this thesis), and to Dr. Scott Glenn for involving me in the SW05 pilot study that resulted in Chapter 4.

I am very grateful for the many researchers and programmers around the world that share their code freely with others. I particularly would like to thank Dr. Peter Chu for providing the code that implements his static stability adjustment scheme. I thank my colleagues from (at that time, if not now) at the Department of Marine and Coastal Sciences for sharing their work, including Donglai Gong, Bob Chant, Peter Zhang, Eli Hunter, and John Wilkin. The gold medal in this category goes hands down to the incredibly useful "nfigaxis.m" written by John Wilkin, which was used to format nearly every figure in this thesis, and saved me (no doubt) hundreds of hours of tweaking.

I am also grateful to the oceanographers who have studied the Middle Atlantic Bight and uploaded their observational data to the online databases accessed for this

work. Data included in this thesis were also kindly provided by Renato Castelao,
Peter Zhang, Gordon Zhang, Joseph Wang, and Glen Gawarkiewicz.

Proofreading services were performed by Andrea Murray of Murray Edits, and by
my husband Ken Clasper.

The color maps in Chapter 9 are from www.ColorBrewer.org by Cynthia A. Brewer,
Geography, Pennsylvania State University, U.S.A.

Table of Contents

List of Tables

List of Figures

1 Introduction

The Middle Atlantic Bight is a coastal oceanic region of strong seasonal cycles in temperature, salinity and circulation. Many previous studies have presented observations and two- or three- dimensional climatologies of portions of the Middle Atlantic Bight, but here a fully four-dimensional climatology of the entire volume is developed and presented.

Chapter 2 introduces the physical oceanography of the Middle Atlantic Bight, and the following two chapters present case studies of two different regions within it. In Chapter 3, a low-salinity river plume from the Hudson River is observed as it passes a moored array near Atlantic City, NJ. Ship transects, wind records and a momentum balance analysis provide insight into the forcing of the localized strong currents or "jet". In Chapter 4, glider transects of temperature, salinity highlight the variability near the shelfbreak front, and the fact that alongshore difference in water properties and current speeds can be substantial.

The data used to compile the MOCHA climatology is outlined in Chapter 5, along with the processing steps taken to select and prepare data for the mapping procedure. The mapping method itself (a weighted least square technique) is detailed in Chapter 6, and the climatology results are examined and validated satisfactorily in Chapter 7.

A detailed four-dimensional analysis of the Middle Atlantic Bight "cold pool" as seen in the MOCHA climatology is presented in Chapter 8, which provides a more complete picture of the timing and extent of the cold pool that has been previously published.

In Chapter 9, a coastal ocean model of circulation and transport is developed, using box budgets of volume and either heat or freshwater to close the equations. Sea-surface slope and bottom stress values are estimated from the model output, allowing current velocity, and the volume, heat and freshwater transports for the Middle Atlantic Bight to be calculated. Transports through the region are studied, to determine the fate of Middle Atlantic Bight waters.

2 Physical Oceanography of the Middle Atlantic Bight

2.1 The Middle Atlantic Bight

The Middle Atlantic Bight is the region of the US eastern continental shelf that lies between Cape Cod and Cape Hatteras (Figure 2-1). It extends from 42°N latitude in the north to 35°N latitude in the south, and from approximately 77°W to 70°W longitude. The term "Middle Atlantic Bight" is commonly abbreviated to "Mid-Atlantic Bight", and to its acronym, MAB. A "bight" is a curved shoreline, and "middle" refers to its location in the mid-latitudes of the North Atlantic Ocean.

The continental shelf of the MAB is wide and shallow, with a gently sloping gradient (1:500). The sea floor on the shelf is mostly sand, with large pockets of sand-gravel and sand-shell, while the slope (200–2000 m depth) is a mixture of silt, silty sand and clay (Wilk and Brown 1980).

In the northern MAB the shelf break occurs approximately 160 km offshore, whereas off the coast of New Jersey the shelf break begins close to 110 km offshore, and the width continues to decrease southwards, until at Cape Hatteras the shelf is only 35 km wide. The depth at the shelf break is around 100–120 m in the northern MAB, and less than 40 m in the south (Uchupi et al. 2001).
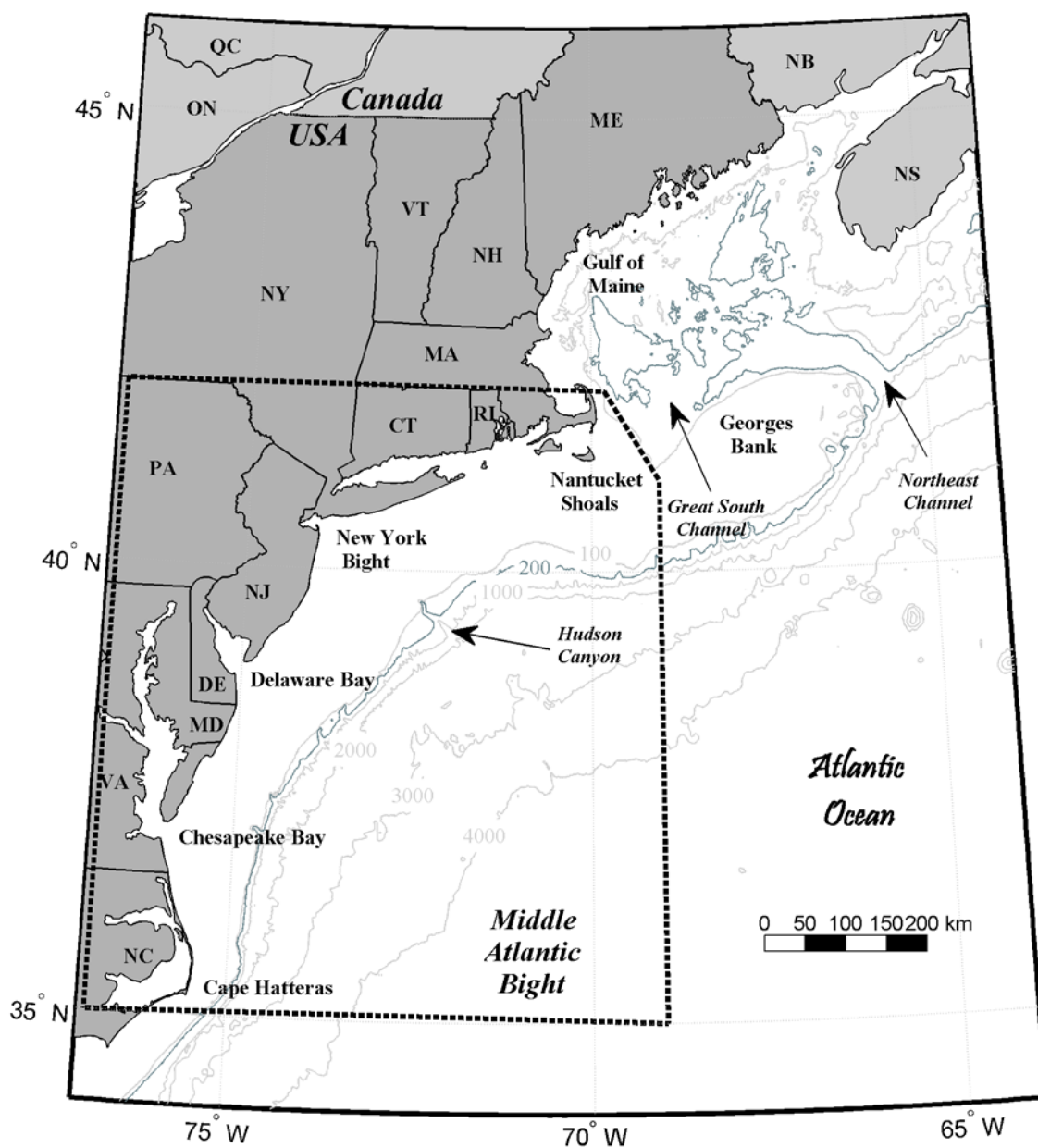
Figure 2-1: The northeast coast of North America, with depth contours in meters. The dashed box outlines the region known as the Middle Atlantic Bight extending from Nantucket Shoals just below Cape Cod, Massachusetts in the north, to Cape Hatteras, North Carolina in the south. The waters of the US coast to the north of the Middle Atlantic Bight are termed the Gulf of Maine.
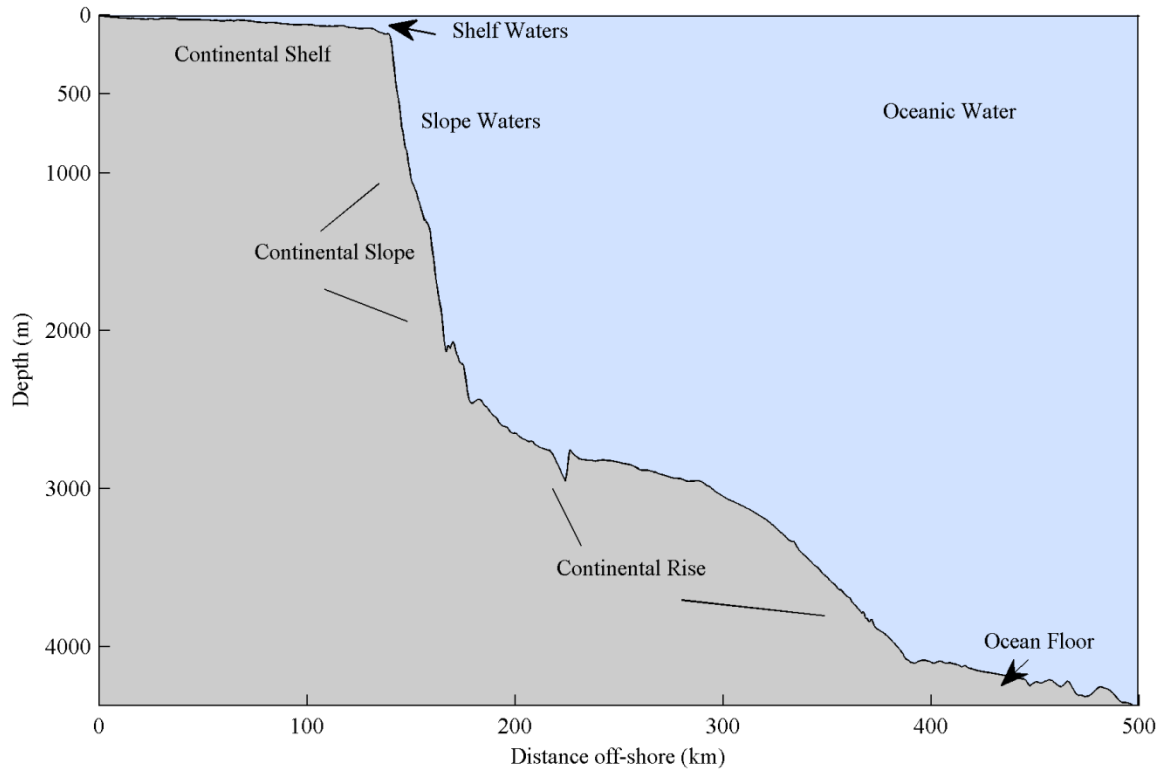
Figure 2-2: A typical cross section across through the MAB and beyond showing a wide, shallow continental shelf region, the shelf-break occurring at approximately 150 km offshore, and oceanic waters overlying over a steep slope out to 200 km offshore. This section is taken across-shore from mid-New Jersey, perpendicular to isobaths. The vertical scale is highly exaggerated.

Beyond the continental shelf break, the continental slope descends steeply with a gradient of about 7:100. The width of the slope varies between 10–50 km. After 2000 m depth the continental rise slopes much more gradually (with a gradient of less than 1:100) and extends a further 100–1000 km offshore, until it meets the ocean floor (Figure 2-2).

2.2 Features of the MAB

2.2.1 The New York Bight

The New York Bight is the name given to the large gulf around the mouth of the Hudson River, extending from Cape May, NJ to Montauk Pt, Long Island. Notable features within this region include the Hudson River Estuary, the Hudson Shelf Valley, the Hudson Canyon (Figure 2-3), and Long Island Sound.
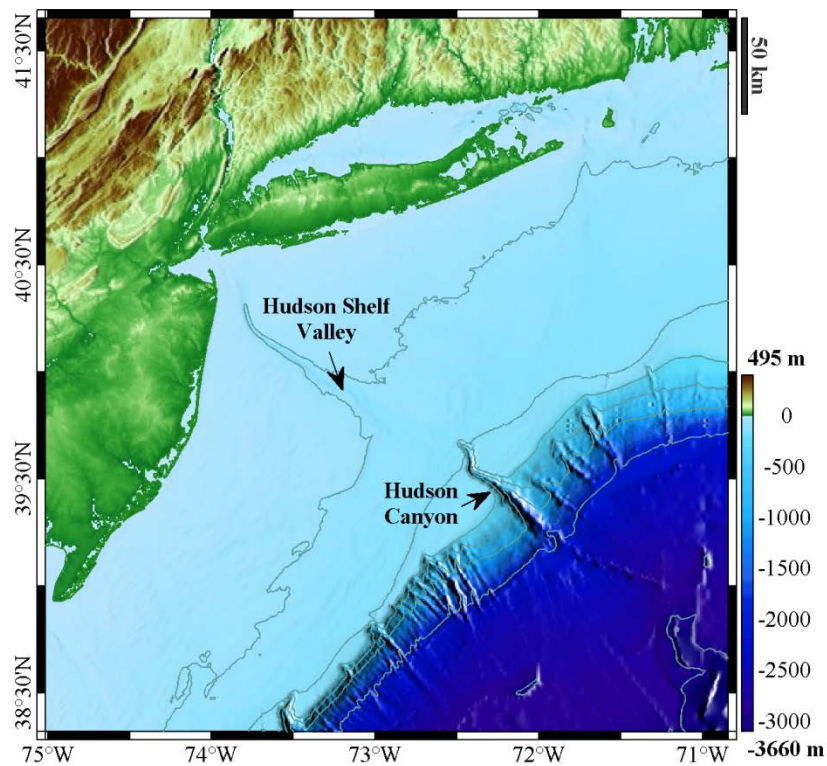
Figure 2-3: The Hudson Shelf Valley on the MAB shelf and the Hudson Canyon, located further offshore in the slope and continental rise.

2.2.2 The Hudson River and Hudson River Estuary

The Hudson River flows 507 km from its origin in the Adirondack Mountains in the state of New York to the New York City Harbor. The distance up river that seawater can be found varies considerably with the season due to changes in river runoff. In spring, the salt front is located near Yonkers, New York, and in the fall, it is located by Newburgh, New York. The Hudson River Estuary is generally taken as being the tidal portion of the Hudson River: up to the dam at Troy, 243 km up river (Cooper et al. 1988). The greatest tidal amplitude occurs at Albany, with a mean of 1.56 m, and the maximum tidal excursion is 21 km (Cooper et al. 1988).

The depth of the Hudson River Estuary ranges from 3–30 m with the mean cross-sectional depths in the lower part of the Hudson (up to Havershaw Bay) decreasing upstream from 10 m to 5 m. It then abruptly increases and the upper Hudson has point depths of up to 66 m (Cooper et al. 1988). The widest part of the estuary is at Havershaw Bay where it is 5.6 km wide, and the narrowest is 175 m, just south of Troy (Abood 1977).

The Hudson River estuary cannot be easily classified with regard to the salinity structure. Freshwater flows seaward in the upper layer of the estuary, with saline ocean water flowing upstream beneath it. River flow is highest in spring and winter, and lowest in summer. Observations have shown the structure of a partially mixed estuary (Hunkins 1981; Geyer et al. 2000), while others consider it a salt-wedge estuary (e.g. Simpson et al. 1973), and yet others have observed a well-mixed

structure (e.g. Howells 1972). Still others observe several different structures within even a short study period (Posmentier and Rachlin 1976). The structure that the estuary takes at any given time depends on the tidal range, freshwater flow, and sometimes on local wind forcing.

The watershed of the upper Hudson (including the Mohawk River) is 25,927 km[2] in extent (Figure 2-4), and accounts for 80% of the river flow (Cooper et al. 1988). The lower Hudson watershed (below the Troy Dam) covers 18,753 km[2]. Annual discharge at New York City, averaged over the years 1966–83 was 18.2×10^9 m^{-3} (Cooper et al. 1988).

2.2.3   The Hudson Shelf Valley

The Hudson Shelf Valley is a 150 km long chasm in the continental shelf, extending from the mouth of the Hudson River to the edge of the continental shelf (Figure 2-3). It is either the ancient path of the Hudson River (Butman et al. 2006), or the result of catastrophic draining of glacial lakes (Uchupi et al. 2001). The upper Hudson Shelf Valley (beginning at Christiansen Basin) is 30 m deep and extends 25 km in a north/south direction to about 65 m depth (Butman et al. 2006). The mid-valley is about 5 km wide and is 20–40 m deeper than the surrounding shelf. It extends in a northwest/southeast direction (Uchupi et al. 2001). The lower valley begins at about 70 m depth, is 10 km or more wide, and ends at shelf break, near the head of the Hudson Canyon (though it does not directly connect to the canyon) (Butman et al. 2006).
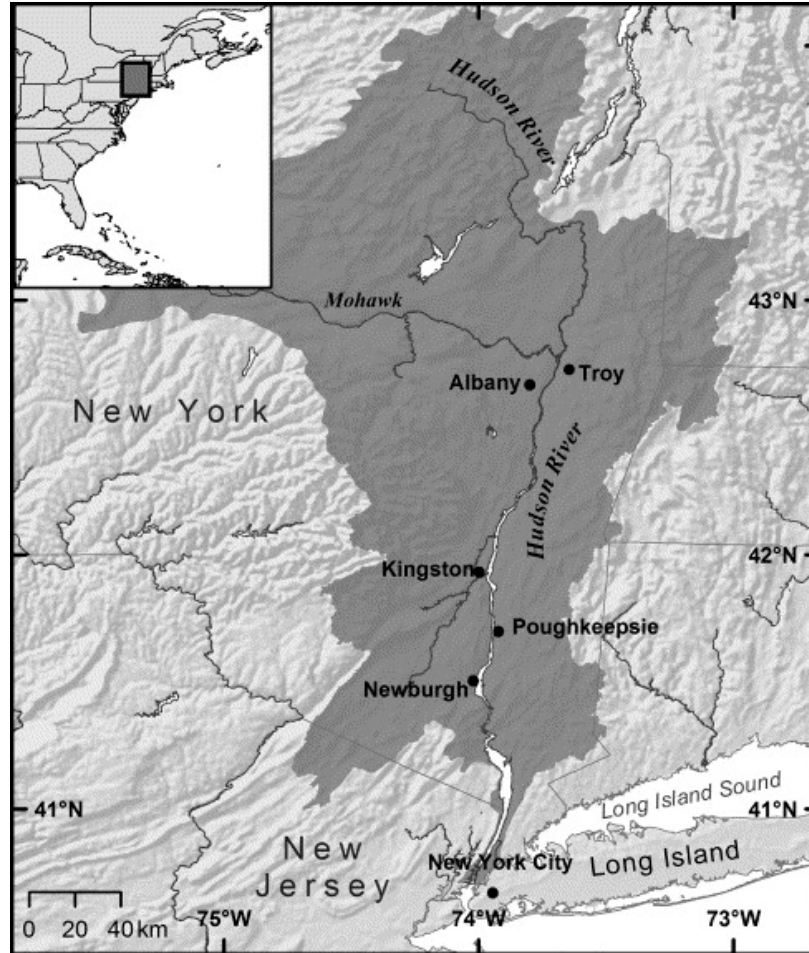
Figure 2-4: The Hudson River, and its watershed (dark gray) in New York and New Jersey. Reproduced with permission from Figure (1) in Nitsche, Ryan et al. (2007) *Regional patterns and local variations of sediment distribution in the Hudson River*. Oxford: Elsevier.

2.2.4   The Hudson Canyon

The Hudson Canyon (Figure 2-3) is the largest of many canyons that cut into the

continental slope of the MAB. It is located 220 km southeast of New York City, and

cuts 200–800 m into the slope, over a distance of 370 km from the shelf break

towards the ocean floor (Keller et al. 1973).

2.2.5   Nantucket Shoals and Georges Bank

The Nantucket Shoals and Georges Bank are large shallow areas of the continental shelf in the northern MAB (Figure 2-5).

Georges Bank, to the north of the MAB, is a large submarine bank separating the Gulf of Maine from the Atlantic Ocean. It is approximately 300 km long and 150 km wide and its depth varies from 30–300 m. It has a steep slope on the northern side, and rises more gently on the southern side. The bank is covered with ridges, some high enough so that the water is less than 5 m deep. The bank itself is generally less than 60 m deep.

The Great South Channel (~70 m deep), separates Georges Bank from the Nantucket shoals, where waters are less than 50 m deep.

A region of fine-grained sediments is located approximately 100 km south of Martha's Vineyard. This region is dubbed the "Mud Patch" in contrast to the sandy bottom sediments found elsewhere in the MAB. The Mud Patch extends approximately 100 km alongshore and 50 km cross-shore, in 60–150 m water depths.

2.2.6   Chesapeake Bay

Chesapeake Bay (Figure 2-6) is the largest estuary in the United States. It stretches over 300 km from 36°50′N (in Virginia) to 39°40′N (in Maryland), and covers ~11,500

km². It is a partially mixed estuary with a tidal range of about 0.6 m (Baird and Ulanowicz 1989).

The bay is shallow, having a mean depth of 9 m, and with a quarter of the bay having depths of less than 2 m. The width of the bay ranges from 5–50 km.

Freshwater flows into the bay from several different rivers, the largest input (~50%) coming from the Susquehanna River. In total, over 150 streams and rivers flow into Chesapeake Bay, from a watershed drainage area of ~166,000 km².
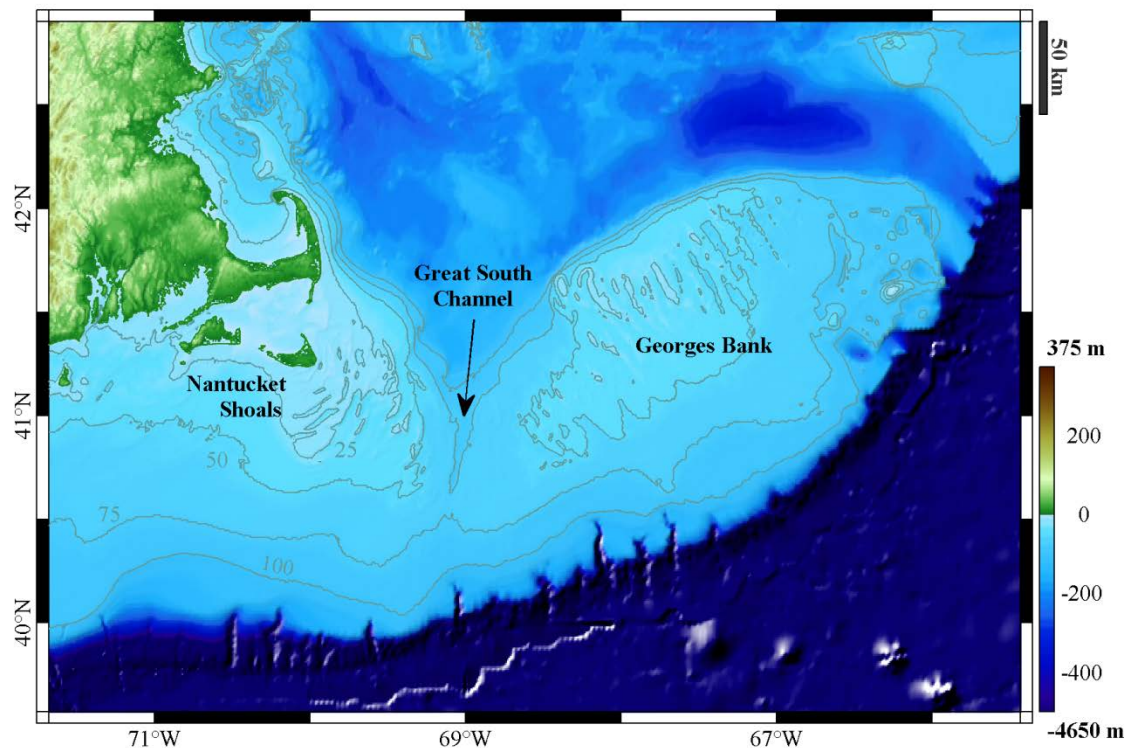
Figure 2-5: Nantucket Shoals and Georges Bank: two shallow regions at the northern end of the Middle Atlantic Bight, lying to the south and east of the easily distinguishable "hook" of the Cape Cod peninsula. Isobaths are labelled as depth in meters. The bathymetry color scale is truncated to −500 m to show detail on the shelf.

2.2.7   Delaware Bay

Delaware Bay (Figure 2-6) extends from Cape May to Trenton in New Jersey, a distance of 210 km. It is a shallow bay with a mean depth of 9.6 m, and with 80% of the bay being less than 9 m in depth. The widest area of the bay measures 43 km
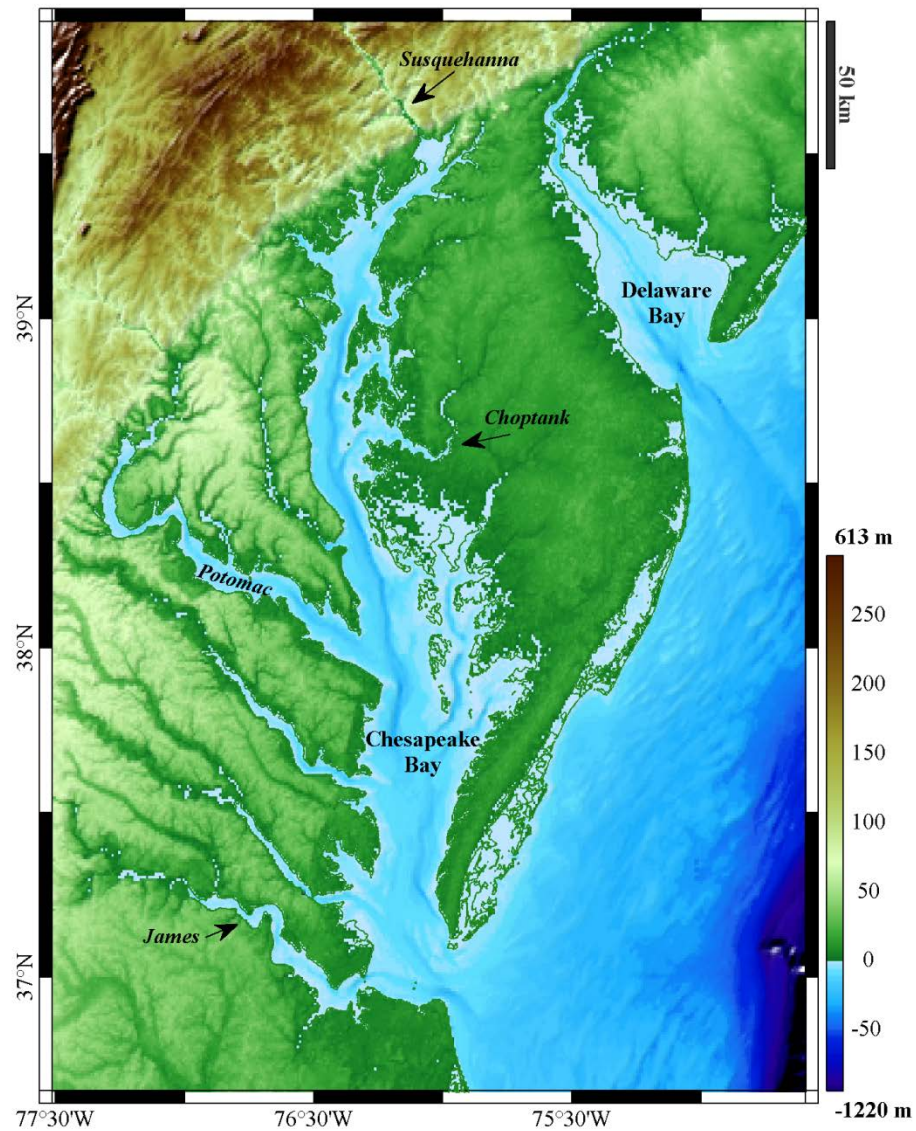
Figure 2-6: Delaware Bay, and Chesapeake Bay with river tributaries (the four largest are labelled in italics).

across. Delaware Bay is a partially mixed estuary, with a tidal range of 1.3 m, and

tidal currents of approximately 1 m s^{-1}. Discharge from the Delaware Bay comes

from the Delaware River (58%), the Schuylkill River (15%), and other sources (each

<1%). The watershed covers an area of 35,000 km^2, and the average annual

discharge at the mouth of the bay is 550 m^3 s^{-1}.

2.3 Water Properties of the MAB

2.3.1 Origin and Fate of MAB Waters

The waters on the MAB shelf are part of the large coastal current that originates in

the Labrador Sea (Chapman and Beardsley 1989; Loder et al. 1998). MAB shelf

water is a mixture of Scotian Shelf water and slope water that enters the Gulf of

Maine through the Northeast Channel (Figure 2-7). This water mixture flows from

the western Gulf of Maine, counter-clockwise around Georges Bank, through

Nantucket Shoals, and into the MAB.

Mean flow is to the southwest, along isobaths, and the mean residence time of water

on the shelf is 100 days (Mountain 1991). As the current approaches Cape Hatteras,

the along-shelf current turns offshore, entraining the relatively cool and fresh shelf

waters into the warmer and salty Gulf Stream frontal system.
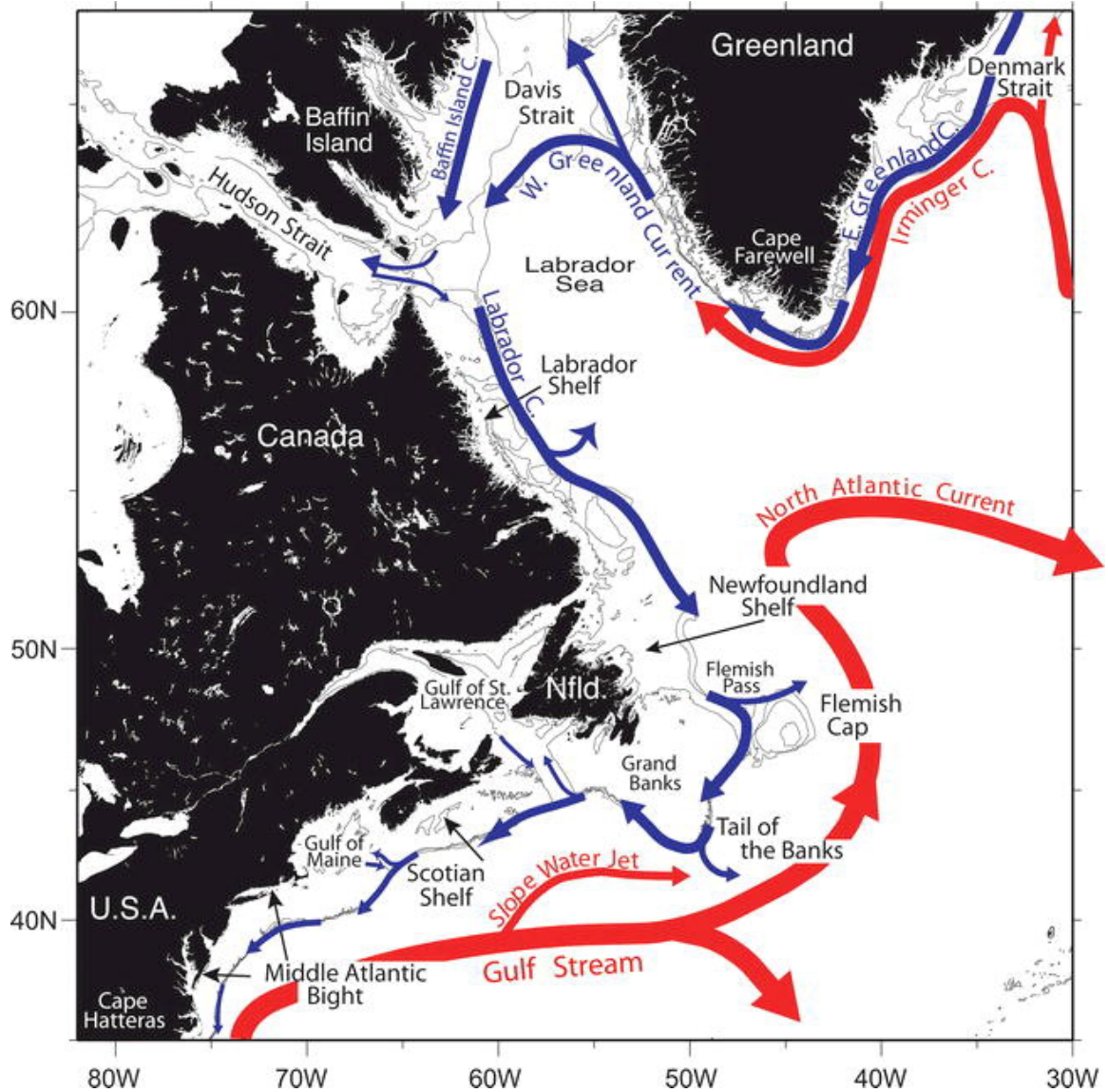
Figure 2-7: Northeast Coast currents, showing origin of MAB water from the north, and the proximity of the Gulf Stream in the southern MAB. From Figure (1) Fratantoni and Pickart (2007) *The Western North Atlantic Shelfbreak Current System in Summer* © American Meteorological Society. Used with permission.

2.3.2 Shelf and Slope Waters

The water overlying the continental shelf of the MAB is referred to simply as "shelf water". The water over the MAB continental slope ("slope water") is warmer and more saline than mid-shelf water, especially in the southern MAB, due to the proximity of the Gulf Stream (Figure 2-8). Between these two water masses, lies a 100-m deep layer termed the "upper slope thermostad". In summer, the temperature is this layer lies between that in the thermocline and that in the deeper slope water below, whereas in wintertime, the upper slope thermostad is warmer and saltier than both the shelf and the slope waters (Wright and Parker 1976).
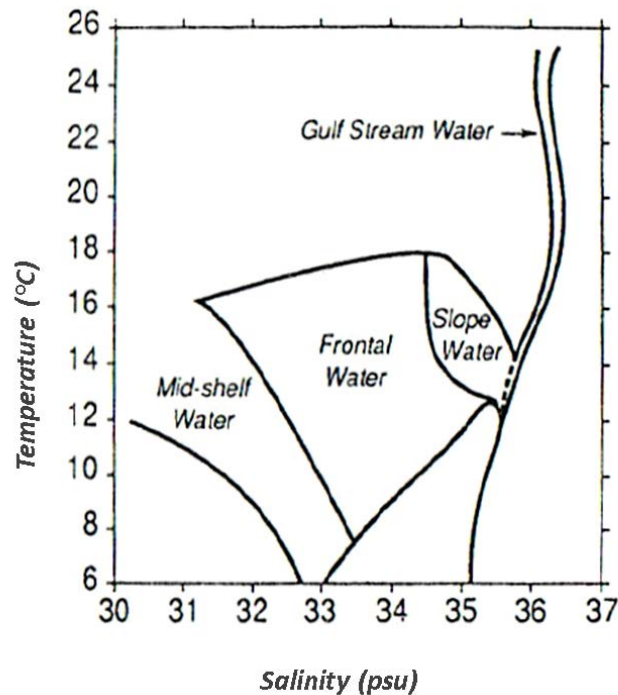
Figure 2-8: An example of water masses in the MAB. Reproduced with permission from Figure 8(a) in Churchill et al. (1993) *Mixing of shelf, slope and Gulf Stream water over the continental slope of the Middle Atlantic Bight.* Oxford: Elsevier.

A warm (>17°C) mixed layer exists permanently above a thermocline at 200–600 m depth. Seasonal variations only penetrate the upper 200 m. In winter, the top 100–150 m is well mixed, due to storms and cold air temperatures. Below the permanent thermocline lies cold (<4°C) North Atlantic Deep Water (NADW).

A persistent front separates the Shelf and Slope waters, often defined by the 34.5-isohaline (e.g. Burrage and Garvine 1988), although it's position is highly variable. The front is commonly referred to as the "shelf/slope front" or the "shelfbreak front".

2.3.3   The Shelf/slope Front

The shelf/slope front is generally located near the shelf break, its foot touching the shelf floor at a mean location between the 75-m and the 120-m isobaths, depending on the season and alongshore location. Its position is highly variable (Mountain 1991), and can be complicated by offshore protrusions of shelf water and onshore intrusions of salty slope water.

 The front slopes upward to the east, and can outcrop at the surface further offshore, particularly during wintertime, while in summer it is overlaid by a strong seasonal pycnocline at up to 40 m depth (Figure 2-9). The strongest signal of the front is in salinity, as the temperature off-sets the salinity signal such that only a weak density gradient exists.
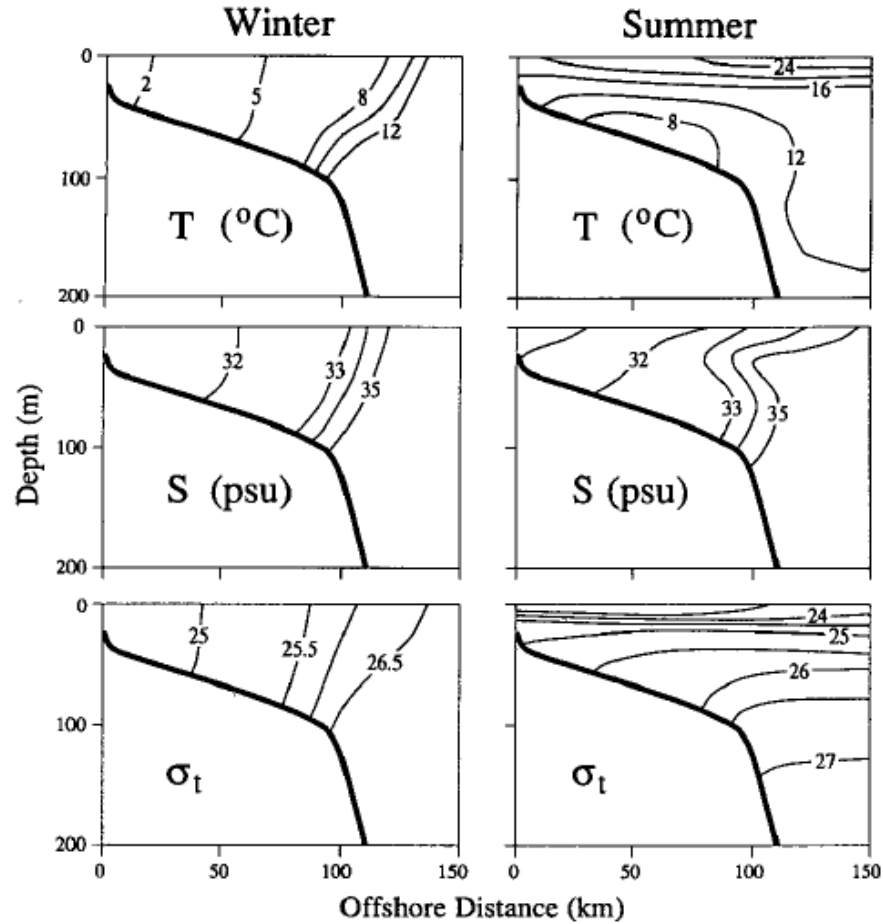
Figure 2-9: Typical MAB shelf/slope frontal structure during winter and summer. Successive rows show temperature, salinity and density. From Chapman and Gawarkiewicz (1993) *On the establishment of the seasonal pycnocline in the Middle Atlantic Bight.* © American Meteorological Society. Used with permission.

Linder and Gawarkiewicz (1998) published a climatology of the shelf/slope front at three different locations, based on nearly 200 years of data. The main study area was in Nantucket Shoals, and this was compared to Georges Bank and to off the coast of New Jersey. They studied the seasonal variation in the front, using the 34.5 isohaline, the 10°C isotherm, and the $\sigma_t = 26.5$ kg m^{-3} isopycnal to define it.

At Nantucket Shoals, the temperature front was observed to be strong and narrow in winter, increasing from 6°C to 12°C offshore, over 20 km. In summer, a strong thermocline develops in the top 40 m of the water column, as the surface is heated, and the shelf/slope front is not evident in the temperature record. The salinity front remains relatively constant throughout the year, other than surface layer freshening during summer, and coincides with the temperature front during winter, with a gradient of 1/20 km in the horizontal, and 1/40 m in the vertical. The shelf/slope front is therefore determined by the position of the 34.5 isohaline. In winter, density gradients are weak due to temperature and salinity effects cancelling each other out, while in summer a strong pycnocline exits due to both higher temperatures and lower salinities in the surface layer.

At Nantucket Shoals, the slope intersects the bottom between the 85-m and 105-m isobaths throughout the year (Figure 2-10a). This corresponds to a horizontal distance of 10 km. The front slopes upward and offshore, but varies significantly with the season. The slope is at its maximum in October and November ($\sim 5 \times 10^{-3}$), with 20 km separating the bottom and surface outcrops. In December and January the surface outcrop move offshore, and the slope gradient halves to $2–3 \times 10^{-3}$. During the rest of the year, the front flattens out in the surface waters, and does not outcrop.

A seasonal migration of the position of the foot of the front is apparent: it is at its extreme onshore position during October–January, and at its maximum offshore position in June and July.
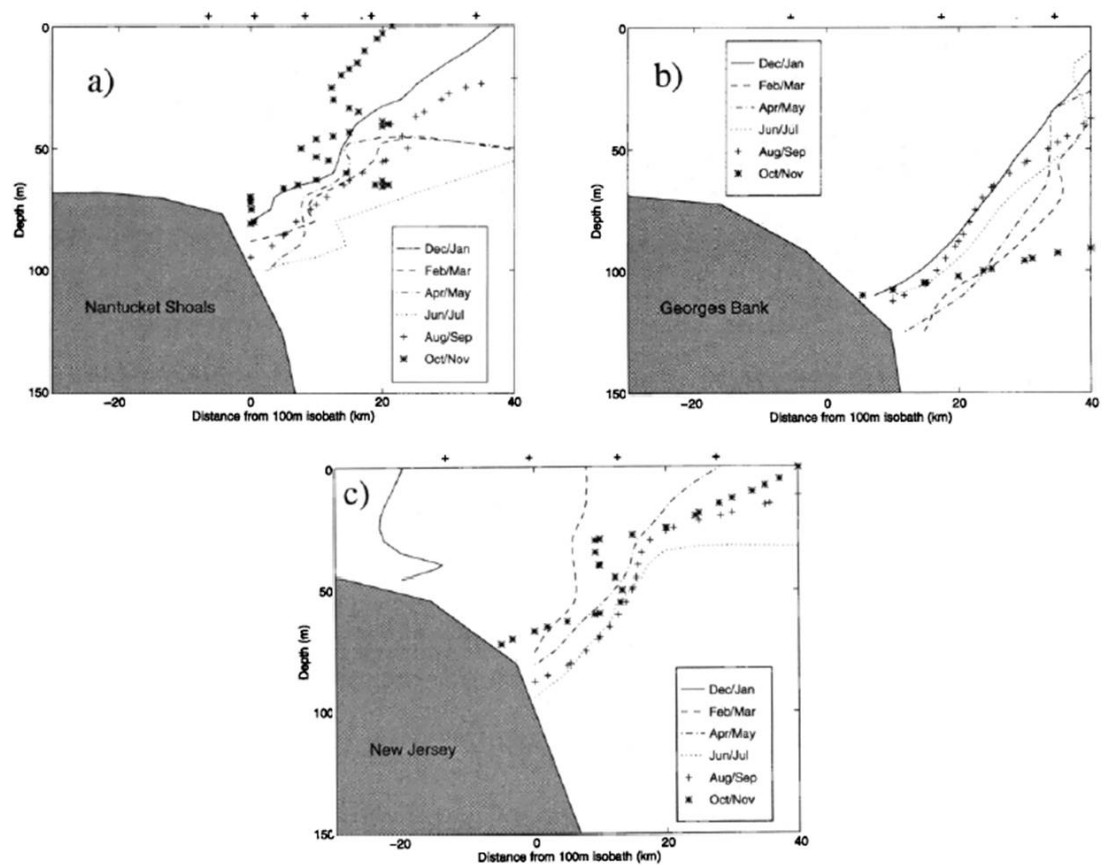
Figure 2-10: The position of the shelf/slope front (as indicated by the 34.5 isohaline) throughout the year at (a) Nantucket Shoals, (b) Georges Bank, (c) New Jersey coast. Reproduced with permission from figure (12) in Linder and Gawarkiewicz (1998) *A climatology of the shelfbreak front in the Middle Atlantic Bight* Hoboken: John Wiley & Sons Inc.

At Georges Bank (Figure 2-10b) the frontal slope is smaller ($\sim 2 \times 10^{-3}$) and shows less seasonal variation than at Nantucket Shoals. There is no isohaline outcrop at any time of year. The average position of the foot of the front is at the 120-m isobath. It is at its minimum depth (110 m) during October to January, at its maximum depth (130 m) during February–May, then moves onshore to ~110 m again in summer.

The frontal structure is different again off the New Jersey coast (Figure 2-10c). The slope of the front is steeper, and the surface outcrops during most of the year (except June–September). An anomalous period occurs in December and January when the front is 20 km further onshore than it is during the rest of year. Otherwise, the bottom of the front remains close to the shelf break, its mean position being at the 75-m isobath.

2.3.4   Seasonal Variation of Shelf Waters

The waters of the Middle Atlantic Bight show a strong seasonal pattern, except for those very shallow regions over Georges Bank and Nantucket shoals where tidal mixing keeps the water profile well mixed all year round.

During the winter months (November–March) the shelf waters are vertically mixed, and temperatures range from 4–7°C. The coldest water is found near shore (Biscaye et al. 1994). The temperature front at the shelf-break front is well defined, with offshore waters at similar depths being about 12°C. Typical mid-shelf salinities are about 33.

In the spring and summer (April–September) the MAB waters become stratified as atmospheric heating forms a warm surface layer. A thermocline develops above the cold winter water, and isolates it throughout the summer months. Shelf temperatures at the surface reach 20–25°C by summertime, with the thermocline deepening to 40 m by late summer.

Surface salinities are lowered due to increased freshwater discharge from the Hudson River and the Delaware and Chesapeake Bays. Upwelling winds are more common, and tend to push the fresher coastal water offshore during sustained periods, which also leads to the lowering of the surface salinity. A strong pycnocline develops at about 20 m depth (Chapman and Gawarkiewicz 1993).

The vertical stratification breaks down in the autumn due to mixing by storms and cooling of the surface waters as the air temperature drops (Beardsley and Flagg 1976). By October/November, the shelf waters return to their vertically mixed winter state.

2.3.5   The Cold Pool

Beneath the thermocline, during summer the cold winter water trapped below is known as the "cold pool" (Houghton et al. 1982; Loder et al. 1998). This water is generally 5°C cooler than waters further offshore, although the temperature gradually increases throughout the summer. The cold pool has been taken variously as water less than 8°C (e.g. Beardsley et al. 1976); 10°C (e.g. Linder and Gawarkiewicz 1998); or 11°C (e.g. Lentz et al. 2003).

Many studies have provided observations of the cold pool (e.g. Houghton et al. 1982; Bignami and Hopkins 2003; Lentz et al. 2003). The cold pool is usually evident as a bottom layer (~35 m thick) along the whole MAB between the 40-m and the 100-m isobaths, representing about 30% by volume of the shelf waters. Minimum

temperatures are 1.1–4.7°C, and occur in the early spring and summer. During June and July the cold pool extends out to the 90-m isobath, nearing the shelf break. During August and September the thermocline deepens, to almost 40 m depth, and the cold pool extends only to the 80-m isobath.

In the northern MAB it is thought that the cold pool remains isolated during the summertime, and is not fed by incoming cooler water from the north, while cool water does flow though the MAB and replenish the cold pool in the southern MAB (Houghton et al. 1982).
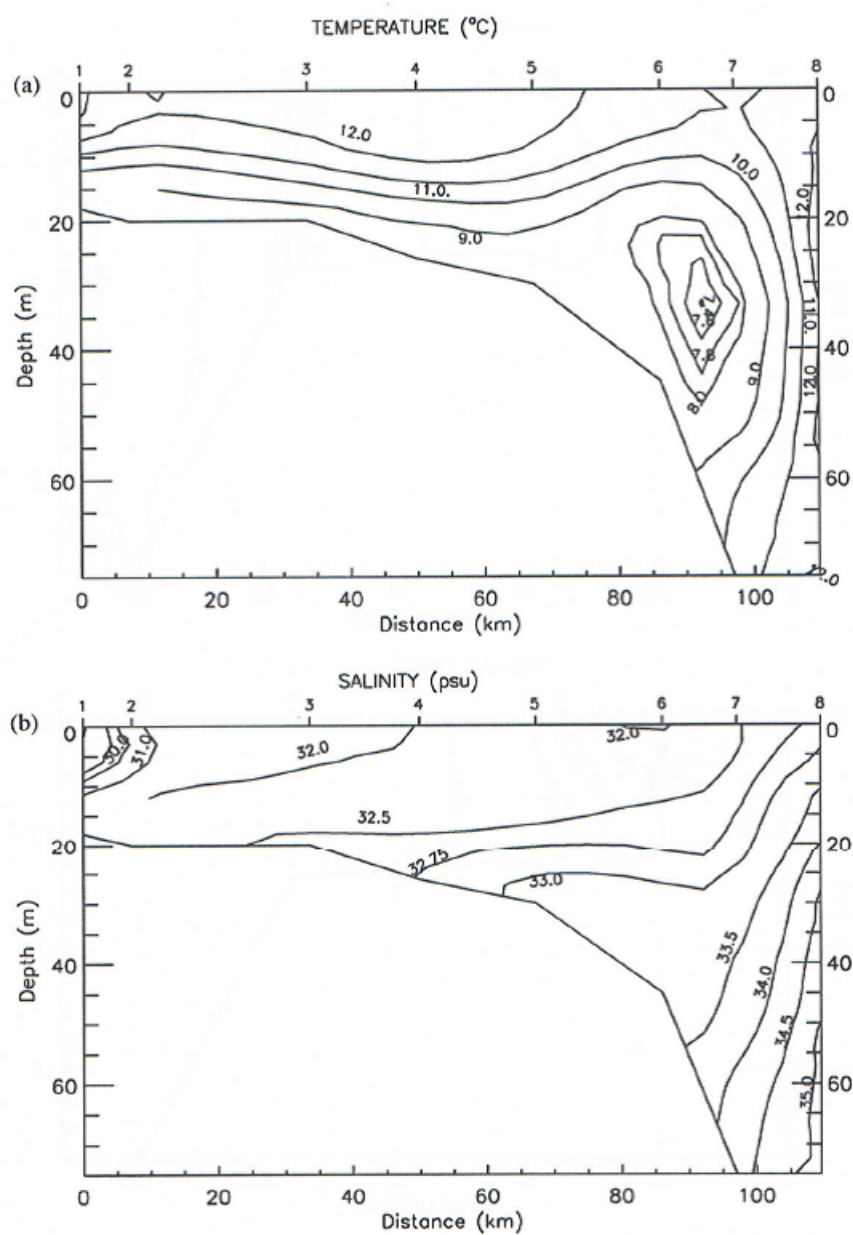
Figure 2-11: The Cold Pool. Reproduced with permission from Figure (6) in Bignami and Hopkins (2003). *Salt and heat trends in the shelf waters of the southern Middle-Atlantic Bight* Oxford: Elsevier.

2.3.6 The Gulf Stream

The Gulf Stream is the Western Boundary current of the North Atlantic Subtropical Gyre, which flows clockwise around the North Atlantic Ocean. The Gulf Stream exits the Gulf of Mexico at the straits of Florida and becomes the "Florida Current". The current then flows northward as the Gulf Stream, following the coast of southeastern USA, until it reaches Cape Hatteras.
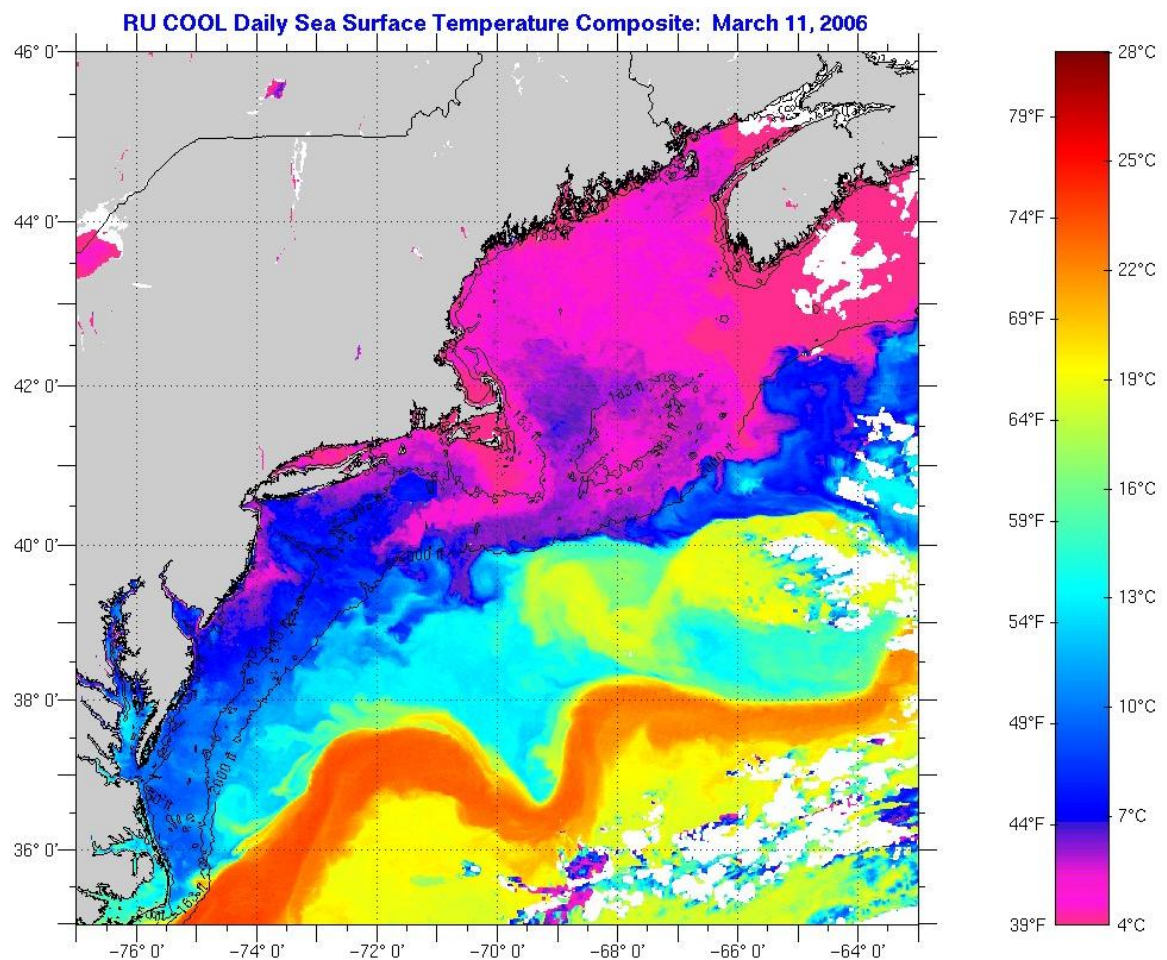
Figure 2-12: The Gulf Stream is easily identified in sea surface temperature (SST) maps. Shown here as it moves offshore from Cape Hatteras, past the MAB region. Reproduced with permission from the Cool Group in the Institute of Marine and Coastal Science, Rutgers University, New Jersey.

At this point the current turns eastward, moving offshore into deeper waters (Figure 2-12). It meanders across the Atlantic until about 50ºN, where is splits into several currents, the largest of which is the North Atlantic Current.

2.3.7   Cross-shelf Exchange

At Cape Hatteras the Gulf Stream flows as close as 30 km to the coast, and even further north, eddies and rings can break off from the Gulf Stream and move towards the MAB shelf (Figure 2-13).

Warm core rings form on the north side of the current every month or two. They are typically 50–100 km across, and move at speeds of about 3–5 km per day (Mann and Lazier 1996).

Eddies and warm core rings formed in the Gulf Stream have been observed to reach the shelf/slope front, and can enhance cross-shelf exchange in the form of subsurface intrusions of slope water (e.g. Gordon and Aikman 1981; Burrage and Garvine 1988; Churchill and Cornillon 1991; Gawarkiewicz et al. 1992; Gawarkiewicz et al. 2001).

This exchange is greatest in summer when shelf waters are stratified, and isopycnals are nearly horizontal (Gawarkiewicz et al. 1990).

Such processes are particularly important near Cape Hatteras, given its close proximity to the Gulf Stream (Flagg et al. 2002; Gawarkiewicz et al. 2008) although

cross-frontal exchange has been observed along the full length of the MAB in a

drifter study described by Lozier and Gawarkiewicz (2001).
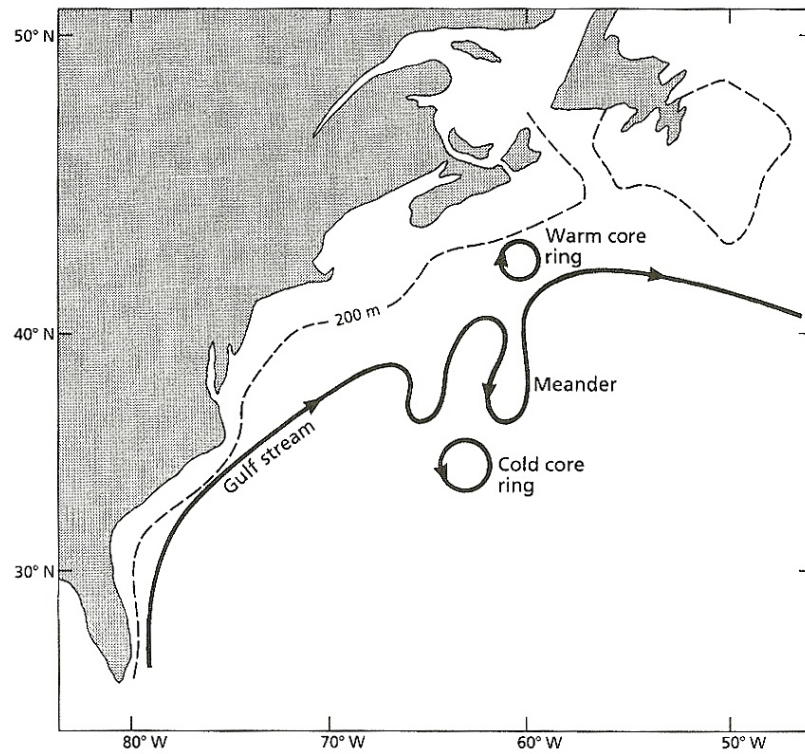
Figure 2-13: Gulf Stream and its meanders: indicating the formation of warm core rings on the north side and cold core rings on the south side. Reproduced with permission from Fig 8.14 in Mann and Lazier (1996) *Dynamics of Marine Ecosystems: Biological-Physical interactions in the oceans, 2nd Edition*. Oxford: Elsevier. Based on Richardson et al. (1978) and Parker (1971).

2.4 Circulation

2.4.1 Mean Shelf Flow

The mean flow on the MAB shelf is along-isobath, that is, southwestward for much of the MAB (Figure 2-14). Annual mean currents are 3–12 cm s^{-1} , with much smaller currents (generally < 2 cm s^{-1}) in the cross-shelf direction (e.g. Beardsley et al. 1985; Biscaye et al. 1994; Shearman and Lentz 2003; Lentz 2008). The along-shelf flow increases offshore and is stronger in winter than in summer (e.g. Gong et al. 2010; Zhang et al. 2011). Near Cape Hatteras, there is also transport in the off-shore direction, as some of the shelf water is entrained into the Gulf Stream (e.g. Churchill and Berger 1998).

The mean circulation on Georges Bank differs from the mean in that it flows counter-clockwise around the bank. Current speeds are of the order of 5–15 cm s^{-1}, except for a jet-like flow on the northern side where northeast currents flow at 25–30 cm s^{-1} (Butman et al. 1982).

Stronger currents exist in general over the shelf-break due to the presence of the shelf-slope front. This "shelf-slope jet" reaches maximum speeds of 30–35 cm s^{-1} in the spring, with annual mean speeds of 15–22 cm s^{-1} (Linder and Gawarkiewicz 1998; Flagg et al. 2006).
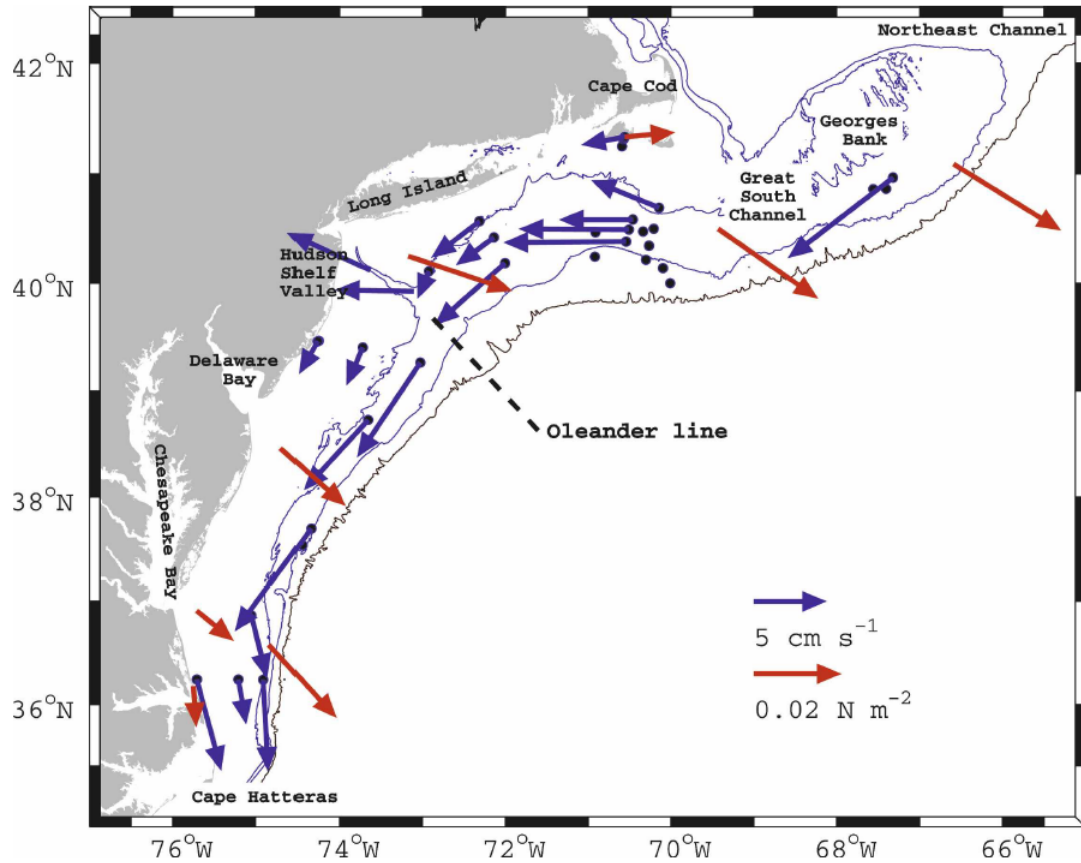
Figure 2-14: Depth-averaged current patterns in the MAB. Blue arrows are the mean depth averaged current vectors, and the red arrows are mean wind stress vectors. Isobaths are 50 m, 100 m, and 1000 m. From figure (1) in Lentz (2008) *Observations and a model of the mean circulation over the Middle Atlantic Bight continental shelf* © American Meteorological Society. Used with permission.

2.4.2   Deep Western Boundary Current

The Deep Western Boundary Current flows to the southwest above the lower continental slope and rise, and consists of North Atlantic Deep Water. It is approximately 50 km wide, and crosses underneath the Gulf Stream just north of Cape Hatteras.

2.5 Weather, Winds and Upwelling

Weather in the MAB is milder than that in inland regions—summers are cooler and winters are milder. January is the coldest month (with an average of −0.2°C) and July the warmest with an average of 24.1°C. The annual average is 12.1°C.

Rain is moderate throughout the year, with an average annual rainfall of 1041 mm. Highest rainfall occurs in August, and the lowest in June. Average snowfall is 432 mm per year. Thunderstorms are frequent in summer, associated with tropical cyclones. Very strong winds are rare.

2.5.1 Wind Speeds

Mean annual winds over the MAB are directed toward the southeast (e.g. Saunders 1977; Beardsley et al. 1985; Gong et al. 2010). Maximum mean winds (of ~7.5 m s^{-2}) occur in winter (December–February) and are directed southeastward. In summertime (June–July), the mean winds are directed northeastward, with mean speeds of ~4.7 m s^{-1} . The months with weakest mean winds are July and August (~4.6 m s^{-1}).
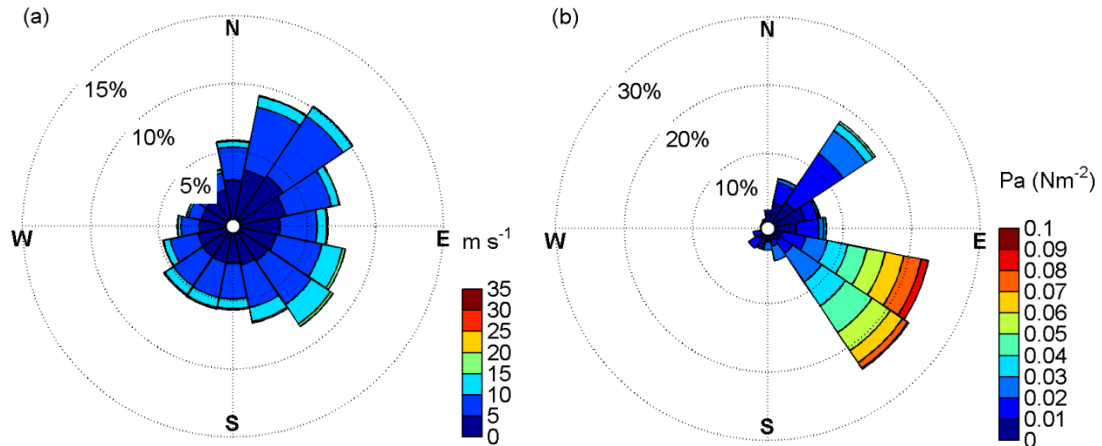
Figure 2-15 Wind rose showing (a) annual wind speed and (b) annual wind stress over the MAB for 1979–2000. Data source: National Centers for Environmental Prediction – North American Regional Reanalysis (NCEP–NARR; Mesinger et al. 2006) provided by the Physical Sciences Division of the Earth System Research Laboratory at the National Oceanic and Atmospheric Administration (NOAA/ESRL PSD), Boulder, Colorado, USA, from their website at http://www.esrl.noaa.gov/psd/.

2.5.2   Upwelling

Southwesterly winds in the MAB region can produce offshore Ekman transport over the inner continental shelf. This offshore flow is compensated at depth by onshore flow of colder, nutrient rich water that can eventually rise to the surface.

Glenn et al. (2004) reviewed nine years of data and summarized summertime upwelling on the New Jersey Shelf. Upwelling events are readily seen in the sea surface temperature (SST) maps: initially a narrow band of cold water is observed along the coast and if southwesterly winds persist this band continues to widen. Discrete upwelling centers may develop which are associated with high primary productivity (Glenn et al. 1996).

2.6 Tides

The principal tidal constituents in the MAB are listed in Table 2-1. The dominant diurnal constituents are the K_1, O_1 and P_1, and the semidiurnal are M_2, N_2 and S_2. The M_2 is the largest by nearly an order of magnitude. The resulting tidal signal on the MAB is predominately semi-diurnal in nature.

Tidal range and currents in the MAB are relatively small. Typical shelf currents are 10–15 cm s^{-1}, with elevation amplitudes of 1–2 m (Loder et al. 1998; Moody 1984). Currents are largest over Nantucket Shoals and Georges Bank with M_2 tidal currents of 70–100 cm s^{-1}, while amplitudes are smallest in this region (30–40 cm) (Loder et al. 1998; Moody 1984; Shearman and Lentz 2004).

Table 2-1: Principal tidal constituents on the MAB.

Tidal Constituent	Period (hours)	Frequency (cycles/hour)
Diurnal:		
K_1 — luni solar	23.93	0.0417807
O_1 — principal lunar	25.82	0.0387307
P_1 — solar	24.07	0.0415526
Semidiurnal:		
M_2 — principal lunar	12.42	0.0805114
N_2 — larger lunar elliptic	12.66	0.0789993
S_2 — principal solar	12.00	0.0833333

3 Case Study I: Observations of a Nearshore Low-salinity Plume

3.1 Introduction

Buoyant plumes are a commonly observed feature in coastal regions. Low-salinity buoyant discharge from rivers typically turns equatorward on reaching the ocean, and can flow for up to hundreds of kilometers along the coast (e.g. Rennie et al. 1999; Fong and Geyer 2001; Garvine 2004). The flow and structure of these plumes are affected by local winds: specifically, downwelling-favorable winds tend to enhance the flow, while upwelling-winds restrict the along-shore movement, and instead induce cross-shore spreading and thinning of the plume, and may even detach from the coast (e.g. Fong and Geyer 2001; Lentz 2004; Hickey et al. 1998; Whitney and Garvine 2006).

In this study, the paths of two low-salinity plumes are observed as they flow from the Hudson River southwestward along the New Jersey coast. A combination of ship tracks and time series of mooring data are using to measure the water properties. The momentum balance of the current is calculated, and correlations between forcing terms and plume measurements are examined. Questions include: what is the role of upwelling in life-cycle of a plume, and what is the relative importance of winds versus density gradients in the region of the plume?

3.2 Study Region: LEO–15

The Long-term Ecosystem Observatory (LEO–15) research site is located off the

coast from the Rutgers Marine Field Stations at Great Bay, New Jersey (Figure 1).

It was established in 1996 with two cabled underwater nodes placed in 15-m of

water (hence the "15" in LEO–15), which provide continuous sampling of physical

and optical properties of the water column above (see von Alt, 1997).

The Coastal Predictive Skill Experiments held each summer from 1998–2001

intensively sampled a 30×30 km area surrounding the original LEO–15 site

(Schofield et al. 2002; Glenn et al. 1998). The experiments are a joint project

between the Coastal Ocean Modeling and Observation Program (COMOP) and the

Hyperspectral Coastal Ocean Dynamics Experiments (HyCODE).

Coastal plumes have been previously observed in the LEO−15 region (e.g.

Yankovsky and Garvine 1998; Yankovsky et al. 2000; Chant et al. 2004; Kohut et al.

2004; Münchow and Chant 2000; Garvine 2004), and other reports of the 2000

research study include Johnson et al. (2003); Chang (2002); and Glenn et al. (2004).

The instrument and survey configuration for the 2000 experiment is detailed in

Figure 3-1. The original LEO–15 nodes (A & B) are complemented by moorings at six

stations in a cross-shore line extending over the shelf from the mouth of Great Bay
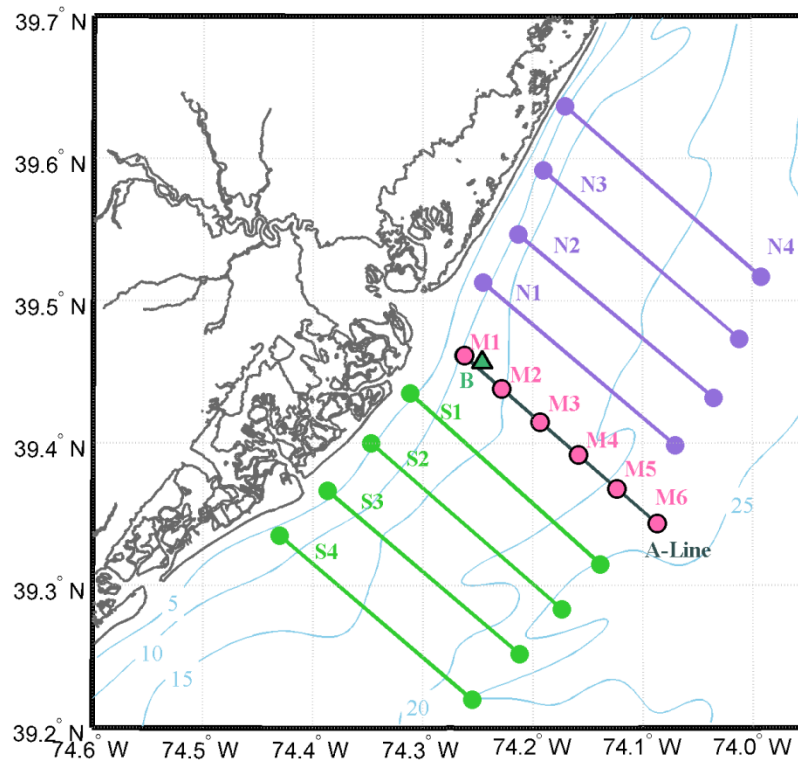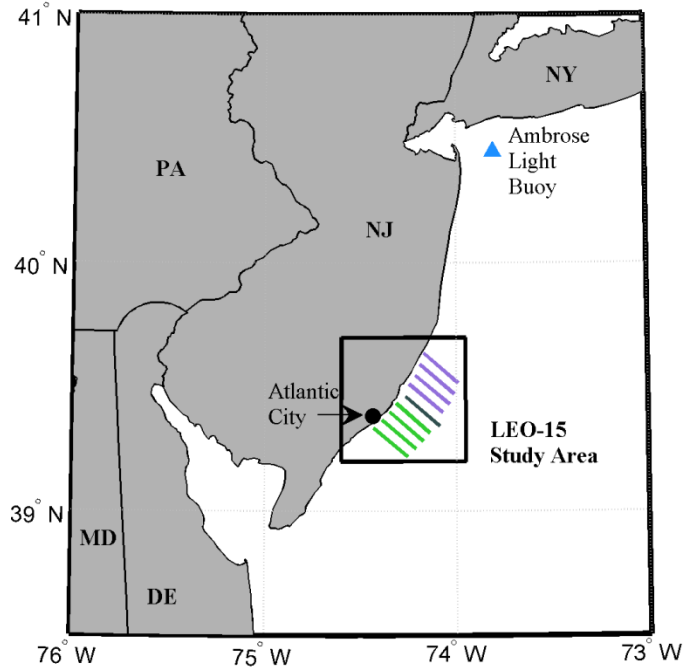
Figure 3-1: (a) The LEO–15 study area and (b) details of 2000 Coastal Predictive Skill Experiment (CPSE) set up: moorings (M1–M6), node (B) and ship tracks (A, S1–S4, N1–N4). The outline of (b) is displayed in (a).

(A-Line). The RV *Caleta* traversed the nine cross-shelf transects: four to the north (N1–N4), and four to the south (S1-S4). The transects extend to between 20–25 km offshore.

3.3 Momentum Balance

A simplified set of the equations of motion, commonly applied to coastal regions is

$$\frac{\partial u}{\partial t} - fv = \frac{1}{\rho_0}\frac{\partial p}{\partial x} + \frac{1}{\rho_0}\frac{\partial \tau^x}{\partial z}$$

$$\frac{\partial v}{\partial t} + fu = \frac{1}{\rho_0}\frac{\partial p}{\partial y} + \frac{1}{\rho_0}\frac{\partial \tau^y}{\partial z}$$

3-1

where u and v are the velocities in the cross-shore (x) and alongshore (y) directions; t is time, p is pressure, ρ_0 is a reference density, τ is the stress term, f is the Coriolis parameter and z is the vertical axis. (See §9.3.1 for further details of these equations).

The depth-averaged version of Eq. 3-4 is

$$\underbrace{\frac{\partial \hat{u}}{\partial t}}_{\text{acceleration}} \quad \underbrace{- f\hat{v}}_{\text{coriolis}} \quad + \underbrace{\int_{-h}^{0}\frac{1}{\rho_0}\frac{\partial p}{\partial x}\,dz}_{\text{pressure gradient}} \quad \underbrace{-\frac{\tau^{sx}}{\rho_0}}_{\text{wind stress}} \quad \underbrace{+\frac{\tau^{bx}}{\rho_0}}_{\text{bottom stress}} \quad = \quad 0$$

$$\underbrace{\frac{\partial \hat{v}}{\partial t}}_{\text{acceleration}} \quad \underbrace{+ f\hat{u}}_{\text{coriolis}} \quad + \underbrace{\int_{-h}^{0}\frac{1}{\rho_0}\frac{\partial p}{\partial y}\,dz}_{\text{pressure gradient}} \quad \underbrace{-\frac{\tau^{sy}}{\rho_0}}_{\text{wind stress}} \quad \underbrace{+\frac{\tau^{by}}{\rho_0}}_{\text{bottom stress}} \quad = \quad 0$$

3-2

where $\hat{u}$ and $\hat{v}$ are the depth-averaged velocities.

For the mooring data, time series of the acceleration and Coriolis terms are calculated from ADCP velocities, the wind stress is calculated from wind speed data, and the bottom stress is estimated using:

$$\tau^{by} = \rho_0 \, r \, u_{\text{bot}}$$

3-3

where $r = 5 \times 10^{-4}$ m s^{-1} is the linear bottom friction coefficient. The pressure gradient is now estimated as the residual of the other terms.

3.4 Data Collection and Processing

Time-series data used in this study are collected from Moorings 2–5 and node B. Each mooring housed a bottom-mounted acoustic Doppler current profiler (ADCP) which measured horizontal current velocity; and Moorings 2 and 4 supplemented this data with temperature profiles from thermistor strings. Bottom salinity data were collected from node B. Wind speed, discharge from the Hudson River, local air temperature and rainfall data were obtained from online databases.

Ship transects provided current velocities from a hull-mounted ADCP, and temperature, salinity, and density from a towed undulating CTD. Data were also collected from towed instruments, and variables include temperature, salinity, pressure, fluorescence and current speed.

Table 3-1: Mooring and node positions.

Instrument	Latitude (ºN)	Longitude (ºW)	Depth (m)	Distance Offshore (km)
Mooring 1	39:27.69	74:15.72	10	4.4
Mooring 2	39:26.30	74:13.70	15	8.3
Mooring 3	39:24.90	74:11.60	18	12.3
Mooring 4	39:23.50	74:09.48	21	16.3
Mooring 5	39:22.08	74:07.40	22	20.2
Mooring 6	39:20.62	74:05.20	25	24.4
Node B	39:27.40	74:14.75		5.8

All vector data (wind speed and current velocity) are rotated into an alongshore/cross-shore coordinate system: with the positive along-shore axis lying 41º degrees clockwise from north. All time-series data are low-passed with a cutoff period of 36 hours, to remove tidal and inertial signals (at this latitude, the inertial period is 18.9 hours). All times are reported in Coordinated Universal Time (UTC).

3.4.1   Mooring Data and Tidal Analysis

The thermistor strings record temperature at every 1 m depth, at seven-minute intervals. These values are interpolated onto the same time intervals as the moored velocity dataset. Bottom salinity at node B is recorded at hourly intervals for 42 days, from 14 July–30 August. The depth at this location is approximately 15 m. Current velocity is measured by the ADCPs in 1-m bins, starting from 1.5 m above the sea-floor and extending to approximately 5 m below the surface. Processed data

ranges from 10 July–7 August, that is, 27 days of data in total, recorded at 30-minute intervals.

Data are detided using T–Tide, a tidal analysis package for MATLAB (Pawlowicz et al. 2002). The dominant tidal frequencies are M_2, O_1, K_1 (refer to §2.6 for definitions), along with the lunisolar synodic fortnightly constituent M_{sf}, with a period of 14.765 days.
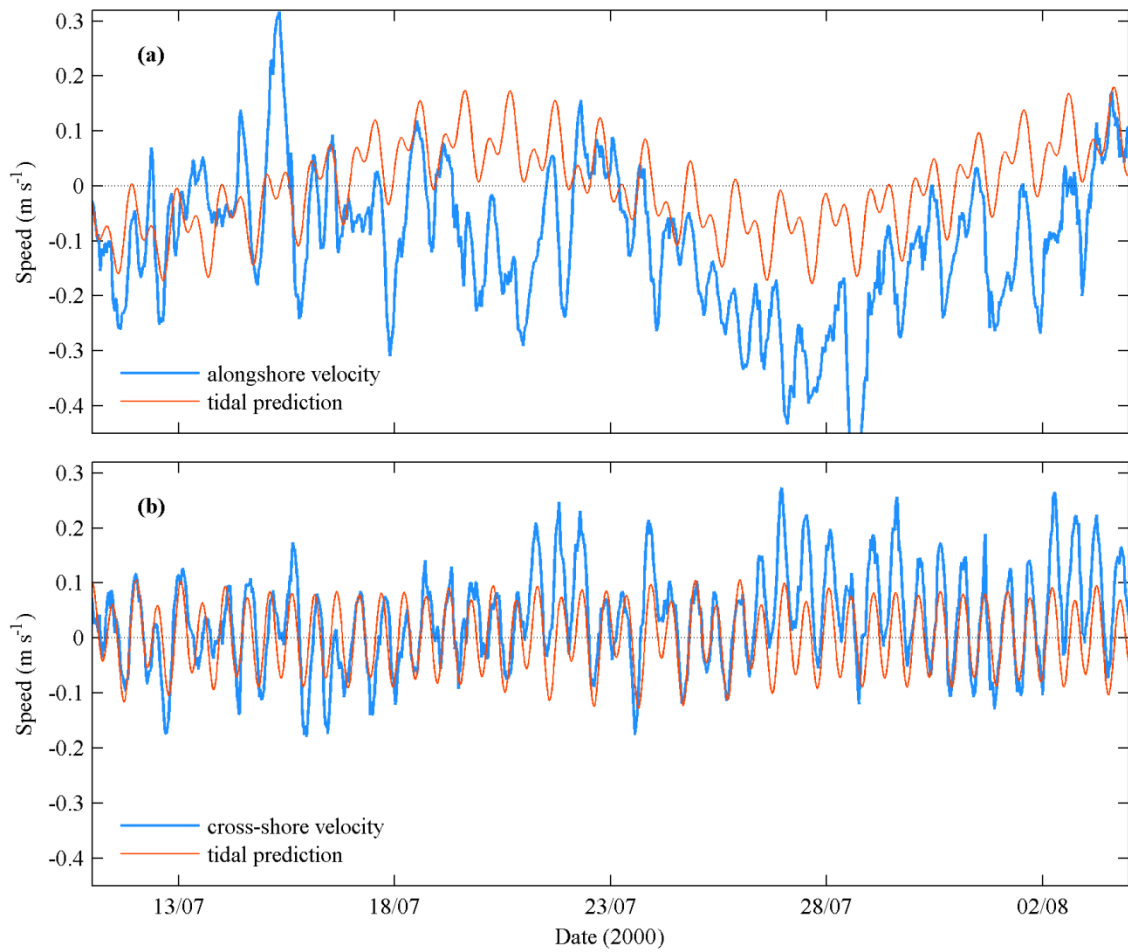
Figure 3-2: (a) Alongshore and (b) cross-shore current speeds (m s^{-1}), with tidal predictions at 5.5 m from Mooring 2.

The alongshore tidal prediction is small compared to the alongshore velocity (Figure 3-2a), however the cross-shore tide is a significant proportion of the cross-shore velocity (Figure 3-2b).

3.4.2   Ship Data

The RV *Caleta* collected data along 35 transects in total, during 10–29 July. Temperature and salinity were collected using a towed, undulating CTD profiler, and current speeds were measured by a ship-mounted ADCP.

Each "cast" from the towed, undulating CTD profiler is treated as a vertical profile and interpolated onto a fixed grid. Any very short casts are deleted. Depths near the surface with many gaps are also deleted, and the remaining gaps are filled using linear extrapolation.

Current speed data from the ADCP is rotated to align with the coastline, and detided using tidal data derived from the moored ADCP records. The time-series current record is not quite long enough to resolve the spring/neap cycle (29.53 days are required), so just three days either side of the transect mid-time are used to fit the diurnal and semi-diurnal components. Three days is insufficient time to resolve the K_1 and O_1 constituents, but the estimated K_1 amplitude will include the effect of the O_1.

Table 3-2: LEO-15 ship tracks.

Adaptive sampling lines	Starting coordinates	Ending coordinates
N4 (North 4)	39:38.2ºN, 74:10.2ºW	39:31.0ºN, 73:59.5ºW
N3 (North 3)	39:35.5ºN, 74:11.4ºW	39:28.4ºN, 74:00.7ºW
N2 (North 2, formerly N-Line)	39:32.8ºN, 74:12.8ºW	39:25.9ºN, 74:02.1ºW
N1 (North 1, formerly X-Line)	39:30.8ºN, 74:14.7ºW	39:23.9ºN, 74:04.2ºW
A-Line	39:27.7ºN, 74:15.8ºW	39:20.6ºN, 74:05.2ºW
S1 (south 1, formerly Y-Line)	39:26.1ºN, 74:18.7ºW	39:18.9ºN, 74:08.3ºW
S2 (south 2, formerly Z-Line)	39:24.0ºN, 74:20.8ºW	39:17.0ºN, 74:10.4ºW
S3 (south 3)	39:22.0ºN, 74:23.2ºW	39:15.1ºN, 74:12.7ºW
S4 (south 4)	39:20.1ºN, 74:25.8ºW	39:13.2ºN, 74:15.3ºW

Table 3-3: RV *Caleta* ship tracks.

Date	Track
10 July	A, S1,
11 July	S1, A, S2, S1
13 July	S1
14 July	S1, S2
17 July	N1, N2, N3
18 July	N1, N2, N3
21 July	S1, S2
24 July	N1, S2
27 July	N1, S1, S2, S3
28 July	N1, S1, S2, S3
29 July	S1

No obvious cross-shore pattern exists to justify interpolating between moorings, so the mean tidal velocity across the mooring was subtracted from the ship-mounted ADCP velocities. Since mooring data did not begin until 14 July, tracks collected on 10–13 July were detided using the first three days of the mooring velocities.

3.4.3   Meteorological Data

Air temperature and rainfall data (Figure 3-3) for Atlantic City, New Jersey were obtained from the National Oceanic and Atmospheric Administration (NOAA)'s National Climatic Data Center (Station GHCND:USW00013724). Data include daily precipitation totals and minimum and maximum daily air temperature.

Wind data from the weather buoy at Ambrose Light, New York (Station ALSN6, 40.450 N 73.800 W) was downloaded from the NOAA National Data Buoy Center online database (located at: http://www.ndbc.noaa.gov/). Wind speeds and directions are reported in 8-minute averages. Wind stress (Figure 3-3) is calculated using the method of Large and Pond (1981), and rotated to align with the coast.

Winds are predominantly alongshore and most frequently (and with the strongest winds), blow to the north.
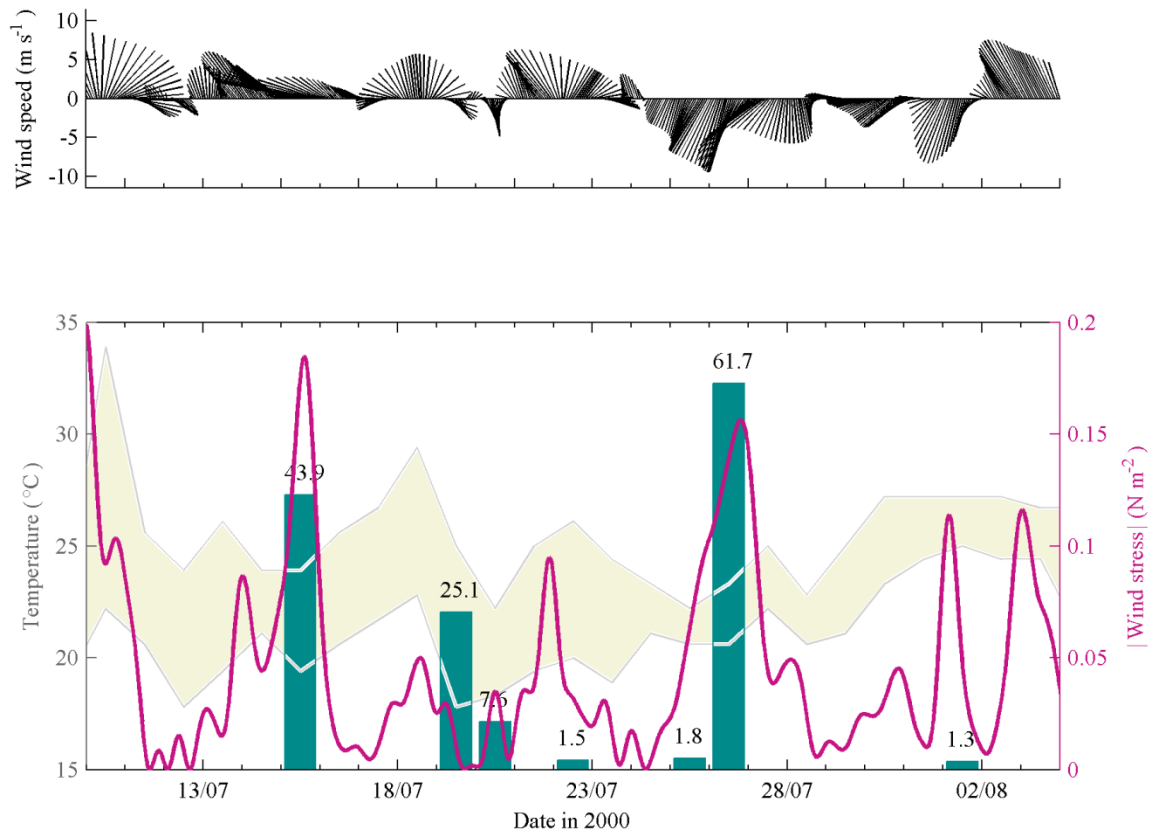
Figure 3-3: (a) Low-passed wind speed vectors rotated to an alongshore/cross-shore coordinate frame: positive y is wind directed upshore, and positive x is directed off-shore. Note that data is decimated here for a clearer view. (b) Air temperature range (gray shading), wind stress magnitude, and rainfall; during 10 July–4 August 2000.

3.4.4   River Discharge

The mean annual Hudson River discharge into the ocean V_H has been estimated by Ketchum et al. (1951), as

$$V_H = \overbrace{V_{GI}}^{\text{upper Hudson}} + \overbrace{1.629 \times V_{GI}}^{\text{lower Hudson}} + \overbrace{V_{Ra}}^{\text{Raritan}} + \overbrace{0.097 \times V_{GI}}^{\text{all other rivers}}$$
$$= 1.726 \times V_{GI} + V_{Ra}$$

3-4

Where V_{GI} is the volume discharge measured at the U.S. Geological Survey (USGS) gauge at Green Island, New York and V_{RA} is the discharge of the Raritan River.

The Green Island gauge was unfortunately not in action for a few months in 2000, during the time period of this study. Instead, discharge from two gauges further upstream at were used: at the Mohawk River recorded near Cohoes V_C, and at the Hudson River near Fort Edward, New York V_{FE}. The discharge at Green Island is 1.3 times the sum of these locations (Chant et al. 2008), so the new estimate is:

$$V_H = 1.726 \times \left[1.3 \times \left(V_C + V_{FE} \right) \right] + V_{Ra}$$
$$= 3.026 \times \left(V_C + V_{FE} \right) + V_{Ra}$$

3-5

Daily mean river discharge from these three gauges was obtained from the USGS database located online at: http://waterdata.usgs.gov/nwis/gw), and the total Hudson River discharge calculated using Eq. 3-2.

It should be noted that this is only a rough estimate of the total discharge on any given day since Eq. 3-1 is derived from annual mean data. Cooper et al. (1988) state the upper Hudson River and the Mohawk contribute approximately 80% of the total

annual freshwater output of the Hudson River, whereas Abood (1977) calculate a

value of approximately 70%, and Ketchum et al. (1951) use a factor of only 61%

(= 1/1.629). Clearly there is yet to be agreement on this relation.

The freshwater discharge in July from the Hudson River was greater in 2000 than in

the neighboring years, mostly due to one large event during 16–19 July. The

discharge on this day was over three times the monthly average, and much greater

than peaks seen in July in either the year before or after. The 16–19 July discharge

reached nearly 1700 m^3 s^{-1} compared with the 300–400 m^3 s^{-1} during the rest of the

month, and the 500 m^3 s^{-1} monthly average. A second larger discharge began at the

very end of the month (31 July–4 August) but it is not considered here as no current

measurements are available during that time.

3.5 Daily Observations

The S1 line is chosen to illustrate the progression of the plumes, since it was

traversed the most times (13 times in total) over the month of July. Ten transects

are chosen to represent the time variation in the towed CTD variables (salinity,

temperature, and calculated density (Figure 3-4)); and three transects are plotted to

illustrate along-shore and across-shore velocity recovered from the ship-mounted

ADCP (Figure 3-5).

3.5.1   Initial Conditions

Prior to the first survey, after a period of gentle to moderate downwelling winds on 7 July and into 8 July, winds turn to moderate to strong upwelling on 9 July–10 July (Figure 3-3). When the first day of ship surveys took place on 10 July, winds reach #5–6 on the Beaufort scale (a fresh to strong breeze) in an upwelling direction. Air temperatures are particularly warm, with a daily maximum of 34°C.

The temperature profile along track S1 (Figure 3-4a) shows the typical summertime structure: a warm surface layer above a sharp thermocline overlying considerably cooler waters. Here, the surface layer is 18–19°C, and the lower layer is around 12°C. The thermocline has a strong gradient: a 5−6°C change over just 2−3 m.   Lower salinity water (31.1) overlies saltier layer (31.8−32), with a pycnocline evident at 11.5 m depth. Small pockets of lower salinity water (30.7-31) lie just above the pycnocline. The density structure closely follows the temperature pattern.

Alongshore currents are positive (flowing up-shore: to the northwest) with a mean of 13 cm s^{-1} and cross-shore currents flow offshore in a surface layer (sloping down from 0−10 m deep), and flow onshore below this, in the classic upwelling pattern. Isotherms curve upwards toward the shore, indicating that cold water is being upwelled from below. Currents reach 36 cm s^{-1} at the surface and up to −21 cm s^{-1} below.

3.5.2   Plume I

On 11 July winds slacken to a variable light breeze, air-temperatures drop, and the along-shore current reverses to flow down-shore. A plume of lower salinity now extends across the shelf to over 15 km offshore at S1, and beyond 20 km at the A-Line. However, this is not apparent at the S2 line, to the south of these (not shown). This lower salinity water is likely a remnant of a Hudson River plume, commonly observed far down the coast from its original source. Across-shore currents are weak, with nearshore flow onshore at the surface and offshore at depth, in the typical downwelling regime. The surface waters are warming, and isotherms tilt down toward the coast as the surface layer deepens near shore with warm surface waters being downwelled.

A light breeze blows on 12 July, and increases slightly to a gentle, and later a moderate, upwelling breeze on 13 July. The wind blows consistently in an upwelling direction on 14 July, with still a gentle to moderate breeze. Air temperatures range from the high teens to the mid-twenties ($^{\circ}$C).

No ship surveys were undertaken on 12 July, however both 13 July and 14 July surveys (covering tracks S1 and S2) show little change to the extent of the plume. Both alongshore and cross-shore currents are light and variable. The surface layer continues to warm and the thermocline deepens.
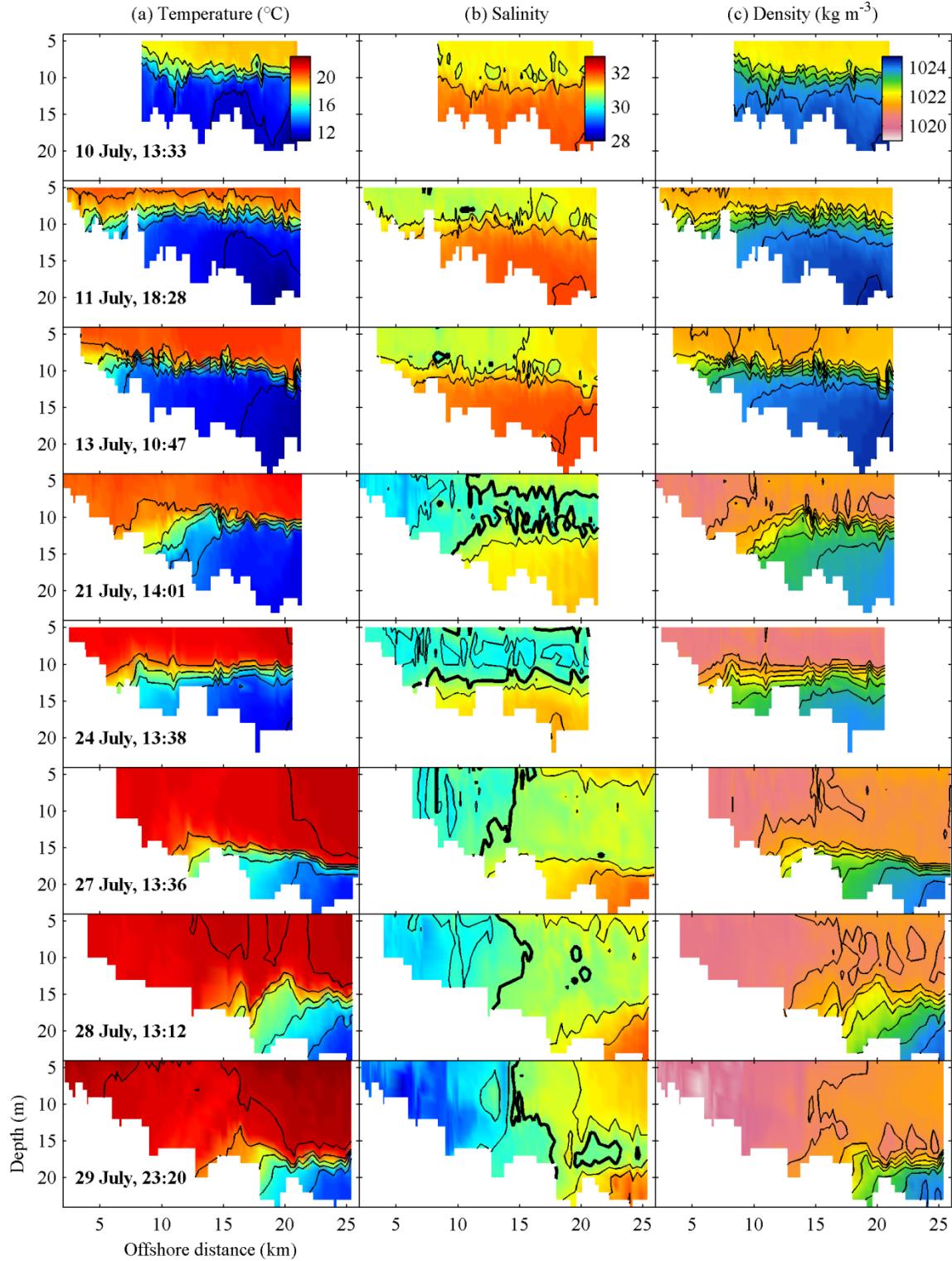
Figure 3-4: Successive transects of (a) temperature, (b) salinity, and (c) density from a towed CTD across Line S1 in July 2000. Isotherms are plotted at intervals of 2°C; isohalines are plotted at intervals of 0.5, with the 30.5 isohaline marked in bold; and isopycnals are plotted at intervals of 0.5 kg m⁻³. Times are in UTC.
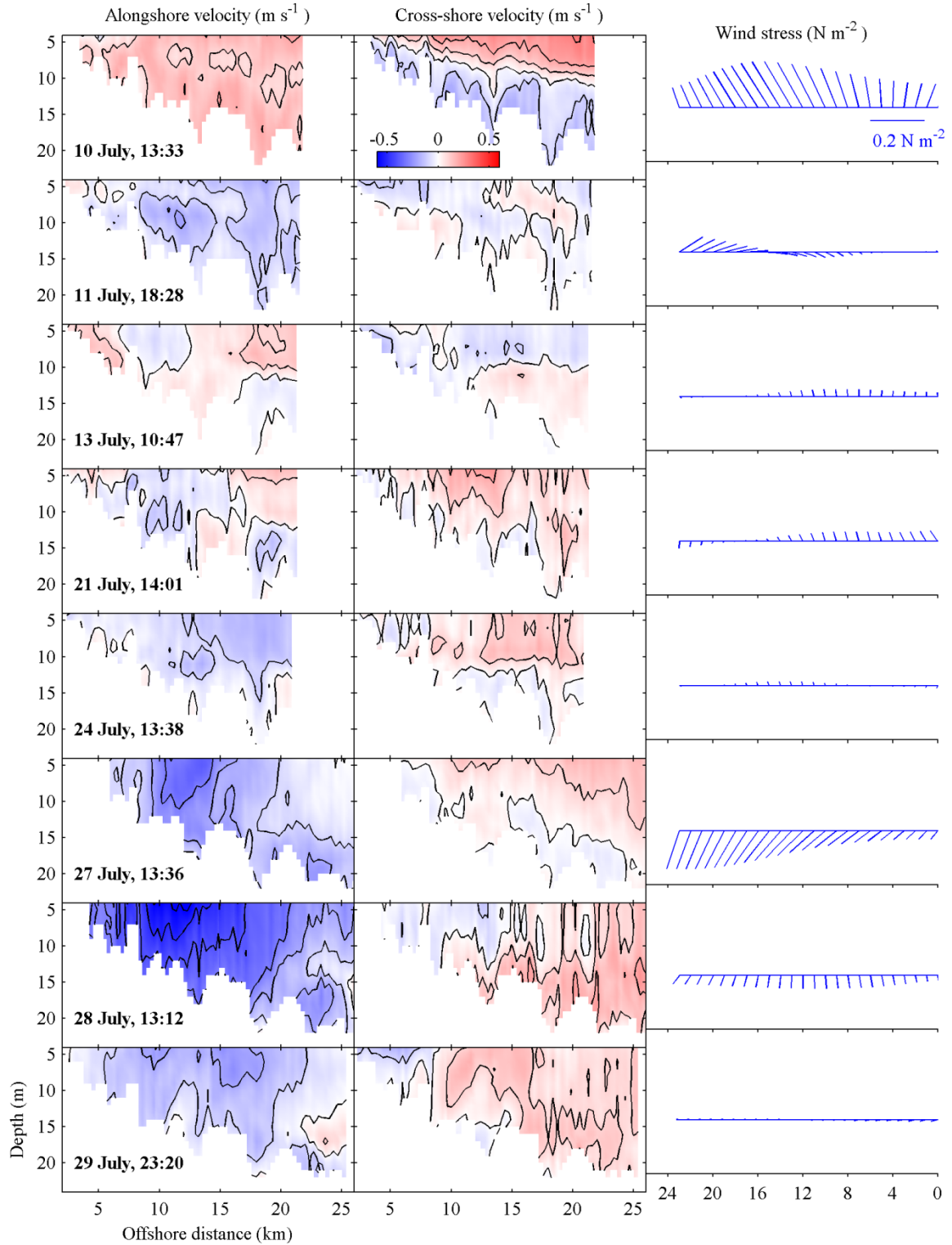
Figure 3-5: Successive ADCP transects showing the (a) alongshore and (b) cross-shore velocity components, along with (c) wind stress during the preceding 24 hours, calculated from wind speed at Ambrose Light, New York. Velocity contours are plotted in intervals of 0.1 m s⁻¹. Times are in UTC.

A density gradient near the off-shore edge of the plume is evident on 13 July. Cyclonic flow is evident around this patch of lower-density water (Figure 3-5): flow is upshore and onshore on the outer edge of this bulge, turning to onshore within it, and down shore on the near-shore side.

3.5.3   Upwelling Storm

A storm occurred on 15–16 July, bringing thunder & lightening, heavy rain and strong upwelling winds, to the study area; thus no ship tracks were attempted.

When ship operations resumed on 17 July, winds drop to a gentle downwelling breeze and air temperatures begin to rise. No S1 tracks were covered on 17–18 July: only the northern tracks were traversed. The plume has spread completely throughout the surface layer, with its outer edge no longer visible on any ship tracks (i.e. past 22 km offshore). Cool, upwelled water lies in the nearshore surface layer, and the thermocline intersects with the surface in the morning tracks.

3.5.4   Plume II

It was rainy and cold on 19–20 July, and the ship remained in dock during this time. Winds were gentle to light in the downwelling direction.

The first track made on the 21 July shows a new plume event: very low salinity water near the coast, and stretching out in subsurface layer right across the

transect. The surface layer is much deeper and cooler, with the thermocline now intersecting the sea-floor at around 7 km off shore in 15 m of water. The low salinity layer (within which the new plume resides) is also much deeper: extending to 15 m, with lower salinity water beneath. None of the lower layer saline waters remain at all.

Winds are upwelling during this time, and currents flow upshore near the coast and offshore, with a middle area of downshore velocity, corresponding to steep density gradients due to downwelled isotherms and isohalines on the edge of the plume.

After a few days of mostly upwelling winds, on 24 July, the lower salinity water has spread throughout the surface layer, and isotherms have risen near the coast. No vertical density gradients are apparent in the surface layer. Winds have relaxed, and the alongshore flow is down shore.

3.5.5   The Coastal Jet

Winds continue to be downwelling favorable through 25–28 July with heavy rain occurring on the 26 July. On the 27 July, transects show a very deep surface layer (the pycnocline now at 18 m, and intersecting the seabed at 15–20 km offshore. Near-vertical gradients in salinity exist 14 km offshore in the upper layer, as the plume once again hugs the coast. For the first time the coastal jet appears: downshore flows of up to 0.4 m s^{-1}. On the 28 July, the coastal jet is at its strongest, with flows up to -0.7 m s^{-1}. Onshore flow persists near shore, with an opposing

offshore flow beneath it. The upper layer continues to deepen. On 29 July, winds

cease, but after four days of sustained moderately-downwelling winds, the upper

layer now nearly completely fills the transect, with the pycnocline intersecting at 35

m, 20 km offshore.   The outer extent of Plume I (at least at the surface) is visible

once more, as well as that of Plume II, as waters are pushed onshore. As winds

recede, the downshore currents slacken a little, and the cross-shore Ekman layers

recede.

3.6 Time Series and Correlations

3.6.1   Time-series Mooring Data

Mooring and wind records (Figure 3-6) clearly show the upwelling storm of 15−16

July. Winds are strong, and cool waters reach toward the surface in the temperature

record, after a period of northward flow at mid-depths. When the bottom salinity

record begins on 15 July, the measurements are at the highest level seen, as the

more saline coastal waters and the plume are upwelled to the surface, and higher-

salinity waters from at depth are brought into the bottom layer. The alongshore

momentum balance (Figure 3-7) shows that the wind stress term is high, and the

pressure gradient term is weak.

The arrival of Plume II is very evident by the large dip in bottom salinity on 20 July,

after a strong downshore current flowing since 18 July. There are no strong winds

during this period, and the momentum balance indicates that the pressure gradient

is driving this flow, not winds. An upwelling wind event during 21−23 July reverses the flow, and bottom salinity increases once more.

The winds then turn to a sustained downwelling direction for several days over 24−29 July, and the along-shore flow is once more flows southward at all depths as the downshore jet. Cross-shore flow is offshore at all depths, and the bottom salinity steadily decreases (reaching its lowest value on 29 July), as the plume water is being downwelled. There is a peak in the wind stress term on 26−27 July, when the jet was observed to be the strongest in the ship transects, but it is still dwarfed by the pressure gradient term.

After a brief period of upwelling winds on 29 July, the jet slackens and cross-shore flow also weakens. The bottom salinity rises once more, and the pressure gradient term drops off.

The wind stress term only dominates the cross-shore momentum balance on 15 July, during the upwelling storm. During Plume II and the downwelling jet, the pressure gradient term is much larger, indicating that while the winds may set up the upwelling and downwelling regimes, the resulting density gradients and sea surface slopes are the main driving force for the alongshore flow.
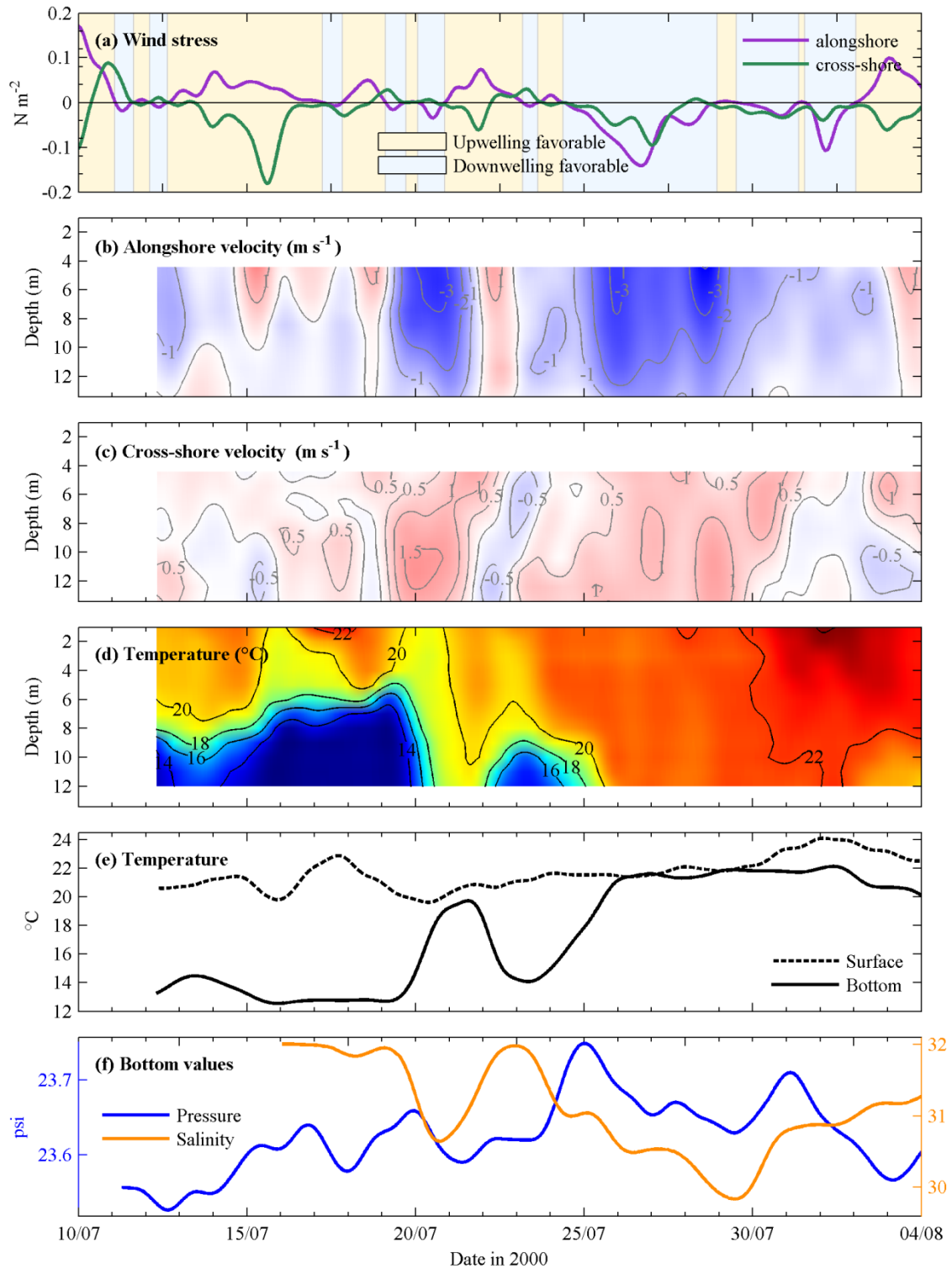
Figure 3-6: (a) Alongshore and cross-shore wind stress components, with downwelling and upwelling regimes shaded; (b) alongshore velocity, (c) cross-shore velocity, (c) temperature, (d) surface and bottom temperature, (f) bottom salinity and bottom pressure, all from Mooring 2.
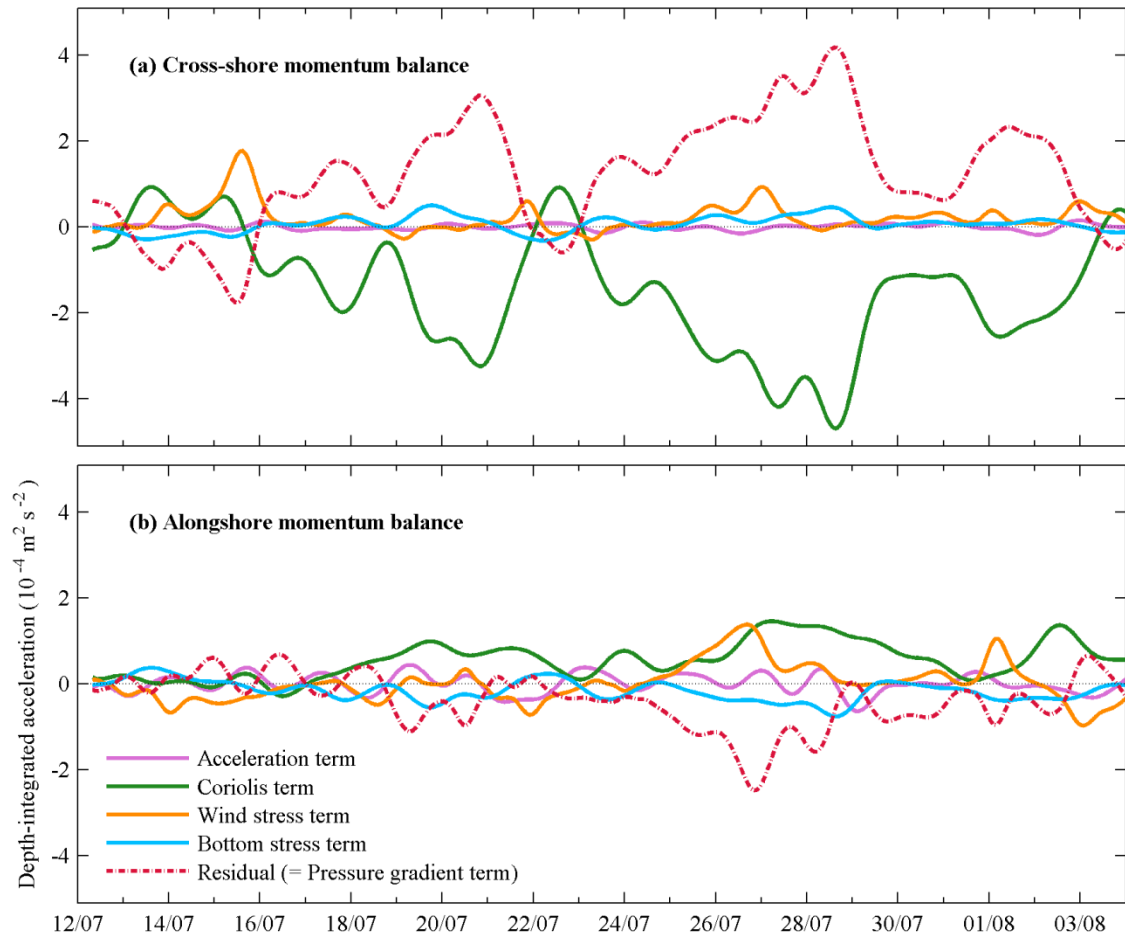
Figure 3-7: Terms in the (a) cross-shore and (b) alongshore momentum balance calculated from Mooring 2. Values are depth integrated accelerations.

A Hovmöller diagram (Figure 3-8) illustrates clearly the existence of an along-shore jet at two time intervals during the study period. The first instance occurs during 19−21 July, and the second, more sustained event, over 24–29 July.
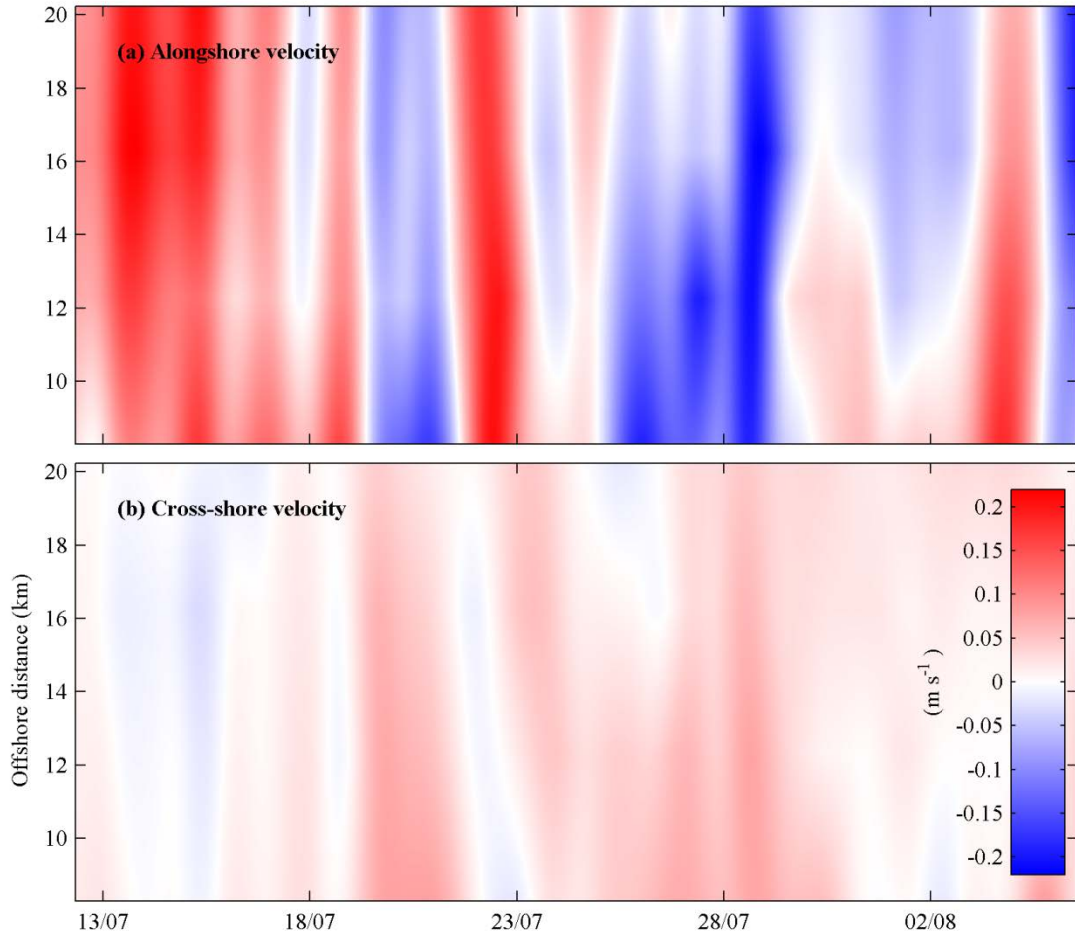
Figure 3-8: Hovmöller diagram of (a) alongshore and (b) cross-shore velocity over time and offshore distance (Moorings 2−5).

3.6.2   Correlations

The velocity/wind stress correlation is greatest at 41º degrees clockwise from north, and thus defined the axis used to split the cross-shore and alongshore components. Correlation coefficients (or, the normalized cross-covariance) of forcing variables (winds, bottom pressure, and the pressure gradient term) paired with observations related to the plume (bottom salinity, velocity) are calculated in order to examine the relative importance of the forcing terms.

Alongshore winds are consistently correlated with alongshore velocity at all moorings (and with both mean and surface velocity) with lags of around 10–12 hours. Correlation coefficients range from 0.56–0.78. Cross-shore velocity does not show a consistent correlation pattern, and cross-shore winds show none at all.

Bottom salinity lags the alongshore wind by 12 hours, with a correlation coefficient of 0.54, and it lags the pressure gradient term by seven hours, with a correlation coefficient of 0.67. The pressure gradient term lags the bottom pressure at both Mooring 2 and Mooring 4 by about one day, with correlation coefficients of 0.72–0.77.

There is a correlation between river discharge and salinity at 11, 12 and 13 days, with correlation coefficients of 0.47–0.49. Periods of several weeks for Hudson River discharge events to reach this region have been reported (e.g. 40 days in Münchow (1992)). While a correlation with this lag is not apparent from correlation coefficients, there does appear to be an approximately 45 day lag between peaks in

Hudson River discharge and lows in the bottom salinity record from a visual

examination (Figure 3-9).
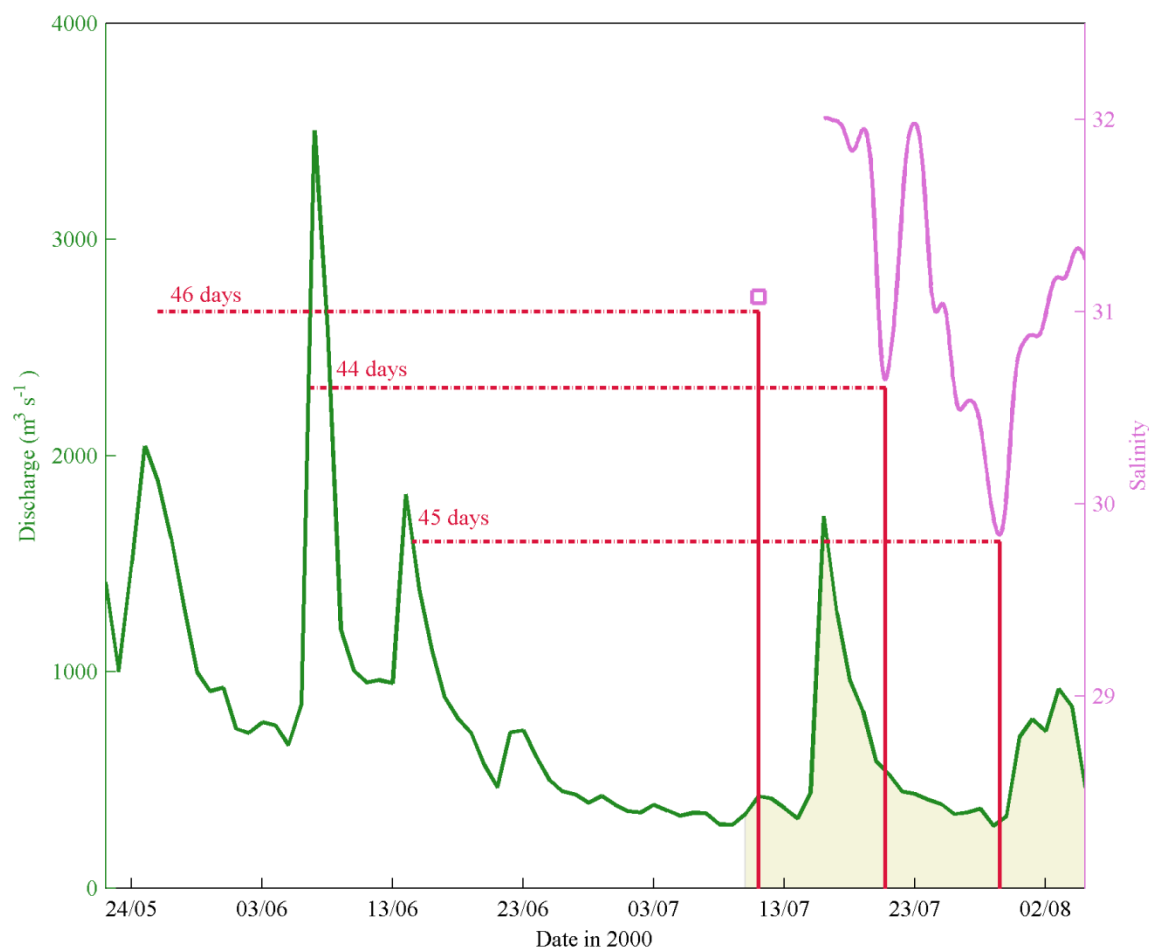
Figure 3-9: Hudson River daily mean discharge (green solid line) and bottom salinity at Node B (purple solid line). The study period (10 July–4 Aug) is shaded, and the advent of the 3 plumes is marked in red (solid lines). A data point is included to represent the first plume on 11 July, which is prior to the first salinity measurement. Its salinity value is arbitrary. The lag from a peak in river discharge is marked and labelled (red dashed lines).

3.7 Summary and Discussion

Two low-salinity river plumes and a downwelling jet were observed during the LEO-15 study period. These events are clearly defined in data from both ship transects and moored instruments. A momentum balance analysis indicates that while wind stress plays a part in the formation of upwelling and downwelling regimes, the pressure gradients within the regimes are the more important factor in sustaining the circulation pattern. The source of the low-salinity plumes is assumed to be from peaks in the Hudson River discharge, approximately 45 days previously. During upwelling winds, the river plume tends to spread out over surface layer.

There does not appear to be a strong correlation between the Hudson River discharge and the jet appearance. While alongshore velocity and wind stress are correlated, a much stronger correlation exists between the pressure gradient term and alongshore velocity. The jet that does occur appears to be the result of a cross-shelf density gradient set up after mixing of the water column by strong winds. This process results in a well-mixed water column, but with a strong cross-shore gradient. The pressure gradient term in the momentum balance is much stronger than the wind stress term during this time.

A moored string of CTDs would clearly be very helpful in future studies to establish a time series profile of salinity and density. This would allow the pressure gradient term to be examined in more detail: the baroclinic component (based on density) could be calculated, and residual term would then be the barotropic (sea surface

slope) term. Underwater autonomous vehicles (e.g. gliders) that can operate during

rougher conditions when ships are unable to leave port, would also contribute

significantly to such observational studies.

4 Case Study: Glider Observations of the MAB Shelf/slope Salinity Front

4.1 The Shelf/slope front

The properties of the MAB shelf/slope front have been investigated many times (e.g. Chapman 1986; Houghton et al. 1994; Lozier et al. 2002; Ou 1983). Due to the large variability in the position of the front and the associated jet, most studies have presented either an average of repeated transects over a short time scale (e.g. Gawarkiewicz et al. 2004; Burrage and Garvine 1988; Pickart et al. 1999) or a seasonal climatology from many years of data, (e.g. Linder and Gawarkiewicz 1998).

Data collected during the pilot study for the Shallow Water 2006 (SW06) experiment provide the motivation for developing a three-dimensional climatology of the region. Significant cross-shore variation in the position of the front within individual transects is observed in just the short two week period, while concurrent cross-shore glider tracks show considerable variability between even closely spaced transects. Climatologies that are heavily averaged in both space and time may be misleading, especially if the mean position of the front is later interpreted to be its typical (i.e. relatively static) location.

4.2 The Shallow Water 2006 Experiment

The Shallow Water 2006 experiment was an interdisciplinary study funded by the office of Naval Research and Defense Research Canada. A large collaboration of investigators studied the oceanographic features and processes of a region of the MAB near the 80-m isobath off Atlantic City, New Jersey (Figure 4-1). The aim of the study is to determine the effect of the ocean environment on shallow water acoustics (Tang et al. 2007).
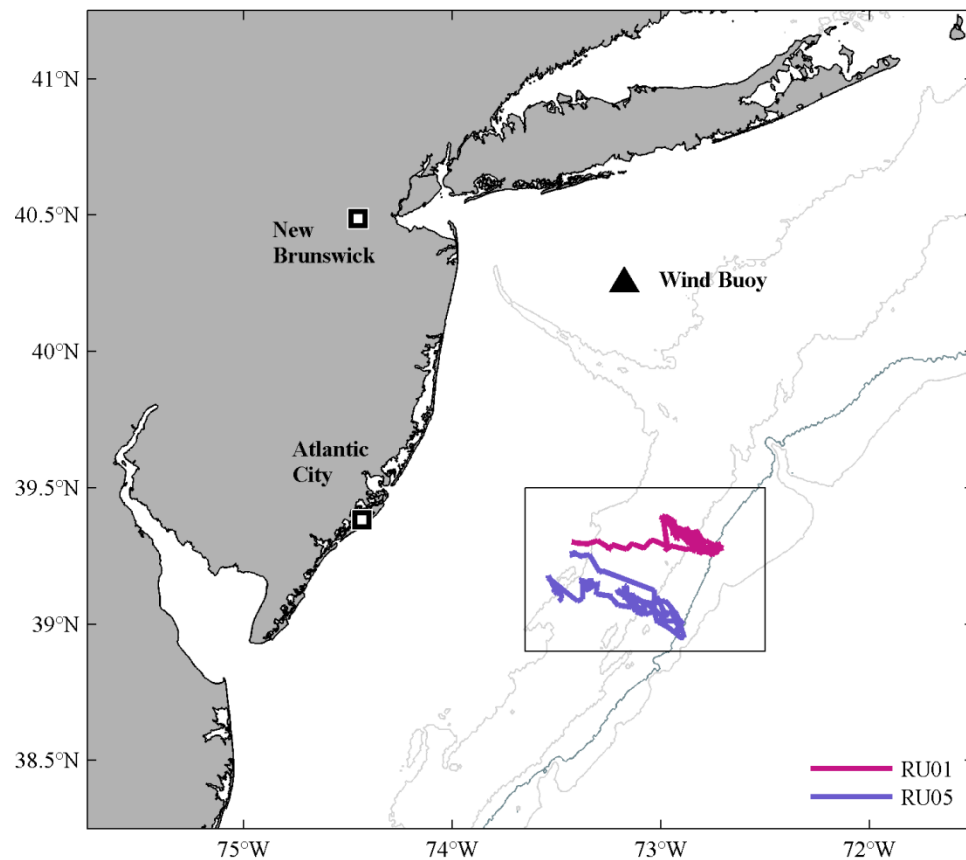
Figure 4-1: The SW06 pilot study region, also showing the RU01 and RU05 glider tracks and the location of the wind buoy. Isobaths plotted are 50 m, 75 m, 100 m (dark) and 200 m. The outlined region is enlarged in Figure 4-2.

The structure of the MAB shelf-break front is an important focus of those studying

the physical oceanography of the region, due to the significant impact such fronts

have on acoustic propagation. The speed of sound in water is highly dependent on

temperature, and to a lesser extent on salinity, and therefore acoustic waves may

change direction abruptly in regions with strong temperature and/or salinity

gradients.

In July 2005, a pilot study for the project (SW05) was conducted to get a preliminary

view of the of the physical properties of the region.

4.3 Data Collection

Two gliders were deployed by the Rutgers University's Coastal Observation Ocean

Laboratory (COOL), near the shelfbreak offshore from Atlantic City, each traversing

a transect perpendicular to the local isobaths. One glider (RU01) was located at

approximately 39°20'N and the other (RU05) at 39°10'N, 40 km to the south. Seven

cross-shore tracks were made by each glider between July 13–28, with RU01

including a longer transect on the initial outward journey. Transects ranged

between 5–60 km in cross-shore distance, with the majority being about 30 km long.
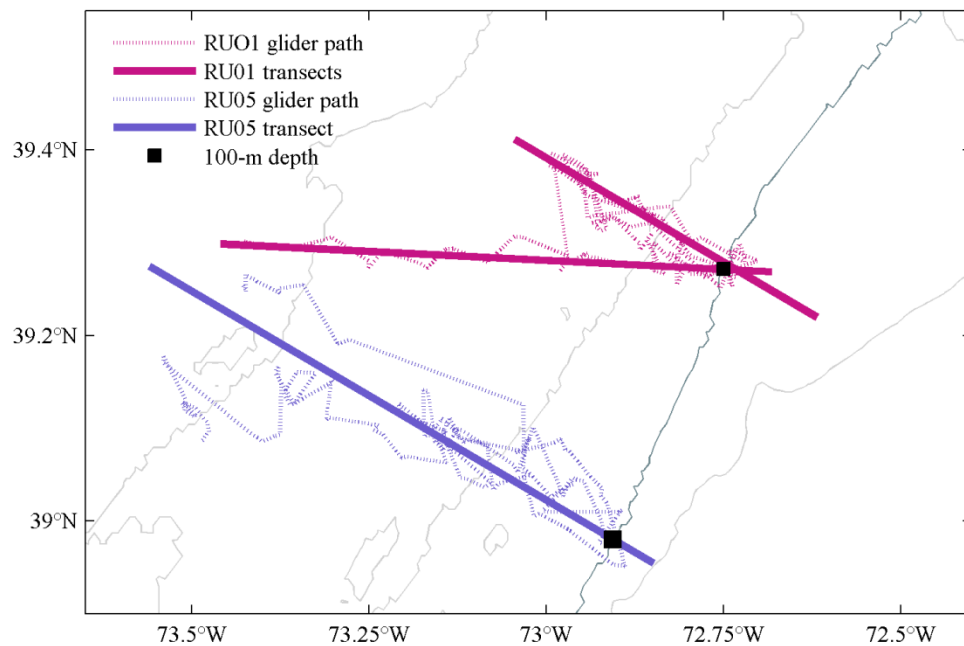
Figure 4-2: `RU01` and `RU05` glider tracks from 13–28 July 2005 and with the superimposed projection lines used to estimate distance from the 100-m isobath.

For comparative purposes the zig-zag track of the gliders is projected onto a straight line that lies perpendicular to the 100-m isobath (except for the first `RU01` transect which ran east-west) (Figure 4-2). Hereafter, "transects" refers to the glider paths projected onto a straight lines perpendicular to isobaths. Distances are measured from the 100-m isobath, with positive values toward shore.

Supporting data are available from CODAR, anemometers, and satellites provide surface velocities, wind speed, and sea surface temperature (SST), respectively. An estimate of the depth averaged velocity can be made from the movement of the glider, and the low passed depth average of this estimated velocity is given for both
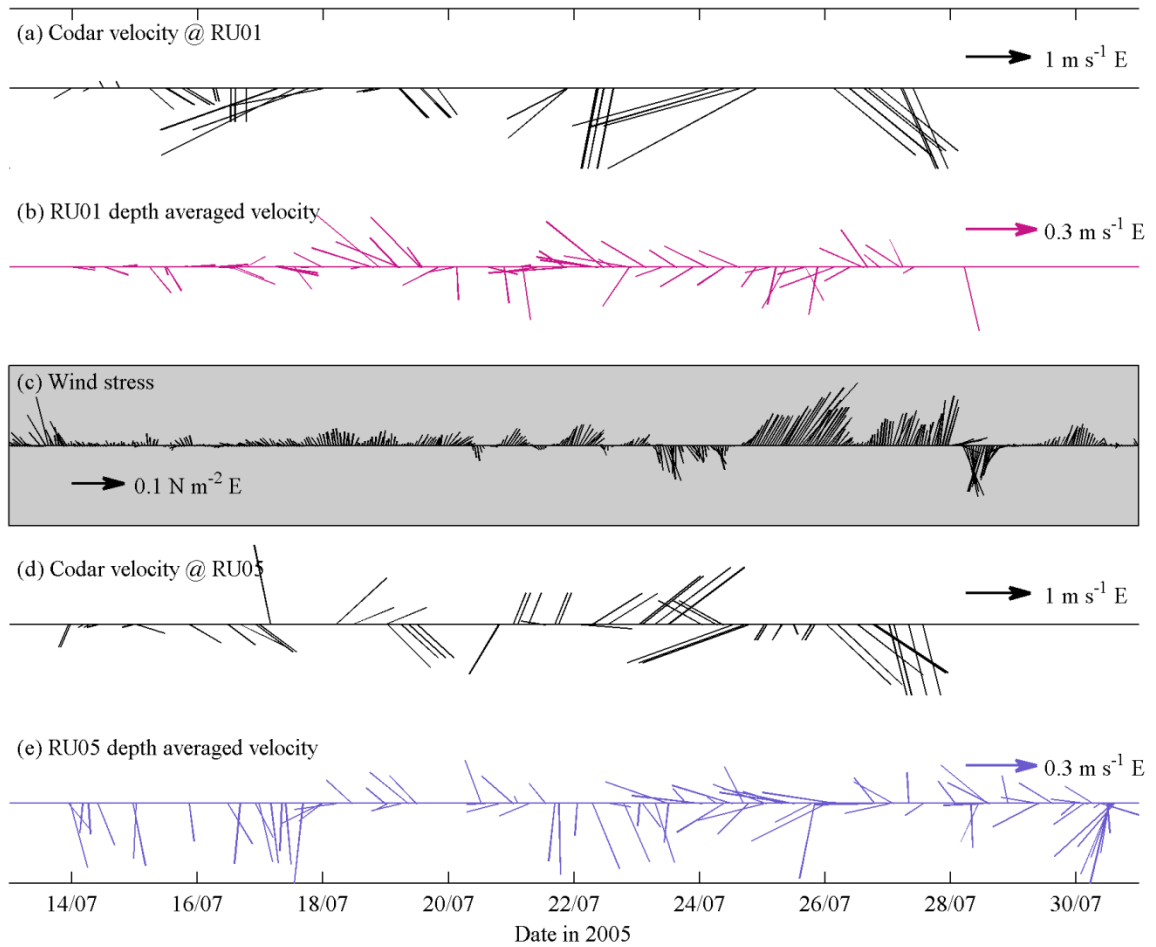
Figure 4-3: Along-track velocities and wind stress. CODAR velocity is interpolated along (a) the RU01 track and (d) the RU05 track. Depth average glider velocity estimates are plotted for (b) RU01 and (e) RU05, and the wind stress at NOAA # 44025 (near Long Island) is shown in (c). All current and wind speeds indicated give the direction they are travelling *to*.

RU01 and RU05 transects (Figure 4-3e). CODAR velocities (Figure 4-3a & d) are obtained from daily-averaged de-tided data, and are located at the RU01 glider position at each time. Wind stress (Figure 4-3c) is calculated from wind speeds obtained from a nearby meteorological buoy (NOAA #44025) located near Long Island (see Figure 4-1).

4.4 Initial Observations

The initial `RU01` glider east-west track is a 60-km long profile covering depths of approximately 50–100 m, and shows the entire frontal region (Figure 4-4a, track #1.1). The glider traversed this distance in four days, from 13–17 July. During this period winds are directed north/northeastward and surface CODAR currents are negligible (Figure 4-3a).

A strong thermocline exists below a warm surface layer (Figure 4-5a, track #1.1). This surface layer extends down to 20 m depth with temperatures above 18°C. Temperature gradients of up to 5°C are present in the thermocline.

A distinct salinity front is apparent with a corresponding weak temperature front. The inshore waters are cold and fresh (temperature is 8–12°C; salinity is 32–34), and the offshore waters are warmer and saltier (temperature is 13–14°C; salinity is 34–34.5). The foot of the salinity front is located at the 60-m isobath with a surface outcrop at approximately the 100-m isobath (40 km distant). Further offshore, beyond the 75-m isobath, cold salty (>35.5) water is seen at depth.

4.5 The Movement of the Salinity Front

Subsequent transects (Figure 4-4a) show considerable displacement of both the surface outcrop and the foot of the salinity front.

By 18 July the surface outcrop of the salinity front is displaced by over 12 km, now appearing to the west of 17 km (onshore of 100-m isobath). The glider does not venture further west of this position until track #1.4, and now the front is clearly seen. Over the next few days, fresh water moves back out over the shelf-break. Winds switch to the southeast for a brief period on 20 July and again on 21 July (Figure 4-4b), and CODAR surface currents are seen moving in the same direction (Figure 4-5b). Strong south-easterlies blow during 23–24 July, and surface currents flow at 90° to this, moving southwestward. On 25 July, the winds abruptly switch direction, and blow steadily and strongly to the northeast for three days. Surface currents during this time are again at right angles to the wind, this time flowing to the southeast. By 27 July shelf waters extend right out to the 100-m isobath (and beyond) in a layer reaching to 50–60 m depth. The slope waters still extend out to 20 km in the lower layer, although the foot of the salinity front is at 12 km, more than 20 km farther off-shore than in the initial transect.

In comparison, the RU05 glider, traversing a parallel line only 40 km to the south, does not show the offshore movement of shelf water (Figure 4-4c; Figure 4-5c). The initial RU05 transect (Figure 4-4c, track #5.1) shows a similar pattern to the initial RU01 line, but with slope water around the 100-m isobath. Succeeding transects shows a two-layer system with salty water extending much higher than at the RU01 line, with the final transect showing the salt front touching the bottom at around 32 km.

A similar pattern in temperature is observed in both `RU01` and `RU05` tracks (Figure 4-5), with cool water generally corresponding to low-salinity water; but with a much less distinct frontal region.

4.6 What Causes the Movement of the Salinity Front?

4.6.1 Winds and Currents?

The depth-averaged velocity along the `RU01` glider track (Figure 4-3b) is weakly southeast and eastward during 13–17 July, while along the `RU05` track (Figure 4-3e), flow is more strongly south/southeastward. During 17–21 July the depth-averaged current flows northwestward, then followed by a period of southward flow once more, before switching back to northwestward flow for the last few days of the deployment. However, there is a two-day lag between the two locations, and a fairly strong southward tendency to the flow at the `RU05` transect is not seen at `RU01`. Without detailed and reliable velocity measurements the shelf-break jet is not resolved.

CODAR surface velocity (Figure 4-6) from 23 July highlights the variability in both magnitude and direction of MAB surface currents over fairly short spatial scales.

4.6.2 Influence of the Hudson River Discharge?

It is unlikely that freshwater discharge from the Hudson river would affect the shelf/slope front at 90 km offshore, however, it is worth noting that very high discharge was recorded in the final two weeks of June (Figure 4-7), prior to this study.

The change in freshwater transport during the length of the glider deployment is compared to this river output. The mean freshwater discharge rate from the Hudson River during the SW06 study period was 290 m^3 s^{-1}. The change in freshwater content in one transect for a unit length in the alongshore direction is calculated, and the alongshore distance needed to discharge the river freshwater volume at this rate is estimated. For the RU01 line, the freshwater volume increased with time, and the rate corresponded to an alongshore length of 81 km. For the RU05 line, the freshwater volume decreased with time, and corresponded to a "negative" distance of 88 km.

These calculations are based on the assumption that freshwater exchange occurs in the across-shore direction. They include no prediction of the fate of the freshwater: without velocity data, there can be no conclusion as to whether any of the freshwater is being permanently transported on- or off- shore, or whether it simply reflects a continual fluctuation in the position of the shelf/slope front.
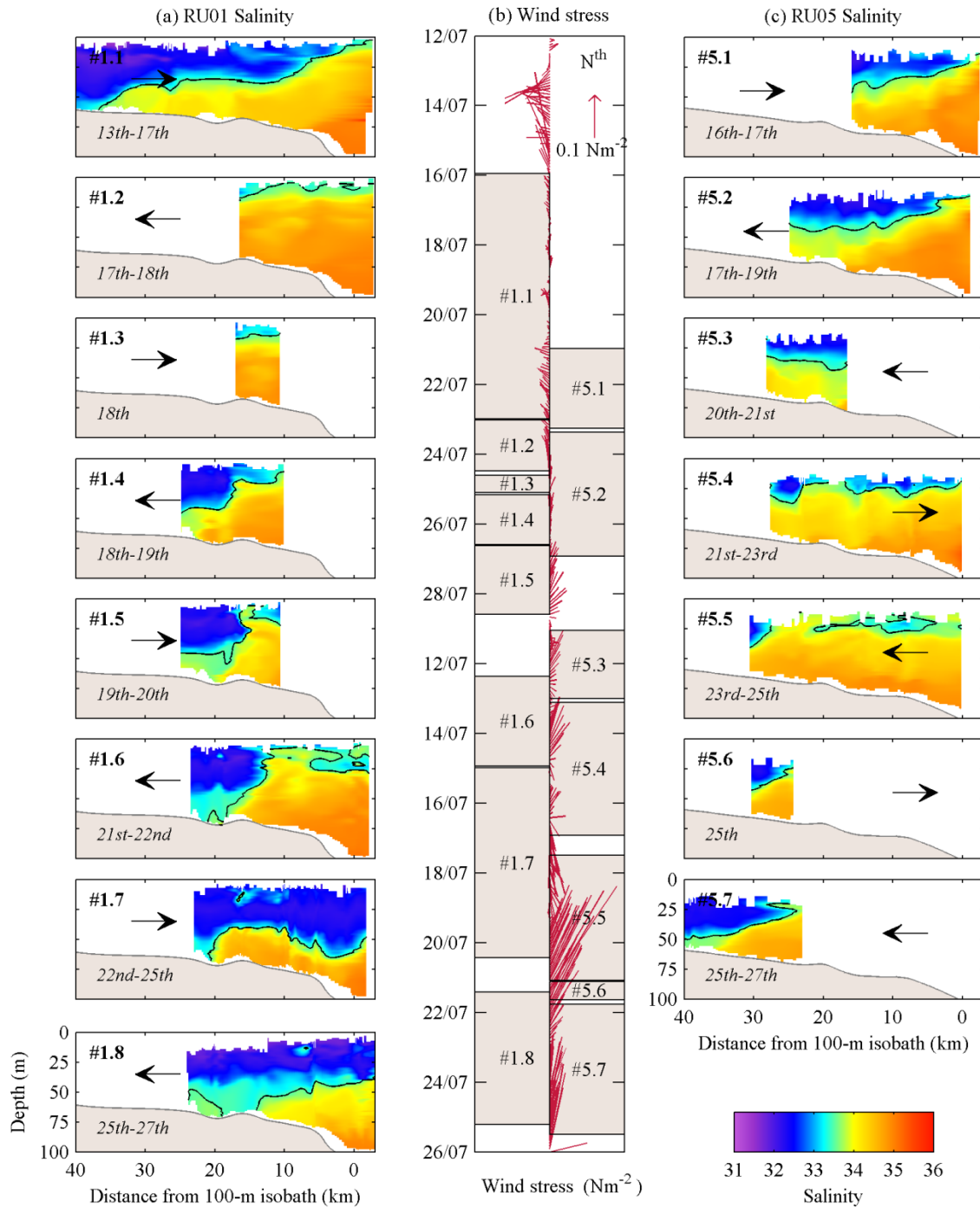
Figure 4-4: Glider salinity and wind stress (N m⁻²) during the SW05 field study, 13–27 July 2005. Panels show (a) RU01 salinity, (b) wind stress and (c) RU05 salinity. Dates refer to days in July 2005; # numbers refer to successive transects of either RU01 or RU05: shaded regions in (b) correspond to the similarly labelled transects in (a) and (c). The arrows in panels (a) and (c) indicate the direction of travel of the glider. Distance is measured from the 100-m isobath (km).
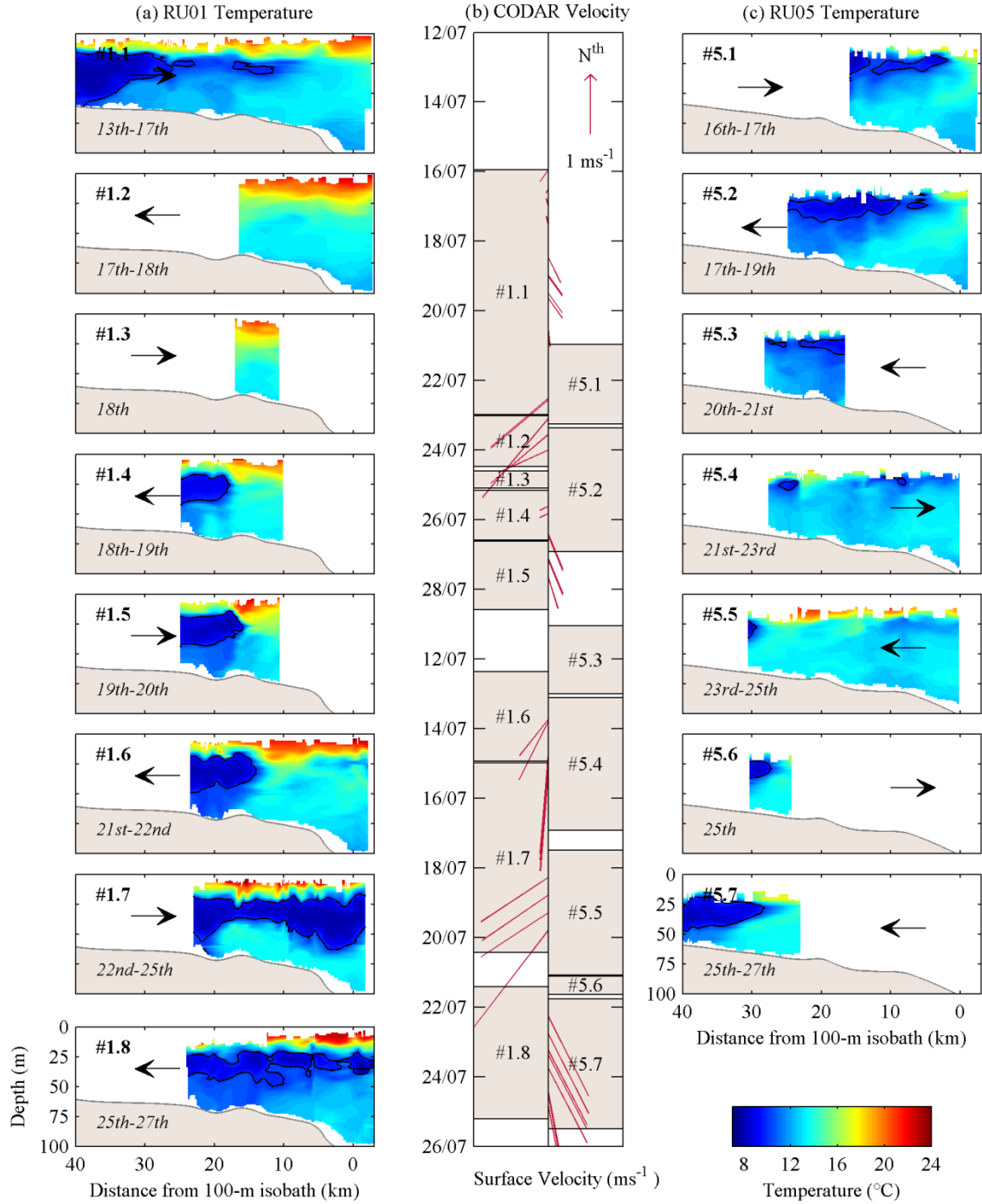
Figure 4-5: As for Figure 4-4 except for glider temperature (ºC) and CODAR surface velocity along the RU01 track (m s⁻¹). Panels show (a) RU01 temperature, (b) CODAR surface velocity and (c) RU05 temperature. The 10ºC isotherm is marked in black.
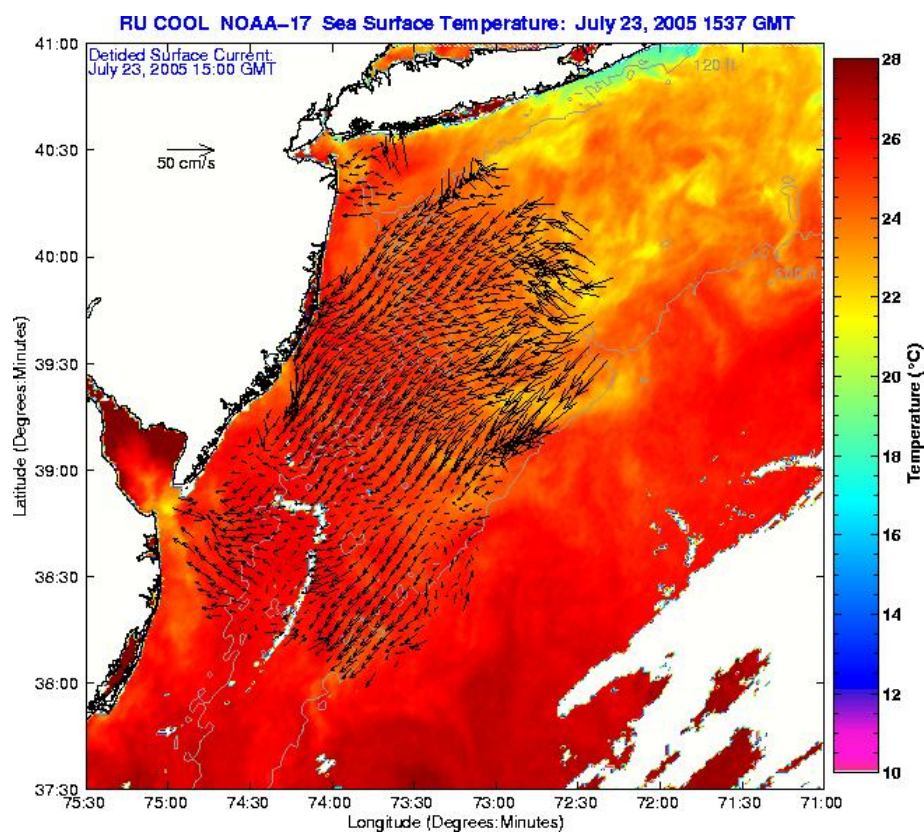
Figure 4-6: CODAR surface velocity and sea surface temperature on July 23 2005 (Reproduced with permission from the COOL Group in the Institute of Marine and Coastal Sciences, Rutgers University, New Jersey).
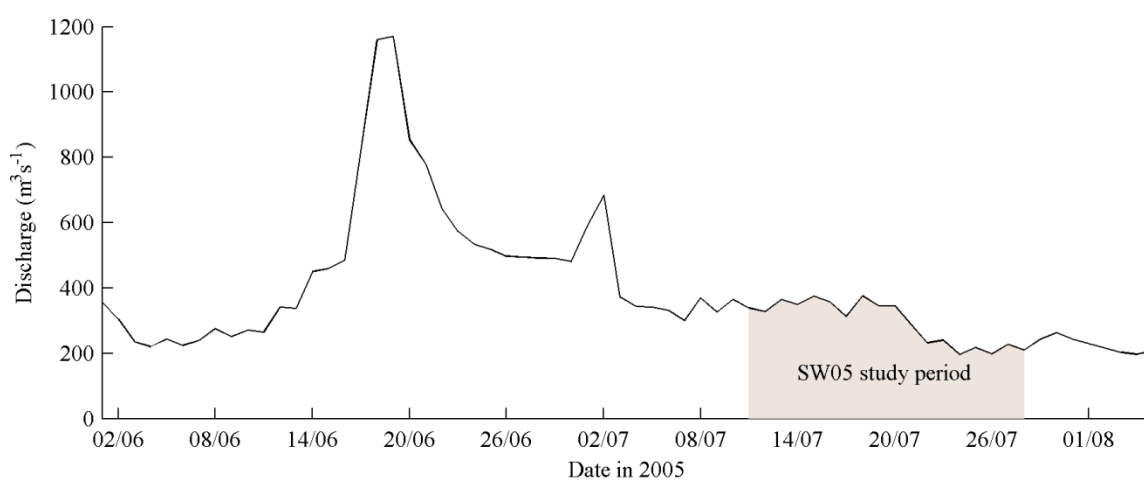
Figure 4-7: Hudson River discharge ($m^3\ s^{-1}$) for June–August 2005. The SW05 study period is shaded in grey.

It is possible that the movement of the freshwater is in the alongshore direction. The numbers match, and the depth-averaged velocity at the RU01 line tends in a southward direction during all times that it was measured, so this freshwater exchange may be from one cross-shore line to the other.

4.6.3   Large Scale Features?

Previous explanations for the variability of the shelf-slope front include instability in the front, the presence of shelf break eddies, Gulf Stream rings, and local winds (see §2.3.6 & §2.3.7).

Sea surface temperature (SST) imagery (Figure 4-8) does not show any large scale feature in this area during this time period. Brief patches of cool water appear in the satellite images, but no consistent pattern is evident, and it is assumed that hazy cloud coverage is a more likely cause of these features. However it must be restated that the gliders are profiling below the surface layer, and one would not necessarily expect to see the underlying features in surface CODAR and SST images.
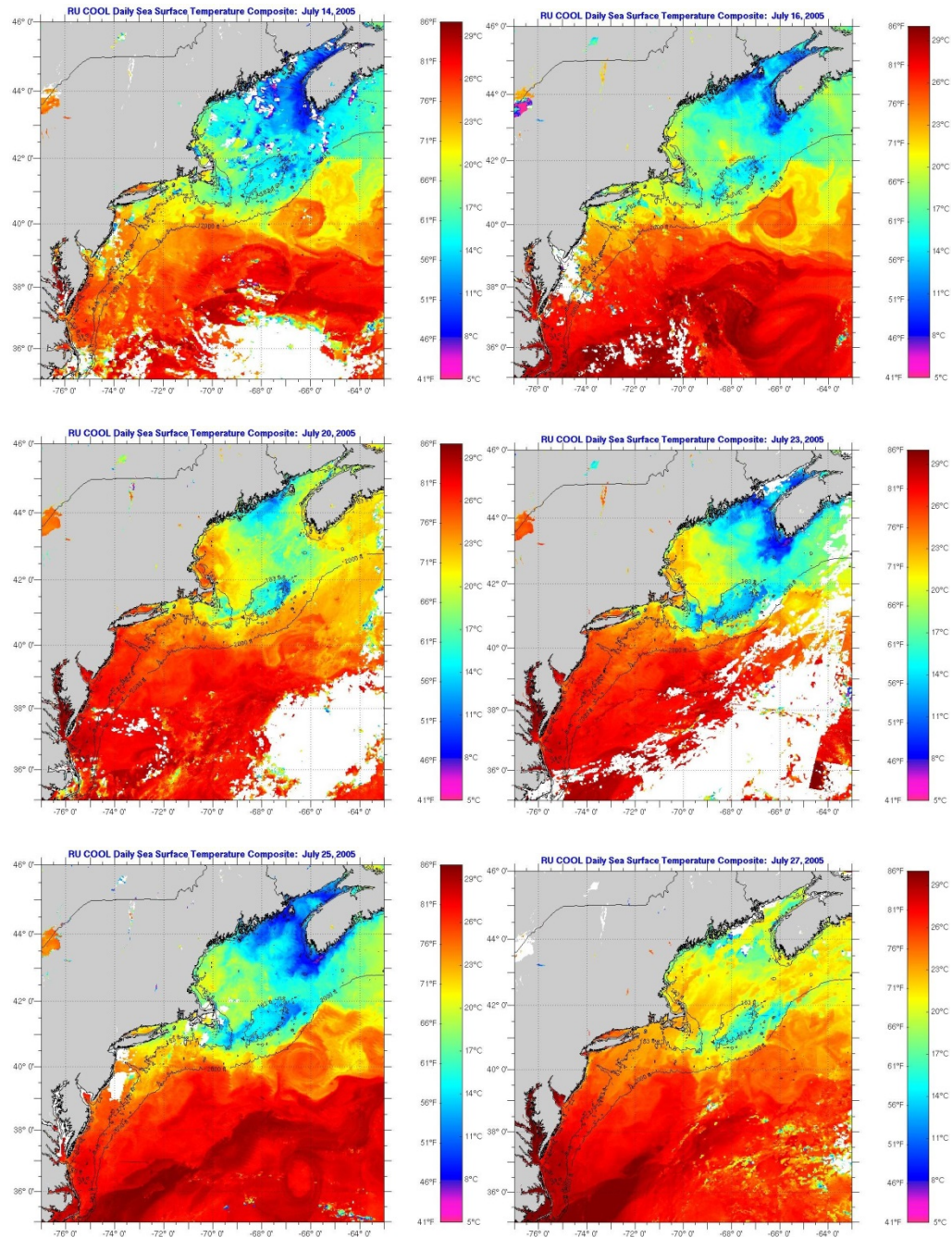
Figure 4-8: Daily composite images of sea surface temperature in the Northeast Atlantic during the SW06 study period in July, 2005. (Reproduced with permission from the COOL Group in the Institute of Marine and Coastal Sciences, Rutgers University, New Jersey).

4.7 Summary and Discussion

In summary, the salinity front observed by the RU01 glider moves at least 10 km shoreward during 17–19 July, and then moves back offshore during 19–27 July, and finally mirrors the initial conditions again by 23 July. The final position of the front is at least 15 km further offshore than the initial position. The slope of front is greatly reduced during the "turning" stage on 18–22 July. This behavior is not observed at the RU05 glider line which is only 40 km to the south.

The lack of strong density gradients indicates that geostrophy does not play a large role in the frontal dynamics. The movement of the front is consistent with the direction of Ekman transport due to the winds, however the shelf waters are well beneath the surface wind driven layer. Additionally, if Ekman transport is the main driving factor, one would expect similar movement of the front at the RU05 location.

While it cannot be resolved whether the freshwater exchange is cross-shore or alongshore, or whether it indicates a single unidirectional event, a meandering current, or a large scale feature, this study does clearly show the high variability that occurs over both short time scales and short spatial scales. In particular, it is seen that the simple theoretical view of cross-shelf density patterns that are uniform along the MAB, does not give a true sense of the complexity of the region.

This study adds to previous knowledge of the properties of the shelf/slope front, and confirms the variability of this front. Data averages may be useful in a general

sense, but are clearly insufficient in describing the exact location and movement of the highly variable front. Surface imagery does not indicate the properties of the water column below, especially during the summertime.

A three-dimensional climatology of the MAB will provide a useful guide to the variability of the mean position of the front in the alongshore direction, along the entire MAB shelfbreak.

5 Data for Developing a 4-D Climatology

5.1 Data Origin

The two main sources of historical temperature and salinity data used to develop the MAB Climatology are the World Ocean Database 2009 (WOD09) and the Northeast Fisheries Science Center (NEFSC) database. Additional data was obtained directly or indirectly from principal investigators of projects based in Delaware Bay, Chesapeake Bay, and offshore of Cape Hatteras.

All historical data from the Middle Atlantic Bight and the Gulf of Maine (an area bounded by 48°N, 30°N, 81°W and 59°W) for temperature and salinity were downloaded, then cut further to a bathymetry-aligned box at an angle of 43^0 east of North, which is approximately 1^0 larger in each direction than the climatology grid. The data box is bounded by corners at: [65.3807ºW, 47.9186ºN], [58.5541ºW, 42.27604ºN], [75.0793ºW, 30.3230ºN], and [81.9059ºW, 35.9656ºN] (Figure 5-1).

The data include profiles taken vertically or near-vertically through the water column (usually from the surface to a certain depth) as well as data recorded at a fixed level (both at the surface and at other subsurface depths). "Cast" is used to
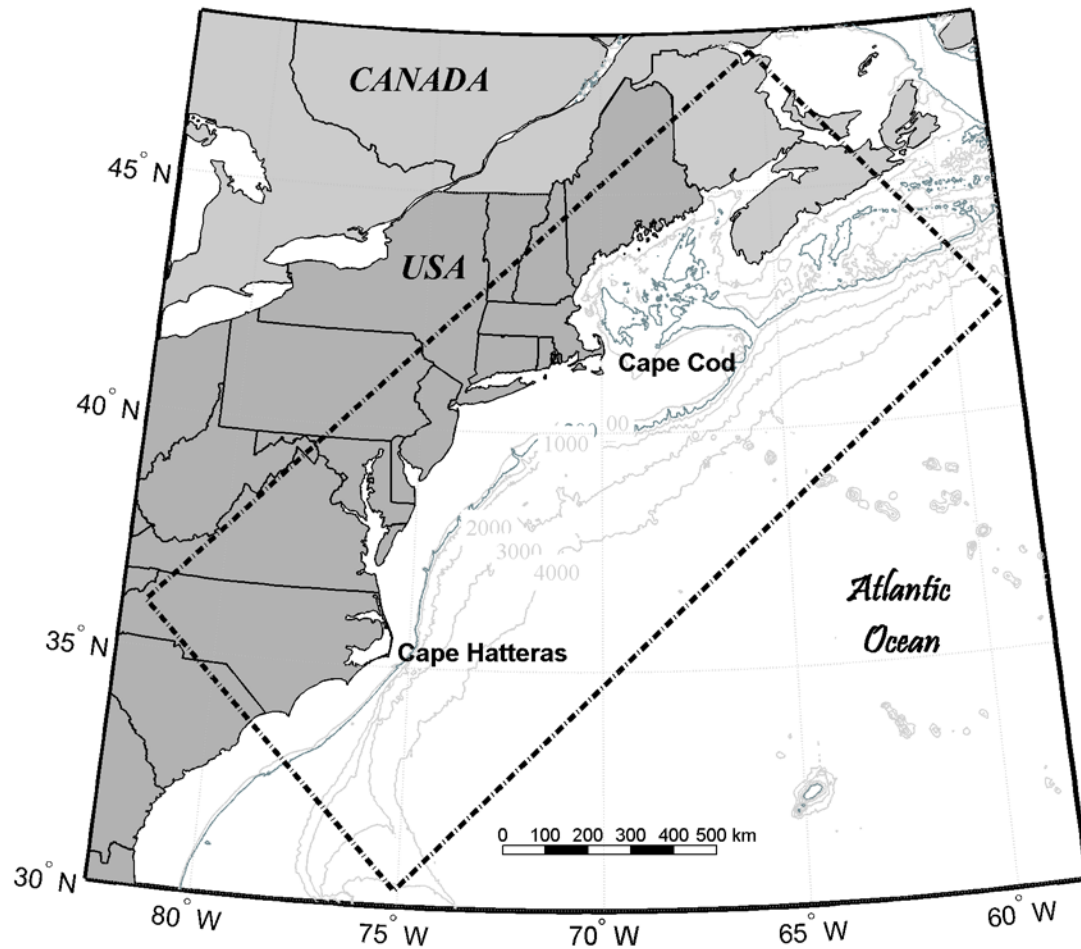
Figure 5-1: The study region encompassing the Middle Atlantic Bight and the Gulf of Maine, on the northeast coast of North America. Data are obtained for the area bounded by the dashed lines.

define either a single vertical profile or a collection of fixed level measurements (e.g. along a ship track for one cruise, or one deployment of a buoy). A vertical profile is assigned a single time, latitude and longitude for all depths, while a fixed-level cast may cover a large extent of times and locations.

5.2 World Ocean Database

The World Ocean Database 2009 of oceanographic data is produced by the Ocean

Climate Laboratory (OCL) at NOAA's National Oceanographic Data Center (NODC).

It is a collection of historical in-situ surface and subsurface oceanographic

measurements used to calculate climatologies of temperature, salinity, oxygen,

phosphate, silicate and nitrate levels. Data from the 2005 version of the database

(WOD05) was originally used in this work, and was later updated from the 2009

dataset (WOD09).

WOD data are available at both raw (observed) depth levels, and at a set of standard

depth levels. Various processing steps and quality control checks were undertaken

before mapping to standard depth levels and some data points were flagged as

potentially erroneous, however no such data is actually removed from the raw data

set (Boyer et al, 2009). The data used in this work are the raw, unedited data

downloaded from the online World Ocean Database.

The World Ocean Database 2009 contains data from a variety of instrument sources.

Table 5-1 outlines the sources that exist for the region of interest, and indicates

whether the instrument records temperature, salinity, or both. The following

section provides a brief overview of each of the instrument classes represented in the

data downloaded for this study. Note that reference is made only to the

measurement of temperature and salinity: many other variables are recorded and

available in WOD 2009, but are not used in this work. Full details of all data are given in the WOD 2009 documentation (Boyer et al. 2009).

Table 5-1: WOD09 instrument source and variables contained in the raw dataset.

Dataset	Acronym	Source[1]	Variables T = temperature S = salinity
Ocean station data	OSD	• bottle • low-resolution conductivity-temperature-depth (CTD) • low-resolution expendable CTD (xCTD) • plankton data	T, S
Conductivity-temperature-depth profiler data	CTD	• high-resolution CTD • high-resolution xCTD	T, S
Mechanical bathythermograph data	MBT	• mechanical bathythermograph (MBT) • digital bathythermograph (DBT) • micro-bathythermograph (µBT)	T
Expendable bathythermograph	XBT	• expendable bathythermograph (XBT)	T
Surface-only data	SUR	• bucket • thermosalinograph	T, S
Moored buoy data	MRB	• moored buoy	T, S
Profiling float data	PFL	• profiling float	T, S
Drifting buoy data	DRB	• surface drifting buoy with thermistor chains	T
Undulating oceanographic recorder data	UOR	• conductivity-temperature-depth profiler mounted on a towed undulating vehicle	T, S

1. After WOD 2009 Introduction, Table 1.1 (Boyer et al. 2009)

5.2.1   MBT Data

The MBT dataset includes measurements from Mechanical Bathythermographs (MBT), Digital Bathythermograph (DBT), and Micro-bathythermographs (µBT).

MBTs were developed in the late 1930's, and are lowered from a stationary or slow moving ship up to maximum depths of 295 m. Temperature is measured by a liquid-in-metal thermometer and pressure is obtained from a Bourdon tube sensor.

A Digital Bathythermograph (DBT) contains a unit that records the profile data electronically underwater. The unit is later plugged into a computer for data retrieval. Temperature and pressure are measured with a thermistor and a strain gauge.

A Micro Bathythermograph (µBT) is a highly accurate sensor for temperature and pressure. It contains a rapid response thermistor and a strain gauge pressure sensor. Data is recorded within the unit, but can also relay real time data through a cable. µBTs can measure temperature to a depth of 1000 m or 7000 m, depending on the model.

5.2.2   XBT Data

Expendable Bathythermographs (XBTs) are small torpedo shaped probes attached to a copper wire that are launched into the ocean from ships, aircraft and submarines.

Temperature is recorded by means of a thermistor in the nose of the probe as it freefalls through the water column. Data is relayed back to a command unit over the copper wire, which breaks when it reaches its limit and the probe is not retrieved (hence the term "expendable"). They were first deployed in the mid-sixties, replacing the MBT.

Depth is calculated using a manufacturer-provided depth-time equation. Corrected and updated versions of these equations have been developed after systematic errors in the depth estimate were discovered.

5.2.3 CTD Data

A conductivity-temperature-depth profiler (CTD) contains a pressure sensor, a resistance thermometer and a conductivity sensor. Pressure is converted to depth, and conductivity to salinity. It is usually mounted on a metal frame and lowered and raised through the water on a cable. Often the CTD software is programmed to bin data into depth intervals, usually chosen to be between 1–5 m, and are capable of measuring up to depths of 10,000 m (though most measurements are to considerably shallower depths).

The WOD 2009 CTD dataset includes both high resolution CTD data and high resolution expendable CTDs (xCTDs). High resolution is considered to be all casts with less than 2-m increments, otherwise the profiles are considered low resolution and included in the Ocean Station Data (OSD) dataset.

xCTD's are small torpedo shaped devices similar to XBT's, and are launched into the ocean from either a ship or airplane. They measure temperature and salinity during their free fall through the ocean. Sensors give temperature and salinity measurements, and depth is estimated using a fall-rate equation given by the manufacturer, with revisions developed by later researchers. Data are communicated via a spool of copper wire to which the xCTD is attached. Data are recorded at intervals varying between models from approximately 14–80 cm, and can reach down to 1500 m depths.

5.2.4   OSD Data

Ocean Station Data (OSD) is a collection of mostly surface and subsurface data obtained from stationary research ships, and a small percentage of low vertical resolution salinity-temperature-depth (STD; a precursor to the CTD), CTD and xCTD profiles.

Stationary research ship measurements are typically made using reversing thermometers and water samples from Nansen or Nisken bottles (or a similar device). Such data are often referred to as "bottle data".

5.2.5   PFL Data

A profiling float (PFL) is a drifting platform situated on the surface of the ocean or at a fixed depth. If at a subsurface depth it rises to the surface at set time intervals

by using external bladders to change its buoyancy, and relays data from the ascent (or previous descent) via satellite. Most PFL's have at a minimum: pressure, temperature and conductivity sensors. Most profiling floats are operated under Argo—an umbrella project which coordinates the deployment, quality control and access of profiling float data (Argo 2014)—as part of the Global Climate Observing System/Global Ocean Observing System (GCOS/GOOS).

5.2.6 UOR Data

Undulating Oceanographic Recorders (UOR) are instruments towed behind a ship at speeds of up to 25 knots. The UOR rises and descends through the water column, and thus provides temperature and salinity measurements at high vertical and horizontal resolutions. The UOR datasets used in this study were collected during the Delaware Circulation and Dye Experiment (DECADE) from a Scanfish instrument.

5.2.7 DRB Data

Drifting buoys (DRB) are buoys equipped with sensors for measuring water and meteorological properties. They relay the information via satellites. DRBs are mostly used to sample inaccessible regions such as the Arctic; only 16 profiles are included in this study.

5.2.8   SUR Data

Surface data (SUR) is not the main goal of the WOD 2009, and thus it only includes surface data from areas and times in which profile data is sparse, and from the ship-of-opportunity programs. Early surface data was collected using bucket or thermosalinographs, while the ship of opportunity program collects surface data from merchant and other volunteer vessels using hull-mounted devices.

5.3   NEFSC Data

The Oceanography Branch of the Ecosystems Processes Division of the Northeast Fisheries Science Center maintains an online database of oceanographic measurements (NEFSC 2014). The purpose of the Oceanography Branch is to study the ecosystems of the Northeast Continental Shelf, and to monitor the seasonal and inter-annual variability of the water by recording temperature and salinity on almost all their research cruises.

Temperature and salinity measurements from three of their datasets (Water Column Properties (WCP), along-track ship, and drifter) are included in this work. Data duplicated in WOD 2009 are identified and removed.

5.3.1   WCP Data

CTDs are used on all NEFSC surveys throughout the Northeast shelf, from Cape Hatteras to the Gulf of Maine. Over 1000 profiles are collected each year. Full description and processing details of the WCP dataset can be found in Mountain and Taylor (1998).

5.3.2   Along-track Ship Data

Along-track ship data, including temperature and salinity, are recorded from a hull-mounted sensor on NEFSC cruises.

5.3.3   Drifter Data

Numerous drifter studies have been undertaken since 2004, in various locations for various research and educational purposes. An overview of these studies is given in Manning et al. (2009).

5.4   Other Data Sources

Other raw datasets were obtained from colleagues to fill in under-sampled areas (e.g. in bays and over the slope region of the southern MAB).

These include datasets from the Delaware Bay region collected by Joseph Wang and Peter Zhang (IMCS, Rutgers University, NJ); from the mouth of the Chesapeake and Delaware Bays, as described by Mannino et al. (2008); Sharp's Delaware Estuary Database (Sharp 2009); and data from cruises near Cape Hatteras supplied by Glen Gawarkiewicz (Woods Hole Oceanographic Institute (WHOI), MA), as described in Churchill and Gawarkiewicz (2009).

5.5 Raw Data Summary

5.5.1 Profile Data

There are 607,184 profiles in the Profile dataset downloaded from all sources, containing 30,306,552 points in space and time; 10,258,727 of these contain salinity measurements, and 30,272,423 contain temperature measurements. Dates range from 11 January 1864 to 14 November 2009, and depths range from 0–6086 m below sea-level. A summary of the data originating from each source is listed in Table 5-2.

5.5.2 Fixed Level Data

There are 2,793,429 salinity points and 2,863,866 temperature points in the Fixed Level dataset, obtained from 1059 casts (Table 5-3). The first recorded points are from 24 February 1874, the last from 1 September 2009. The depth of casts ranges from 0 to 100 m.

Table 5-2: Summary of raw profile data.

Source	Temperature		Salinity		Date range	Depth Range (m)
	Data Points	Profiles	Data Points	Profiles		
NEFSC WCP	1,806,343	24,422	1,754,771	23,523	1980 – 2007	0 – 1360
WOD OSD	712,075	92,633	654,707	81,971	1864 – 2006	0 – 6086
WOD CTD	7,440,613	68,708	7,125,945	67,142	1961 – 2009	0 – 5888
WOD XBT	14,542,120	129,432	0	0	1966 – 2009	0 – 3018
WOD PFL	265,619	3,126	203,406	2,392	1997 – 2009	0 – 3884
WOD MBT	4,979,622	245,472	0	0	1933 – 1998	0 – 1830
WOD UOR	502,269	41,485	502,269	41,485	2003 – 2004	0 – 376
WOD DRB	162	16	0	0	1999	0 – 50
Other PR	23,600	1266	17,629	729	1978 – 2008	0 – 497
Total	30,272,423	606,560	10,258,727	217,242	1864 – 2009	0 – 6086

5.5.3 Overview of Data from Each Source

The following pages illustrate the data obtained from each source (Figure 5-2–Figure 5-14). In each figure, data coverage for all depths is mapped in panel (a); the distribution of data by depth is shown in panel (b); by year in panel (c); and by month in panel (d).

Table 5-3: Summary of raw fixed level data.

Source	Temperature		Salinity		Date range	Cast Depths (m)
	Data Points	Casts	Data Points	Casts		
NEFSC Drifters	55,707	86	55,707	86	1988 – 2006	0, 1, 5, 6, 14, 15, 50
NEFSC Surface	2,487,858	87	2,429,158	86	2000 – 2006	0
WOD Surface	9132	831	4,833	806	1874 – 1987	0
Other	311,169	55	303,731	42	1978 – 2009	0 – 100
TOTALS	2,863,866	1059	2,793,429	1020	1874 – 2009	0 – 100
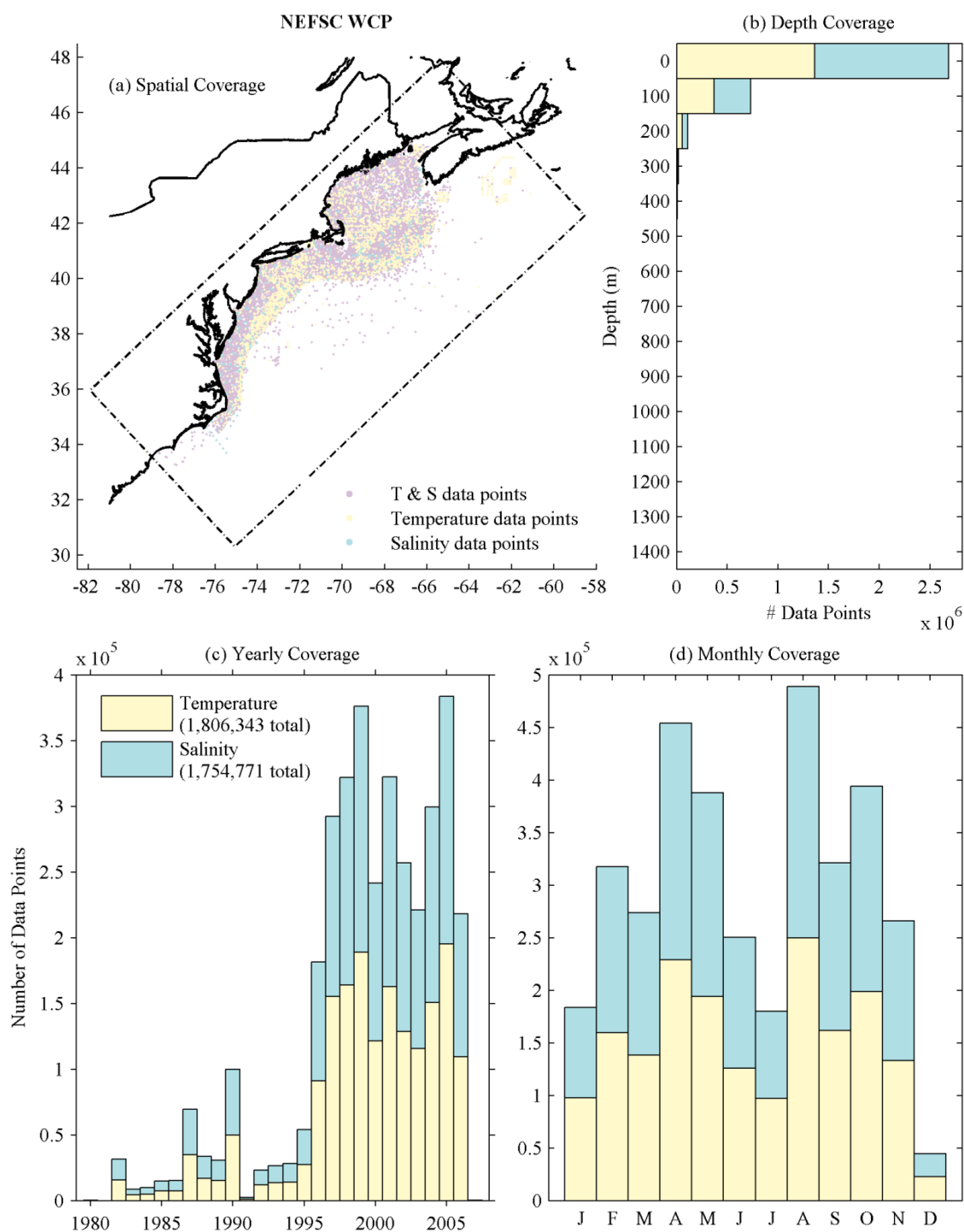
Figure 5-2: Overview of NEFSC Water Column Profile data: (a) spatial coverage of temperature and salinity data at all depths, and histograms showing data coverage by (b) depth (c) year and (d) month.
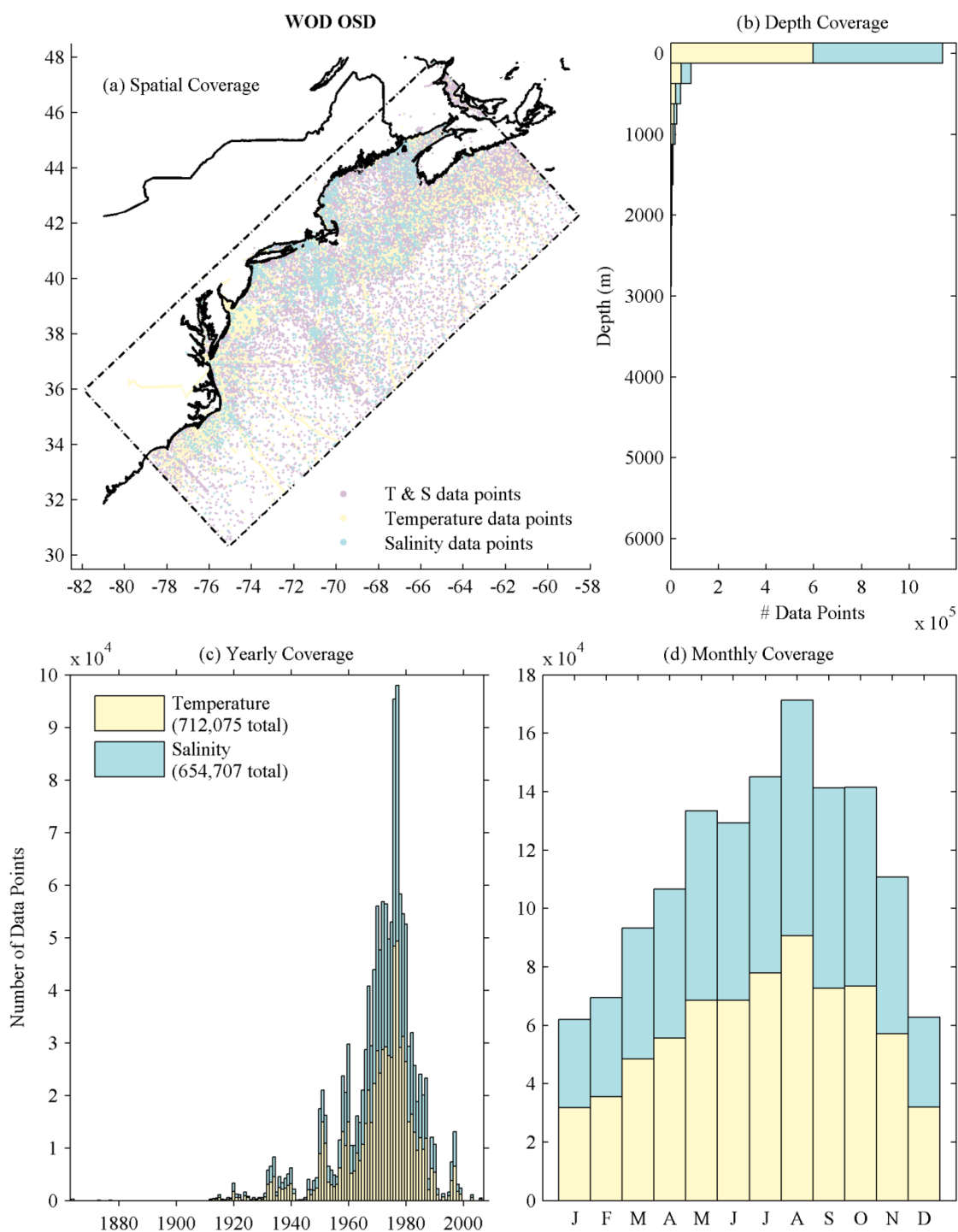
Figure 5-3: As for Figure 5-2, except for WOD Ocean Station data.
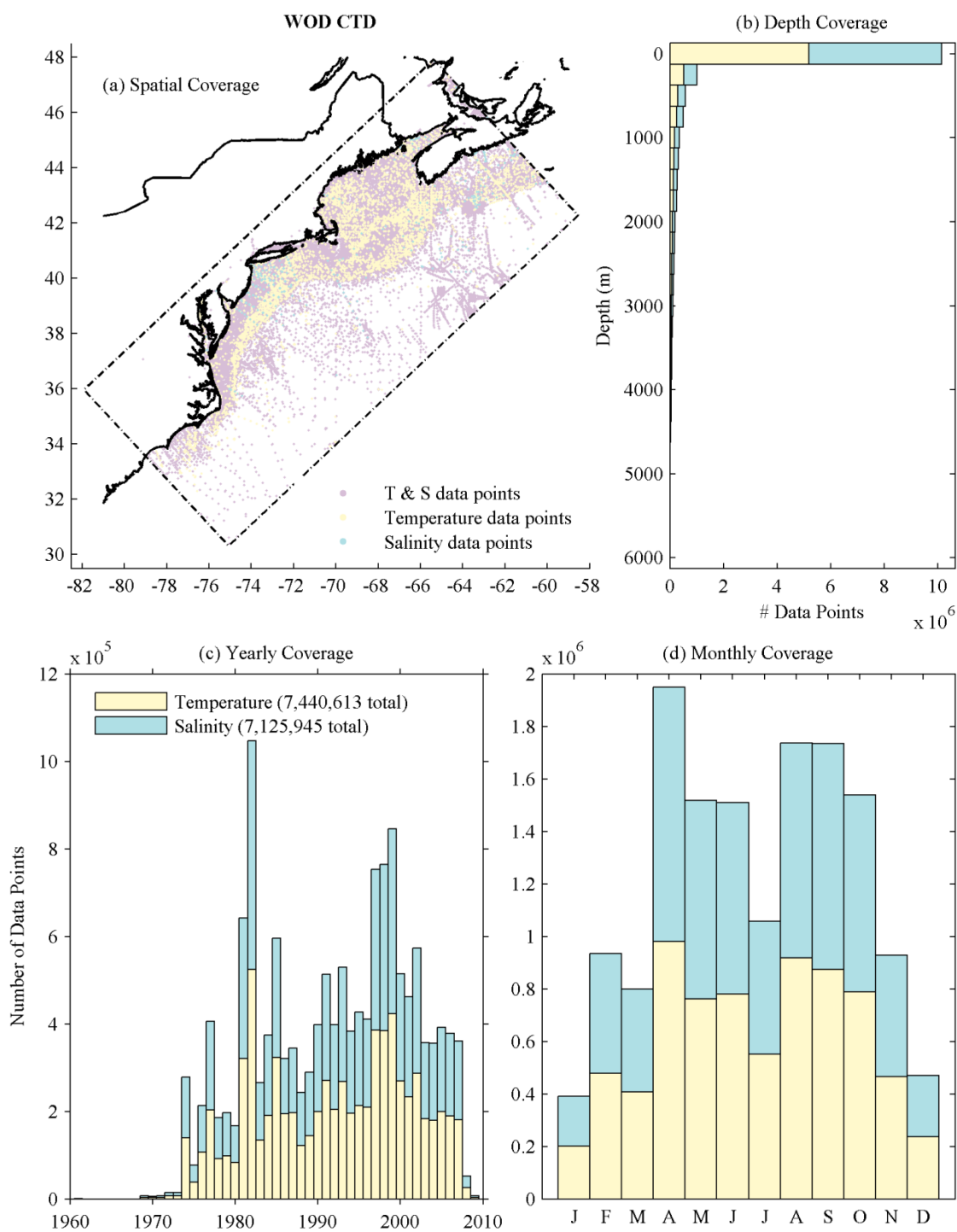
Figure 5-4: As for Figure 5-2, except for WOD CTD data.
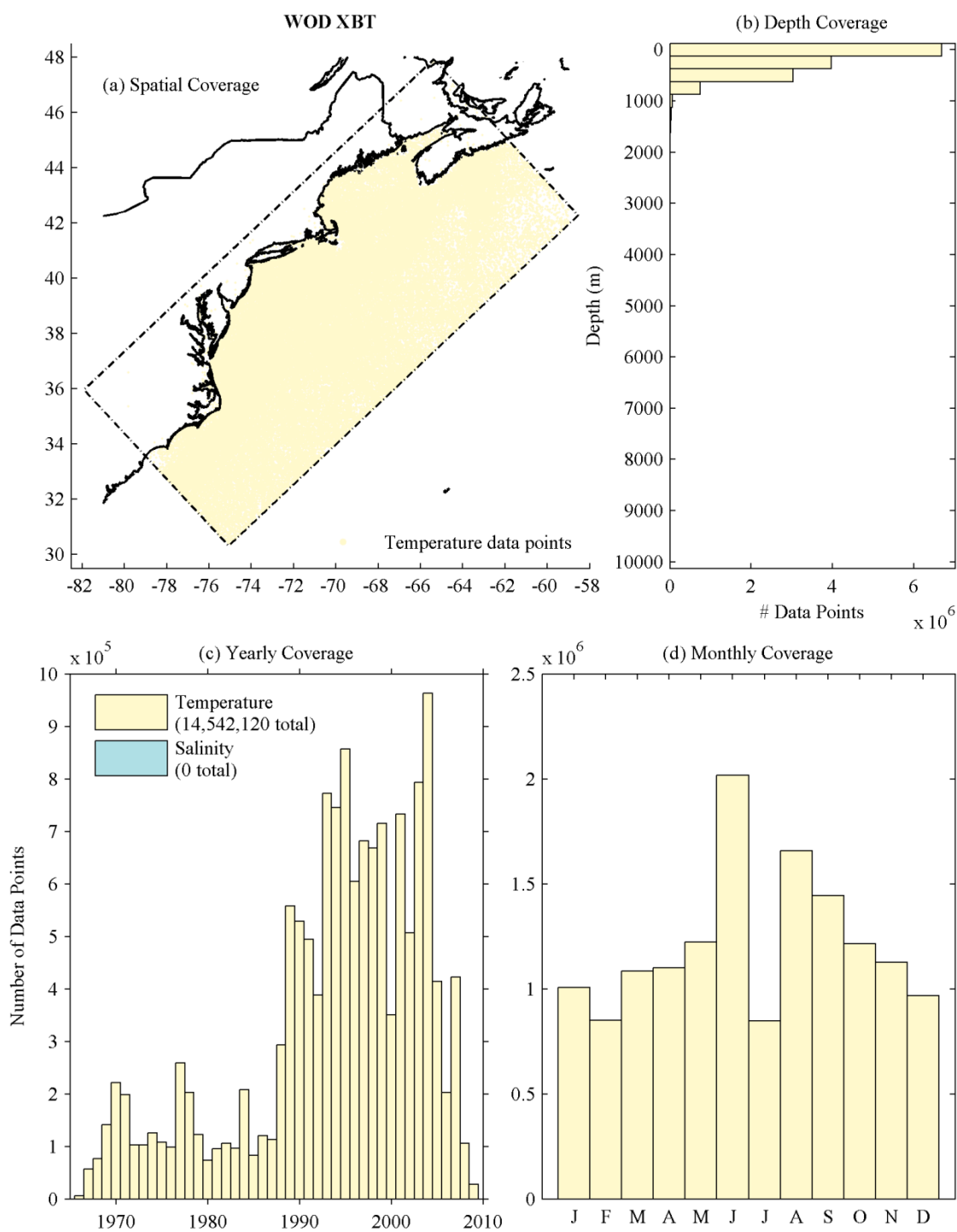
Figure 5-5: As for Figure 5-2, except for WOD XBT data.
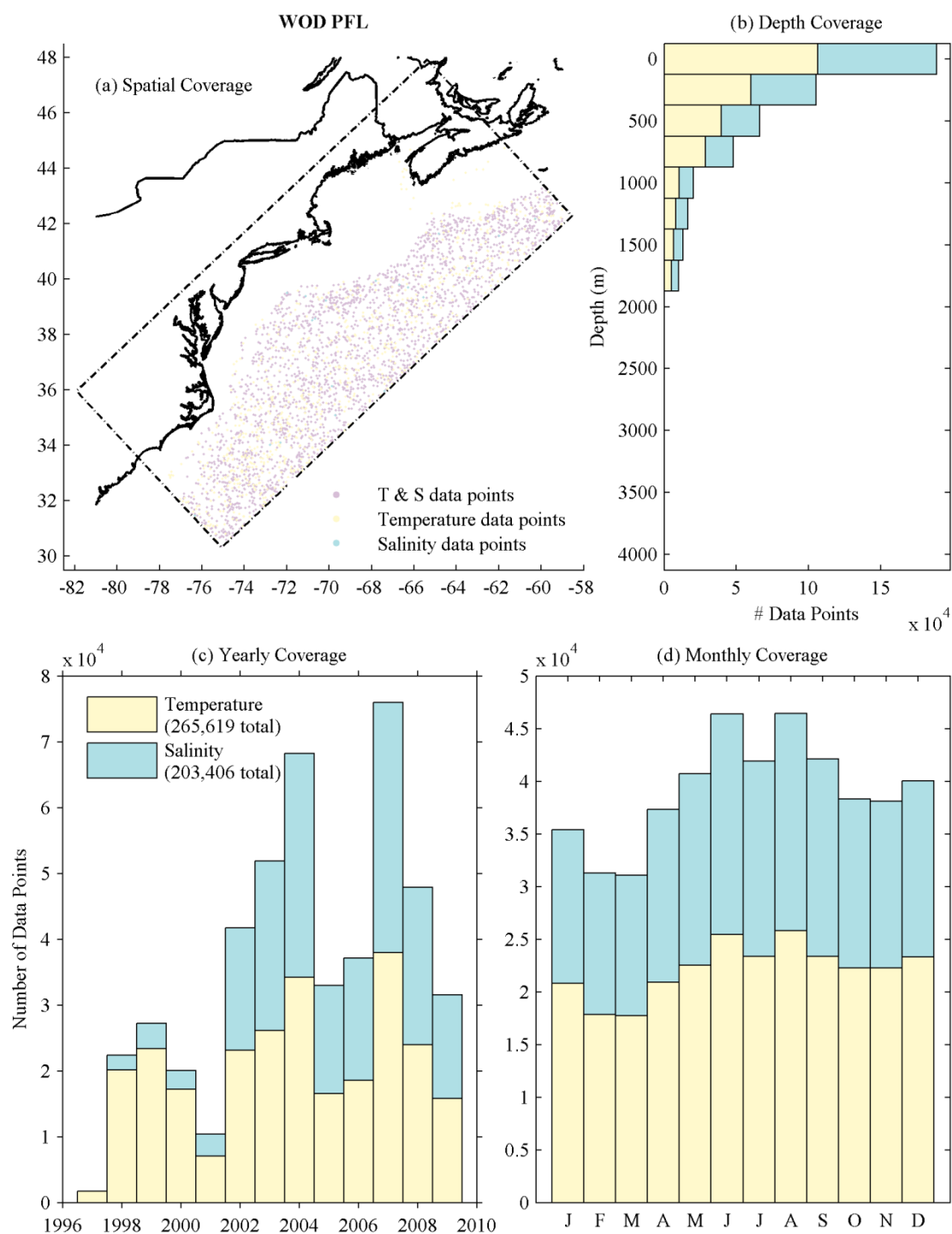
Figure 5-6: As for Figure 5-2, except for Profiling Float data.
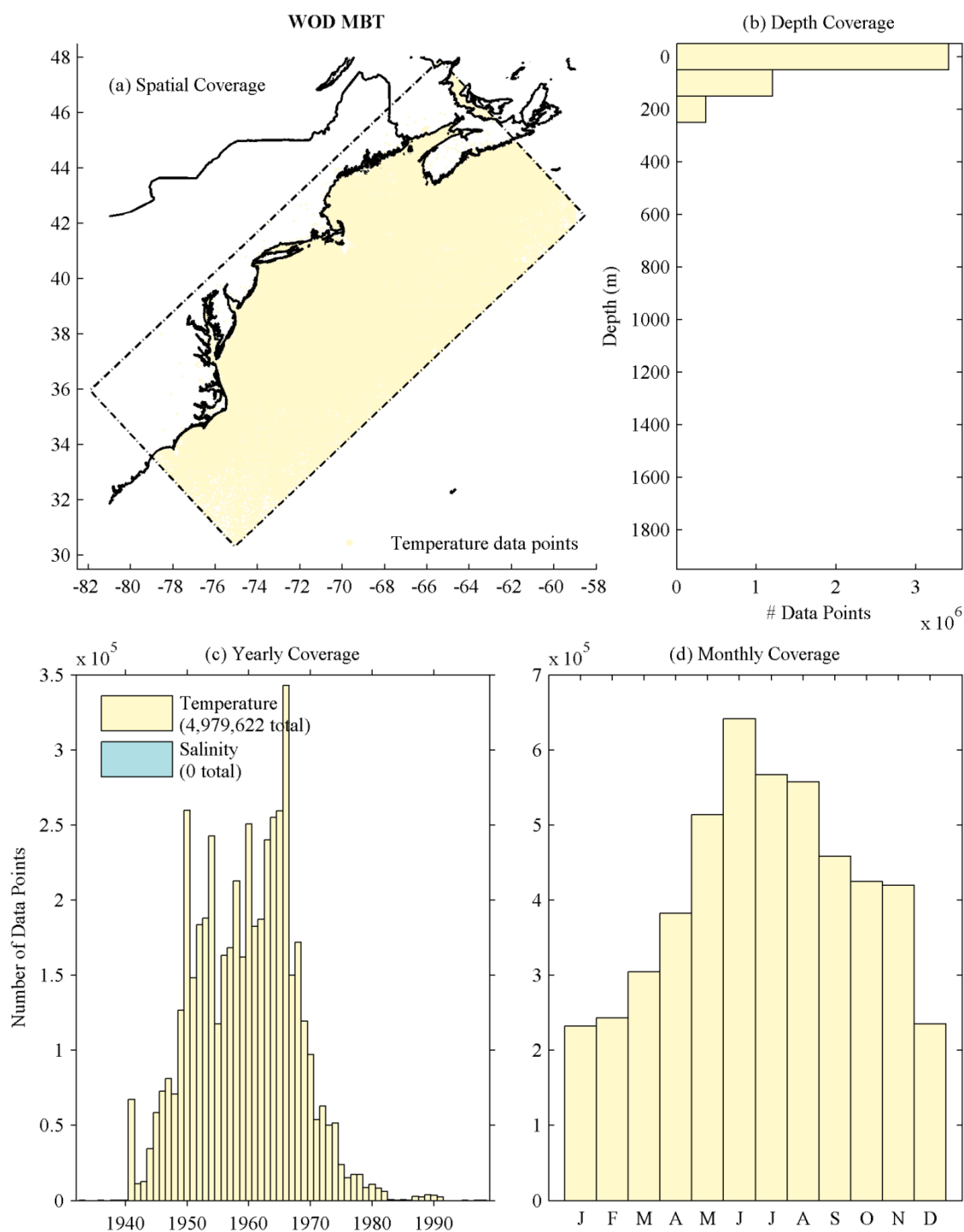
Figure 5-7: As for Figure 5-2, except for MBT data.
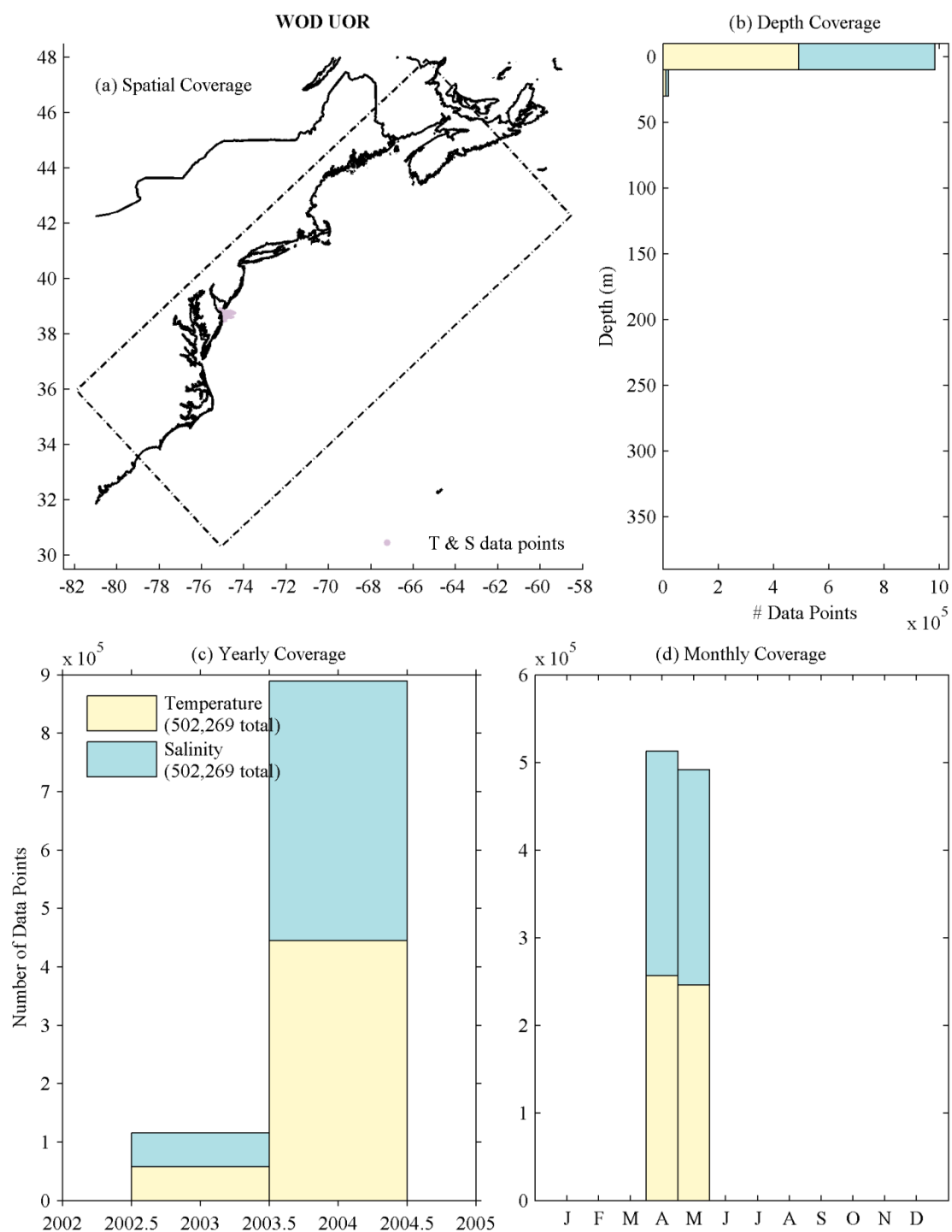
Figure 5-8: As for Figure 5-2, except for UOR data.
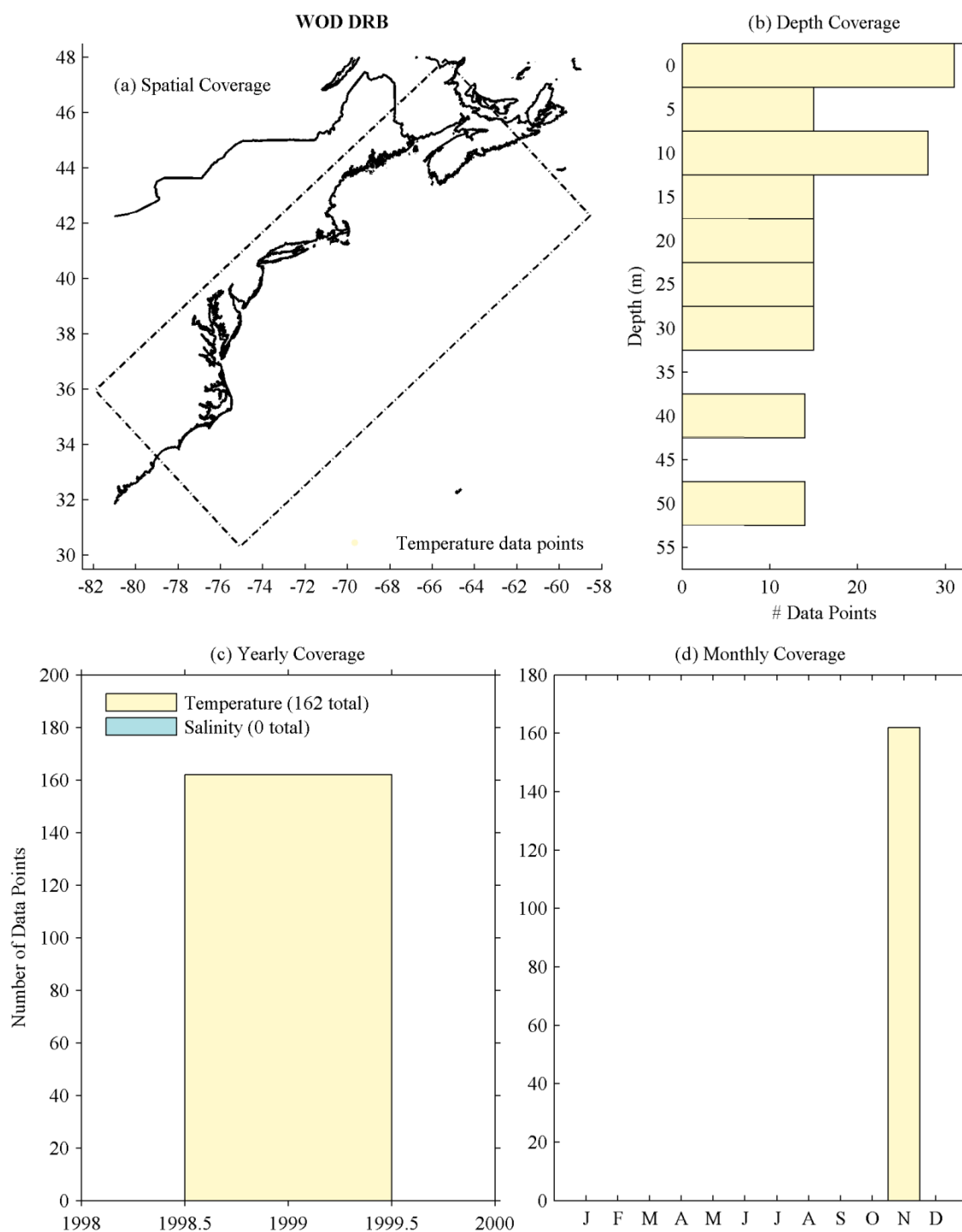
Figure 5-9: As for Figure 5-2, except for Drifting Buoy data.
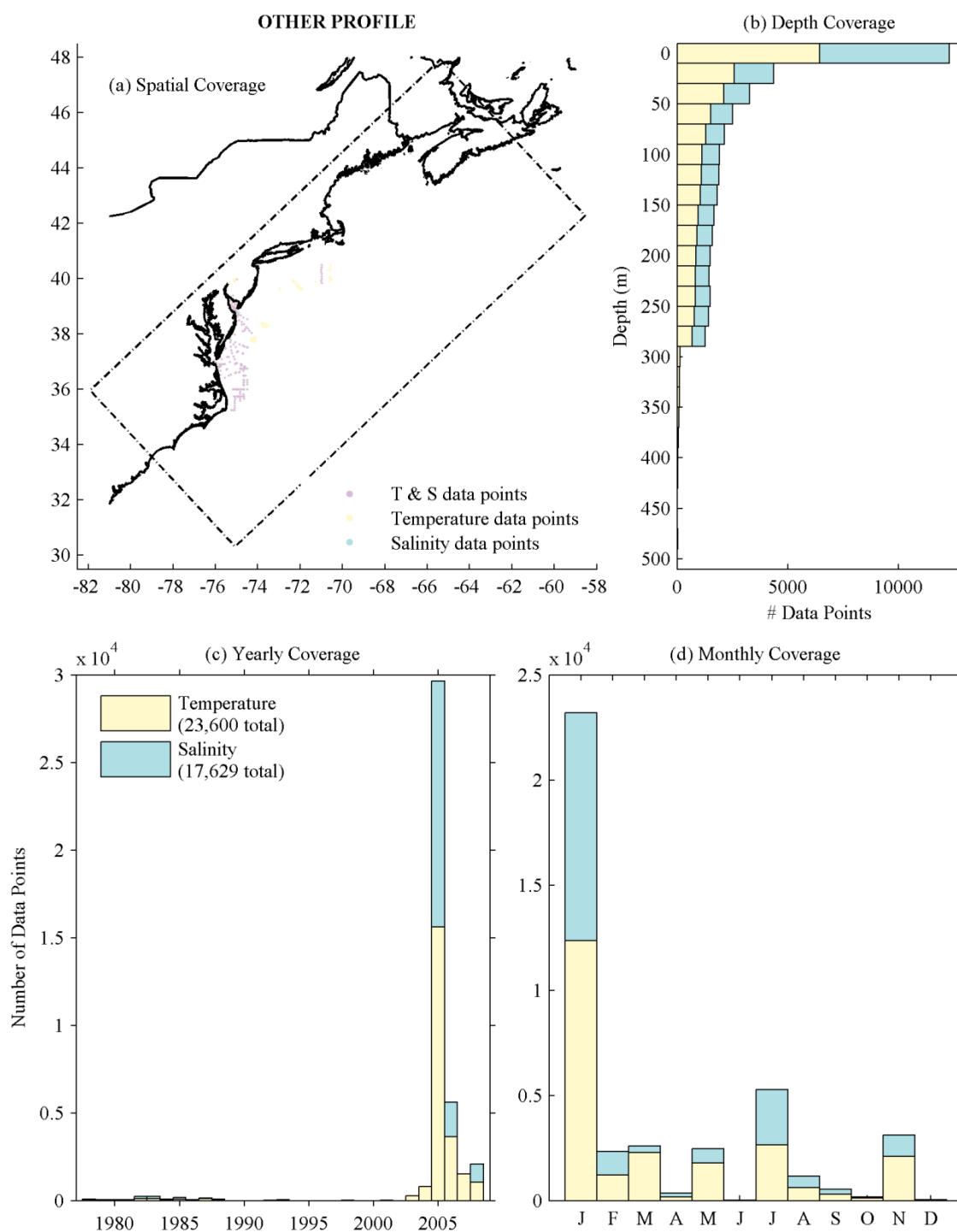
Figure 5-10: As for Figure 5-2, except for profile data obtained from other sources.
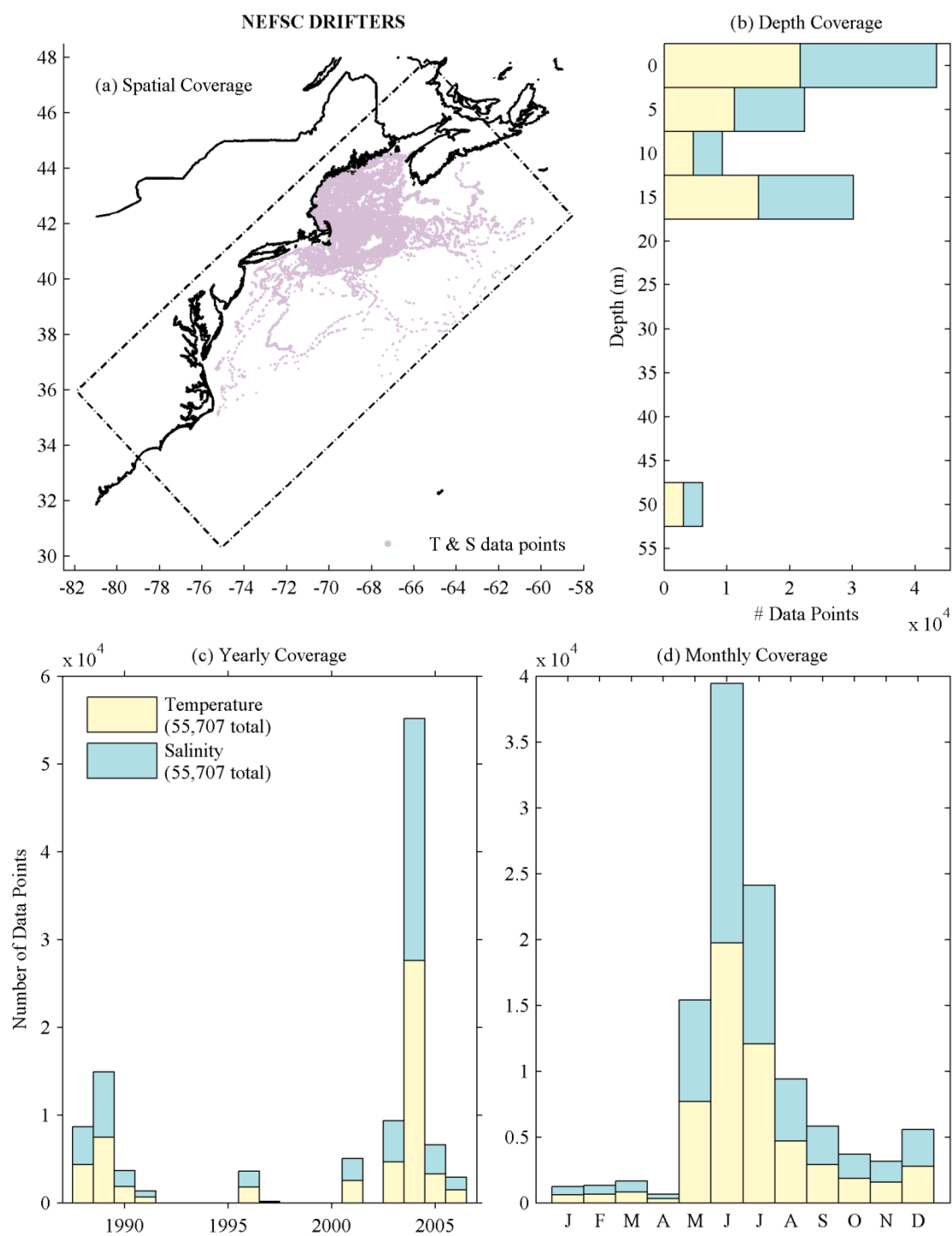
Figure 5-11: As for Figure 5-2, except for NEFSC Drifter data.
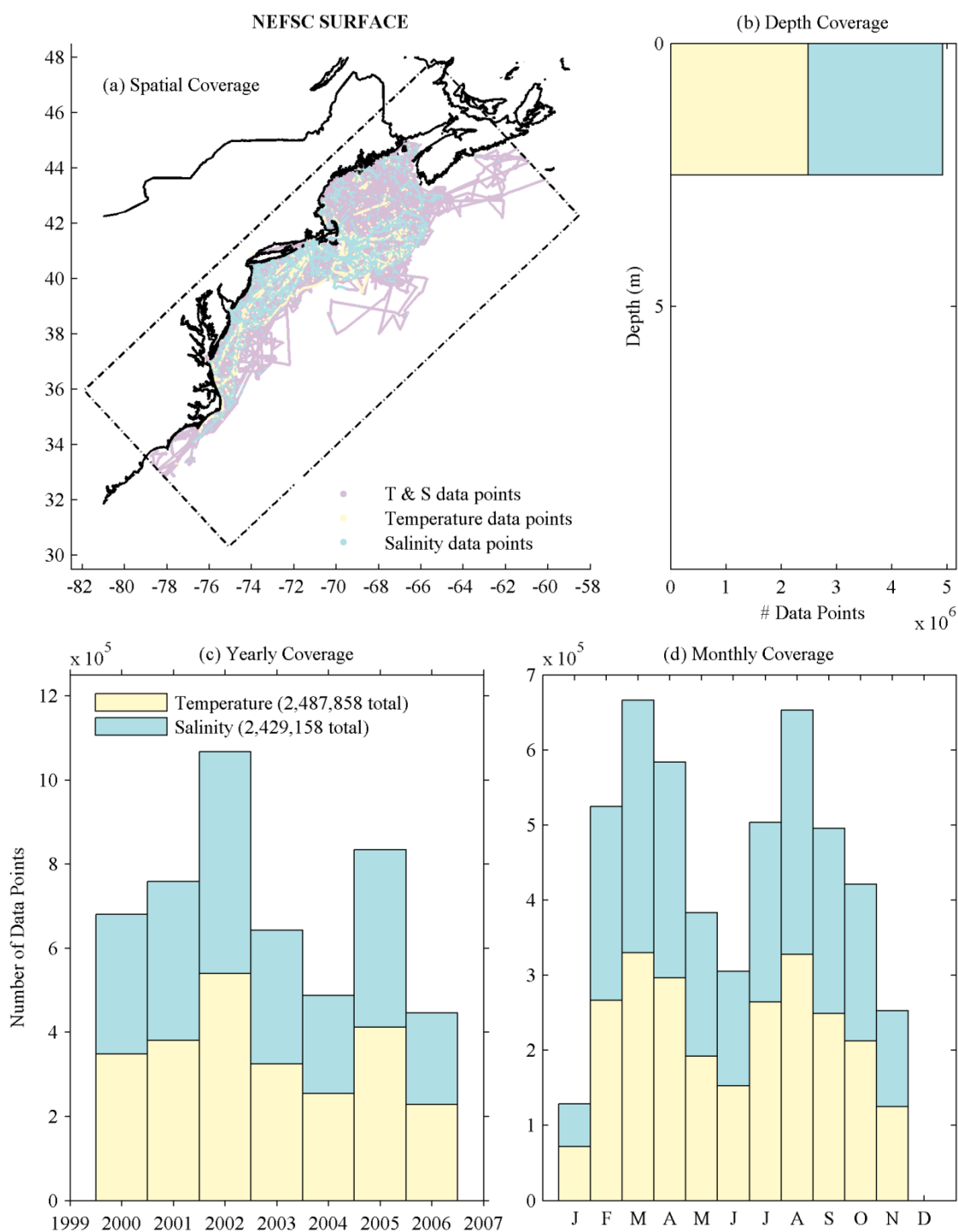
Figure 5-12: As for Figure 5-2, except for NEFSC Surface data.
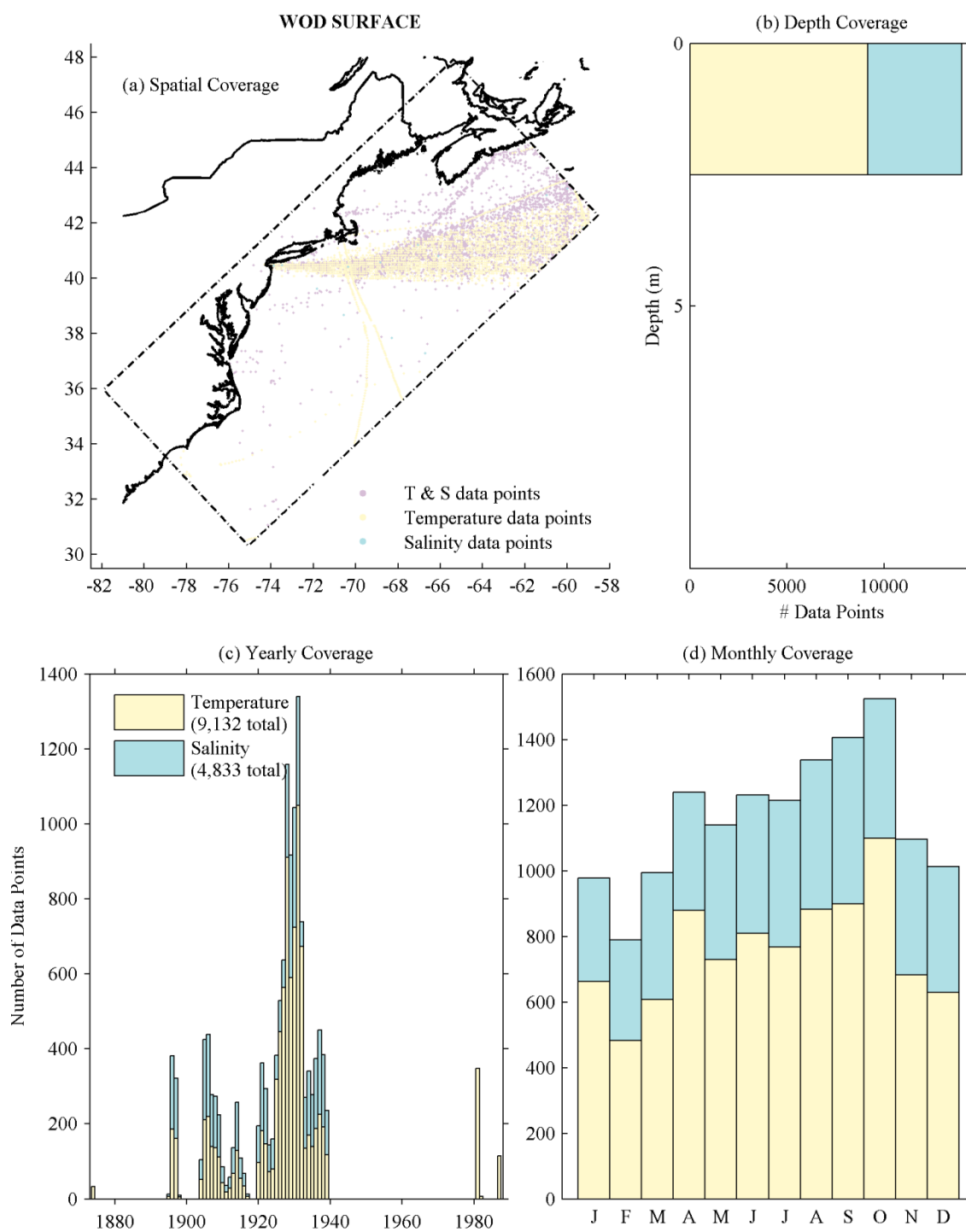
Figure 5-13: As for Figure 5-2, except for WOD Surface data.
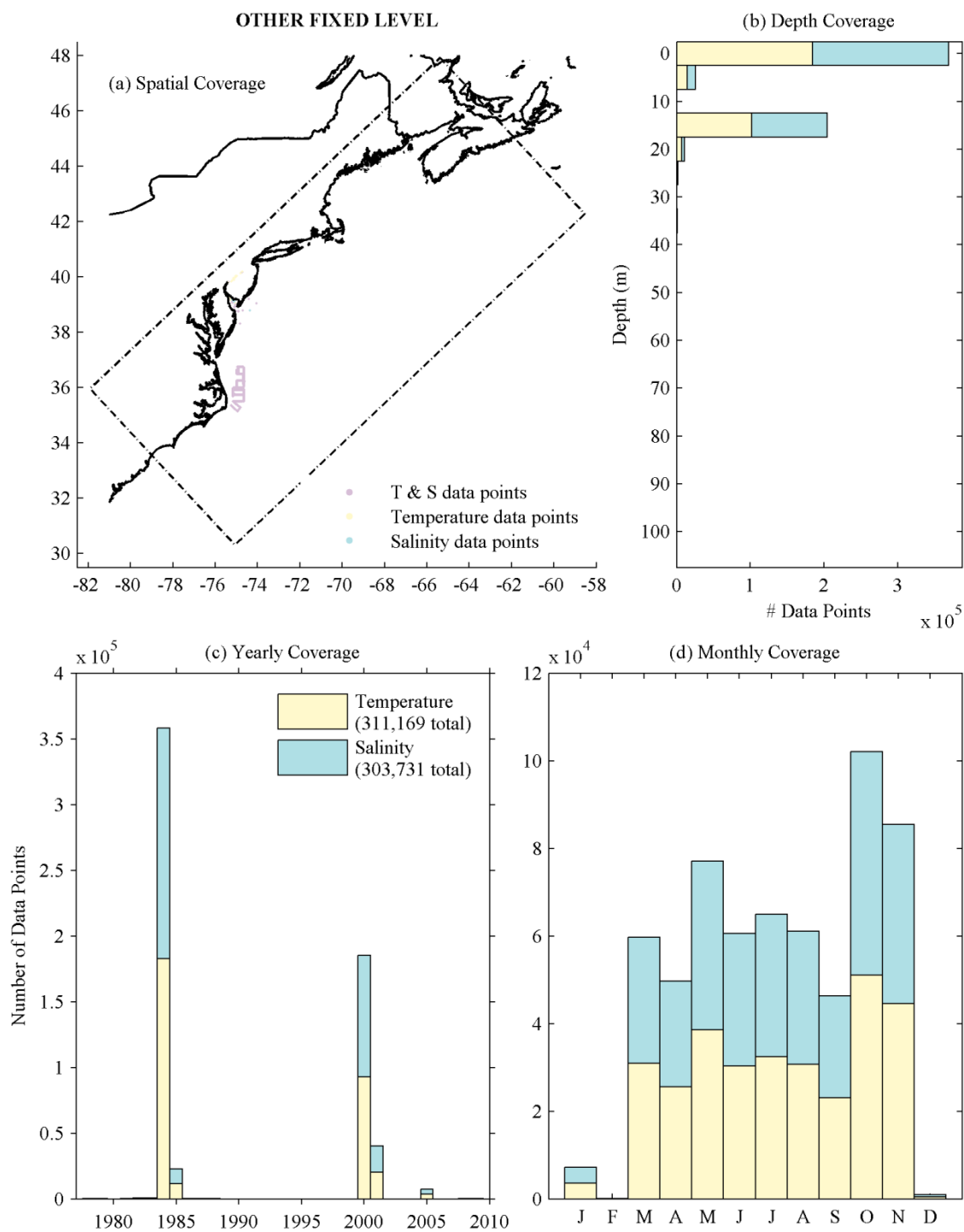
Figure 5-14: As for Figure 5-2, except for fixed level data obtained from other sources.

5.6 Quality Control

Various checks were performed on the data for quality control. Any data points that appeared to be on land were deleted, along with any points whose recorded depth was greater than the bathymetry. Any data points located within sand bars and well-sheltered coastal bays, (e.g. within Albemarle and Pamlico Sounds, at Cape Hatteras) as well as river points far upstream were all removed.

Any "bad" data were removed, e.g. temperature and salinity filler values (commonly 99.99, −99.99 or similar), as well as any data points that had missing values in the location data such as latitude, longitude, depth or time.

All temperature and salinity "wild" points (those that lie well outside the normal range of seawater values) were removed. For temperature this was deemed to be any values greater than 37ºC, and for salinity, any values greater than 50, or less than zero. Temperature data were further restricted to values above the freezing point of water for that depth, salinity and latitude. If no salinity was recorded, then a value of 40 was used to estimate the freezing point.

A very high density of data in both spatial and temporal extents existed in NEFSC drifter and surface data, as well as in the Scanfish data from offshore Cape Hatteras. These data were decimated heavily to reduce their overwhelming effect on nearby data from other sources and thereby giving undue weighting to those casts. The decimating interval was determined individually, based on the time and space

intervals of the data it contained. For longer casts (of many days or even weeks) where the sampling rate was high, a general decimating interval that retained three points per day was used. In total, 104 casts were decimated, reducing their combined 2,881,934 points down to 379,856.

5.7 Temperature/salinity Screening for Outliers

Temperature and salinity outliers were removed by first dividing the MAB into 48 regions, plus an offshore region, (Figure 5-15) as defined by Hofmann et al. (2008). Each data point was assigned to its corresponding region, and the data further broken down by time (into four seasons) and into depth bins. Each group of data points was then analyzed for outliers, first by calculating the density of those data that contain both temperature and salinity measurements. The mean and standard deviation of the density was then calculated, and any points lying beyond three standard deviations from the mean removed. The mean and standard deviation of the temperature-only points, and the salinity-only points were then screened using the same method. If any group of points contained fewer than 30 data pairs, no action was taken. Using this method, 0.34% of salinity measurements were discarded, as well as 0.55% of temperature measurements.
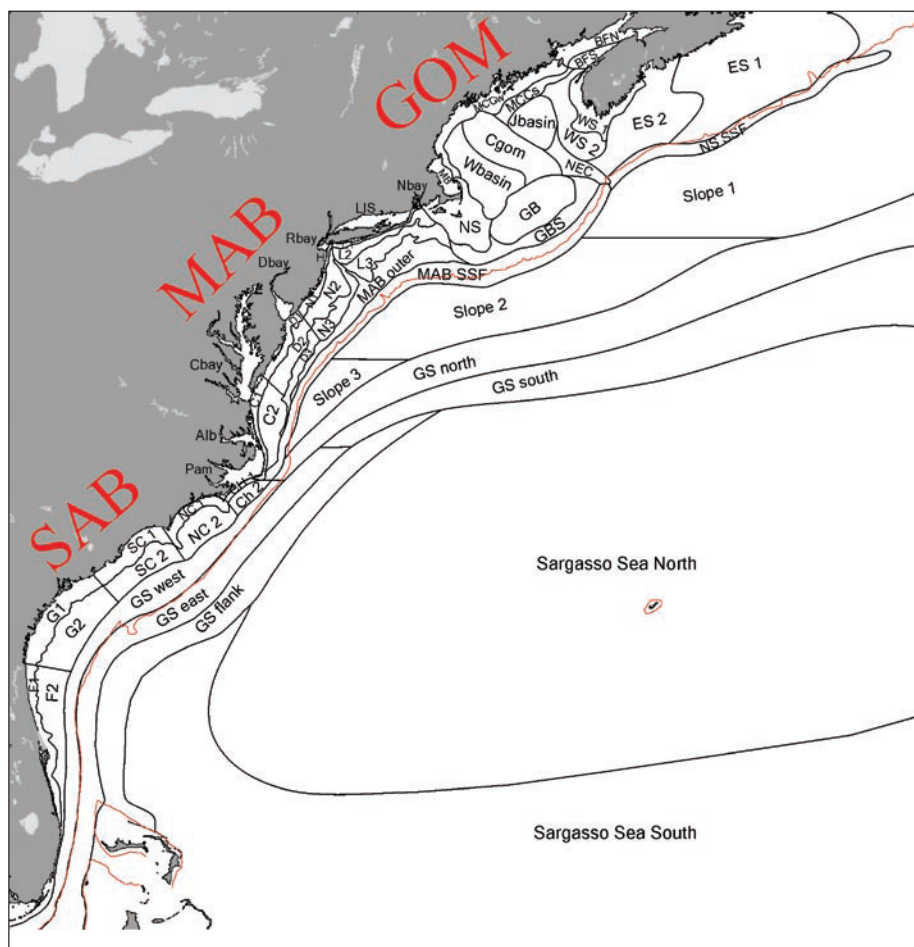
Figure 5-15: MAB subregions. Forty-eight of the 56 illustrated regions lie within the climatology data domain. Those regions are listed in Table 5-6. Reproduced with permission from Hofmann et al. (2008).

5.8 Final Observed Data Summary

After all cleaning up procedures, in total 28.6 million temperature points remain, along with 10.2 million salinity points. A summary of the data, split into profile data and fixed-level data is found in Table 5-4.

Table 5-4: Quality-controlled observed level data summary.

Data point category	Profile Data	Fixed Level Data	Total
All Temperature	28,263,165	353,078	28,616,243
All Salinity	9,862,547	317,734	10,180,281
			(in 589,361
			profiles)
Temperature & Salinity	9,844,097	317,148	10,161,245
Only Temperature	18,419,068	35,930	18,454,998
Only Salinity	18,450	586	19,036
Total	28,281,615	353,664	28,635,279

Data range in time from 1864 to 2009, however early measurements are few and sparse: 99% of the data were recorded from 1946 onwards and 50% of the data are recorded from 1993 onwards (Figure 5-17b).

Depths range from the sea surface to 5367 m below sea level (Figure 5-16). Approximately 45% of the data are within the top 100 m of the water column, and 86% are within the top 500 m. Only 1% of the data is from below 2900 m.
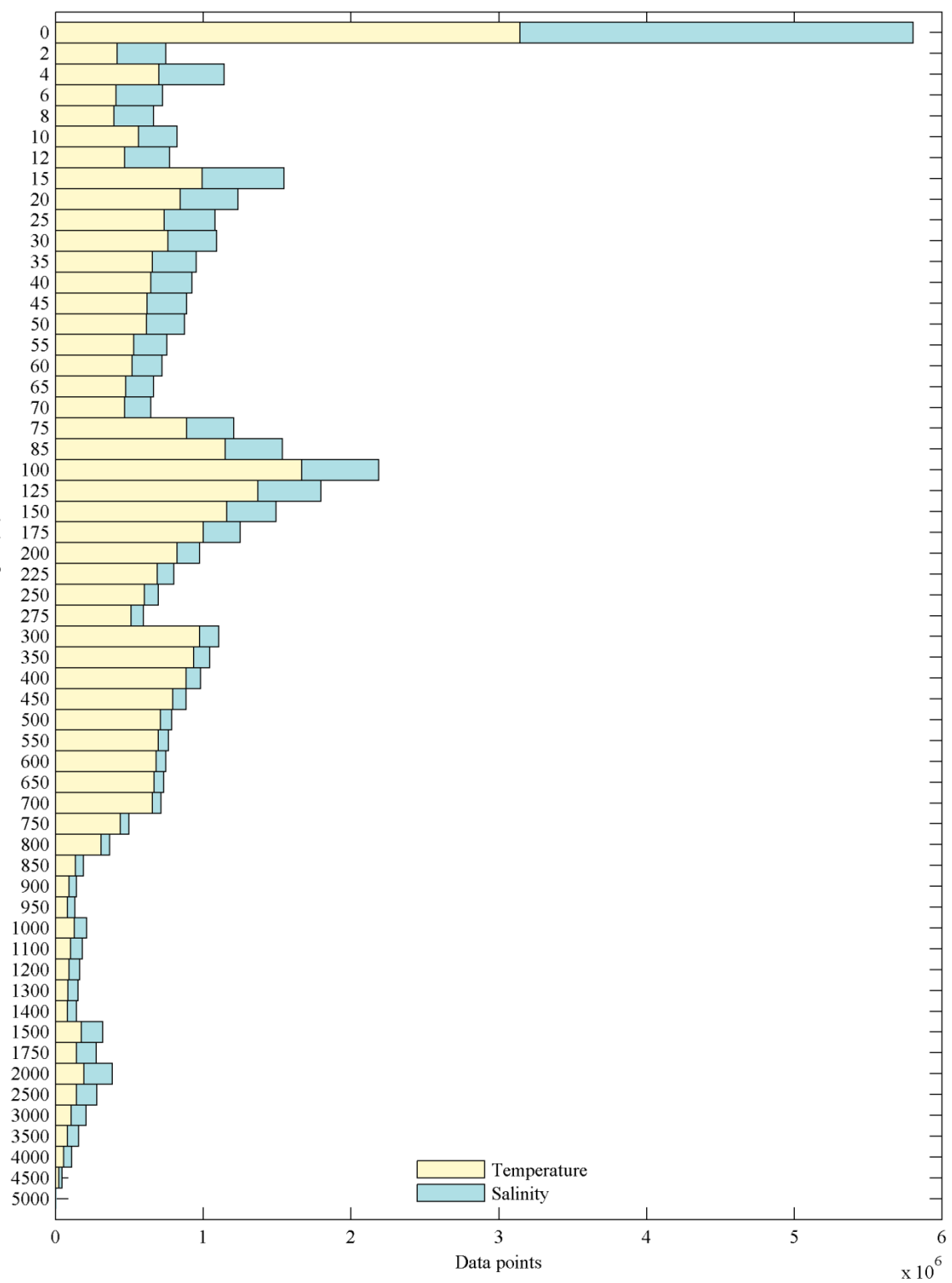
Figure 5-16: Depth distribution of data points at observed levels.

The seasonal distribution of data (Figure 5-17a) shows a dearth of data from the winter months, particularly December and January, when winds are strongest and seas are rough. Seventy percent of the data is collected during April–October, with the largest data collection occurring in the summer months, even with a dip in observations occurring in July (which is the most popular vacation month in the USA).

5.9 Interpolation onto Standard Depth Levels

Measured data were interpolated onto standard depths using a method based on that outlined by Reiniger and Ross (1968), which builds on Rattray Jr (1962) along with the modifications suggested in the WOD 2009 Documentation (Johnson et al. 2009).

The Lagrangian interpolation method of Rattray Jr (1962) takes the two points above and two points below the level of interest, and uses the simple average of the interpolations of two three-point parabolas through the upper three and the lower three points, as the interpolated value. Reiniger and Ross (1968) argue that in regions of strong gradients this may lead to "offshoots", whereby one of the two parabolas may give a bad interpolated value, which when incorporated into a simple arithmetic mean, results in a bad final interpolation value (see Figure 5-18a). Instead, they use a simple reference curve of the straight lines joining the points, and weight the two linearly interpolated results by an amount that is inversely

proportional to the distance between the interpolated and extrapolated points

(Figure 5-18b), (Reiniger and Ross 1968).
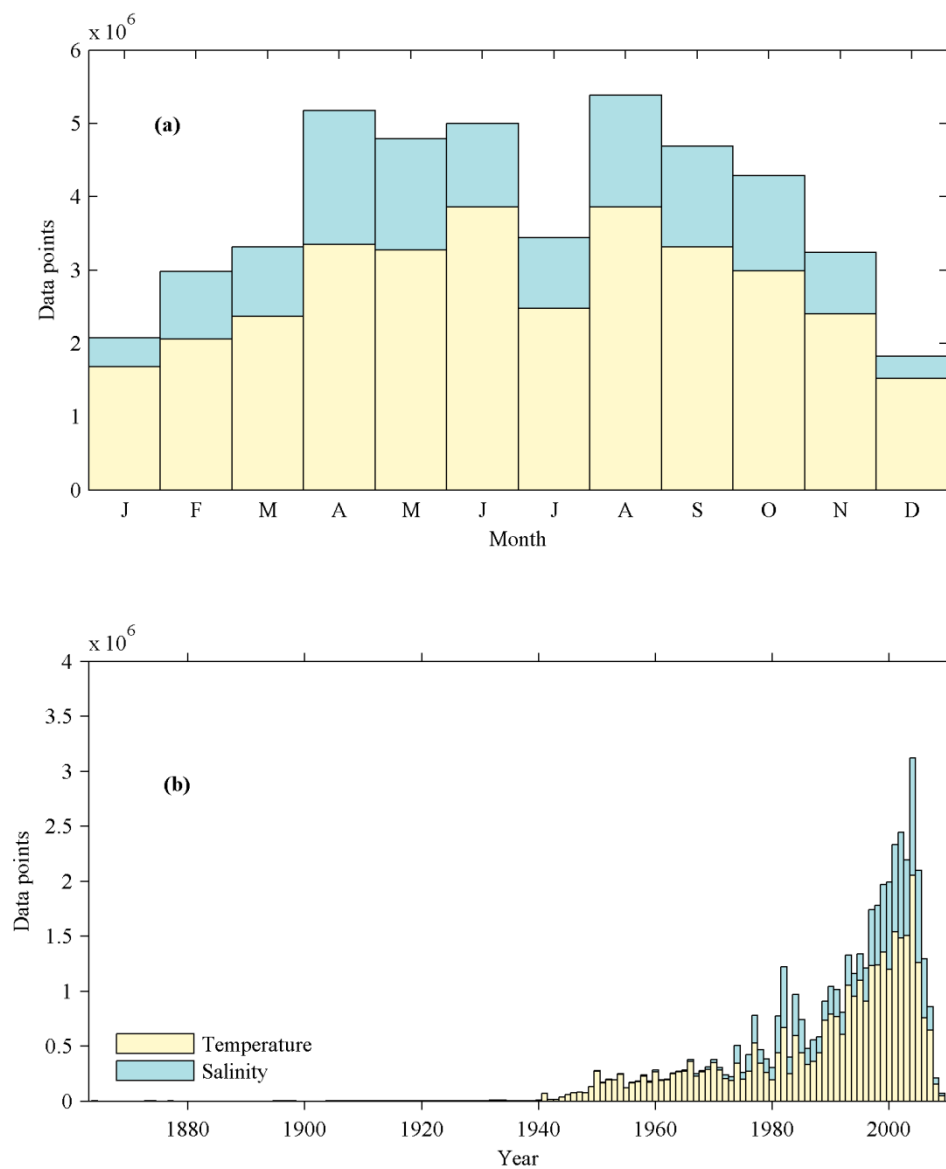
Figure 5-17: (a) Monthly distribution of final observed-level dataset, and (b) yearly distribution of final observed-level dataset.

In this work, fifty-seven standard depth levels are used, increasing in spacing with depth, as listed in Table 5-5, column 1. Following the simple reference curve method (Reiniger and Ross 1968), the four points surrounding each standard depth level are selected: the closest two above the level, and the closest two below it. The closest point above and the closest point below are referred to as "inside points" and the outer two points as "outside points".

This weighted parabola method (Reiniger and Ross 1968) is applied to all interior standard depth levels of profile data (with the exception that any data point that lies exactly on a standard depth level is directly substituted). At the top and the bottom (where only one point exists above or below the interpolation level) a linear interpolation is applied.

Next, the four points surrounding the values found by the weighted parabola method are examined, using criteria based on the method outlined by Johnson et al. (2009). For the interpolated value to be realistic, the four points used to construct the weighted parabolas must lie within a reasonably close distance from the level of interest. The distance criteria for the two inside points and for the two outside points at each depth, are listed in columns 2 and 3, respectively, of Table 5-5.

If an outside point lies beyond the corresponding maximum distance criteria, the interpolated value is instead calculated using the three-point Lagrangian interpolation method on the remaining three points. However, if an inside point lies outside its distance criteria, or if both outside points fail their criteria, then no value is returned for that standard level.
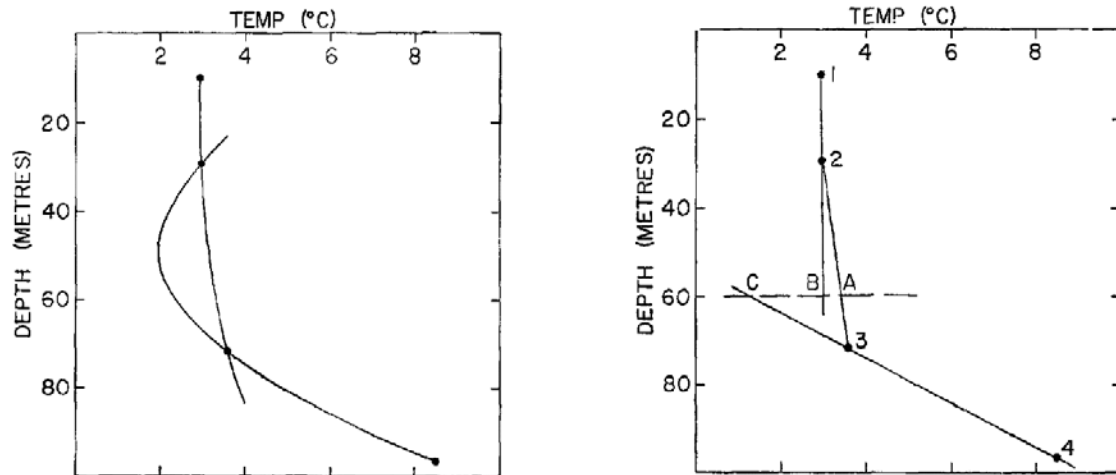
Figure 5-18: (a) Rattray's three-point Lagrangian interpolation method using overlapping sets of points, illustrating a case with a badly fitted parabola (b) The improved method fitting simple linear curves between each point. The linearly interpolated value A is adjusted by an amount relating to the distance between it and the two extrapolated values, B and C. Reproduced with permission from Figure (1) and Figure (2) of Reiniger and Ross (1968) *A method of interpolation with application to oceanographic data.* Oxford:Elsevier.

If all the distance criteria of an interpolated point are met, the interpolated value is further examined to determine whether it lies between its closest neighbors on either side. If it does not lie within these limits, then it is replaced by the linear interpolation of those two neighbors.

Values at the top and bottom of the data profile, which were determined by linear interpolation, are also screened based on the same distance criteria as listed in Table 5-5. If one of the inside points fails its distance criteria, the value is discarded. Finally, direct substitution of close-by points is used to fill any remaining gaps, where possible. If no value is assigned to 0 m, the closest point within the top 1 m is assigned to that level. If no value exists for the 2 m level, then the closest point below 1 m and greater than or equal to 3 m, is assigned to that level. Any other

remaining gaps are assigned the value of the closest point, if that point lies within the "close-point criteria" for its depth, as listed in column 4 of Table 5-5. These criteria equate to one fifth of the interval between standard depth levels around that depth.

Once interpolation was complete, 35% of temperature points were interpolated using the weighted parabola method, 37% came from direct substitution, 16% from linear interpolation at the top and bottom regions, and 9% from linear substitution because they were not between their nearest neighbors. One percent were found by substituting a close point, 1% were 0 m or 2 m points substituted from nearby, and only a tiny fraction utilized the three-point Lagrangian method. Salinity data followed a similar pattern, with the only major difference being that the top two methods were distributed differently: 54% were found by weighted point parabolas, and 18% by direct substitution. Since there are considerably fewer salinity measurements, it is expected that fewer will happen to fall on a standard depth level and be directly substituted, than with temperature.

At the 0-m level, 83.5% of temperature values, and 37.4% of salinity are directly substituted, with 16.5% of temperature and 62.6% of salinity substituted from the closest point in the top meter.

Fixed level data were mapped directly to a standard depth level if their depth fell within the closest point criteria. Those data which fell outside the criteria were discarded.

Table 5-5: Standard depth levels and distance criteria.

SDL (m)	IDC (m)	ODC (m)	Close Point Criteria (m)	SDL (m)	IDC (m)	ODC (m)	Close Point Criteria (m)
0	5	200	n/a	300	100	200	10
2	50	200	n/a	350	100	200	10
4	50	200	0.4	400	100	200	10
6	50	200	0.4	450	100	200	10
8	50	200	0.4	500	100	400	10
10	50	200	0.4	550	100	400	10
12	50	200	0.6	600	100	400	10
15	50	200	0.6	650	100	400	10
20	50	200	0.6	700	100	400	10
25	50	200	0.6	750	100	400	10
30	50	200	0.6	800	100	400	10
35	50	200	0.6	850	100	400	10
40	50	200	0.6	900	200	400	10
45	50	200	0.6	950	200	400	10
50	50	200	0.6	1000	200	400	20
55	50	200	0.6	1100	200	400	20
60	50	200	0.6	1200	200	400	20
65	50	200	0.6	1300	200	1000	20
70	50	200	0.6	1400	200	1000	20
75	50	200	2	1500	200	1000	50
85	50	200	3	1750	200	1000	50
100	50	200	5	2000	1000	1000	100
125	50	200	5	2500	1000	1000	100
150	50	200	5	3000	1000	1000	100
175	50	200	5	3500	1000	1000	100
200	50	200	5	4000	1000	1000	100
225	50	200	5	4500	1000	1000	100
250	100	200	5	5000	1000	1000	100
275	100	200	5				

5.10 Further Processing

5.10.1 T/S Screening of Interpolated Data

An additional Temperature/Salinity (T/S) screening was performed in exactly the same manner as on the interpolated data set (§5.7). This screening removed 2.5% of salinity data points along with 0.6% of temperature data points.

5.10.2 Clusters

A final processing step of removing large clusters of profiles was undertaken in a method similar to that of Ridgway et al. (2002).

Firstly, profiles were identified that existed at the exact same coordinates, and any groups larger than 30 were assessed. If in any month more than 20 profiles were found at the same location, those profiles were replaced by a single average at each depth. 349,886 such clusters were found and replaced by 1265 averaged profiles.

Next, large clusters of nearby points were identified. "Nearby" is defined as more than 30 profiles within a radius of 0.03° (approximately 250 m). Again, if in any month more than 20 profiles existed inside a cluster, a single average was substituted. 12,429 clusters were discovered and replaced by 401 averages in this way.

5.11 Final Data Summary: The Interpolated Standard Level Dataset

A final interpolated dataset of 464,260 profiles, containing 9,751,559 temperature points and 2,610,432 salinity points is used to calculate the climatology. Of these "profiles", 26,682 temperature profiles and 14,833 salinity profiles contain just a single point (i.e. they originate from the fixed-level dataset, or were reduced to one point during screening and processing). 2,592,243 point locations contain both temperature and salinity measurements.

The number of temperature points used to calculate the climatological value at each depth and month is illustrated in Figure 5-19, and the number of salinity points in Figure 5-20.

5.12 Coastline and Bathymetry

5.12.1 Coastline

A coastline dataset for the MAB region (82^0W to 58^0W, and from 30^0N to 48^0N) was obtained using the National Oceanic and Atmospheric Administration (NOAA)'s National Geophysical Data Center Coastline Extractor (Signel 2005). The data are part of the NOAA National Ocean Service (NOS) Medium Resolution Digital Vector Shoreline of the United States, at 1:70,000 resolution.
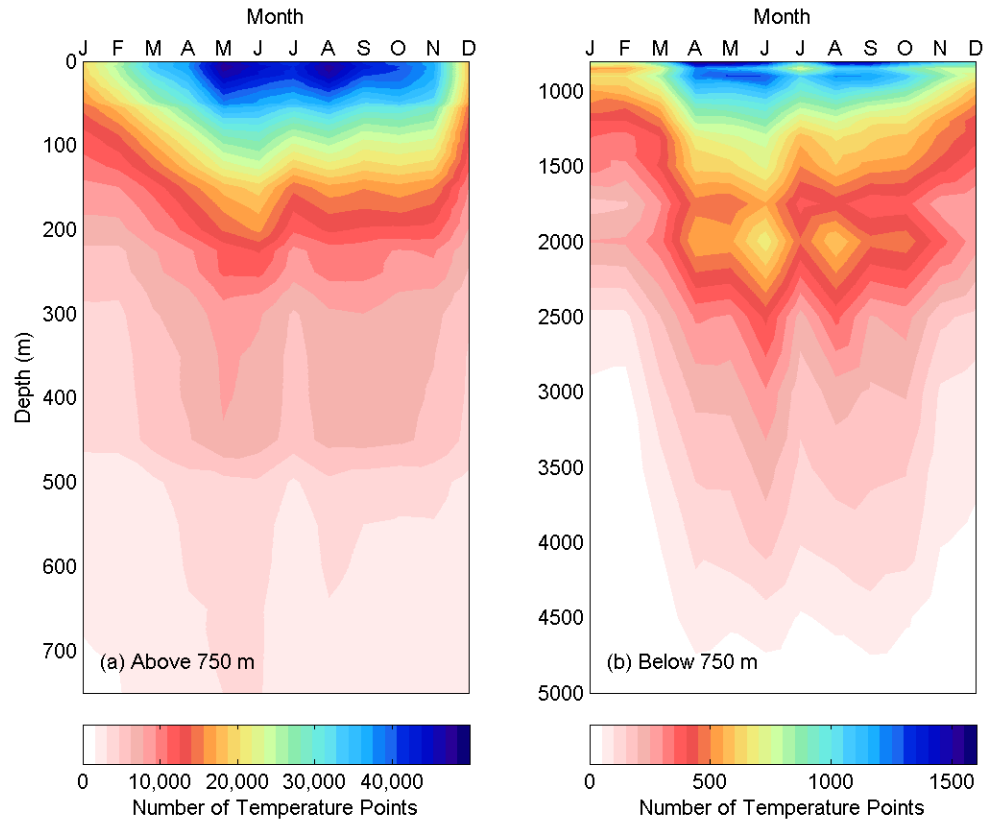
Figure 5-19: Temperature data points included in the climatological estimate, at each month and standard depth level for (a) 0–750 m (b) 750–5000 m. Note the different color scale in each panel.

5.12.2 Bathymetry

The bathymetry dataset used in this study was taken from the Shuttle Radar

Topography Mission (SRTM) bathymetry dataset in 30 arc second resolution

(Becker et al. 2009).
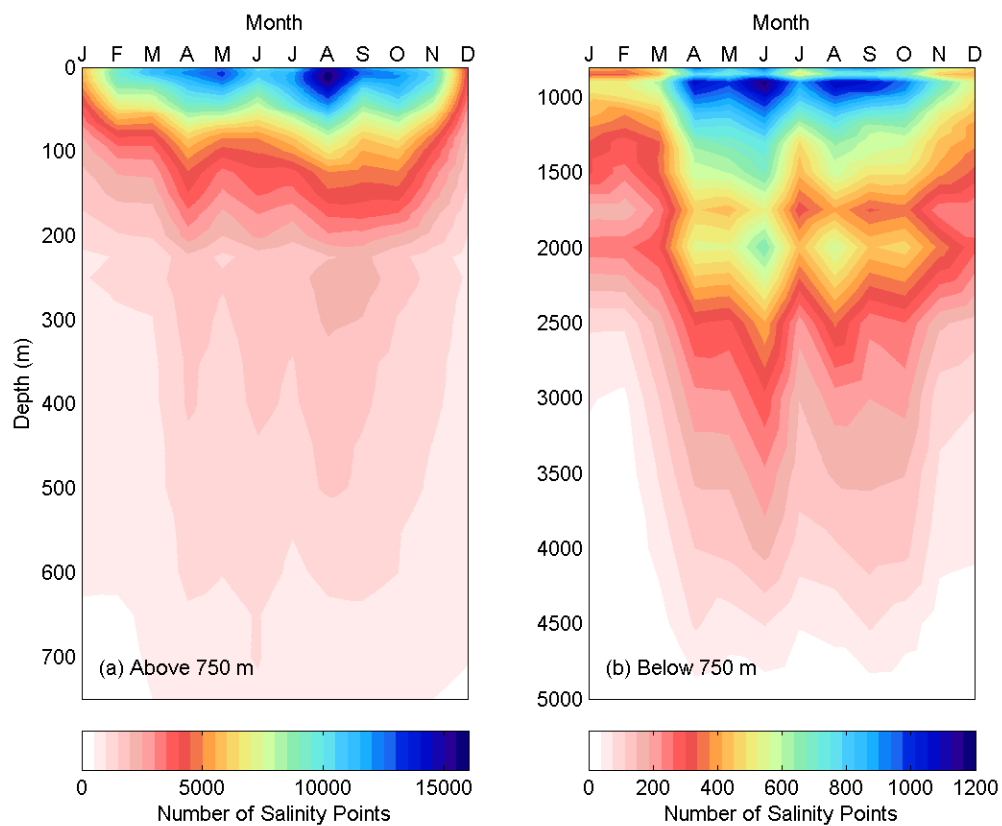
Figure 5-20: As for Figure 5-19, except for salinity.

Table 5-6: MAB Regions found within the climatology data domain. From Hofmann et al. (2008).

Region Label	Region Name	Region Label	Region Name
BFN	Bay of Fundy - North	MABO	Outer Middle Atlantic Bight Outer Shelf
BFS	Bay of Fundy - South	MABSSF	Middle Atlantic Bight Shelf Slope Front
C1	Coastal Chesapeake Bay Shelf	MB	Massachusetts Bay
C2	Outer Chesapeake Bay Shelf	MCCS	Maine Coastal Current - South
CBAY	Chesapeake Bay	MCCW	Maine Coastal Current - West
CGOM	Central Gulf of Maine	N1	Coastal New Jersey
CH1	Coastal Cape Hatteras Shelf	N2	Mid New Jersey Shelf
CH2	Outer Cape Hatteras Shelf	N3	Outer New Jersey Shelf
D1	Coastal Delaware Bay Shelf	NBAY	Narragansett Bay
D2	Mid Delaware Bay Shelf	NC1	Coastal North Carolina Shelf
D3	Outer Delaware Bay Shelf	NC2	Outer North Carolina Shelf
DBAY	Delaware Bay	NEC	Northeast Channel
ES1	Northeast Nova Scotia Shelf	NS	Nantucket Shoals
ES2	Southeast Nova Scotia Shelf	NSSSF	Nova Scotia Shelf Slope Front
GB	Georges Bank	PAM	Pamlico Sound
GBS	Georges Bank - South	RBAY	Raritan Bay
GSE	Gulf Stream East	SC1	Coastal South Carolina Shelf
GSF	Gulf Stream Flank	SC2	Outer South Carolina Shelf
GSN	Gulf Stream North	SLOPE1	Nova Scotian Slope
GSW	Gulf Stream West	SLOPE2	Northern MAB Slope
H	New York Harbor	SLOPE3	Southern MAB Slope
JBASIN	Jordan Basin	SSN	Sargasso Sea North
L1	Coastal Long Island Shelf	WBASIN	Wilkinson Basin
L2	Mid Long Island Shelf	WS1	Coastal Western Nova Scotia Shelf
L3	Outer Long Island Shelf	WS2	Outer Western Nova Scotia Shelf
LIS	Long Island Sound	WS2	Outer Western Nova Scotia Shelf

6 Constructing the Climatology

6.1 Introduction

The Mid-Atlantic Ocean Climatological and Hydrographic Atlas (MOCHA), is a three-dimensional atlas of the temperature and salinity constructed from historical records in the MAB. It is composed of spatial maps of temperature and salinity at each depth, for each month of the year, resulting in 684 (12 months × 57 depths) separate maps for each of temperature and salinity. Each grid point in a map is a weighted least squares (loess) fit of the surrounding data points, with the weightings dependent on horizontal distance, vertical distance, time and bathymetric depth.

6.2 The Climatology Grid

The climatology grid covers the Mid Atlantic Bight and the Gulf of Maine, with its orientation aligned (54.8º from north) to the bathymetry of the shelfbreak off the New Jersey shore (Figure 1). Initially the climatology covered only the Mid Atlantic Bight, however it was extended to include the Gulf of Maine to enable colleagues to use the results as initial conditions in the Regional Ocean Modeling System (ROMS) for studies in the wider region. Discussion and analysis in this work will focus solely on the Mid Atlantic Bight.
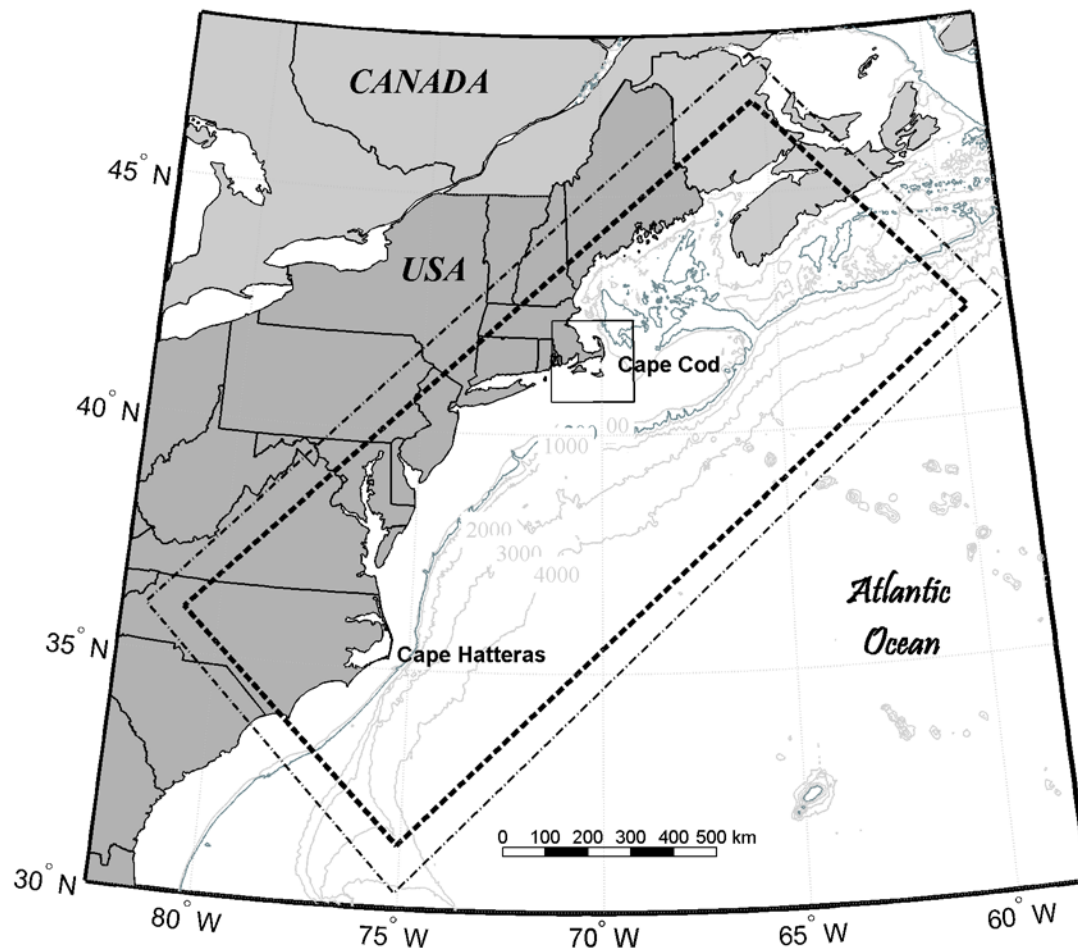
Figure 6-1: The MOCHA grid (---), encompassing the Mid Atlantic Bight and the Gulf of Maine. Data is taken from a larger surrounding region (-·-). The region around Cape Cod (—) is enlarged in Figure 6-2.

The climatology grid is comprised of 57,150 cells (381 alongshore by 150 cross-shore), with cell centers 0.05º apart. The northwest corner of the grid lies at (46.9186ºN, 65.3807ºW), the northeast corner at (42.2760ºN, 59.5541ºW), the southwest is situated at 35.9656ºN, 80.9059ºW and the southeast at (31.3230ºN, 75.0793ºW).

Of the 57,150 grid cells, 12,128 are on land or within coastal sounds (such as Pamlico and Albemarle Sounds at Cape Hatteras), leaving 45,022 grid cells located
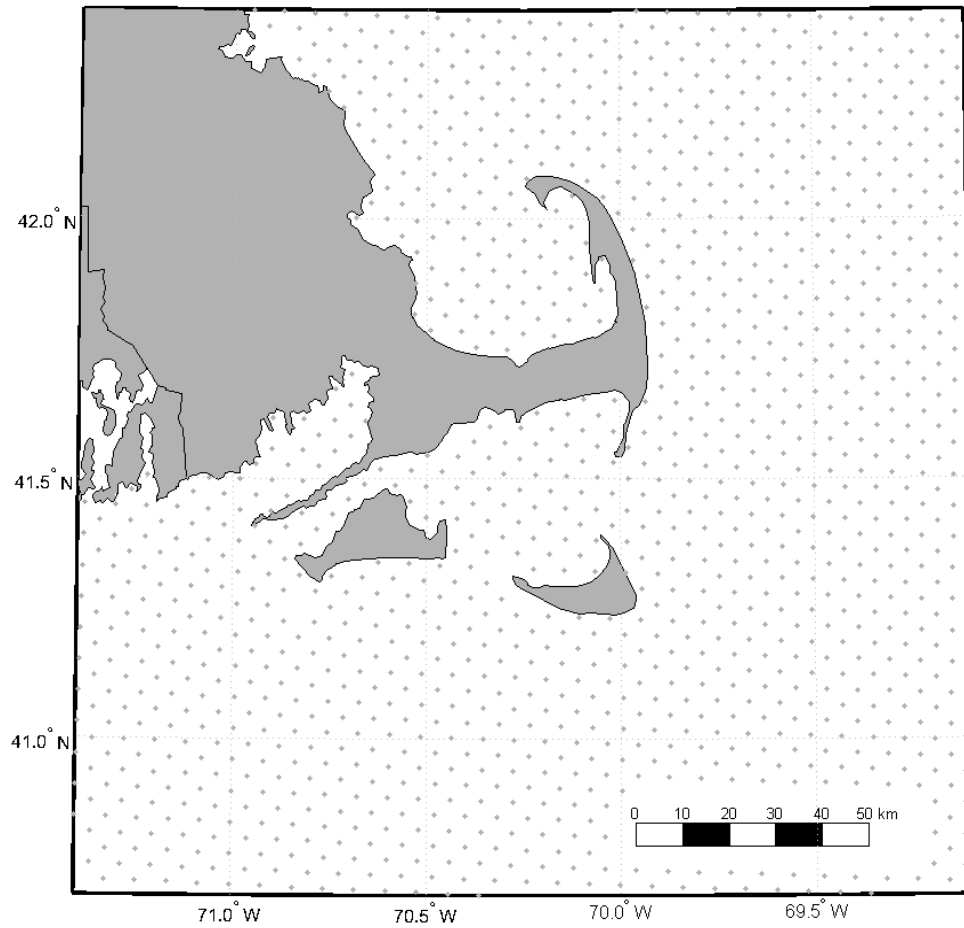
Figure 6-2: Close of up view of the climatology grid points around Cape Cod. Grid spacing is 0.05°.

in the ocean, or in estuaries, inlets and rivers that are open to oceanic influence. The climatology grid is calculated at cell centers, hereafter referred to as *grid points*.

The distance in kilometers between grid points changes with latitude, due to the spherical shape of the earth. Grid points are approximately 5.6 km apart in the alongshore direction, and vary with latitude from 3.9–4.7 km across shore. The area of the grid cells ranges from 21.7–26.4 km².

The greatest bathymetric depth in this region is 5312 m, and the climatology

consists of 57 depth levels, from 0 m to 5000 m, as given in Table 5.5.

6.3 Loess Regression

Locally weighted regression, or "loess" was first introduced by Cleveland (1979) and

expanded on in later articles, (e.g. Cleveland and Devlin 1988). It builds on least

squares regression by giving more weight during the fitting procedure to data near

the point of interest, and less weight to data that lie further away. The data,

modified by a weight function (traditionally a tri-cubic function), are then fitted to a

low-order polynomial.

The mapping technique used to create the MOCHA climatology is a modified version

of the loess procedure used by Ridgway et al. (2002) and Dunn and Ridgway (2002)

to develop the CSIRO (Commonwealth Scientific and Industrial Research

Organization) Atlas of Regional Seas (CARS). Their method employs 3-D spatial

loess mapping performed simultaneously with annual and semi-annual harmonic

fitting, and employs a weighting term to adjust for land barriers between

observations and grid points. In MOCHA, the time weighting is instead also

performed as a quadratic loess fit, and the land barrier term is not used.

Following the basic procedure of Ridgway et al. (2002), the aim is to find the

climatological estimate $\hat{\phi}\left(x_n, y_n, z_s, t_m\right)$ of temperature or salinity at some grid point

x_n, y_n with a standard depth z_s at time t_m. The standard depths are listed in Table

(5.5) and times t_n are at the mid-point of each month.

Initially, all data points in the month in question, in the months either side (but only

at depth in question), and at the standard depth levels above and below (but only

during month in question) are selected (Figure 6-3). A weighted least squares fit is

applied to the set of neighboring observations for each grid point, at each depth, and

at each month, resulting in a 4-dimensional climatology. The technique is applied

separately to both temperature and salinity.

The fitted function is assumed to be of the form:

$$\hat{\phi}\left(x_n, y_n, z_s, t_m\right) = a_0 + a_1 x + a_2 y + a_3 x^2 + a_4 y^2 + a_5 xy + a_6 z + a_7 z^2 + a_8 t + a_9 t^2 \quad \text{6-1}$$

For K neighboring data points, x_k, y_k, z_k, and t_k are the longitude, latitude,

depth, and time of each observation; x, y and z are the distances from the

observation location to the grid point (where $x = x_k - x_n$, $y = y_k - y_n$, $z = z_k - z_s$);

and t is the time difference between the observation and the mid-point of the month:

$t = t_k - t_m$.
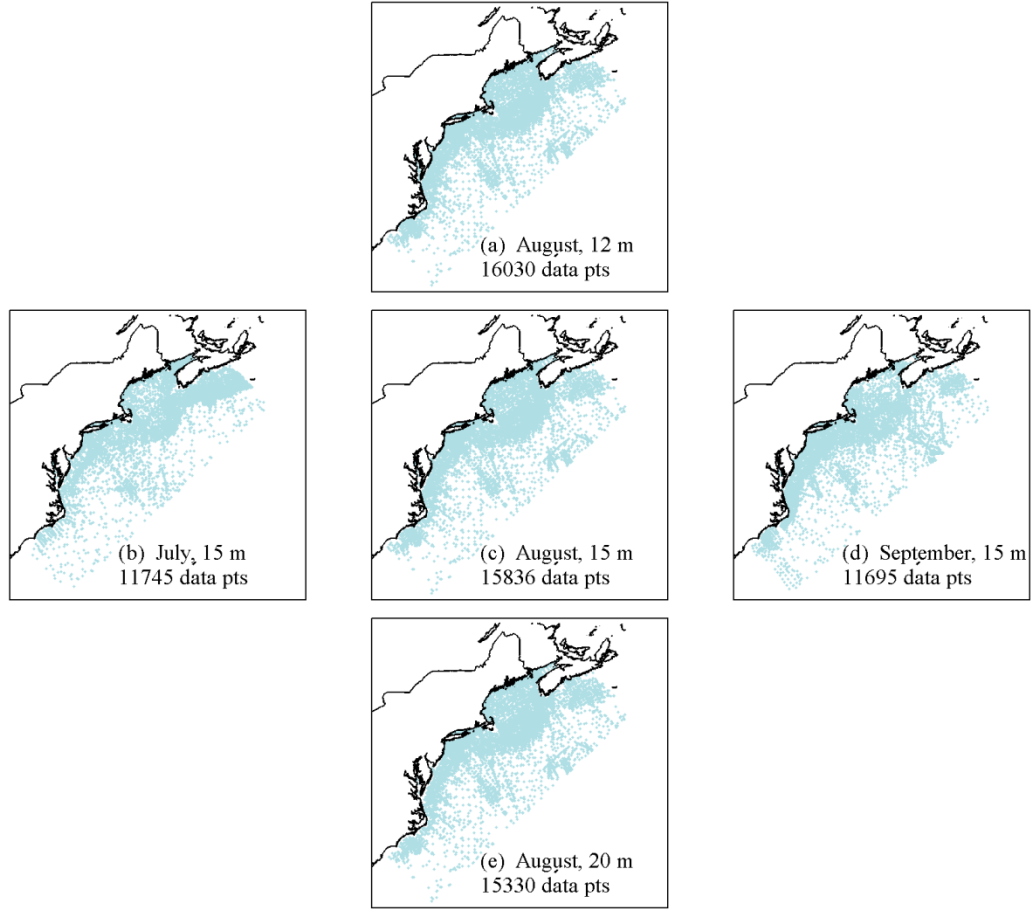
Figure 6-3: Distribution of data points available for evaluation of the climatological estimate for August at 15m (c) . Data are also taken from the months either side (b) and (d), and the depths above and below (a) and (e).

A solution for the regression coefficients a_n , is found by minimizing the weighted sum of squared errors between the observations, $\phi_k = \phi\left(x_k, y_k, z_k, t_k\right)$ and the expression for the fitted values, $\hat{\phi}_k$:

$$\Psi = \sum_{k=1}^{K} w_k^{\,2} \left(\hat{\phi}_k - \phi_k\right)^2 \qquad\qquad 6\text{-}2$$

Since the observations have been centered on the grid point, the climatological

estimate is simply a_0.

The traditional function for defining the weighting coefficients, w_k is the tri-cubic

function:

$$w_k = \begin{cases} \left(1-r^3\right)^3 & 0 < r < 1 \\ 0 & r > 1 \end{cases}$$

6-3

where r is the normalized distance metric, a term which indicates the separation

between an observation and the estimated grid point. This separation is expressed

here in terms of spatial distance, time and bathymetric difference:

$$r\left(x_k, y_k, z_k, t_k, d_k, d_n\right) = \left(r_{dist}^{\ 2} + r_{bathy}^{\ 2} + r_{vert}^{\ 2} + r_{time}^{\ 2}\right)^{\frac{1}{2}}$$

6-4

where r_{dist} is the function of the radial distance between an observation and the grid

point; r_{bathy} relates the difference in bottom depth (bathymetry), r_{vert} expresses the

vertical separation; and r_{time} is a function of the time difference.

6.4 Loess Weightings

6.4.1 Distance Weighting

The distance metric, r_{dist}, is the normalized distance between the observation and the grid point:

$$r_{\text{dist}} = \frac{\sqrt{(x_k - x_n)^2 + (y_k - y_n)^2}}{R} \qquad \qquad 6\text{-}5$$

where R is the maximum distance, i.e. the radius encircling the set of observations.

Initially R is set to the distance of the 2000th point in the month and depth of interest (hereafter referred to as R_{initial}). The total number of data points initially selected is therefore roughly 5×2000 (= 10,000) for internal depth levels , or 4×2000 (= 8000) at the top and bottom standard levels, although the exact number depends on the varying data distribution in each month and depth.

In areas of high data density, a minimum radius of 100 km is imposed on R_{initial}, while in regions of sparse data, an outer radius maximum of 1500 km is set. Thus the resolution of the climatology varies, depending on the data distribution surrounding the grid point.

An example of the distance metric r_{dist} calculated using $K_{\text{(initial)}}$ data points and $R = R_{\text{initial}}$ for one grid point is given in Figure 6-4. Note that if the weighting w

were calculated solely from the distance metric, full weighting would result from

$r_{dist} = 0$ and no weight would be given when $r_{dist} = 1$.
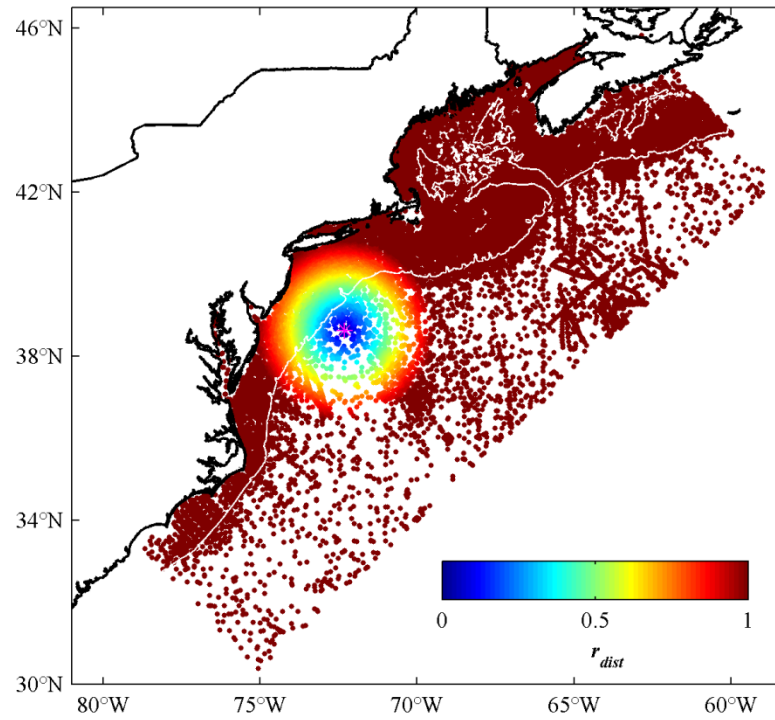
Figure 6-4: Normalized distance metric, r_{dist} for estimating salinity at a grid cell in August at 15 m depth. There are 9214 weighted data points K, and the distance radius R is 249 km. Closest values ($r_{dist} = 0$) are given full weighting, while any points greater than one are given zero weighting.

6.4.2 Bathymetry Weighting

The Topographic Adjusted Relief (TAR) scheme of Dunn and Ridgway (2002) was used to determine the weighting of observations for the influence of varying bathymetric depth. The normalized function has the form:

$$r_{bathy} = 1 - \left[\max\left(0, \ 1 - \mu \frac{d_k}{d_n} \right) - \max\left(0, \ 1 - \lambda \frac{d_k}{d_n} \right) \right]$$

6-6

where d_k is the bottom depth at the observation and d_n is the bottom depth at the grid point. Constants control the rate of inshore cutoff (λ) and the rate of offshore cutoff (μ).

After much experimentation values of λ = 1.5 and μ = 0.006 were chosen for this study. These values give a smooth result throughout the MAB, while retaining the separation across the shelf-slope (Figure 6-5).

In some regions of very steep bathymetry, no choice of parameters provided a meaningful solution. In particular, the shelf edge offshore from Cape Hatteras is an area of steep bathymetry, sparse data (especially in the winter months), and contains strong temperature and salinity gradients due to the nearby presence of the Gulf Stream. It is therefore a very difficult region to map successfully.
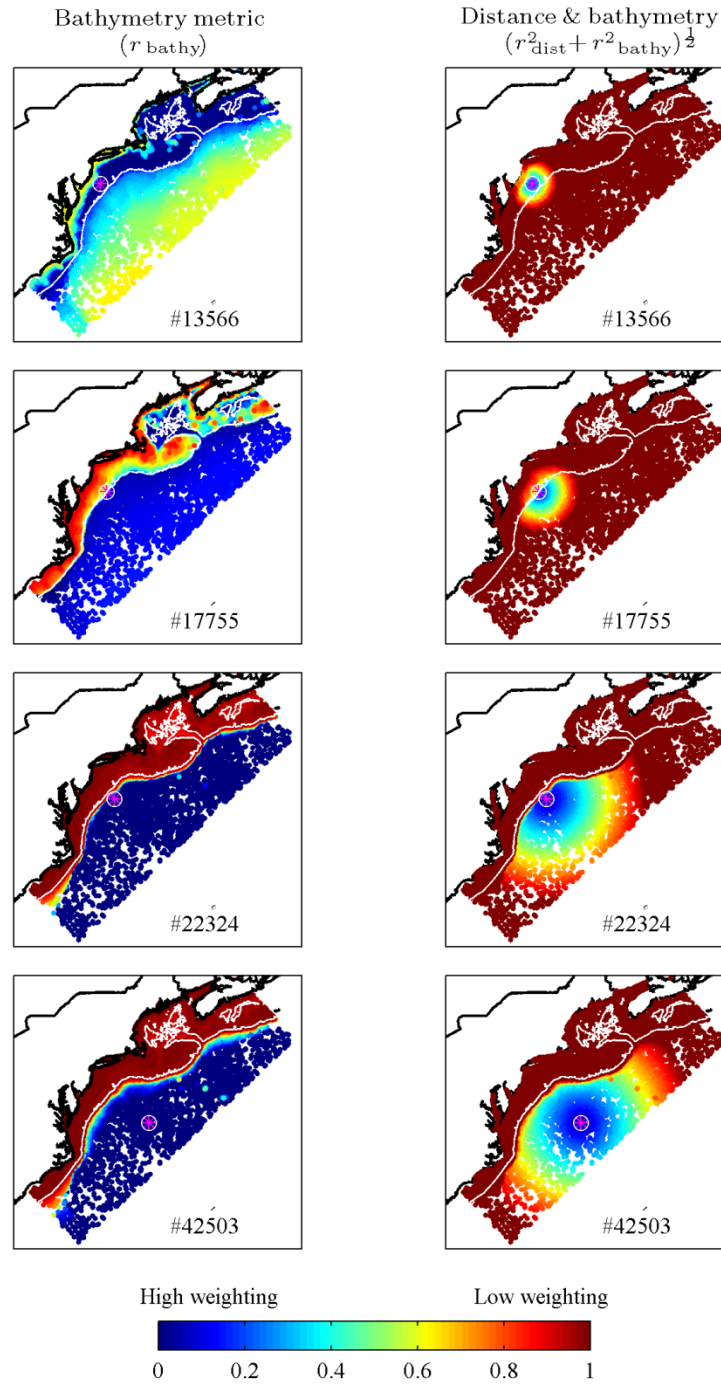
Figure 6-5: Bathymetry weighting function (left-hand panel) and the combined distance and bathymetry functions (right-hand panel) for salinity during August at 15 m depth. The first row shows the effect of the two weightings on a grid points located on the shelf, the second row shows a grid point near the shelf break, the third row on the ocean side of the shelf break, and the fourth row displays the weightings for a grid point located far offshore.

6.4.3 Vertical Weighting

Data points on the standard depths above and below the grid cell of interest are included in the loess fit, to compensate for differences in the number of data observations at different standard depths, and to provide a smooth result in the vertical. Data points at the depth levels above and below are given a fixed weighting of 50% of the weighting of the corresponding point on the grid cell's actual depth level. Thus, the vertical "radius" changes with each grid cell, and will equal twice the difference in depth between the standard level, z_s, and the level above or below, z_k :

$$r_{\text{vert}} = \frac{z_k - z_s}{R_z}$$
6-7

For example, at $z_s = 12\,\text{m}$, the upper level is at 10 m. We require $r_{\text{vert}} = 0.5$, therefore $R_z = (10 - 12) / 0.5 = -4$ m. At the lower level (15 m), $R_z = (15 - 12) / 0.5 = 6$ m. At the level of interest $R_{\text{vert}} = 0$.

6.4.4 Time Weighting

For each month, data in the month either side are also included in the loess fit. Observations made during the month of interest are given full weighting ($r_{\text{time}} = 0$), and an inverse Gaussian curve determines the decreasing weighting over the neighboring month (Figure 6-6).
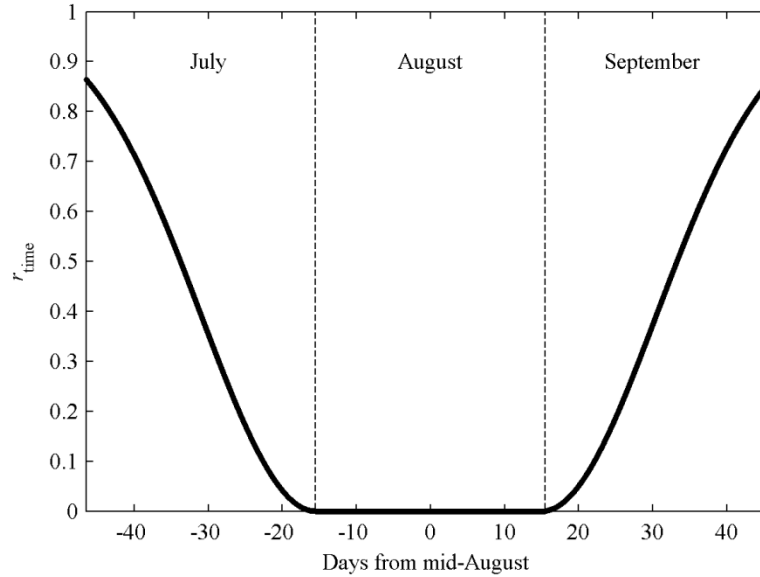
Figure 6-6: Time weighting term for August. Full weight ($r_{time} = 0$) is given to all points taken during August, and weight decreases along a Gaussian curve for data points observed in the months either side. Time is measured in days from the mid-point of the month.

6.4.5   Combining Weights

The final equation used for the normalized distance metric is:

$$r\left(x_k, y_k, z_k, d_k, d_n, t_n\right) = \left(\left(\frac{\sqrt{x^2 + y^2}}{R}\right)^2 + \left(\frac{r_b}{R_b}\right)^2 + \left(\frac{z_k - z_s}{R_z}\right)^2 + r_{time}^2\right)^{\frac{1}{2}}$$ 6-8

The weightings, w_k, are first calculated using $K_{initial}$ data points and setting

$R = R_{initial}$, then all data points with non-zero weighting are retained. If few data

points remain, then R is increased by 20 km, and the weightings re-calculated.

This iteration continues until at least $\frac{7}{8}$ of the original number of data points

($K_{initial}$) are selected, or all data points have been selected. The weightings are

calculated a final time with for these K points with the final value of R. An example of the final weightings w_k (for August at 15 m) are illustrated in Figure 6-7. An example of the final K and R for estimating climatological values for August at 15 m are shown in Figure 6-8.
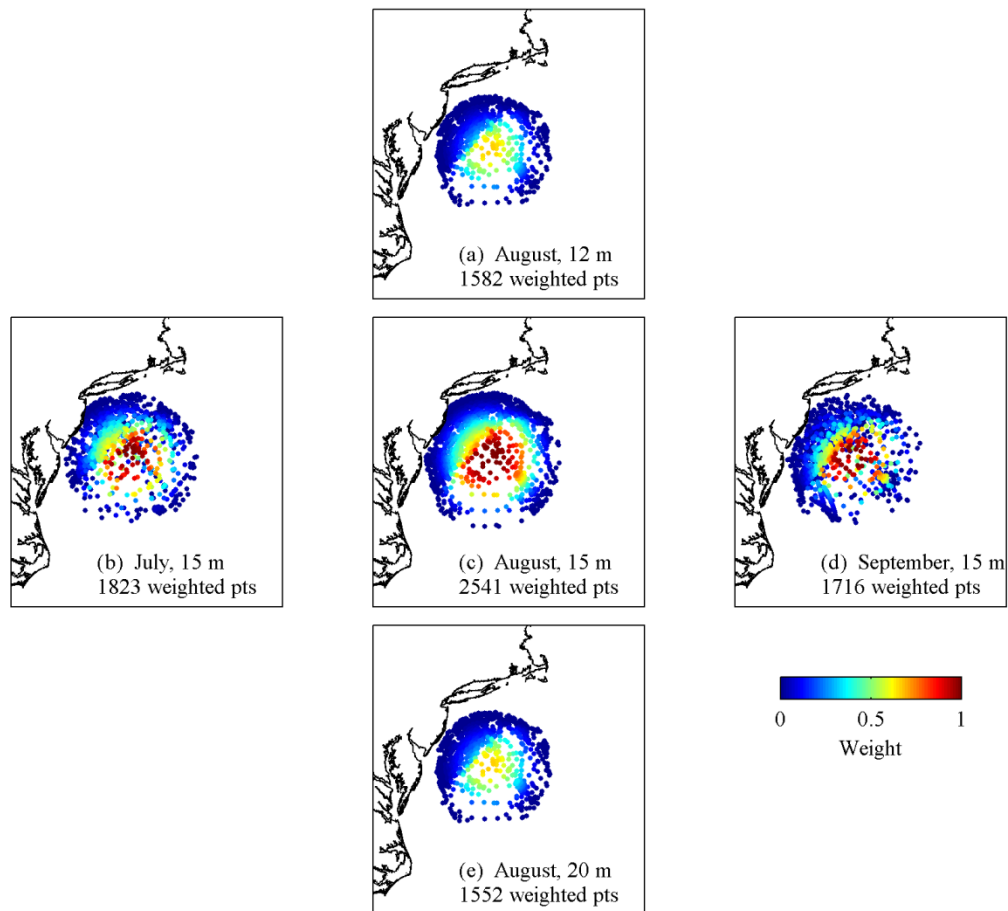
Figure 6-7: Final weightings w for salinity at a grid cell in August at 15 m. Points from (a) depths above and (e) below the 15-m level have both fewer points and clearly lower weightings than those at (c) 15 m. Observations from neighboring months (b) July, and (d) September, are also significantly fewer.
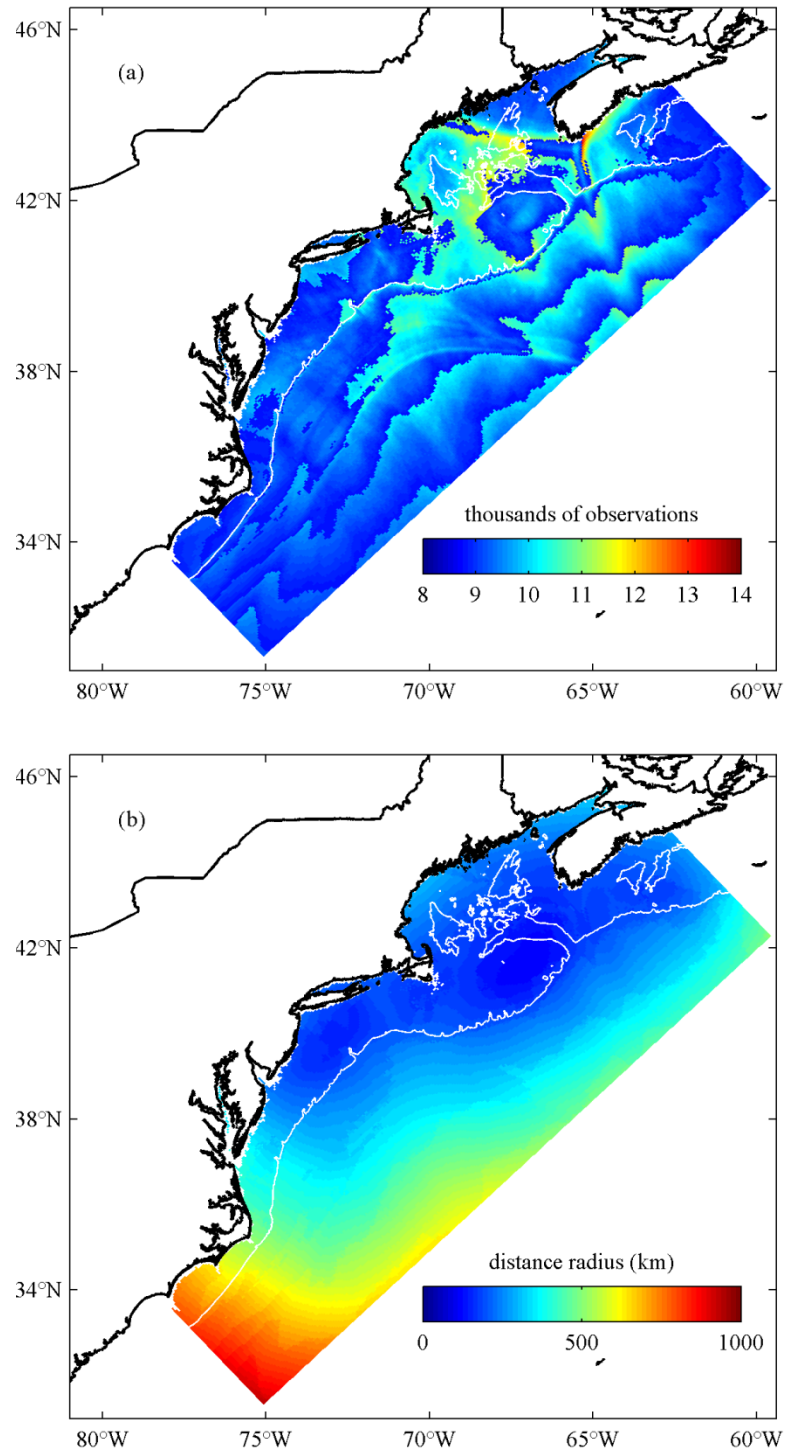
Figure 6-8: The final values for salinity during August at 15 m: (a) final number of weighted observations K, and (b) the final distance radius (the maximum distance to observations included in the fit to the grid point being estimated).

6.4.6   Quadrant Check

To ensure a good spread of data is used for each fit, in regions of sparse data, the K weighted observations are divided into four quadrants divided by north-south and east-west lines. If the observations do not lie in at least three of the four quadrants, the estimate is not made.

6.4.7   Bogus Data Points

An additional "bogus" data point is created for each grid point by taking the weighted inverse distance average of the closest 10% of weighted data points, and setting it to full weighting at the exact grid location, and at the mid-point of the month. This technique compensates for regions where the loess scheme tends to become unstable, particularly in regions of sparse data (see Ridgway et al. (2002)'s Figure 8 for an example of the success of bogusing in such a case).

6.4.8   The Loess Fit

Finally, the weighted data is fitted to Eq. 6-1 and the climatological value at the grid location obtained, separately, for both temperature and salinity (e.g. Figure 6-9). Thus temperature and salinity maps each have different K and R values and therefore different weights w. The resolution of each map depends on data density, which is everywhere much greater for temperature than for salinity.
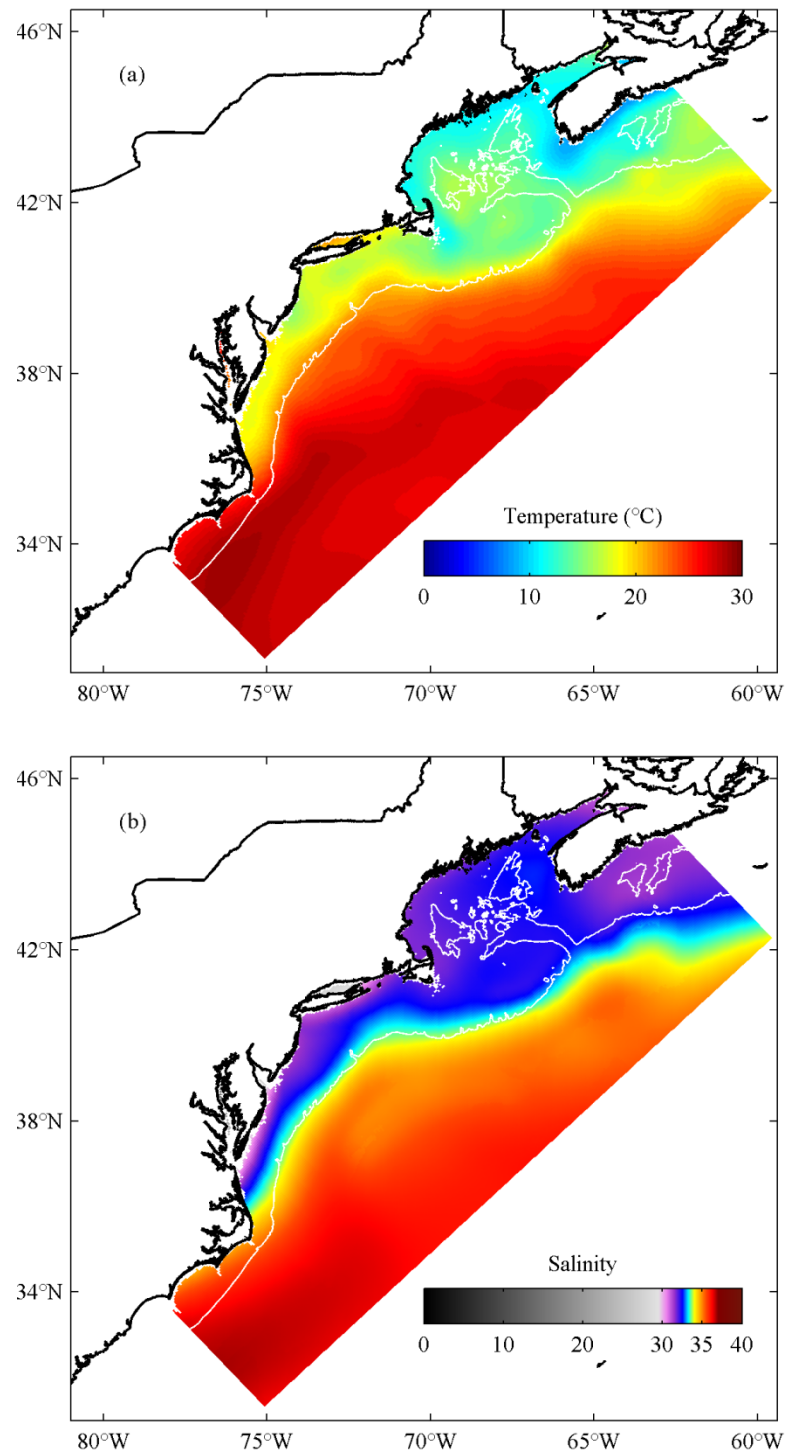
Figure 6-9: Climatological result for the entire MOCHA grid for August at 15 m: (a) temperature and (b) salinity.

6.5 Filling Gaps

Once the loess fit has been calculated, all data spikes and unrealistic outliers are removed. These gaps, along with any others (e.g. from failing the quadrant check) of a single level in a vertical profile are filled by linear interpolation of the point above and below. Any gaps of more than one level in the vertical direction are filled by the averaged values of the neighboring (in the horizontal plane) grid points, provided that at least five of the neighboring eight grid estimates exist.

6.6 Correcting for Static Stability

The final step in completing the MOCHA climatology is to adjust data values to ensure static stability in the water column.

Static stability E is a measure of the change in potential density ρ between two parcels of water. In a water column, static stability is calculated by:

$$E = \rho_{\text{lower level}} - \rho_{\text{upper level}} \qquad\qquad\qquad \text{6-9}$$

An unstable region (i.e. a density inversion) occurs wherever E is negative. In a climatology, such unstable profiles may be common since the result is an averaged estimate, not a real-time snapshot of the ocean. A common approach is to adjust the individual salinity and temperature profiles to reduce the instability in the corresponding density profile.

The method used to stabilize MOCHA is that developed by Chu and Fan (2010): a
scheme which minimally adjusts temperature and salinity profiles, while
maintaining the conservation of heat and salt.

A profile is considered unstable if any pair of values within the profile result in a
stability of $E < -0.03\,\mathrm{kg\,m^{-3}}$ at depths from the surface down to 30 m,
$E < -0.02\,\mathrm{kg\,m^{-3}}$ at depths beyond 30 m and up to 400 m, and $E < 0\,\mathrm{kg\,m^{-3}}$ beyond
400 m. Values slightly below zero are used in the upper waters to allow for precision
limitations in the measurements. All such profiles are either adjusted iteratively
until stability is reached (as in Figure 6-10), or an iteration limit is reached; or the
profile is deemed so unstable that adjustment is not attempted and values at all
depths are replaced by the depth averaged temperature and salinity.

Details of the adjustment process are summarized in Table 6-1. Over all months,
76.2% of profiles were found to be unstable at least one level. Of these unstable
profiles, 98.9% were successfully adjusted, 0.7% failed after 20 iterations (the limit
set), and 0.4% were replaced by depth-averaged values without attempting to adjust.
At most, four iterations were sufficient to obtain stability for all successfully
adjusted profiles. After adjustment, only 0.5% of profiles remained unstable.

Table 6-1: Results of the adjustment process for achieving static stability.

Month	Stable Profiles	Unstable Profiles			Total Profiles
		Adjusted	Failed	Averaged	
January	8,287	36,115	283	118	44,803
February	6,490	37,291	978	107	44,866
March	5,912	37,764	731	462	44,869
April	10,517	33,964	293	93	44,867
May	10,440	34,301	61	67	44,869
June	11,911	32,913	8	22	44,854
July	15,458	29,388	2	11	44,859
August	15,471	29,365	7	25	44,868
September	12,014	32,719	30	106	44,869
October	11,333	33,508	16	12	44,869
November	11,256	33,126	374	93	44,849
December	9,063	35,276	30	465	44,834
Total	128,152	405,730	2,813	1,581	538,276
%	23.8%	75.4%	0.5%	0.3%	
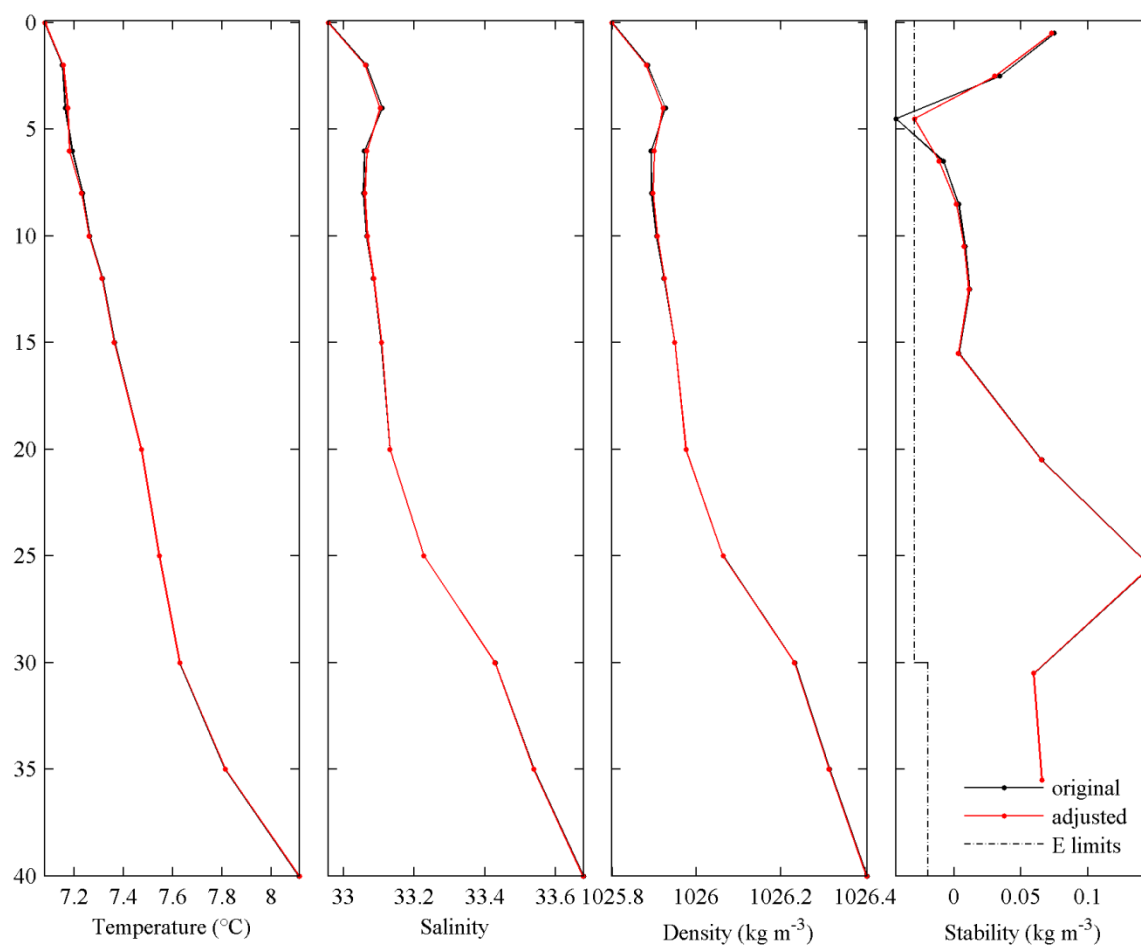
Figure 6-10: An example of original and adjusted profiles at grid location 74.0608ºW, 38.7974ºN in 45 m of water: (a) temperature, (b) salinity, (c) density and (d) stability. The original density and stability profiles show one region of instability between 4 and 6 m, which is corrected by adjusting both temperature and salinity values in the profile. Adjustment is made until the stability profile just reaches satisfactory limits (black dashed), which is $> 0.03\,\mathrm{kg\,m}^{-3}$ at this depth.

7 Validation

7.1 Introduction

The first questions to ask after completing a climatology are: does it accurately portray the data that it is compiled from; does it portray the features of interest in the region, and how does it compare with other models and climatologies?

In this chapter the MOCHA climatology is compared to the input dataset; to an independent dataset from glider recordings; to typical cross-shelf transects developed by other researchers; and to two other regional climatologies. The first section outlines the statistics used to make these comparisons. The ways in which MOCHA has already been put to use by researchers is also discussed.

7.2 Comparison Statistics

Univariate statistics are commonly used to describe the difference between two fields (e.g. a model or climatology, and a dataset). Statistical values used to quantify these differences include the correlation coefficient R, root-mean-square (RMS) difference E, the centered pattern RMS difference E', the mean bias ($\overline{E}$ or B) and the standard deviation σ. No single statistical value can incorporate all elements of

comparison between two fields: some statistics quantify the difference in the *pattern*

of two fields, while others look at the *magnitude* of the variation within each field.

Which of these two elements (the pattern, or the magnitude of variation), and which

statistic(s) are most important to the researcher will depend on each application.

A summary of these statistics, and an outline of the Target and Taylor diagrams

that are used to visualize combinations of them, is presented in the following

sections. Further details can be found in Taylor (2001); Jolliff et al. (2009); Hofmann

et al. (2008) and Stow et al. (2009).

7.2.1   Correlation Coefficient

The correlation coefficient R is used to quantify the similarity in the pattern of two

variables. For a model or climatology m_n, and observations o_n, both defined at N

discrete points in time or space, the (non-weighted) correlation coefficient is:

$$R = \frac{\frac{1}{N}\sum_{n=1}^{N}\left(m_n - \overline{m}\right)\left(o_n - \overline{o}\right)}{\sigma_m \sigma_o} \qquad \text{7-1}$$

R varies from -1 to 1, with a value of 1 meaning the two fields have the same

centered pattern of variation, (but not necessarily the same magnitude: the

correlation coefficient gives no information regarding a magnitude difference).

7.2.2 RMS Difference

The RMS difference E is a measure of the average magnitude of difference between the two functions:

$$E = \sqrt{\frac{1}{N}\sum_{n=1}^{N}\left(m_n - o_n\right)^2}$$

7-2

This is a positive number, with a value of zero indicating perfect agreement between the two fields. As a magnitude, it avoids positive and negative differences from cancelling each other out, but provides no information regarding the direction of the difference.

7.2.3 Mean Bias and Centered Pattern RMS Difference

The total RMS difference E can be split into two components: the overall bias (the difference in the means), B and the centered pattern RMS difference, E':

$$E^2 = B^2 + E'^2$$

7-3

where

$$B = \overline{m} - \overline{o}$$

7-4

and

$$E' = \sqrt{\frac{1}{N}\sum_{n=1}^{N}\left[\left(m_n - \overline{m}\right) - \left(o_n - \overline{o}\right)\right]^2}$$

7-5

There is no bias in a model if B is zero, that is, if the mean in each field is the same.

If the two patterns are identical, the centered pattern RMS difference is zero.

7.2.4 Variance and Standard Deviation

The standard deviation,

$$\sigma_m = \sqrt{\frac{1}{N}\sum_{n=1}^{N}\left(m_n - \overline{m}\right)^2}$$

7-6

or its square, the variance, are commonly used statistical measures. In a normally distributed dataset, 95.4% of the data lie within two standard deviations of the mean, while 99.7% lie within three standard deviations.

7.2.5 Visualizing Comparison Statistics

Taylor (2001) identified a useful geometric relationship between some of these statistics, and used this to create a figure axis to visualize multiple values at once, that is, a "Taylor Diagram".

E' and R are related to the standard deviations in the following way:

$$E'^2 = \sigma_m{}^2 + \sigma_o{}^2 - 2\sigma_m\sigma_o R$$

7-7

By using the law of the cosines:

$$c^2 = a^2 + b^2 - 2ab\cos\phi$$

7-8

a geometric relationship is revealed (Figure 7-1).
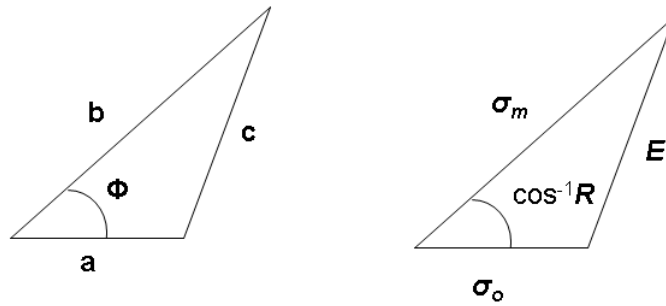
Figure 7-1: Relationship between standard deviations, the correlation coefficient and the centered RMS error, used as the basis for Taylor Diagrams (after Taylor, 2001).

From this basis, the Taylor Diagram was developed, and also a later variant named a Target diagram (Jolliff, Kindle, et al, 2008).

If the standard deviations are normalized, many comparisons may be plotted on a single graph: for example, the output of several models can be compared with each other, or the results from different months of the year in one model can be plotted. The x-axis now displays the normalized standard deviation:

$$\sigma^* = \frac{\sigma_m}{\sigma_o}$$

7-9

Table 7-1: Statistical measures.

Names & Symbols	Formula	Identifies:	Value
Correlation Coefficient, R Cross-correlation coefficient r	$R = \dfrac{\dfrac{1}{N}\sum\limits_{n=1}^{N}\left(m_n - \overline{m}\right)\left(o_n - \overline{o}\right)}{\sigma_m \sigma_o}$	Pattern similarity	$-1:1$ *(most similar:* $R = 1$ *)*
Standard deviation, σ_m, σ_o, S	e.g. $\sigma_m = \sqrt{\dfrac{1}{N}\sum\limits_{n=1}^{N}\left(m_n - \overline{m}\right)^2}$	Variation (spread) data within a dataset	$-\infty:\infty$ *(most similar:* $\sigma_m = \sigma_o$ *)*
RMS difference, E Root-mean-square difference (RMSD) RMS error (RMSE)	$E = \sqrt{\dfrac{1}{N}\sum\limits_{n=1}^{N}\left(m_n - o_n\right)^2}$	Total magnitude of difference	$0:\infty$ *(most similar:* $E = 0$ *)*
Bias, B or $\overline{E}$ Average error (AE) Mean bias (MB)	$B = \overline{m} - \overline{o}$	Difference between the means (offset)	$-\infty:\infty$ *(most similar:* $B = 0$ *)*
Centered pattern RMS difference, E' Centered RMS error (CRMS) RMSD$_{CP}$, RMS$_{CP}$,	$E' = \sqrt{\dfrac{1}{N}\sum\limits_{n=1}^{N}\left[\left(m_n - \overline{m}\right) - \left(o_n - \overline{o}\right)\right]^2}$	Magnitude of difference, after offset is removed.	$0:\infty$ *(most similar:* $E' = 0$ *)*

7.2.6   Example Diagrams

These statistics and the use of Target and Taylor diagrams may be more readily understood by illustration. An artificial set of 100 "observations" is generated by adding random noise to a sine curve. Six "models" are created from simple transformations and translations of the original theoretical sine curve (Figure 7-2). The comparison statistics for each of the six models, compared to the observations, and results are displayed on a Taylor diagram (Figure 7-3) and a Target diagram (Figure 7-4).

7.2.7   Taylor Diagrams

The Taylor diagram is a polar coordinate plot displaying three of the above statistics: the standard deviation, the correlation coefficient and the RMS error, on a single diagram. A fourth statistic (e.g. bias or a skill score) can be illustrated using contour lines or by plotting color-coded points.

The radial distance from the origin to the points is proportional to their standard deviations σ. The reference point lies at $\sigma^* = 1$ and $R = 1$. The azimuthal position of the test field gives the correlation coefficient between the two fields R , and the dashed lines (showing distance from the reference point) represent the (unbiased) RMS error E' .
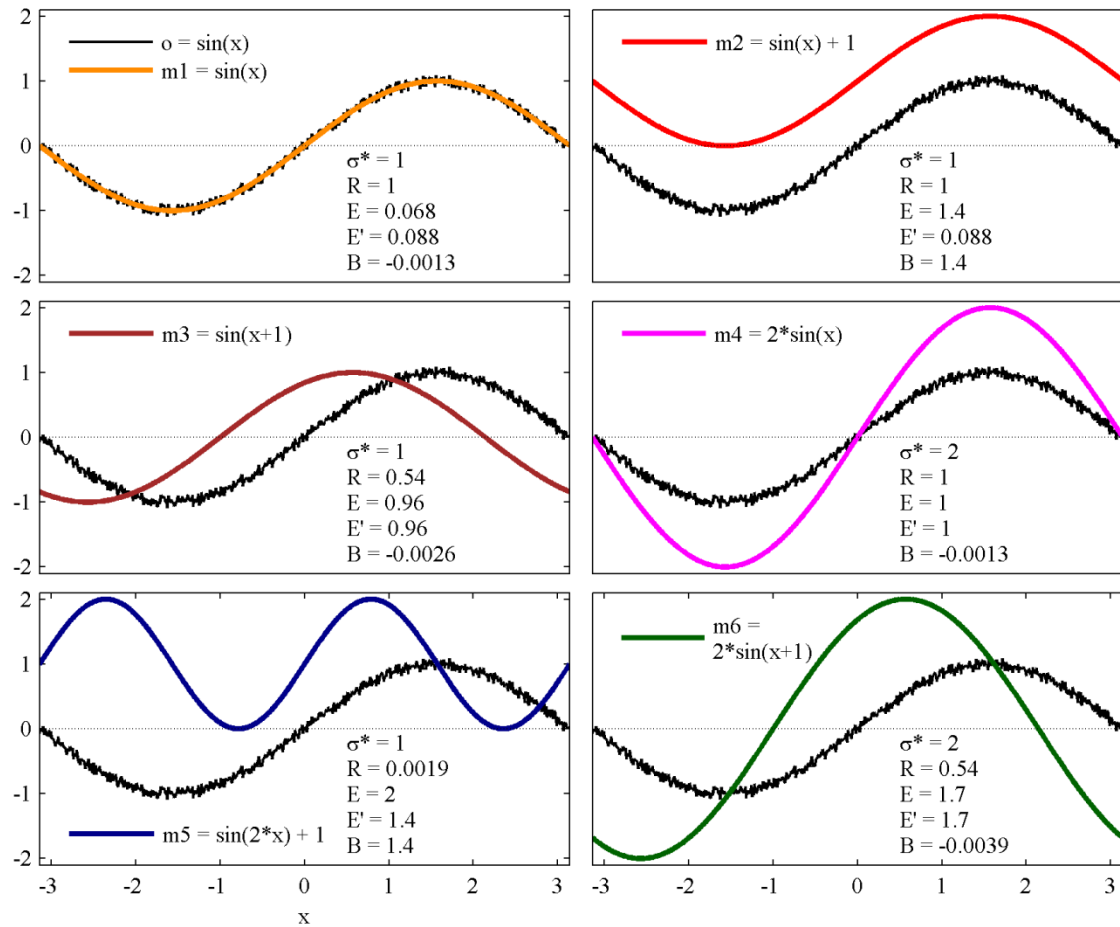
Figure 7-2: Sine curves used to illustrate target and Taylor diagrams: $o = \sin x + \text{noise}$ is the generated "observational" data: $\sin x$ with random noise added to it. Each colored curve (m1 : m6) is a simulated "model". The statistics of each model compared to the "observational" data, o, is displayed: normalized standard deviation, $\sigma*$, the correlation coefficient, R, RMS difference E, centered pattern RMS difference E', and bias B.

7.2.8 Target Diagrams

The Target diagram shows the bias B, the unbiased RMS difference E', and the total RMS difference E. These quantities may be normalized by the standard deviation of the reference field, to remove the units.

Equation 7-7 becomes:

$$E*' = \left(1 + \sigma*^{2} - 2\sigma*R\right)^{\frac{1}{2}}$$

7-10

where $E*'$ is now the normalized unbiased RMS difference, and B^* is the normalized bias:

$$B^* = \frac{\left(\overline{m} - \overline{r}\right)}{\sigma_o}$$

7-11

The y-axis shows the normalized bias B^*, the x-axis shows the normalized unbiased RMS difference E'^*, and the distance from the origin to any point is the total normalized RMS difference E^*. E'^* is multiplied by the sign of the standard deviation difference, $\sigma_d = sign\left(\sigma_m - \sigma_o\right)$ to illustrate whether the model standard deviation is larger (on the right of the origin) or smaller (on the left) than the reference field standard deviation. The radial marker (M_0) at $E^* = 1$ indicates that all points between it and the origin are positively correlated. A second marker may be added for a second positive correlation coefficient R, for which all points between it and the origin are greater than R. In this example, $R \geq 0.7$ for all $E^* \leq 0.71$.
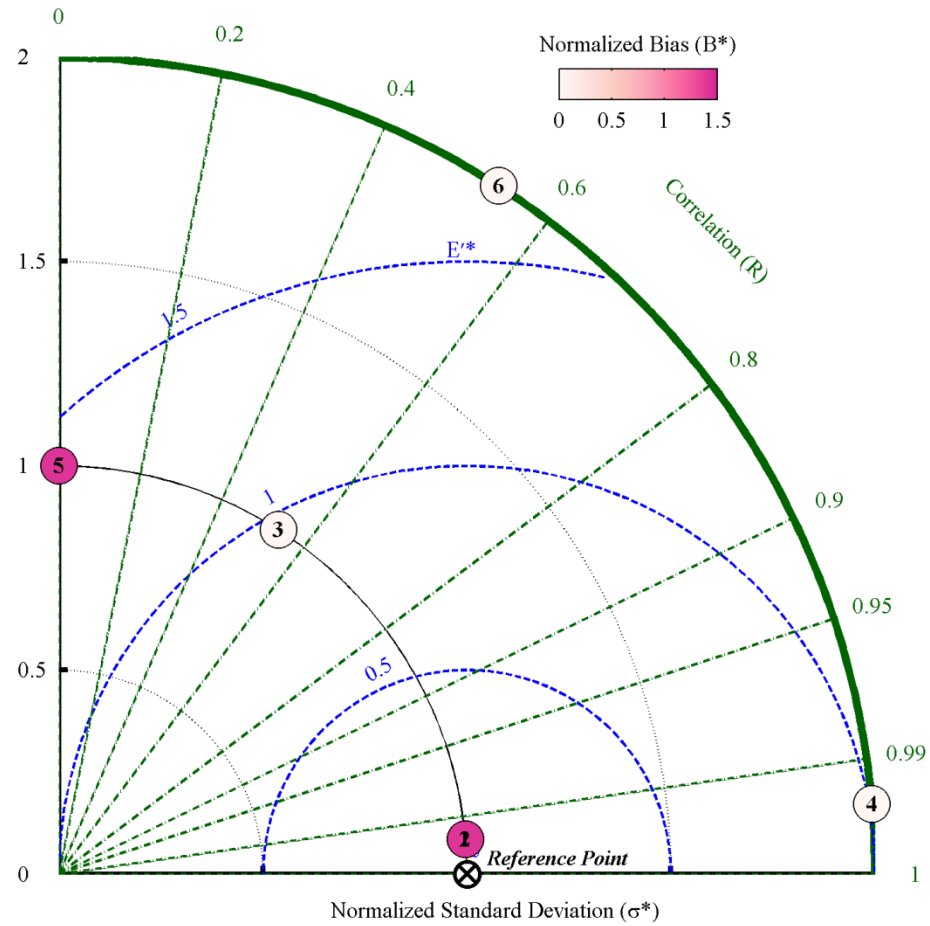
Figure 7-3: A Taylor diagram showing the comparison between each of the six models (labelled 1–6) and the "observational" data. The radial distance from the origin is the normalized standard deviation (black solid line), the angle from the horizontal indicates the correlation coefficient (green lines), with the reference point lying at $R = 1$ and $\sigma^* = 1$. Semi-circular lines centered on the reference point indicate the normalized centered RMS difference (E'; blue dashed lines), while the color scale indicates the normalized bias B.
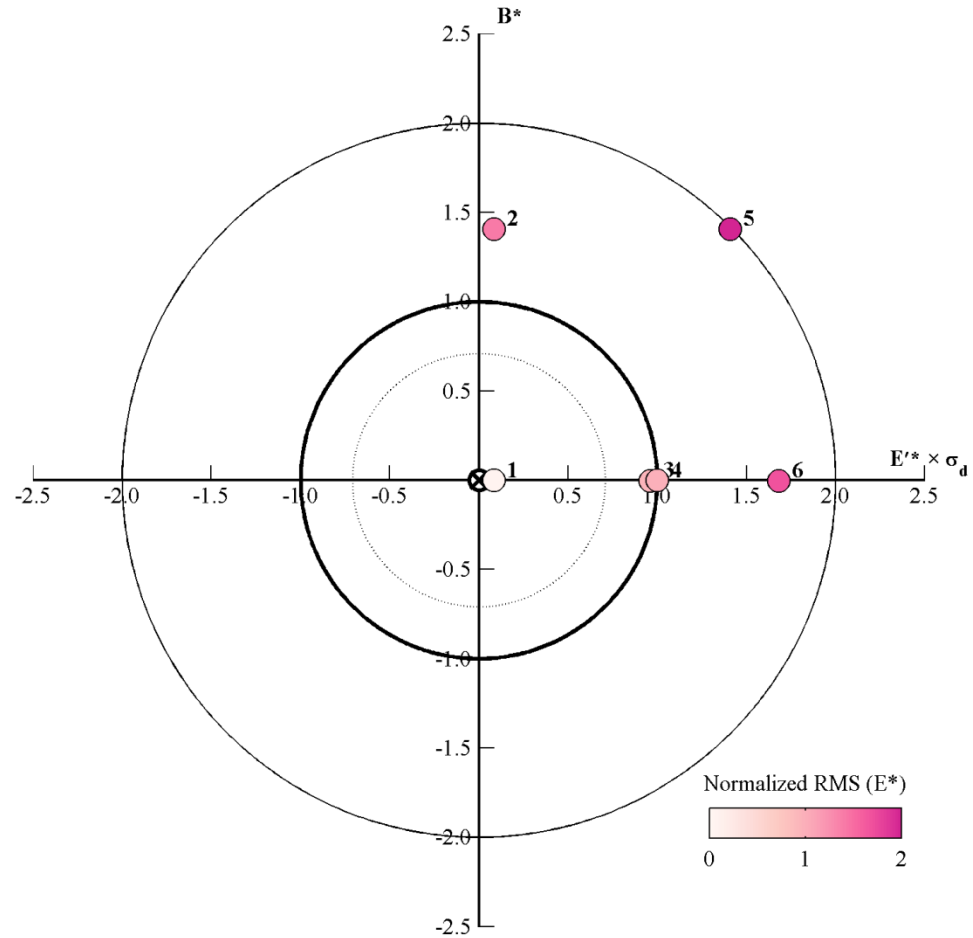
Figure 7-4: A Target diagram showing the comparison between each of the six models to the "observational" data. The normalized bias B^* lies on the vertical axis, and the normalized centered RMS difference (E'^*; multiplied by the sign of the standard deviation difference, σ_d) on the horizontal. The radial distance from the center is the normalized total RMS error E^*. This is further emphasized by use of a color scale. The circles are $E = 2$ (solid line), $E = 1$ (bold solid line). The "target point" lies at the center ($B^* = 0$, $E'^* = 0$; $E^* = 0$). All points between the dashed line and the origin have a correlation coefficient of 0.7 or more.

An additional circular line (not shown) can be drawn to indicate an estimate of the uncertainty in the observational data. Any points that lie between this line and the origin indicate that the model and data agree within the limits of observational uncertainty. As with a Taylor Diagram, the points may be color coded to indicate a fourth statistic or property. Here, E^* is emphasized using the color coding.

7.2.9 Example Results

Model #1 (the original sine curve: $m_1 = \sin x$) has the best agreement with the observations, as expected: it has the same variance, and the same cross-correlation (which in a time series, as illustrated here, can be understood as phase), a very small RMS difference (although not zero), and an even smaller bias. This model is very close to the reference point on the Taylor diagram, and very close to the center of the Target diagram.

Model #2 ($m_2 = \sin x + 1$) is more interesting: it is exactly the same shape as model #1, but translated in the positive y-direction. The variance and cross-correlation, and the centered RMS difference are all the same (since the *shape* of the curve is the same), but the RMS difference is much larger. This is entirely due to an increase in the bias - since it is a measure of that translation distance (i.e. difference in the means). On the Target diagram this shifts Model #2 well outside the "good" fit zone, while on a Taylor diagram it lies exactly in the location that Model #1 does. This is an excellent example of the importance of including the bias in some way: although note that even adding it as a color scale to a Taylor diagram is insufficient for examples such as this: since the two comparisons are otherwise identical, the points overlay each other, and the two colors of the different bias values are not visible.

Model #3 ($m_3 = \sin(x + 1)$) is the original sine curve translated in the horizontal direction: that is, a phase-shifted version of Model #1. Here the cross-correlation is lower, and the centered pattern RMS higher than Model #1, reflecting the change in

the shape of the curve. It still maintains the same amplitude, so the standard

deviation is the same, and the bias is still almost zero. This time, the total RMS

value reflects entirely the increase in the centered pattern RMS.

Model #4 ($m_4 = 2\sin x$) is an amplitude increase of the original sinusoid. The

amplitude doubles (and hence the standard deviation does also), but the phase is the

same, and so the cross-correlation coefficient is a perfect value of one. Again, the

centered pattern difference is increased, and the bias remains close to zero, so the

total RMS reflects the centered pattern RMS.

Comparing Model #3 and Model #4 illustrates the issue in deciding what defines the

"best" fit. Neither model is an excellent fit, however either might be considered an

acceptable fit (both fall on or just inside the target area on the Target diagram, for

example). Depending on whether a researcher is more interested modelling the

amplitude or the phase of a signal will determine which is more important. The

points fall distant on the Taylor diagram: but they are about the same distance away

from the reference point. On the target diagram they are very close.

Two poor fits are included for comparison: Model #5 ($m_5 = 2\sin(x+1)$) has both a

phase shift and an increase in amplitude. The correlation is lowered, and the

centered pattern RMS is increased, although the bias remains at zero.

On the Taylor diagram, Model #5 is the worst fit (i.e. furthest from the reference

point), due to its low correlation and large standard deviation. In the Target

diagram Model #6 occupies that distinction, due to its large bias. This illustrates once again the importance of considering all four statistics when comparing fits.

7.3   Comparing MOCHA to the Input Dataset

The first validation step is to check that the mapping technique results in a good representation of the input data. The total RMS difference, the centered pattern difference and the mean bias are used to quantify this.

The "input" data used in this assessment is the data obtained from raw observational data that has been interpolated onto standard depth levels (hereafter "SDL data"; §5.9). These data are grouped horizontally into "bins": each bin is the area encompassing nine (3 × 3) grid cells. Climatological values for comparison are found by interpolating MOCHA at the same depth level, onto the latitude and longitude of the SDL data point. Two sets of statistical values are calculated for (1) each bin (at each month and depth), and (2) for the whole MOCHA region, at each month and depth.

The total RMS difference and its components (the centered pattern RMS difference and the bias) for each bin are collated in Figure 7-5. Histograms for temperature and salinity are truncated at the 99th percentile (and below the 1st for the bias) to remove outliers in order to display results in more detail. The truncated temperature data show total RMS values of up to 7ºC in temperature with a peak at 1.1ºC, with a much smaller difference in salinity: total RMS values are less than or

equal to 2, with a peak at 0.2. The bias appears to influence the total RMS more than the centered pattern difference, especially in salinity: 78% of the temperature data centered pattern differences have a value of 2°C or less, and 76% of the salinity data has a value of 0.25 or less. The mean bias in temperature ranges from ±5.3°C, but with 50% of the data having a bias of 0.75 of less. Salinity biases range from ±1.7, with 50% of the bins having a bias of 0.21 or less.
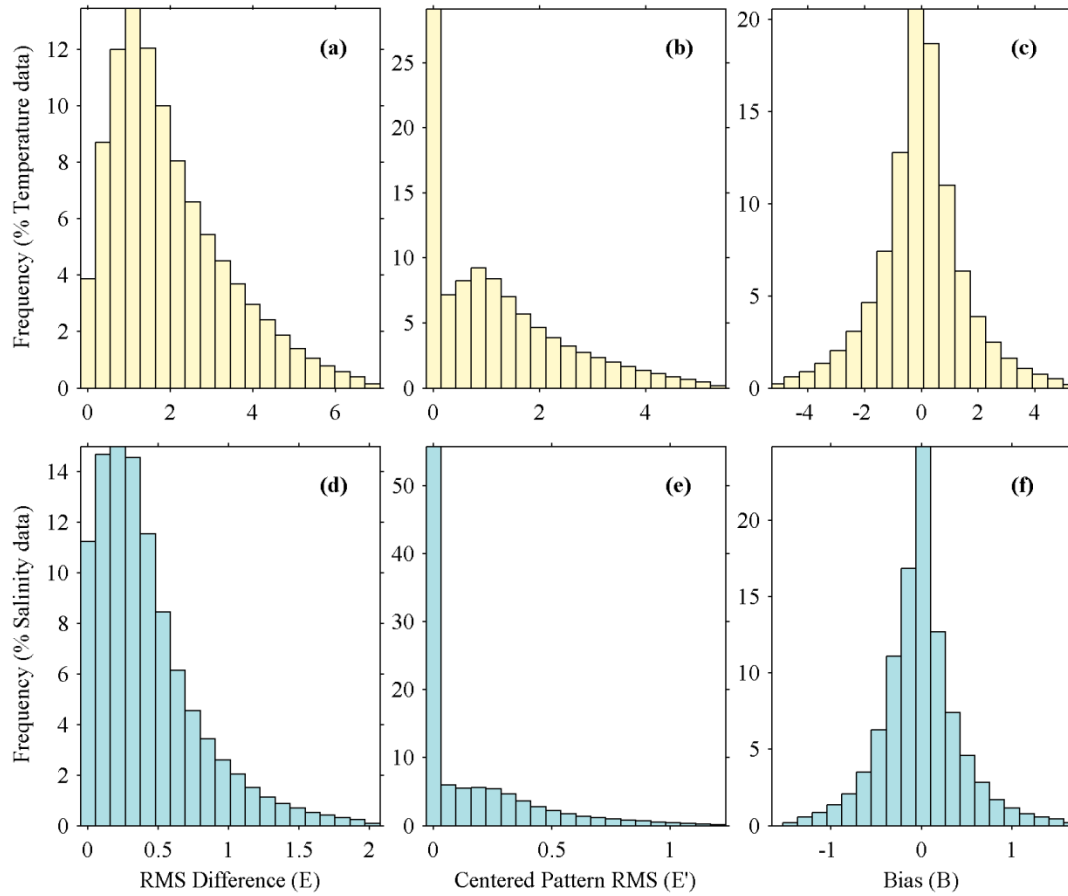
Figure 7-5: Histograms of statistical properties for binned SDL data points. Upper panels show statistics for temperature comparisons, and lower panels display salinity values. Total RMS difference E is given in panels (a) and (d); centered pattern RMS E' in (b) and (e) and bias $B*$ in (c) and (f). Note that data are truncated at the 99th percentile (and below the 1st percentile for the bias) to allow for better visualization. Note also that the vertical scale is different in each panel.

To further investigate patterns in E' and B, maps showing the spatial values of the surface bins are plotted below. General patterns of the statistical values are similar at all depths.

MOCHA temperatures differ most from the input data at off-shelf locations (e.g. for the surface waters: Figure 7-6). The regions of higher E' often contain rings and eddies, which cause considerable variability in water temperature over fairly short time and space scales. The greatest overall E' (bracketed numbers in Figure 7-6) occurs in May, when the spring thermocline is developing and there is a large range in surface water temperatures. Differences are low in deep waters (Figure 7-10a), with the highest mismatch occurring in the top 100 m (Figure 7-10b), and over the slope (400–700 m). Temperatures are much higher and their range is larger in shallow regions; and few observations exist over slope waters. The largest differences occur during summer and fall at mid-depths on the shelf.

No systematic bias is apparent in the spatial temperature comparisons (Figure 7-7). Larger biases (in both directions) are seen in off-shelf regions. This again indicates a region of high variability in temperature that is not well represented by a monthly climatology. There are also far fewer data available in the off-shelf regions, than in the heavily-studied coastal areas. Figure 7-11a & d show highest bias occurring in wintertime, with positive bias on the shelf during later summer to autumn, and low to positive bias at other times.

Salinity differences display a different pattern from temperature: higher E' occurs

near the coast (Figure 7-8) and no regions of high E' difference are seen off the

shelf. However, once again, the highest overall E' at the surface occurs in spring,

when river-runoff is largest (and which is highly variable from year to year).

Differences are slightly higher in shallower regions (Figure 7-11c & d).

There does appear to be a persistent bias in coastal salinity throughout the MAB.

MOCHA underestimates the salinity at the mouths of the larger rivers (Hudson

River, Delaware Bay and Chesapeake Bay), and in nearby coastal regions. This

could be due to inclusion of river data in the loess fit of neighboring grid coastal

cells. The highest bias in shallow regions occurs in June (Figure 7-11d), and negative

bias occurs in the top few meters throughout all months of year except December.
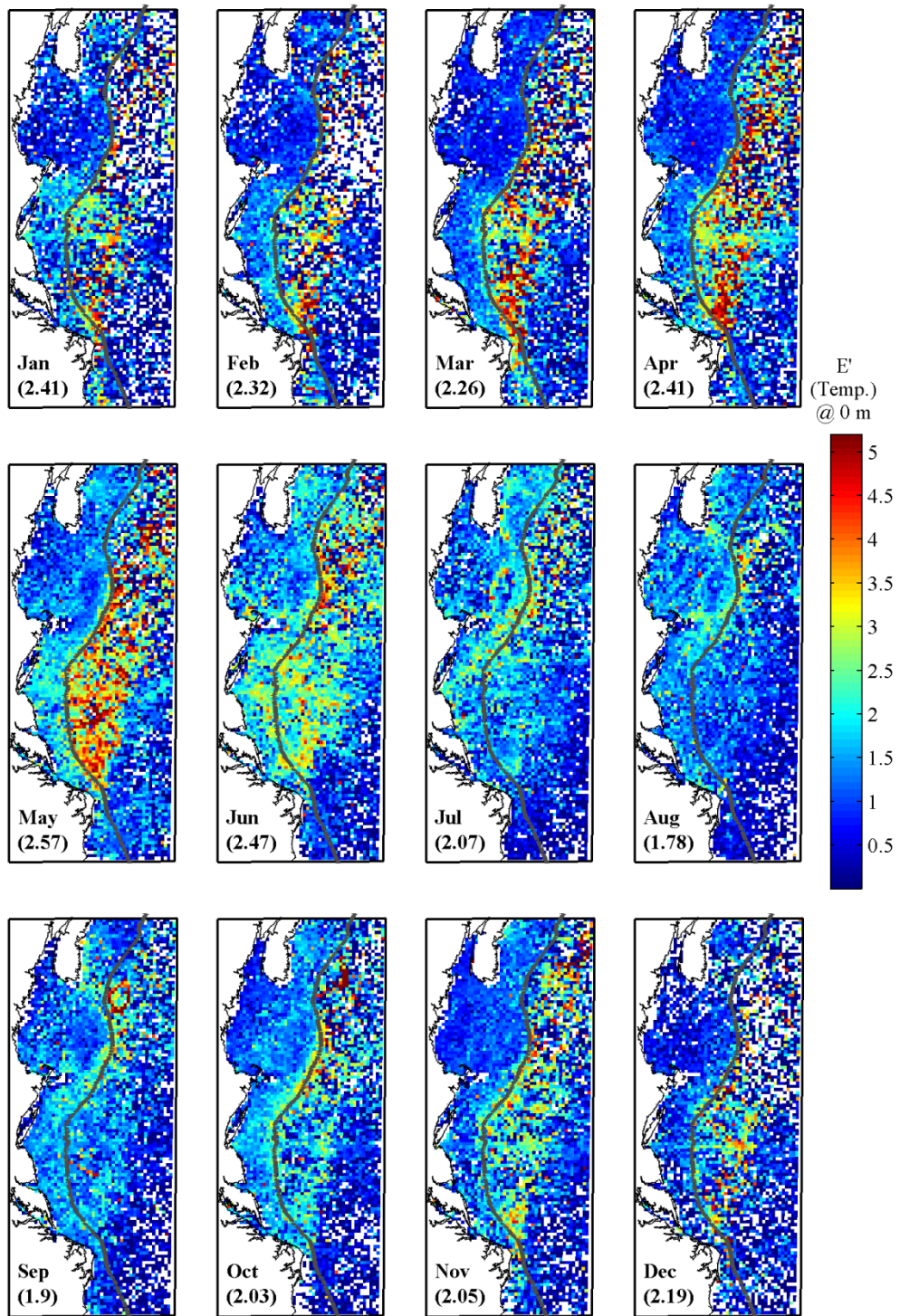
Figure 7-6: Centered RMS difference E' of the surface (0-m bin) temperature for each month of the year. Data is truncated at the 99th percentile to show detail. E' for the entire field is displayed in parentheses. The 1000-m isobath is depicted in gray.
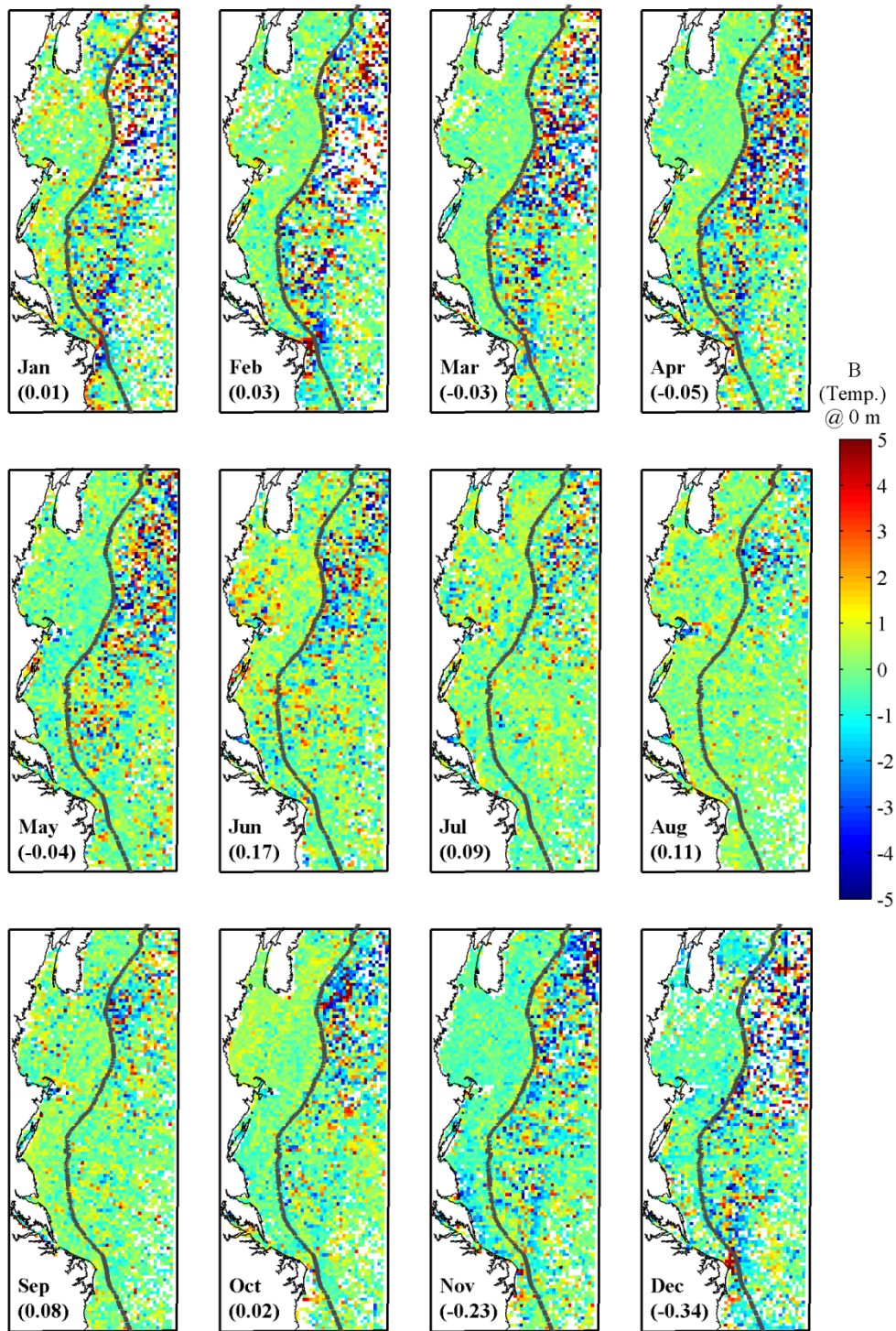
Figure 7-7: As for Figure 7-6, except for bias B. $B > 0$ zero indicates that MOCHA has a higher temperature than the SDL data.
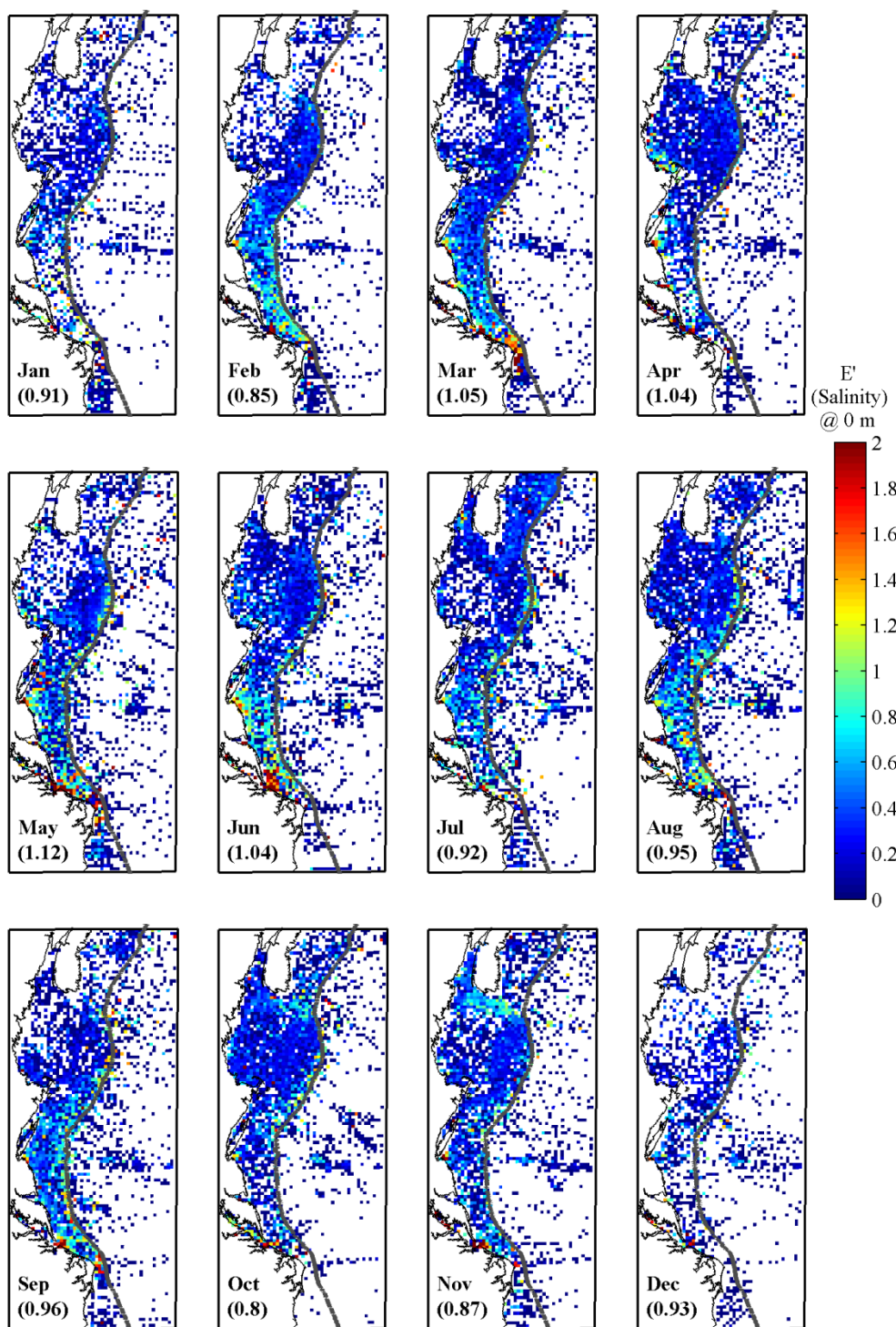
Figure 7-8: As for Figure 7-6, except for salinity.
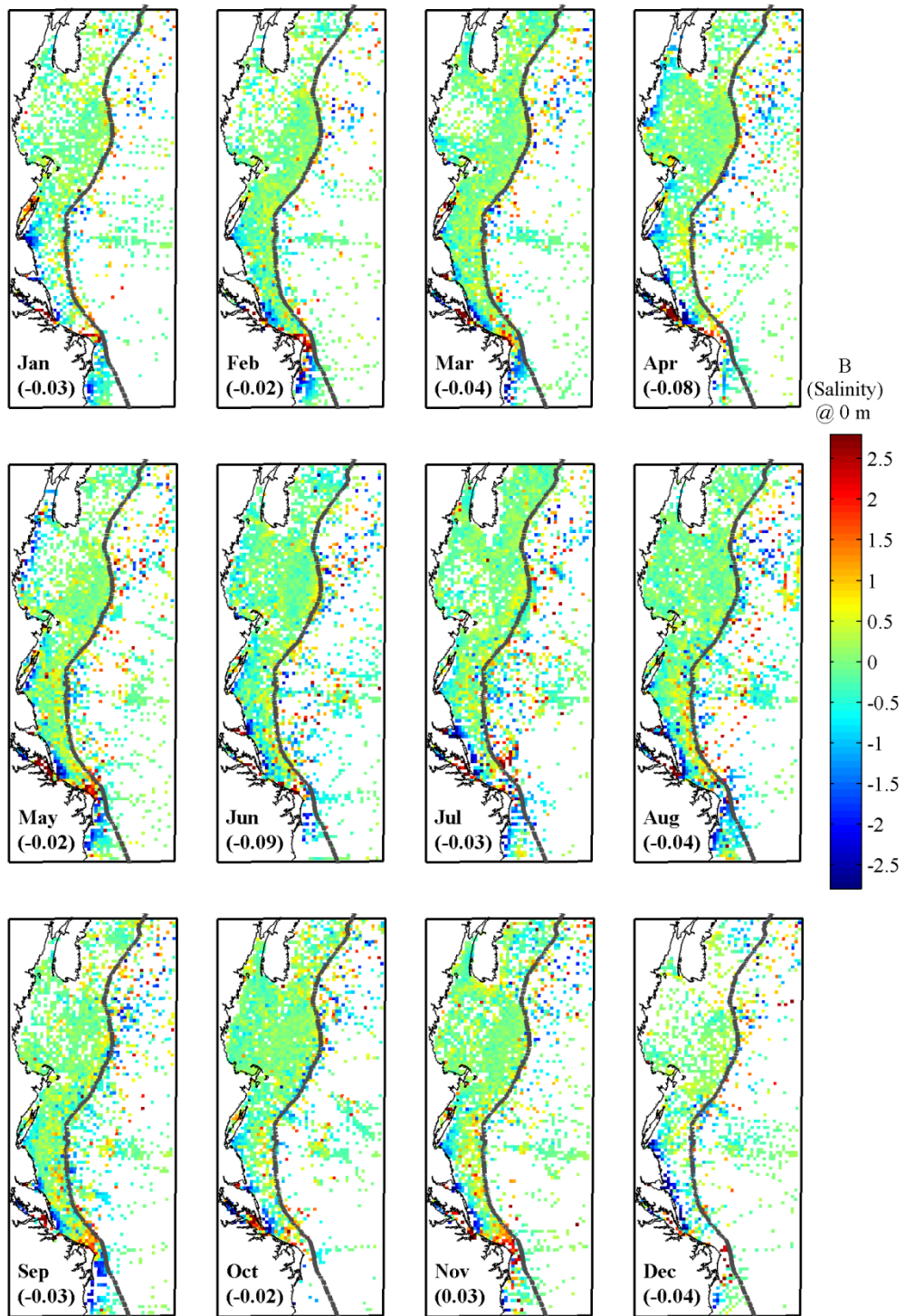
Figure 7-9: As for Figure 7-7, except for salinity. $B > 0$ indicates that MOCHA has a higher salinity than the SDL data.
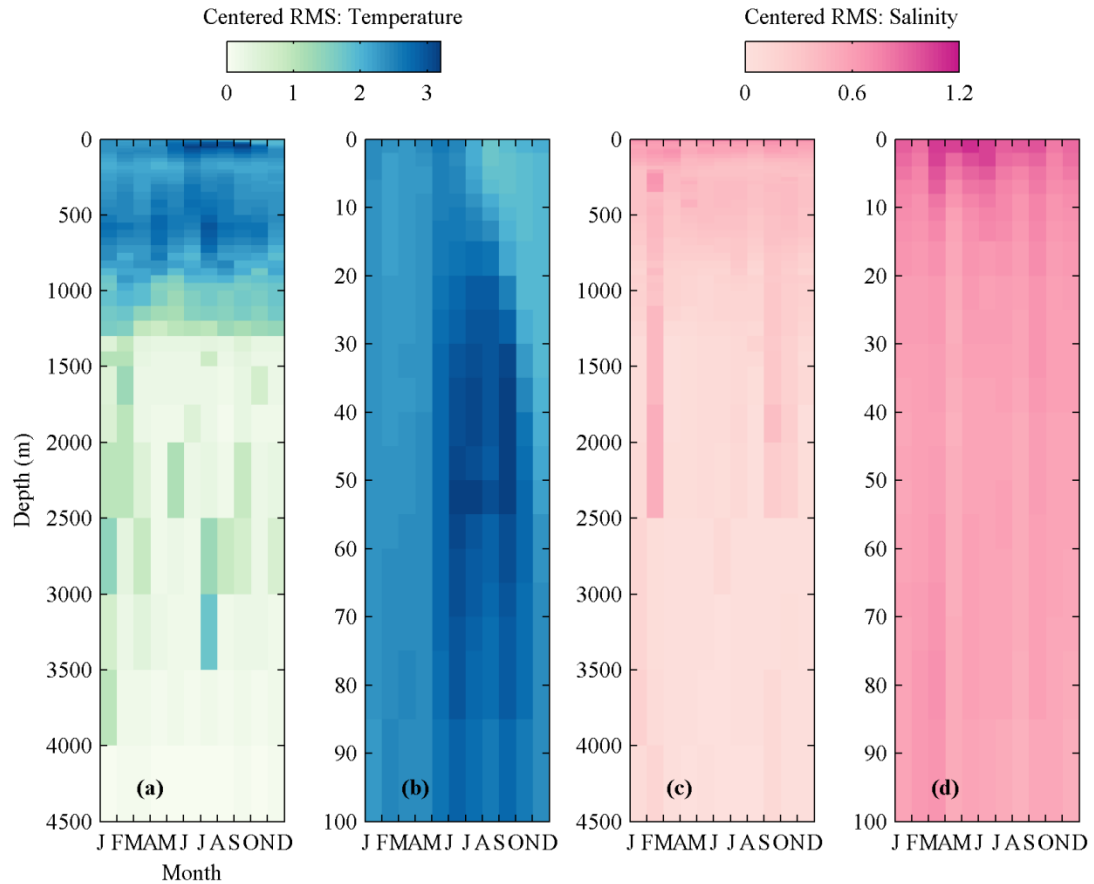
Figure 7-10: Centered pattern RMS difference $E'*$ for all SDL data points and MOCHA at each month and standard depth level, for temperature (left two panels) and salinity (right two panels). Panels (a) and (c) display results for all depths, while (b) and (d) are close-ups of the upper 100 m.

One region that has higher errors in both temperature and salinity, is the shelf water off the tip of Cape Hatteras. One reason for this could be that the shelf is very narrow at this location, and known to be a particularly difficult area to reproduce using a bathymetry-weighted fit. A second reason is that the equatorward current flowing through the MAB meets here the poleward flowing water of the SAB (since both currents turn aside from the coastline and merge together into the Gulf
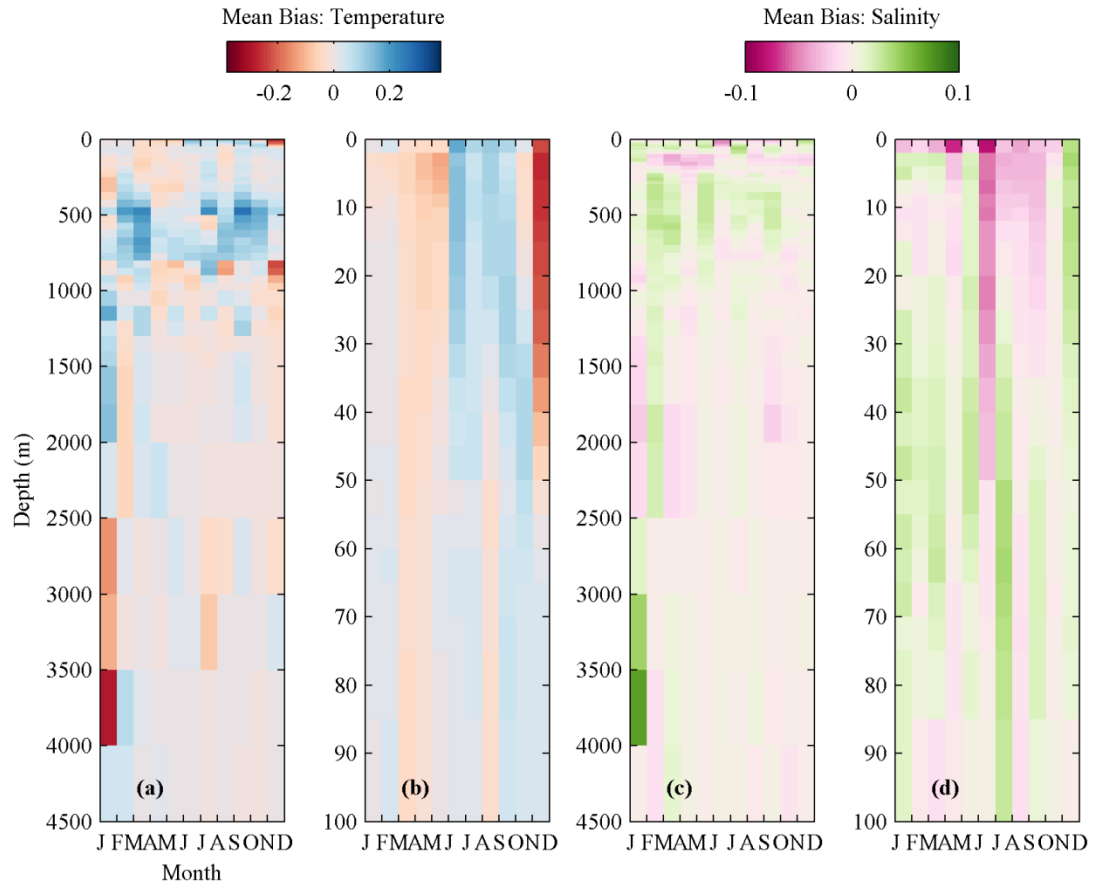
Figure 7-11: As for Figure 7-10, except for bias B.

Stream) thus it is a region of considerable range and variability in both temperature and salinity.

7.4 Comparing MOCHA to 2-D Climatologies at the MAB Shelfbreak

The value of a new climatology can also be established by comparing and contrasting it to existing climatologies. In this section a qualitative comparison will be made between MOCHA and two existing 2-D climatologies of the MAB shelfbreak.

Linder and Gawarkiewicz (1998) produced a climatology of the shelfbreak front over three regions within the MAB, including the New Jersey shelf (Figure 7-12). They use historical data from HydroBase dating from the early 1900's until April 1990. Data in each region is projected onto a single, average, cross-shelf transect, aligned perpendicular to the local isobaths. Data are grouped into bins with 10-m resolution over the shelf and 50-m resolution in deep water. For the New Jersey region, 2,765 stations are averaged this way into bi-monthly fields. It should be noted that this climatology was later updated using a new methodolody after the authors concluded that the depth-bin averaging technique distorted cross-shelf gradients in some areas (Linder et al. 2006).

Fratantoni and Pickart (2007) created a climatology of the shelf break front along the western north Atlantic from Cape Farewell in Greenland to Cape Hatteras in North Carolina. They used 12 years of summertime (April–September) temperature and salinity data extracted from the Bedford Institute of Oceanography (BIO) Climate Database. The length of the shelf is divided into sub-regions, each with similar topography. The southernmost regions, Box 26 and Box 27, lie within the
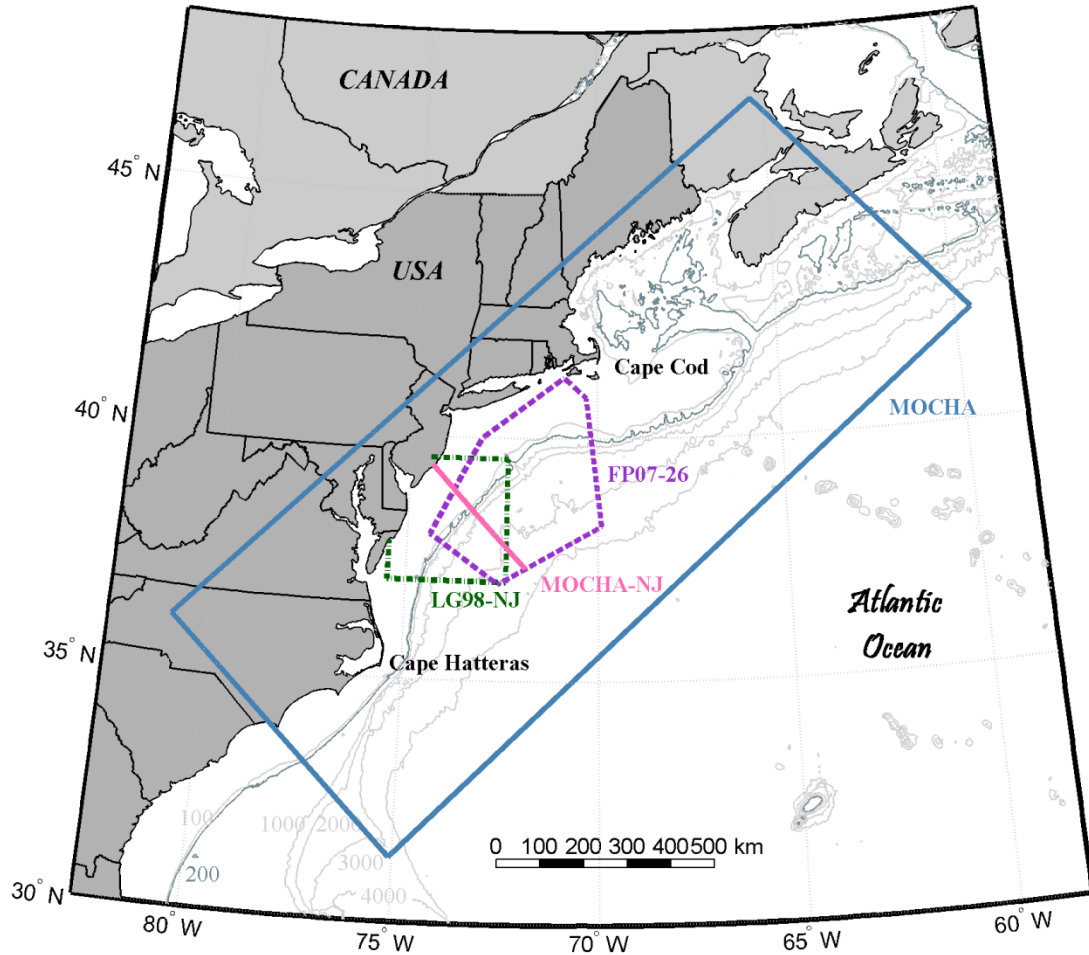
Figure 7-12: Map illustrating climatology regions: MOCHA (blue solid line), Fratantoni & Pickart's (2007) Box #26 (dashed purple line), Linder & Gawarkiewicz's (1998) New Jersey box (dash-dot green line); and the interpolated MOCHA track (solid pink line).

MAB. Box 26 includes the mid- and north MAB (Figure 7-12) and Box 27 contains the southern MAB.

Using a different averaging approach, synoptic sections within each sub region are identified and interpolated onto a standard grid first, before they are then averaged together. Grid spacing within each transect is 5 km in the across-shelf direction and

10 m in the vertical. The final climatology is a series of cross-shore transects, one for each sub-region, with cross-shore distance measured from the shelf break. Thirty-eight sections are mapped to produce Box #26.

The New Jersey climatology from Linder and Gawarkiewicz (1998) (hereafter referred to as "LG98-NJ") and Box #26 from Fratantoni and Pickart (2007 (hereafter referred to as "FP07-26"), are compared to MOCHA. A cross-shelf section located off the New Jersey coast where these two sub regions overlap (hereafter "MOCHA-NJ"; Figure 7-12) is extracted from MOCHA and averaged over the two different "summertime" periods as the two other climatologies. The LG98-NJ summertime transect is for August/September, and the FP07-26 transect is the average for April–September.

MOCHA-NJ shows a very similar pattern in both temperature and salinity to LG98-26 (Figure 7-13). A warm surface mixed layer and a strong thermocline, both of which deepen offshore, are apparent. A cold pool of water is evident below this on the outer shelf. A low salinity (< 32) pool of water lies over near the shelf break in LG98-26, which is not matched in MOCHA-NJ. Otherwise, the structure is very similar, with salinity increasing offshore and haloclines sloping offshore and upwards. The foot of the shelf/slope front (depicted by the 34.5 isohaline) is at a similar isobath.

MOCHA-NJ and FP07-26 also compare well (Figure 7-14) when looking at the general features of the MAB, and when remembering they depict an average over six months of the year (April–September). A warm layer is evident in shallow waters
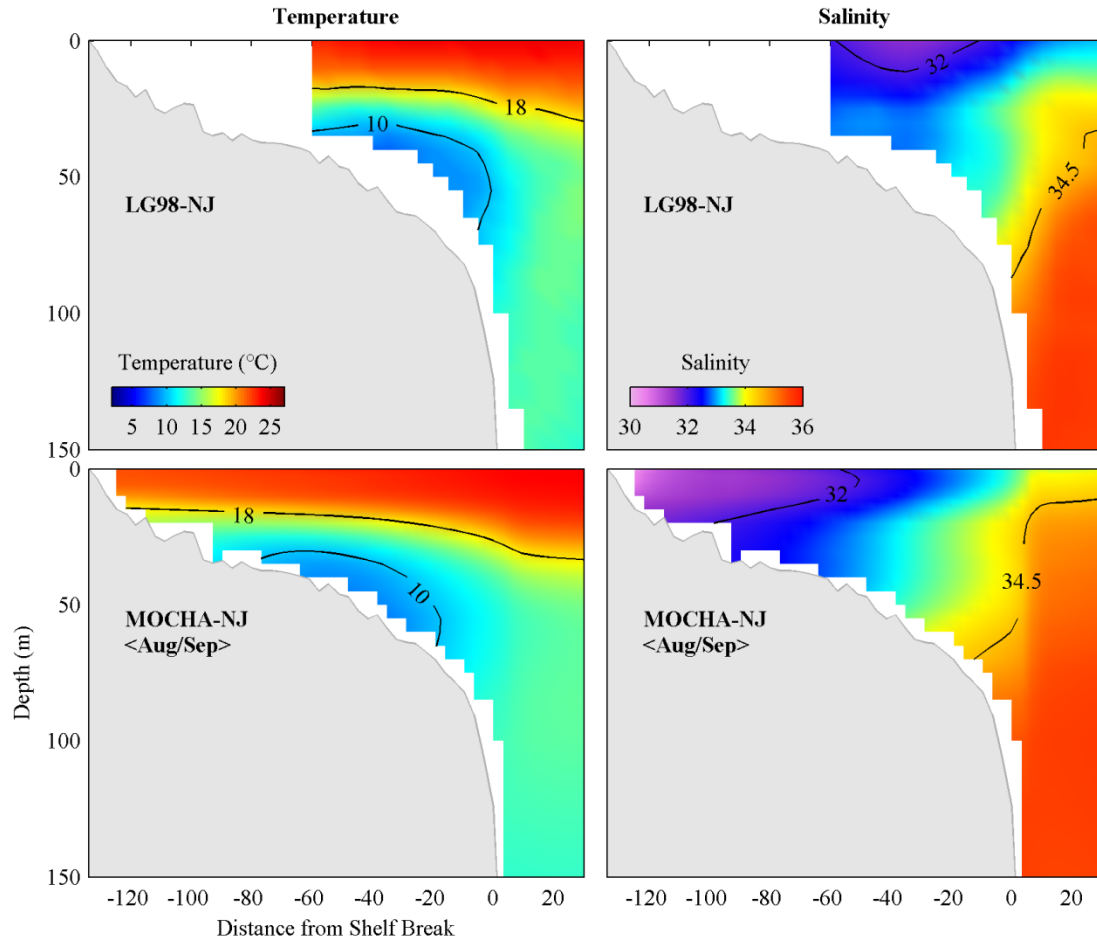
Figure 7-13: Upper panels: Linder and Gawarkiewicz (1998)'s New Jersey summertime (August/September) climatology (LG98-NJ). Lower panels: interpolated MOCHA cross-shelf transect off New Jersey coast (MOCHA-NJ) averaged over August and September. Temperature is displayed on the panels to the left, and salinity on the panels to the right. The 10 and 18ºC isotherms, and the 32 and 34.5 isohalines are depicted.

over the shelf, with a cold pool beneath it, although there is only a faint trace of it in FP07-26. The thermocline slopes down beyond the shelf-break, but with a significant deepening of the mixed layer beyond 100 km offshore of the shelfbreak in FP07-26, which does not appear in MOCHA-NJ. This "dip" in temperature exists throughout the visible water column, with FP07-26 deep offshore waters being somewhat warmer than in MOCHA-NJ. Salinity patterns are very similar, but with isohalines
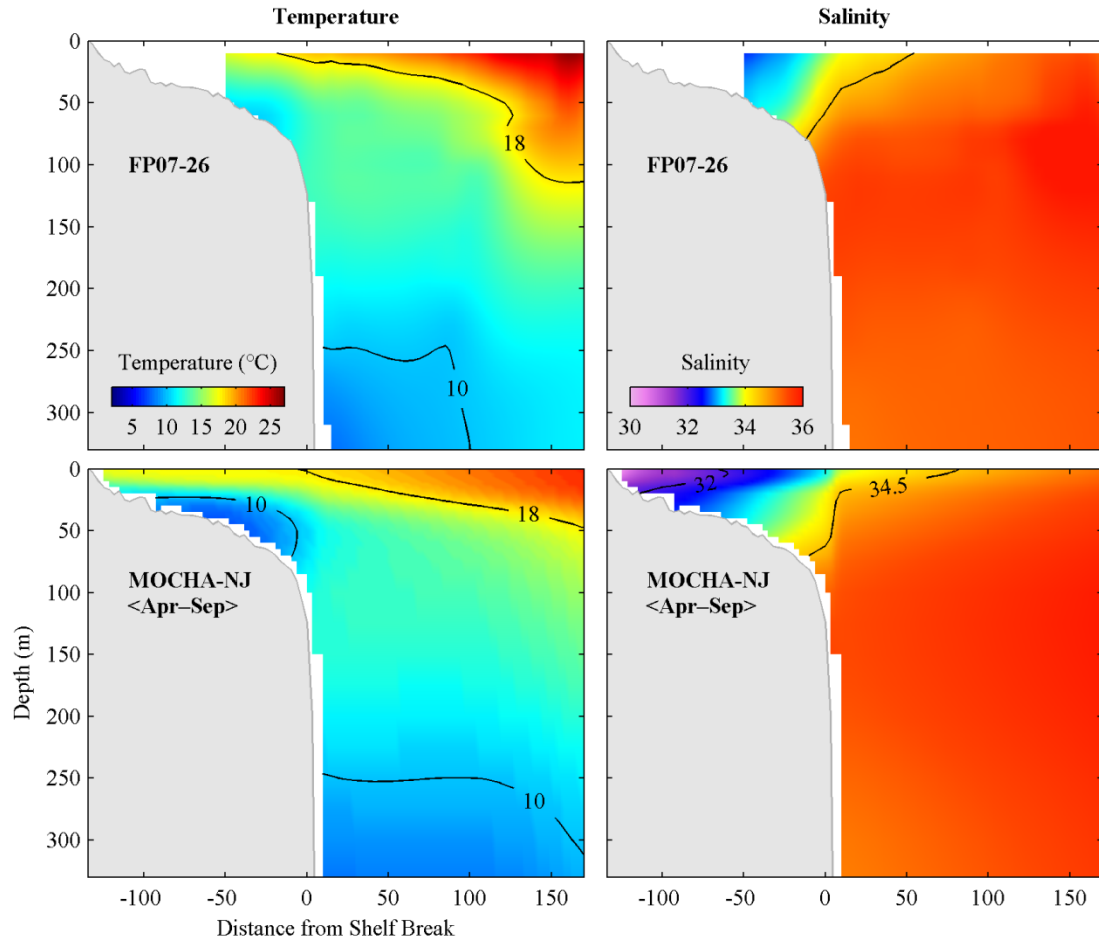
Figure 7-14: Upper panels: Fratantoni and Pickart (2007)'s Box #26 summertime (April–September) climatology (FP07-26). Lower panels: interpolated MOCHA cross-shelf transect off New Jersey coast (MOCHA-NJ) averaged over April–September. Temperature is displayed on the panels to the left, and salinity on the panels to the right. The 10 and 18°C isotherms, and the 32 and 34.5 isohalines are depicted.

in FP07-26 being somewhat steeper than in MOCHA-NJ resulting in slightly fresher

water near shore in MOCHA-NJ.

Overall, MOCHA compares well in both temperature and salinity to these existing 2-

D climatologies. The typical summertime patterns in the MAB are clearly visible,

and fields are smooth and complete.

MOCHA is superior to both climatologies in that it provides values extending to the coast, and in that it is spatially 3-D: cross-shelf transects from any along-shore location could be similarly interpolated, providing the additional information about along-shore variations. Instead of just two or three representative transects for the entire MAB, MOCHA provides a fully 3-D view, and at more closely spaced time intervals (at every month instead of two or six month averages).

7.5 Comparison to an Independent Dataset: Glider Averages

The next step in establishing the validity of the MOCHA climatology is comparing it to an independent data set. Data from gliders is the obvious choice as no glider data is incorporated into MOCHA. Monthly averages of temperature and salinity along a single cross-shore transect in the MAB is kindly provided by Renato Castelao (then at IMCS, Rutgers University, NJ). The transect is known as the "Endurance Line" (E-Line) and lies across the shelf from the Rutgers Marine Field Station at Tuckerton, New Jersey (Figure 7-15).

Rutgers University has operated gliders along the Endurance Line since October 2003, and the dataset used here contains averages from four years of data from October 2003–October 2008, discarding data from 2005: a total of 103 transects. Each glider transect is projected onto a standard line, and averaged into 1 db bins in the vertical, and 500-m bins in the horizontal. (See Castelao et al. (2010) for further details of this dataset.)
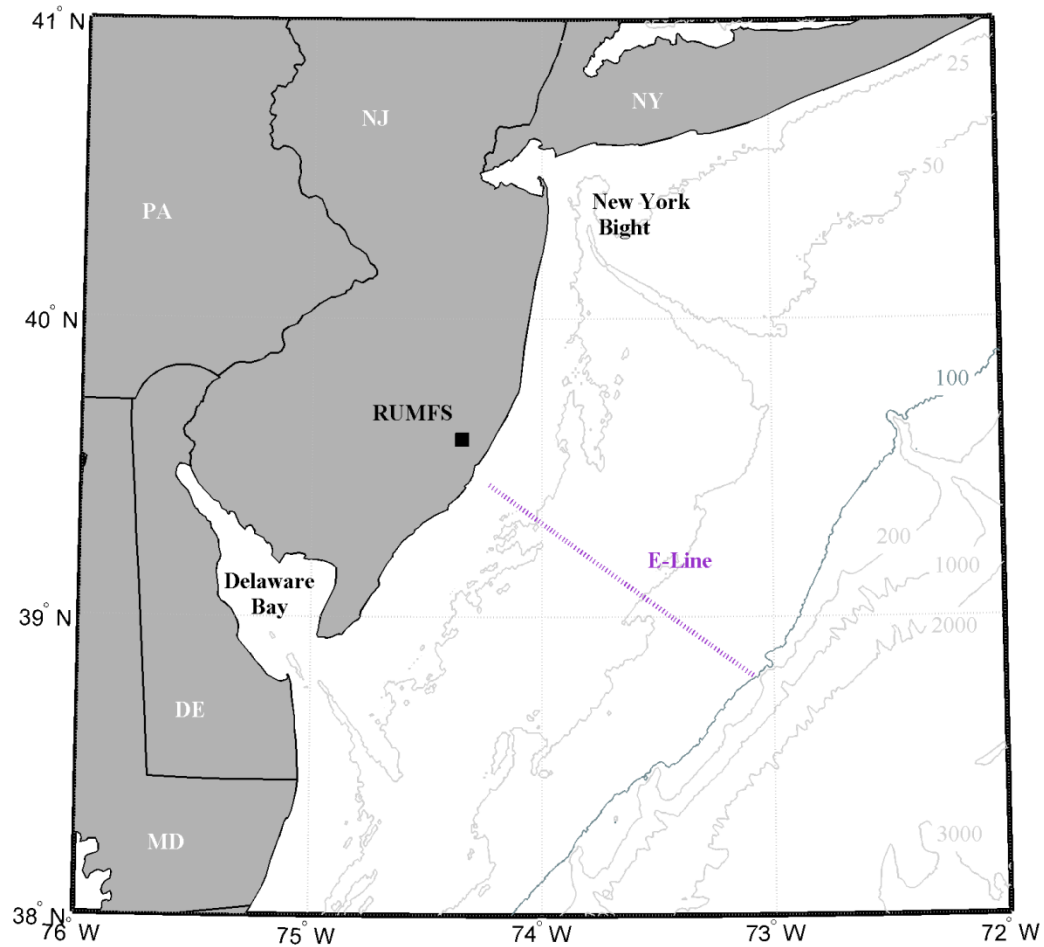
Figure 7-15: Endurance Line glider track, extending cross-isobaths from the coast near the Rutgers University Marine Field Station to the 100-m isobath (dark gray line).

MOCHA is interpolated along the E-Line and the difference between the two climatologies is calculated.

The seasonal cycle of summer warming of the surface layer, the trapping of a "cold pool" below the thermocline; and vertical mixing in autumn are all clearly represented by both MOCHA and the glider averages (Figure 7-16 & Figure 7-17). The glider data are noisy, however the overall structure compares well, with
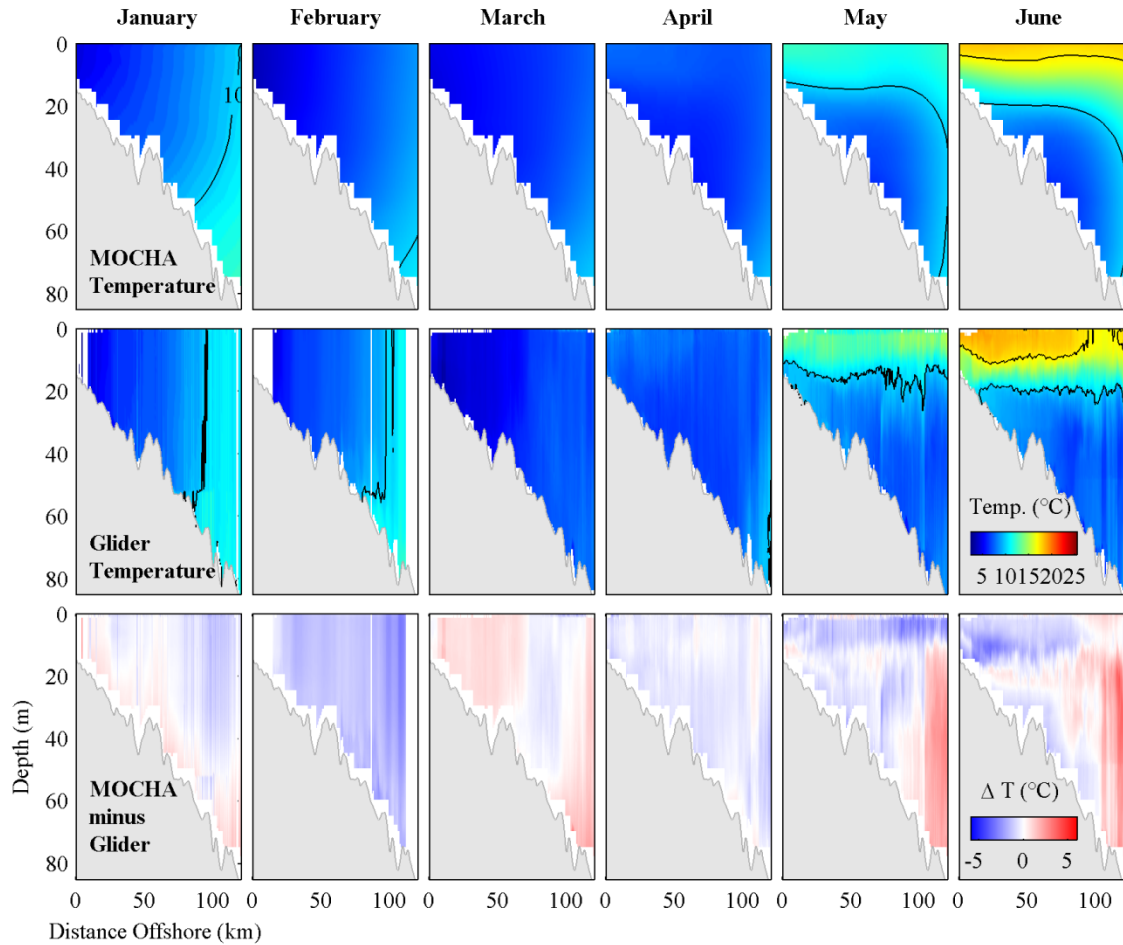
Figure 7-16: Comparing Glider and MOCHA temperature along the Endurance Line (E-Line), from January to June. The upper panels display MOCHA temperature interpolated along the E-Line for each month, the middle panels displays the glider monthly average temperature, and the lower panels display the difference between the two: (MOCHA minus Glider). Isotherms are drawn at 10ºC and 17ºC.

differences in temperature below 5ºC. Glider averages are generally warmer in the wintertime than MOCHA, while offshore below the thermocline, glider temperatures are cooler. Larger differences are apparent across the thermocline in summer, which is to be expected in a region of high variability over a small spatial scale.
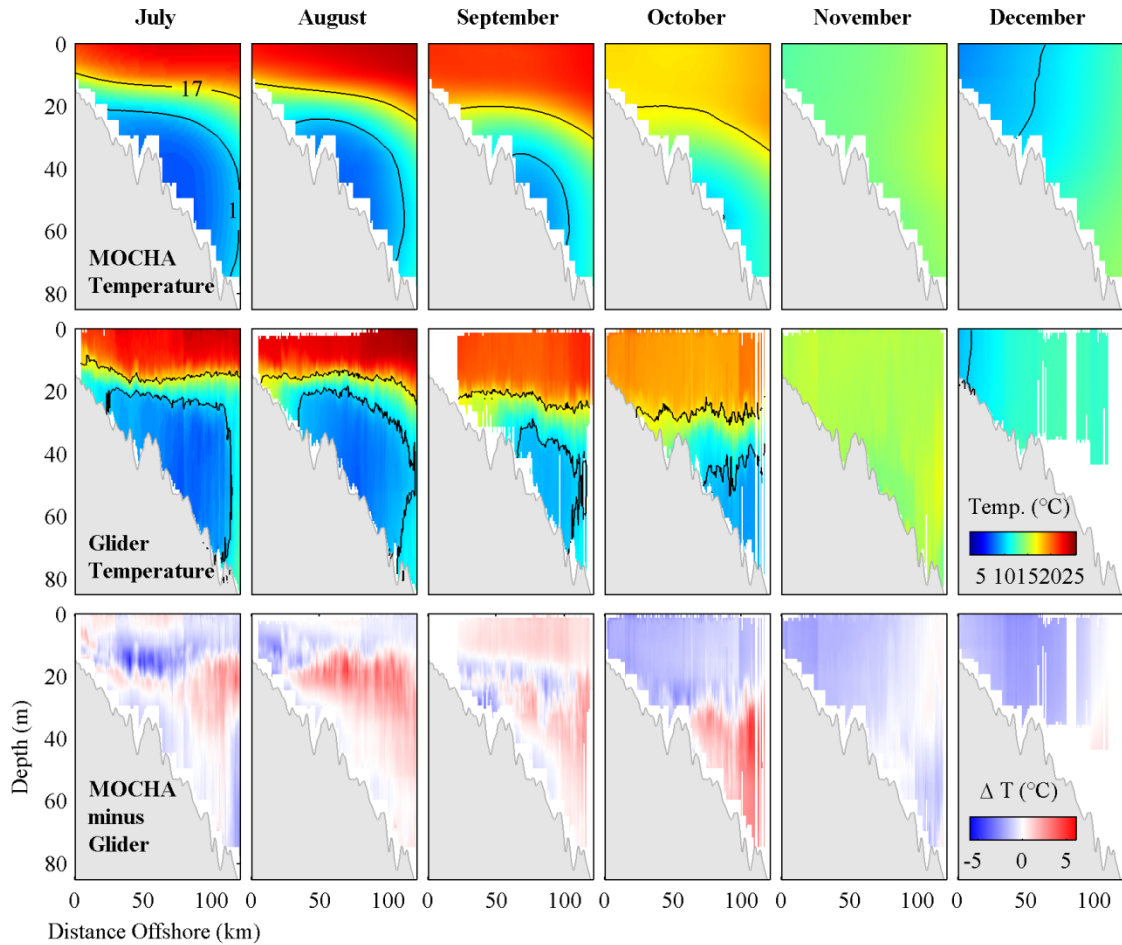
Figure 7-17: As for Figure 7-16, except for July–December.

There is a less obvious seasonal cycle of salinity in the Mid-Atlantic Bight than there is of temperature, however both MOCHA and the glider averages display a freshening of the in-shore and surface layers through spring and summer (a time of enhanced river run-off). Overall, the glider salinity is fresher than MOCHA: the fresher water extends farther offshore throughout much of the year, especially in the surface layer. Since the input of freshwater due to river run-off is highly variable from year to year, it is not surprising that this difference occurs, given that the
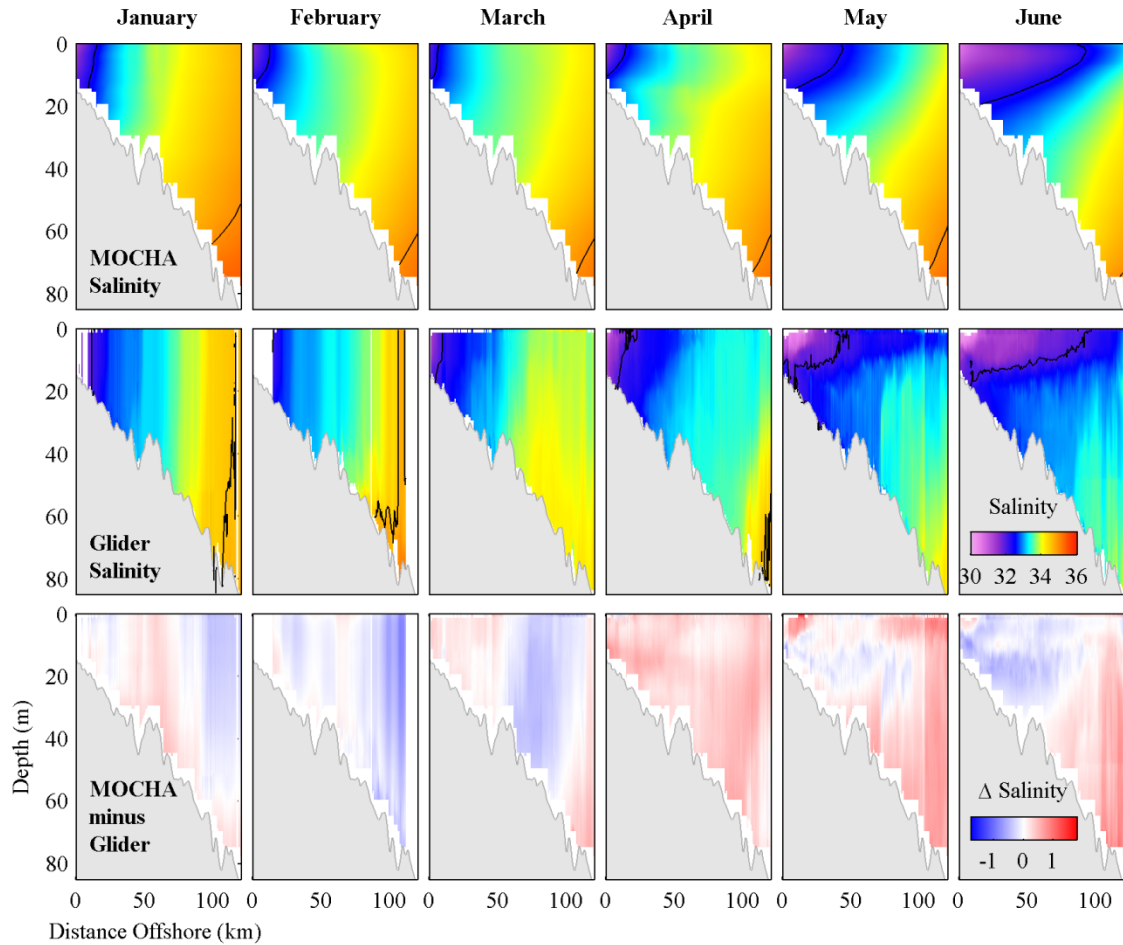
Figure 7-18: As for Figure 7-16, except for salinity. Isohalines drawn at 32 and 34.5.

glider observations are an average of 4 years of data, while MOCHA is compiled from over 150 years of data. Anomalously large freshwater discharge events occurred in September 2004 and June/July 2006 (Figure 8-4), and the resulting freshening during those months is very evident in the glider climatology.
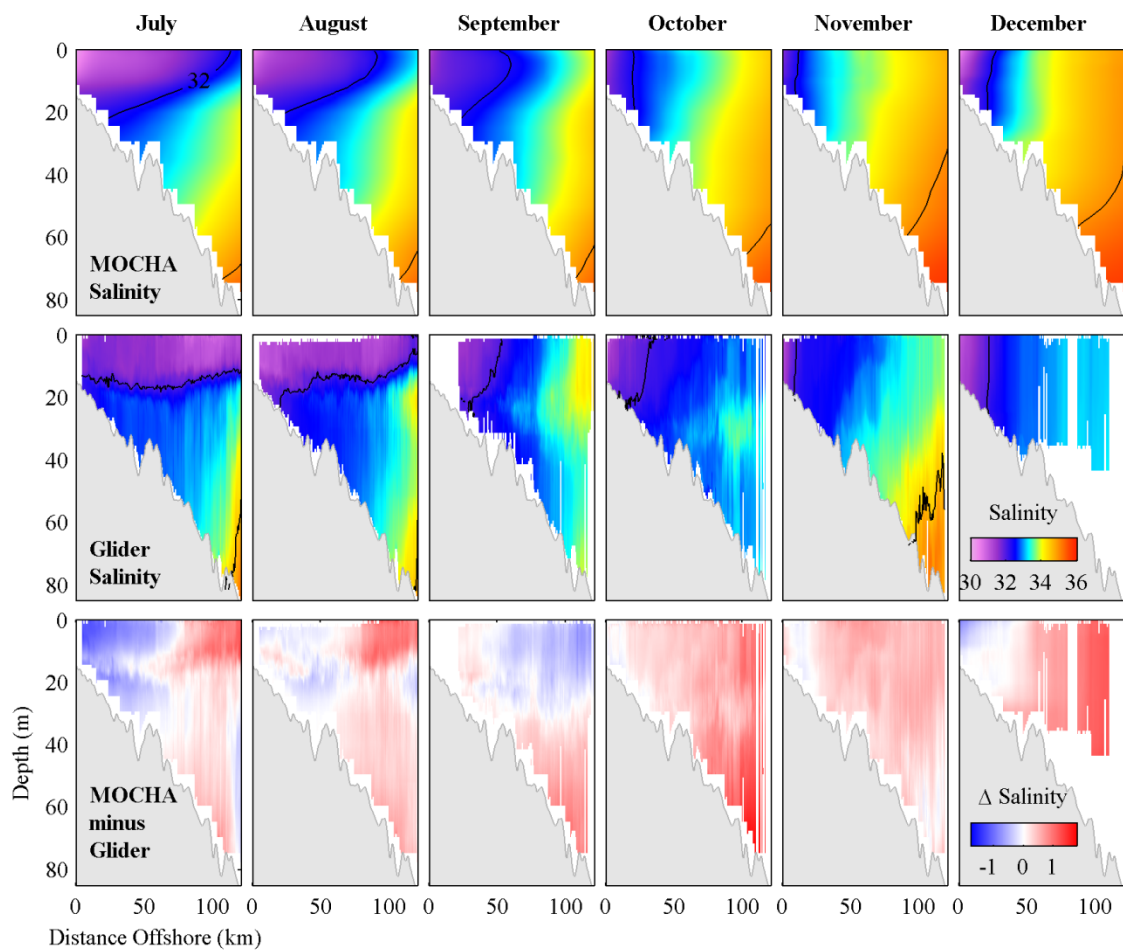
Figure 7-19: As for Figure 7-18, except for July–December.
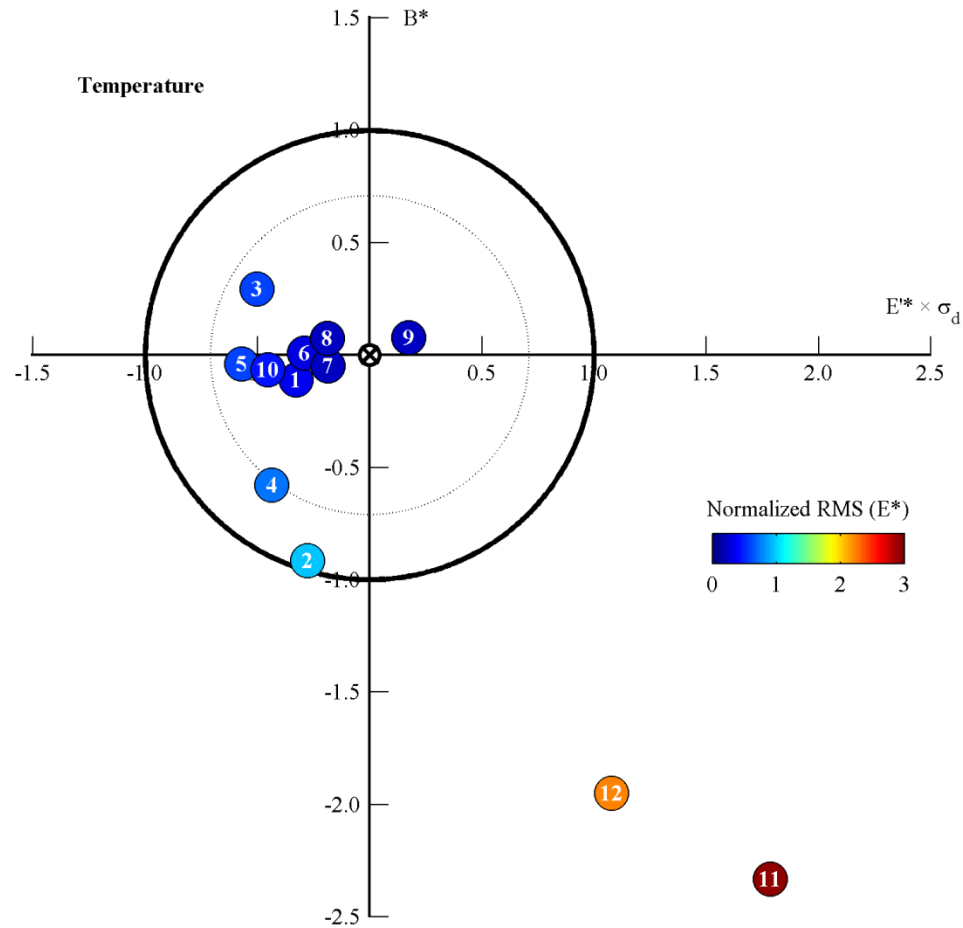
Figure 7-20: Target diagram comparing Glider and MOCHA temperature along the E-Line for each month. The vertical axis measures normalized bias $B*$, the horizontal axis measures normalized centered pattern RMS difference $E'*$ multiplied by the sign of the standard deviation difference σ_d, and distance from the origin measures total normalized RMS, $E*$. Visualization of $E*$ is enhanced by use of a color scale. All points that lie between the dashed line and the origin have a correlation coefficient of 0.7 or less.

A target diagram (Figure 7-20) and a Taylor diagram (Figure 7-21a) comparing temperature from MOCHA with the glider averages indicates that during most months the data compare well. However, data during November and December do not compare well using these statistics. In these months, the standard deviation within each dataset is small compared to the other months, but there is a
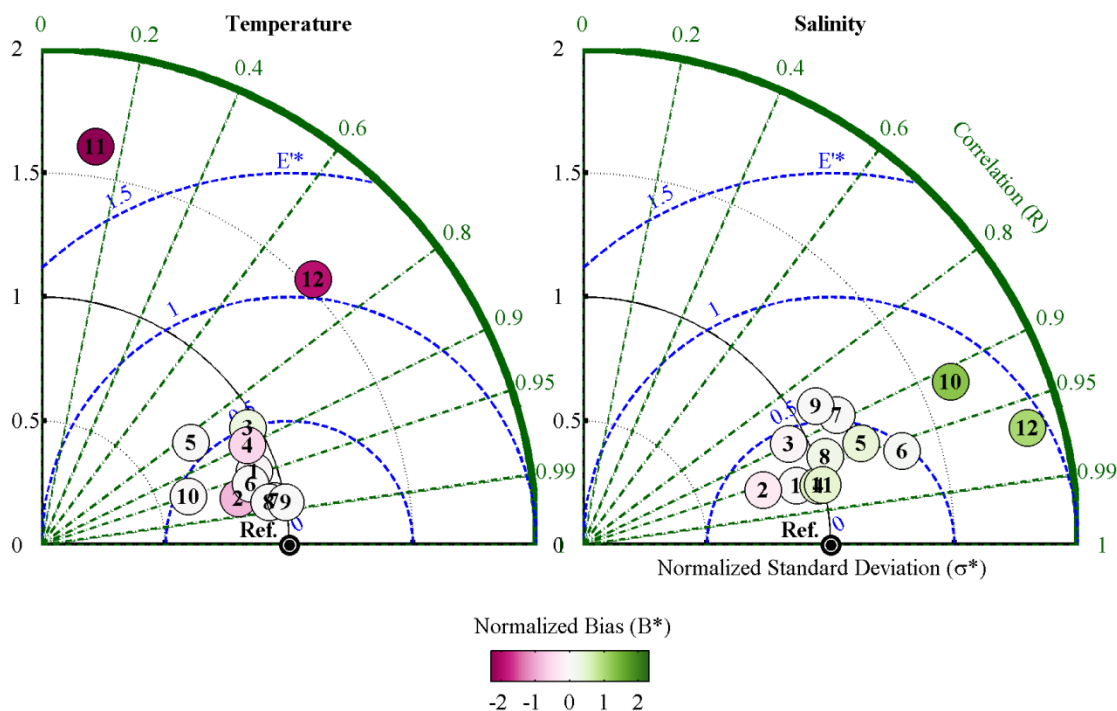
Figure 7-21: Taylor diagrams of temperature (left panel) and salinity (right panel) comparisons between glider monthly averages and MOCHA interpolated values. A positive bias indicates that MOCHA temperature or salinity is higher in value than the glider. Axis and lines are as in Figure 7-3.

substantially larger variation within MOCHA than within the glider data, producing

a higher normalized standard deviation, and thus contributing to their outlying

position. It is also noteworthy that the glider averages for December do not include

any values below 50 m, and so statistics are summed over a significantly smaller

number of data comparisons.
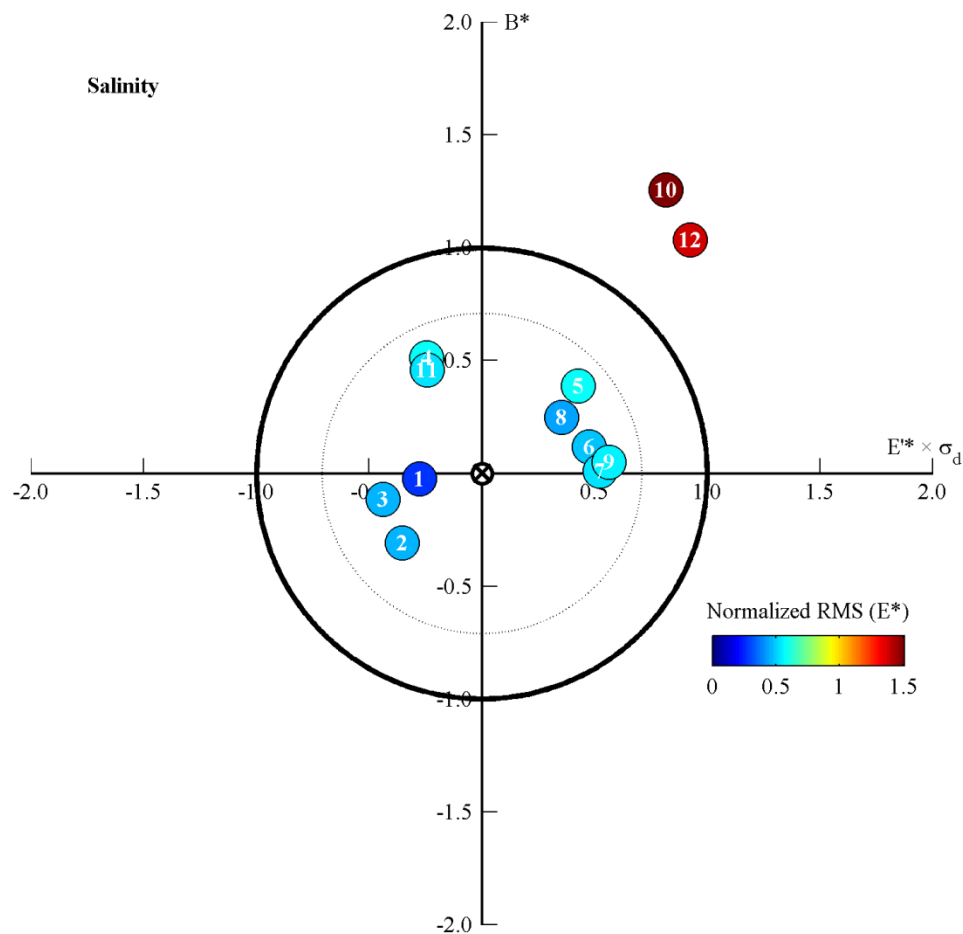
Figure 7-22: As for Figure 7-20, except for salinity.

Taylor (Figure 7-21b) and target (Figure 7-22) diagrams highlight that during ten months of the year there is good correspondence in salinity, while during October and December there is not. The glider average for October is much fresher over the whole transect, with no slope water ($\geq 34.5^{\circ}$C) visible. The glider average for December also shows fresher waters further offshore in the upper layer, but does not contain any values for deeper water.

7.6 Comparison to 3-D climatologies: The World Ocean Atlas (2005) and Hydrobase2

MOCHA is further compared to two existing 3-D climatologies, both available as long-term monthly averages: The global World Ocean Atlas (WOA) and the regional Hydrobase2.

The World Ocean Atlas (WOA) is a series compiled by NODC/NOAA. The version used in this study is a ¼° monthly climatology Boyer et al. 2005 which is objectively analyzed from the World Ocean Database (WOD) 2001 (see §5.2 for further details on the WOD series). While a later version of the atlas was available, this version was preferred due to its higher resolution (¼° rather than 1°). Hereafter it is referred to as "WOA–2005"

HydroBase2 (Curry 2001) uses isopycnal averaging of data collected from the World Ocean Database 1998 and the World Ocean Circulation Experiment (WOCE), together with many other data sets obtained directly from oceanographers, to produce a climatology of temperature, salinity and other oceanographic variables of the North Atlantic, at standard depth levels. The HydroBase2 1° monthly climatology of temperature and salinity with one iteration of smoothing (using a 5-point Laplacian filter) is used here.

The WOA–2005, HydroBase2 and MOCHA climatologies are each compared against the glider data. They are interpolated to the E-Line location and statistics are calculated for each month.

Target diagrams of temperature and salinity (Figure 7-23) which add the WOA–2005 and HydroBase2 values to the MOCHA data presented in Figure 7-20 and Figure 7-22, show a clear pattern: overall, MOCHA appears to be closest fit to the glider averages, with WOA–2005 performing second, and HydroBase2 being the worst fit.

It is important to remember, however, that while the glider climatology does provide a very high resolution view, it is only drawn from four years of data. Two of those years (2004 & 2006) had a very high freshwater discharge events from the Hudson River, and one of those years (2004) was found by Forsyth et al. (2015) to be the coldest year out of the 37 years examinged, from 1977–2013 (at the Oleander Line).

Detailed monthly views of the temperature fit (Figure 7-24) illustrate that MOCHA performs the best for ten months of the year. The two months that MOCHA performs poorly (November and December) are also not well represented by either HydroBase2 or WOA–2005, although interestingly, December is the one month that HydroBase2 performs the best.

In comparing salinity between the three climatologies, MOCHA performs best less consistently, but still does so during eight months of the year. WOA–2005 performs best in April, October and November, and once again HydroBase2 is the best fit to

data in December. The two months that MOCHA salinity is seen to fit poorly

(October and December) are the months that both of the other models also perform

their worst. Overall, MOCHA is clearly a closer fit to the glider monthly averages

than either WOA–2005 or HydroBase2.
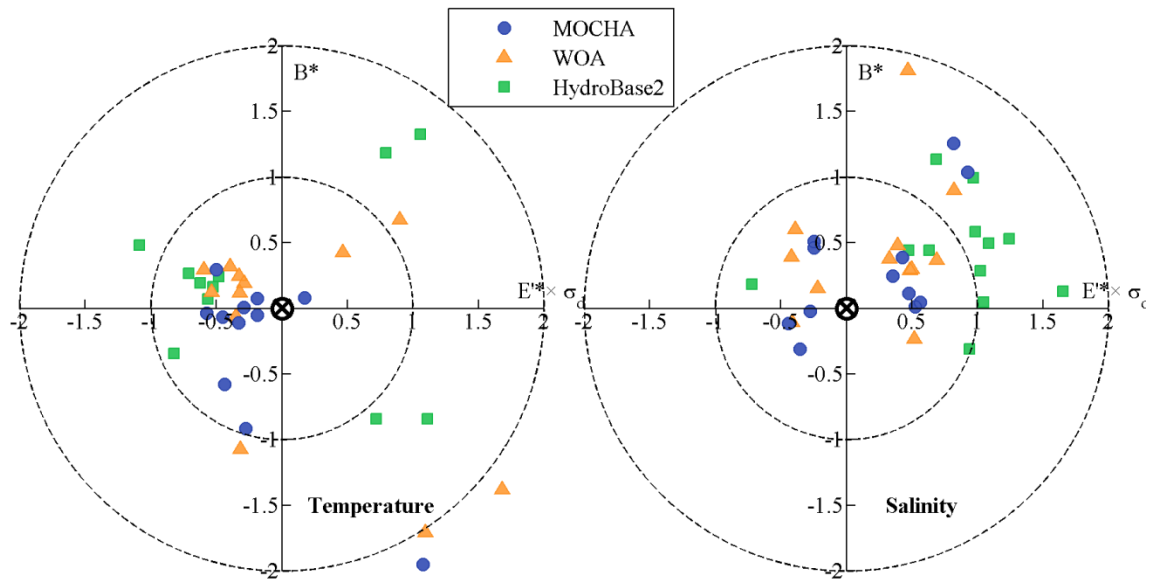
Figure 7-23: Target diagrams of temperature (left panel) and salinity (right panel) comparisons of MOCHA ,WOA–2005, and HydroBase2 for each month. Dashed lines are $E* = 1$ and $E* = 2$.
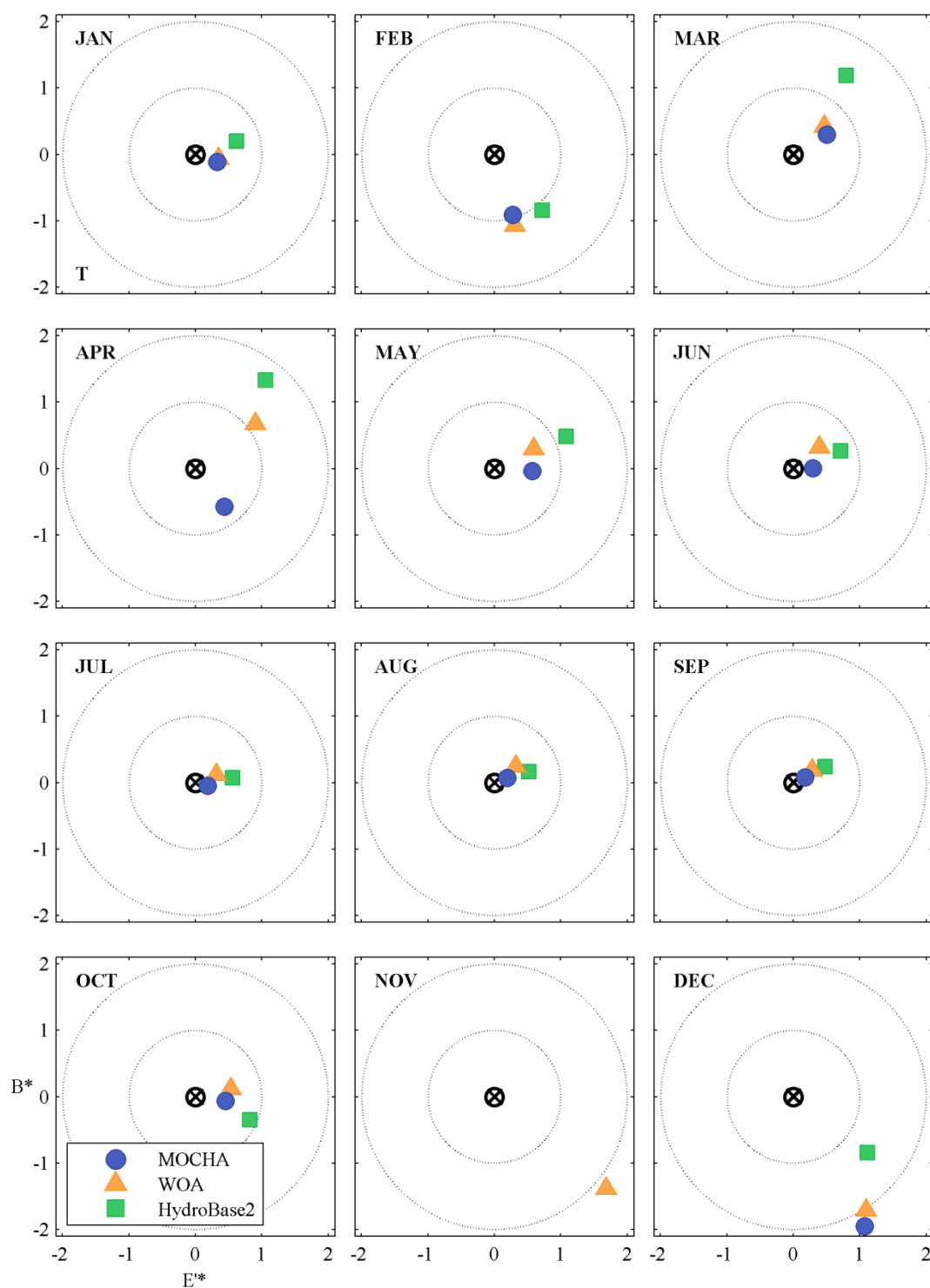
Figure 7-24: Target diagrams illustrating temperature comparisons for each month between subset input data (SDL data) and MOCHA (purple circles), WOA–2005 (orange triangles) and HydroBase2 (green squares). Dotted lines are $E^* = 1$ and $E^* = 2$. Note that MOCHA and HydroBase2 values in November are off the scale.

180
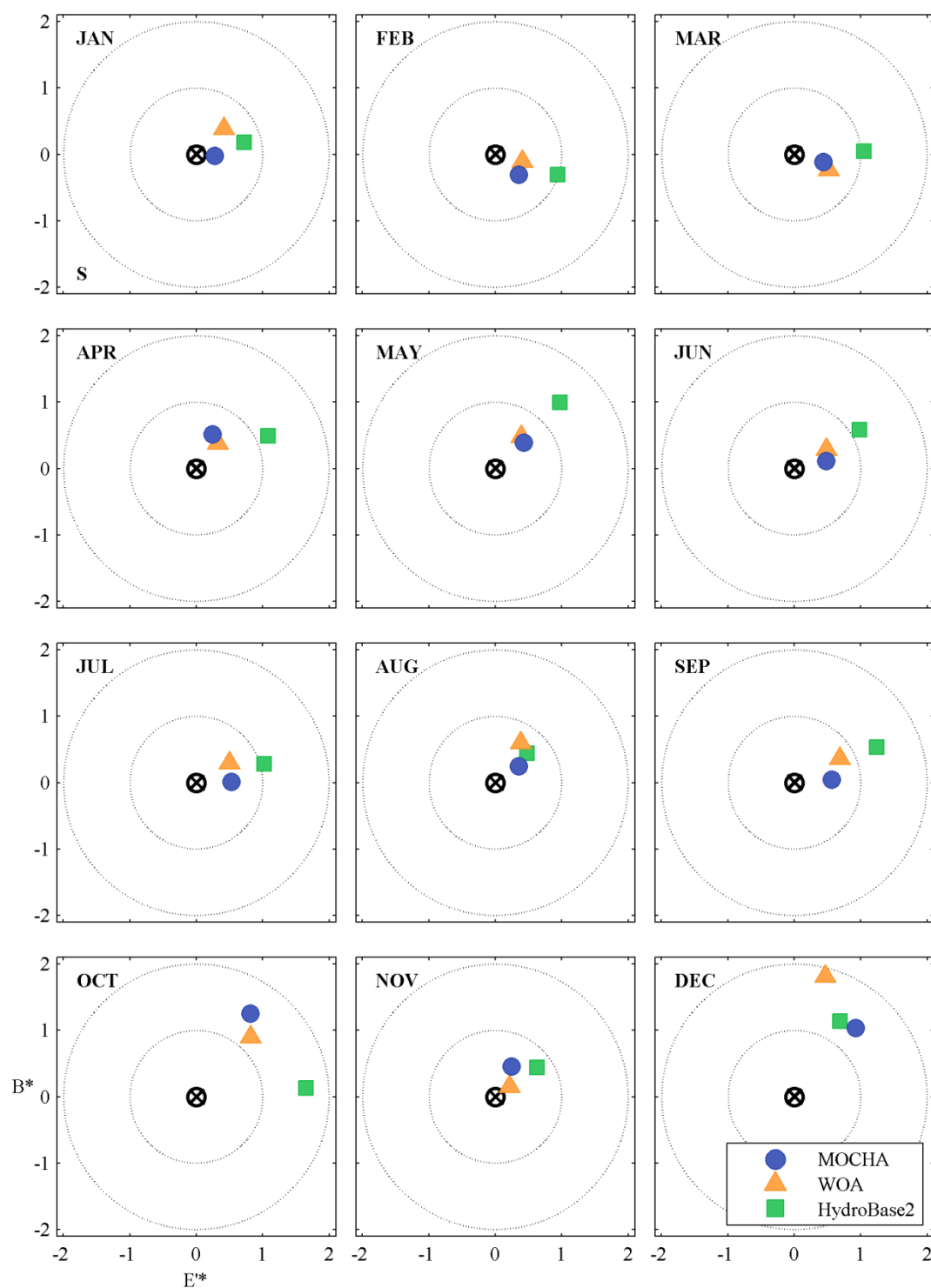
Figure 7-25: As for Figure 7-24, except for salinity.

7.7 MOCHA Versus Real-time Models

Wilkin and Hunter (2013) compare the skill of seven coastal ocean models (Table 7-2) and the MOCHA climatology. Each of the seven models ran in real time during 2010–2011 and testing is performed against MAB glider and CTD profile data collected during these years.

Table 7-2: Key features of the models evaluated (after Wilkin and Hunter (2013) their Table 1)

Model	Full Name	Domain	MAB Resolution		Assimilation Data
			Horizontal (km)	Vertical	
HYCOM	Hybrid Coordinate Ocean Model	Global	7	10 depth levels *below 100 m*	SSH, SST, T/S profiles
NCOM	Navy Coastal Ocean Model	Global	11	19 terrain following levels *below 100 m*	SSH, SST, T/S profiles
MERCATOR		Global	7	12 z levels *below 100 m*	SSH, SST, T/S profiles
NYHOPS	New York Harbor Observing and Prediction System	U.S. East coast	4.5	10 terrain following levels	NY Harbor T/S
ESPreSSO	Experimental System for Predicting Shelf and Slope Optics	U.S. East coast	5	36 terrain following levels	SSH, SST, CODAR
UMAssHOPS	University of Massachusetts' Harvard Ocean Prediction System	U.S. East coast	15	16 terrain following levels	SSH,SST
COAWST	Coupled Ocean-Atmosphere-Waves and Sediment Transport	U.S. East coast	5	16 terrain following levels	HYCOM T/S
MOCHA	Mid-Atlantic Ocean Climatological Hydrographic Atlas	U.S. East coast	~5	21 depth levels *below 100 m*	T/S profiles

After examining comparison statistics (E^*, E'^*, B^* and R), they conclude that the best-performing of the seven models are NYHOPS, ESPreSSO and NCOM. However, the authors go on to say "their skill is comparable to, but often eclipsed by, MOCHA climatology".

In particular, MOCHA performs better than all models in predicting winter temperature, and is one of the best performers in predicting summer salinity. It does not do so well in predicting winter salinity. Overall, the authors conclude that "MOCHA climatology is as good or better than several of the dynamic models in many situations".

7.8 MOCHA in Use

7.8.1 Availability

MOCHA has been made available online to researchers using the Rutgers University Institute of Marine and Coastal Sciences' THREDDS (Thematic Real-time Environmental Distributed Data Source) data server. A netCDF file of MOCHA temperature and salinity is downloadable from:

http://tds.marine.rutgers.edu/thredds/catalog/other/climatology/mocha/catalog.html

MOCHA has been utilized by a number of researchers working on different projects throughout the MAB. The role of MOCHA in these projects is briefly described below.

7.8.2   Model Initial Conditions and Nudging

Zhang et al. (2011) uses MOCHA in conjunction with ROMS to study the ocean circulation of the New England shelf break. They average MOCHA to produce seasonal and annual 2-D sections across the shelf break, and use this as an initial condition in their model. They further test the effect of nudging the model toward the MOCHA-derived 2-D sections.

The mean circulation is calculated by balancing wind stress with an along-shelf sea-level tilt and bottom stress, while the along-shelf density gradient is assumed to be zero. Model results are compared to velocity observations, and they conclude that nudging the model to the climatology provides a robust comparison, while without nudging the results are unsteady and unrealistic.

Later, Zhang et al. (2013) added a four-component planktonic ecosystem model to the 2-D physical model of Zhang et al. (2011) to study the impact of shelfbreak upwelling on biological production.

7.8.3   Correcting Model Initial Conditions and Data Assimilation in ESPreSSO

ESPreSSO is one of four models used in assessment of glider path planning during the Cyber Infrastructure Project Observing System Simulation Experiment (CI−OSSE) in November 2009 (Wang et al. 2013). Multi-model ensemble

forecasting is tested by comparing each individual model forecast to combined forecasts: firstly using an equal weighting method (simply the mean of the four models), and secondly using an objective weighting method. The weightings are based on the performance of each model during a testing phase where model outputs are compared to sea surface temperature and HF coastal radar surface current observations.

The ESPreSSO model for this experiment uses HYCOM/NCODA and MOCHA for its boundary conditions and in weak data assimilation. MOCHA is used to correct the HYCOM forecast, biases in temperature and salinity on the shelf, as in Zhang et al. (2011), resulting in "a much more realistic shelf current".

ESPreSSO is found to give the best SST and surface current forecasts of the four models, although objective weighting improves upon ESPreSSO for SST and both the objective weighting and equal weighting methods improve on the surface current.

7.8.4   Model Boundary and Initial Conditions

Zhang et al. (2015) use MOCHA to verify and correct boundary and initial conditions for the MABGOM (Mid Atlantic Bight and Gulf of Maine) model. Their aims are to model the circulation of the MAB, Georges Bank and Gulf of Maine in order to study surf clam larval dispersal.

The model is set up using ROMS and nested within a global model: the Hybrid Coordinate Ocean Model/ Navy Coupled Ocean Data Assimilation model: (HYCOM/NCODA). Temperature, salinity and barotropic and baroclinic velocities from 2006–2009 were taken from HYCOM for initial conditions in MABGOM. However, comparison of the HYCOM temperature and salinity to MOCHA values uncovered a net bias in HYCOM: waters are 2–3 ºC warmer, and salinity higher by 1–10 or more, especially in regions with freshwater inflow such as Chesapeake Bay and Delaware Bay. The mean geostrophic barotropic and baroclinic velocities were instead calculated from MOCHA, along the model boundaries, and these values used to correct the biased HYCOM values.

The MABGOM model is validated from comparison to NEFSC data during the study period (2006–2009) and the authors conclude that the model reproduces the surface and bottom temperature distributions in the MAB with acceptable accuracy.

7.9 Conclusions

MOCHA has been shown to compare well with its own input data, an independent dataset, 2-D cross-shore models, 3-D models, and with real-time models. As such it is a very useful tool for oceanographers studying the MAB region.

Of particular note is MOCHA's performance in comparison to real-time models. So while MOCHA is useful for model input and boundary conditions, for nudging, and

for data assimilation, it may also be used on its own as a good first predictor of the ocean conditions for a particular month.

MOCHA's weakness' include the mapping of temperature and salinity beyond the shelf break of the MAB, where considerable variability on short time and space scales exists, and are therefore not well represented by a monthly climatology. Similarly, coastal areas impacted by highly varying river runoff are not well mapped.

Future versions of MOCHA would no doubt improve from increased data: especially salinity data, data taken during late fall and winter, and data from beyond the shelf break. The waters off-shore of Cape Hatteras stand out as being poorly mapped in several months, and would also benefit from more data input. With the increased use (and range) of underwater autonomous vehicles (e.g. gliders), more data should be available in the future in what has been historically less accessible regions and times of the year. However, even gliders are limited by weather conditions and winter data will no doubt remain more sparse, especially in regions far off-shore and in areas of rough seas, for the foreseeable future. On the other hand, MOCHA could be very useful as a baseline from which to compare inter-annual variability in the future.

The use of a variable bathymetry-weighting scheme, hand-selected to be suitable for different regimes, could improve both the coastal salinity bias and the poorly mapped Cape Hatteras region. Additionally, including land barriers in the data weighting selection process would prevent the "seeping" of data from one

disconnected region into another (e.g. from a river to coastal region not usually impacted by the outflow, or from Long Island Sound into oceanic areas).

8 Annual Cycle of the Mid-Atlantic Bight Waters

8.1 Introduction

A strong seasonal temperature cycle has long been observed in the MAB, with a warm surface layer developing in summer over a sharp thermocline in response to surface heating, which breaks down in the autumn due to cooling, and mixing from storms (e.g. Beardsley et al. 1985; Linder and Gawarkiewicz 1998; Shearman and Lentz 2003; Lentz et al. 2003; Mountain 2003; Castelao et al. 2010). Below the summer-time thermocline, colder waters remain trapped in what is known as the "cold pool" (see §2.3.5), extending from Cape Cod to Chesapeake Bay on the mid to outer shelf (e.g. Bigelow 1933; Houghton et al. 1982).

Previous studies of hydrographic properties of the region have often been limited in at least one regard: synoptic studies usually provide high resolution, but are only a short snapshot in time: one year, one season, or even just a couple of days (e.g. Rasmussen et al. 2005; Savidge et al. 2013; Kohut et al. 2004), or in repeated years in just a small region (e.g. Flagg et al. 2002). Long term mooring arrays conversely supply a longer duration dataset but usually at only a limited number of discrete point locations (e.g. Beardsley et al. 1985; Houghton et al. 1994; Lentz et al. 2003; Lentz 2008). Studies based on historical data measurements (e.g. Mountain 2003)

provide a medium resolution. Two-dimensional climatologies have been produced from historical data which reduce large alongshore sections of the MAB down to a single cross-shore transect (e.g. Linder and Gawarkiewicz 1998; Fratantoni and Pickart 2007). Castelao et al. (2008) show glider results in very high resolution, and Castelao et al. (2010) include data from multiple years, however both results are only over a single cross-shelf transect in the central MAB.

MOCHA provides a unique opportunity to study the three-dimensional mean annual cycle of the MAB. Here, the seasonal cycle of the temperature and salinity of MAB waters are visualized using cross-shelf and along-isobath temperature and salinity transects selected from MOCHA. Alongshore patterns are examined, and the cold pool is observed in detail.

8.2 Study Region

Cross-shore transects (L1–L8) are spaced approximately every 120 km along the 100-m isobath from Cape Code to Cape Hatteras, and are perpendicular to it (Figure 8-1). They extend from the coastline out to the 1000-m isobath.
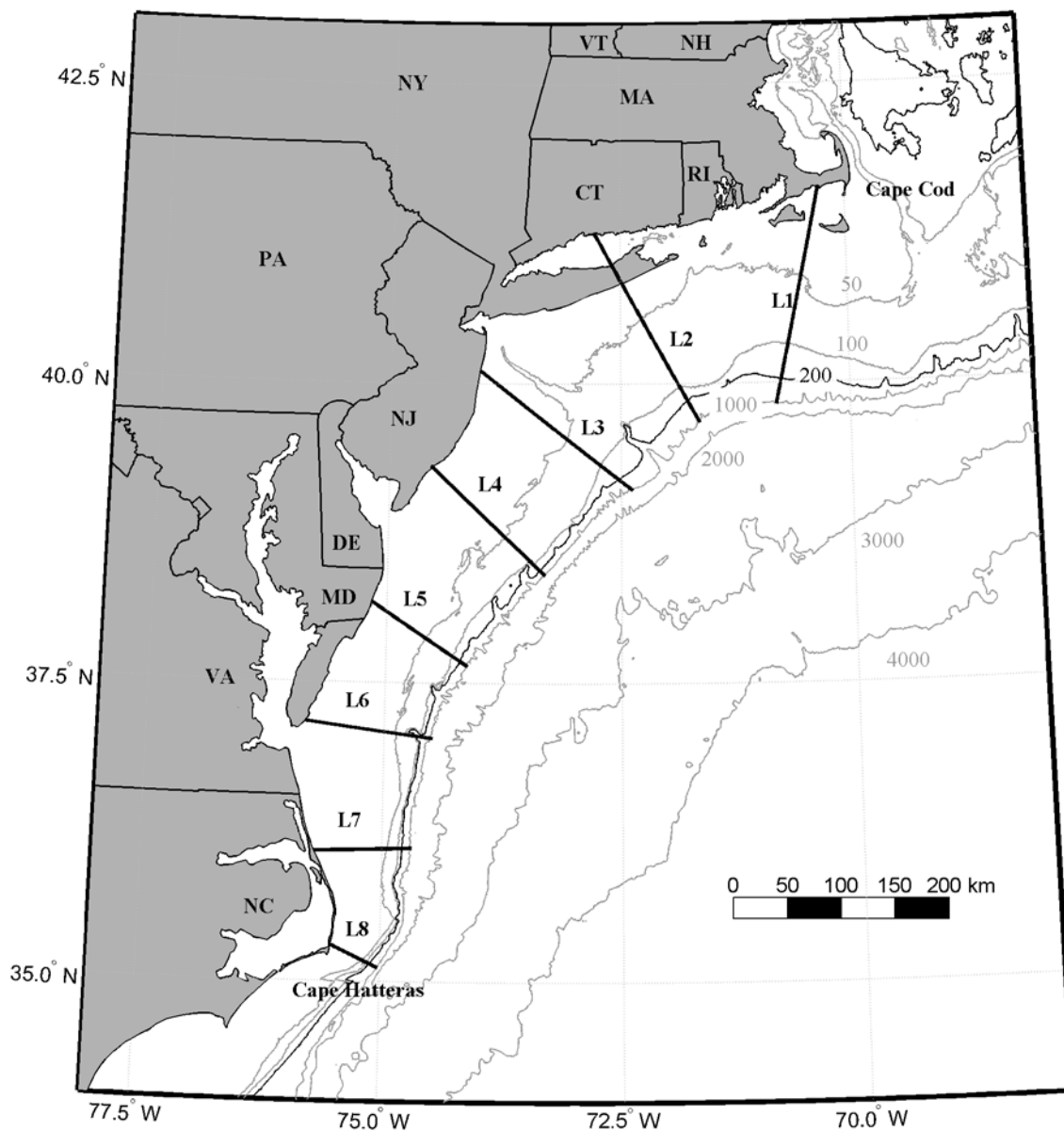
Figure 8-1: Study region: the Middle Atlantic Bight. Cross-sections of temperature and salinity are interpolated from MOCHA at the lines indicated (L1–L8). Alongshore patterns are studied using tracks interpolated along-isobaths. Lines are 100 km apart along the 1000-m isobath, and approximately perpendicular to isobaths.

8.3 MAB Annual Cycle

A cross-shelf temperature transect interpolated from MOCHA at L4 illustrates the classic MAB annual temperature cycle (Figure 8-2). Winter time waters on the MAB shelf are vertically well mixed, with a distinct cross-shelf temperature gradient: waters are coolest near the coast, and warm towards the shelf break. Coldest overall annual temperatures occur in March when cold water (<8ºC) extends across the entire shelf.

In spring, the vertical homogeneity starts to break down, and by May, the warming of the waters in response to solar heating becomes apparent. The cold pool (as represented by the 10ºC isotherm) is now cut off below the thermocline.

Surface waters progressively warm throughout the summer months: the mixed layer deepens and a strong thermocline is established below. Surface waters approach maximum temperatures in August, reaching higher than 24ºC in the 10-m deep surface mixed layer, and are bounded by a strong thermocline (temperature decreases from 22 ºC to 10ºC, in just 15 m). The cold pool remains trapped at the bottom, covering the 30–70-m isobaths, with temperatures less than 8ºC lying over the 35–45-m isobaths.
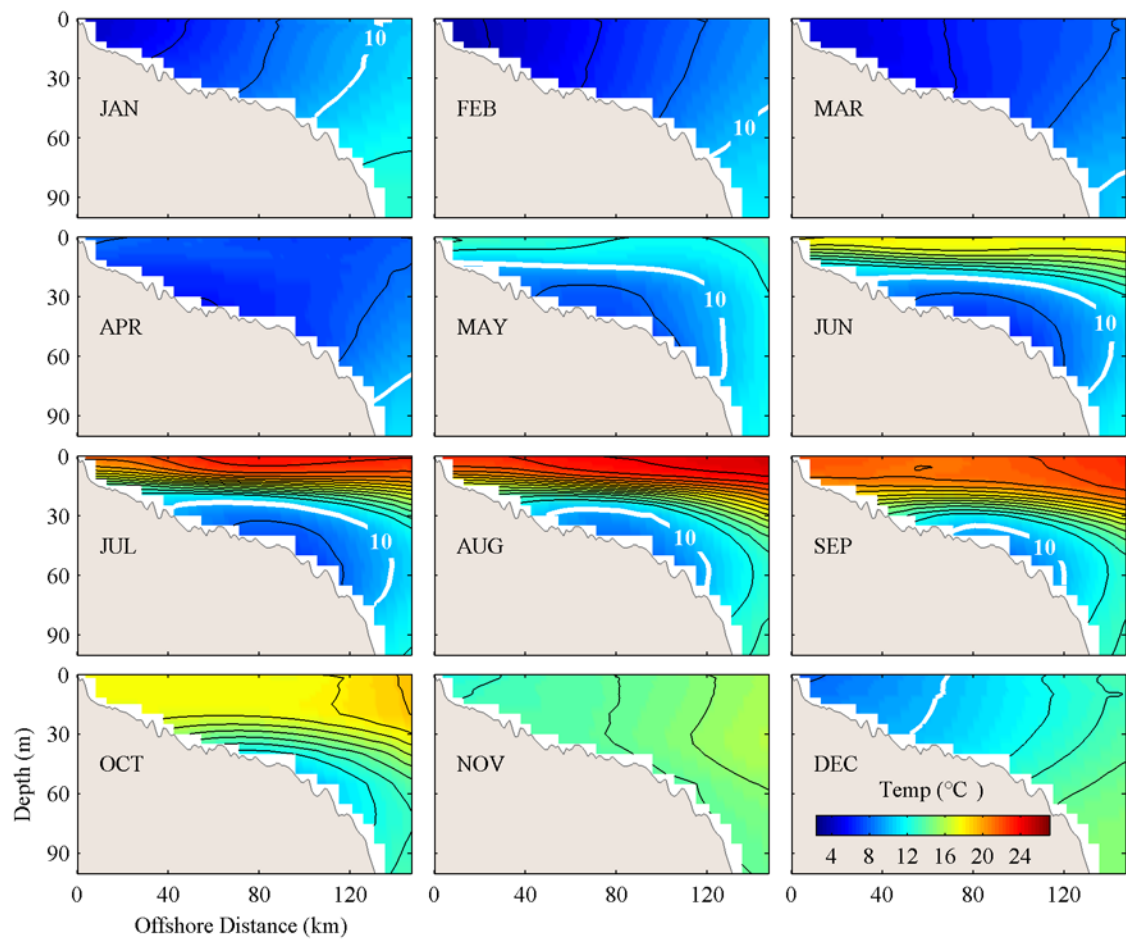
Figure 8-2: Water temperature (ºC) from a cross-shelf transect off mid-New Jersey (L3) for each month of the year. Offshore distance is measured in kilometers from the coast, and depths are in meters. The boundary of the cold pool is indicated by the 10ºC isotherm (in white).

In autumn, the surface layer cools and the thermocline weakens, and by October the cold pool is mostly diminished. In November, waters are well mixed across the shelf with temperatures near 15ºC, and the cold pool has disappeared. Winter cooling is apparent in December, as the cross-shore temperature pattern returns to the winter-time cross-shore gradient with cooler waters near the coast, and this cooling continues until March.
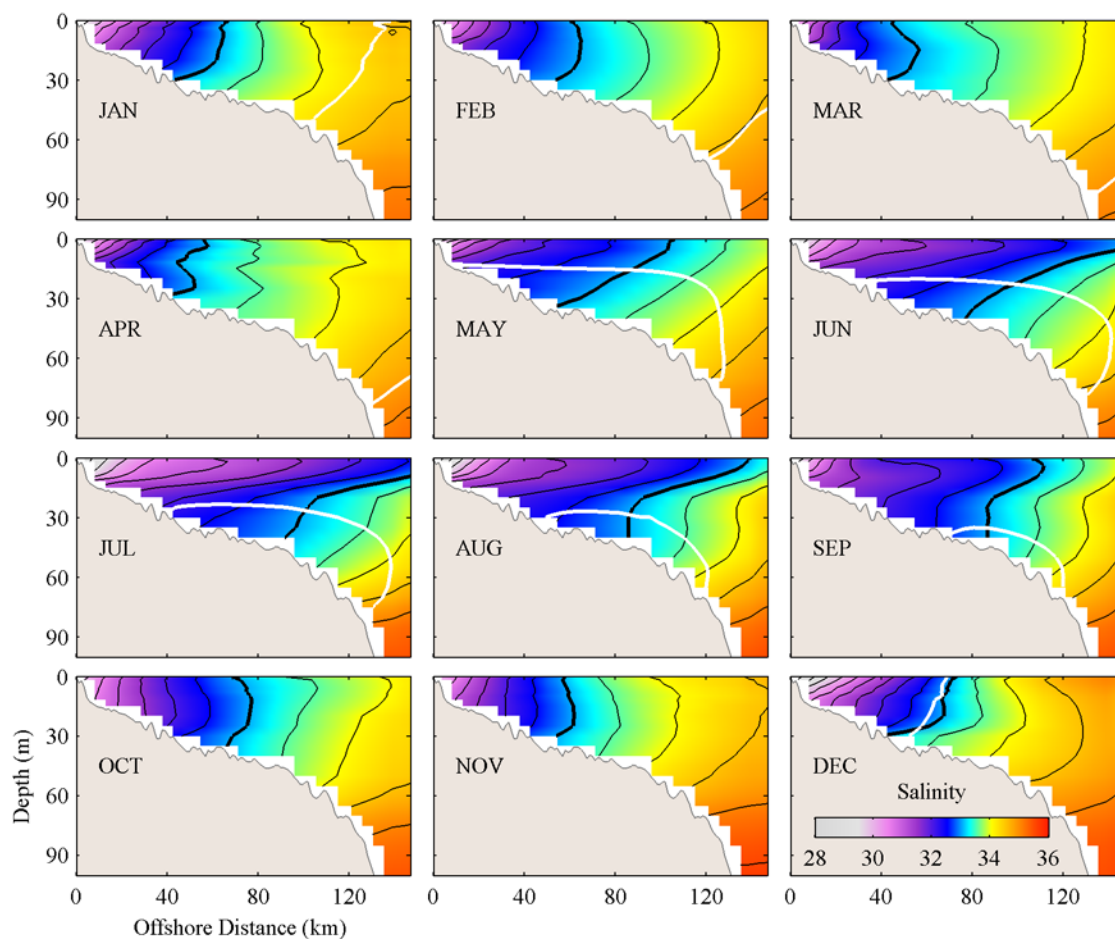
Figure 8-3: As for Figure 8-2, except for salinity. Isohalines are in black, with the 10ºC isotherm overlaid in white.

A cross-shore salinity gradient exists year-round in the MAB (Figure 8-3), with fresher waters near the coast (<31) and saltier water offshore (>34). Fresher waters extend out across the shelf as a surface layer during summer, after the peak river run-off in spring (Figure 8-4). Freshest waters appear near the shore in December.
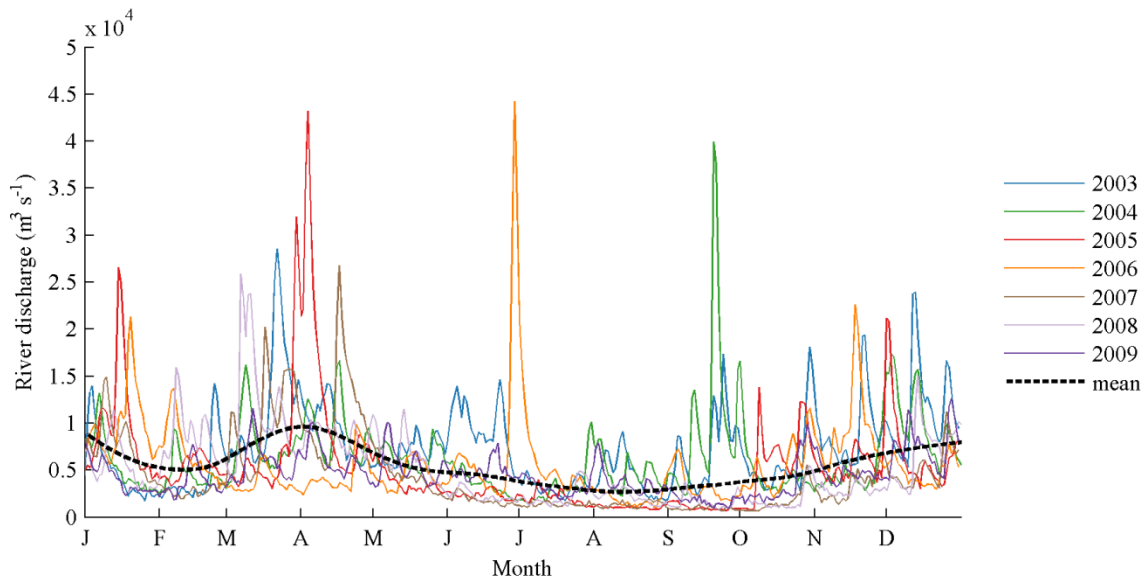
Figure 8-4: River discharge into the MAB: the sum of seven rivers for each year from 2003–2009, and the mean of all years. The rivers are: the Connecticut, Hudson, Delaware, Susquehanna, Potomac, Choptank and the James.

The density of MAB waters is dependent on both temperature and salinity. From January to April at L4 waters are uniformly dense (approximately 1026 kg m³) except for very near the coast where low salinity reduces the density (Figure 8-5). Both salinity and temperature increase offshore, which results in the near-uniform density. In summer the combination of fresher water extending further offshore and the surface warming result in a less dense surface layer with a strong pycnocline at approximately 10–20m depth. In October, the fresh water near the coast causes near-vertical isopycnals, while at depth the density pattern follows the weak horizontal thermocline. The near-uniform temperatures in November result in a density pattern that follows the salinity structure, and further cooling by
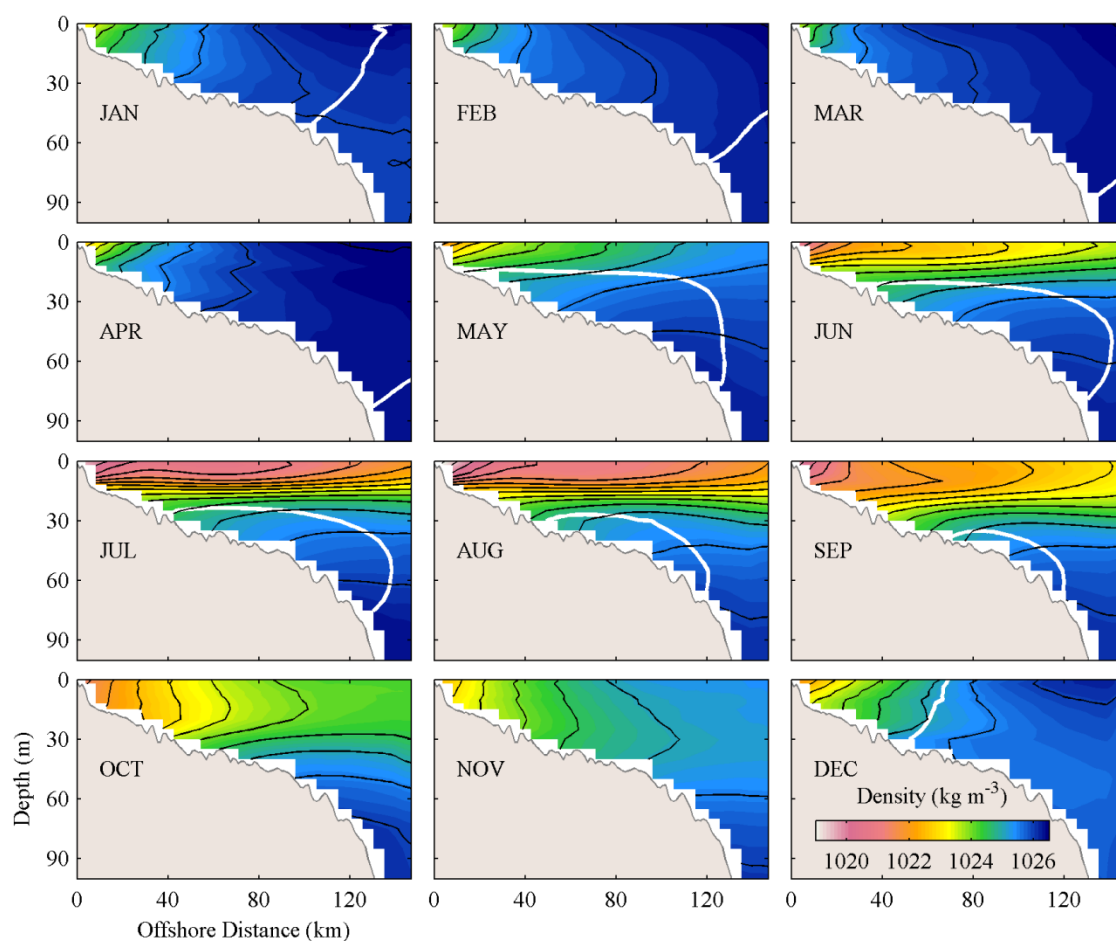
Figure 8-5: As for Figure 8-2, except for density. Isopyncals are in black with the 10ºC isotherm overlaid in white.

December bring the pattern back to lighter water near the coast due to fresher

water, and near-uniform high density off-shore.

8.4 Alongshore Patterns in Temperature

Cross-shore transects of temperature (Figure 8-6) indicate the existence of an

alongshore gradient and a time lag. Temperatures to the north are cooler during all

months of the year, with a maximum along-isobath difference in the surface waters

of greater than 7ºC in May and June at mid-depths. Typical north-to-south

differences in bottom waters are +3–4ºC during the winter months, and +0–3ºC in

the summer. The largest temperature differences are again observed at mid-depths.

In the south, the thermocline develops earlier, the surface layer is warmer, and it

persists longer. These alongshore differences are highlighted in an along-isobath

view (Figure 8-7), where months May–October clearly illustrate the development of

the thermocline along the 60-m isobath. Cold water extends to the surface in the

north during May, while a warmer layer is developing over the cold pool to the

south, deepening further to the south, and terminating at Chesapeake Bay. The

surface layer is much warmer in the south in the summer months. In October, the

northern waters are nearly vertically mixed, while a deep surface layer and

thermocline still exist in the south. By November, this surface layer disappears, and

the waters are completey mixed.

Waters are consistently much warmer in the far south, where the influence of the

Gulf Stream is seen in the year round warm temperatures and vertical isotherms.

From November through April, alongshore differences are dominated by the
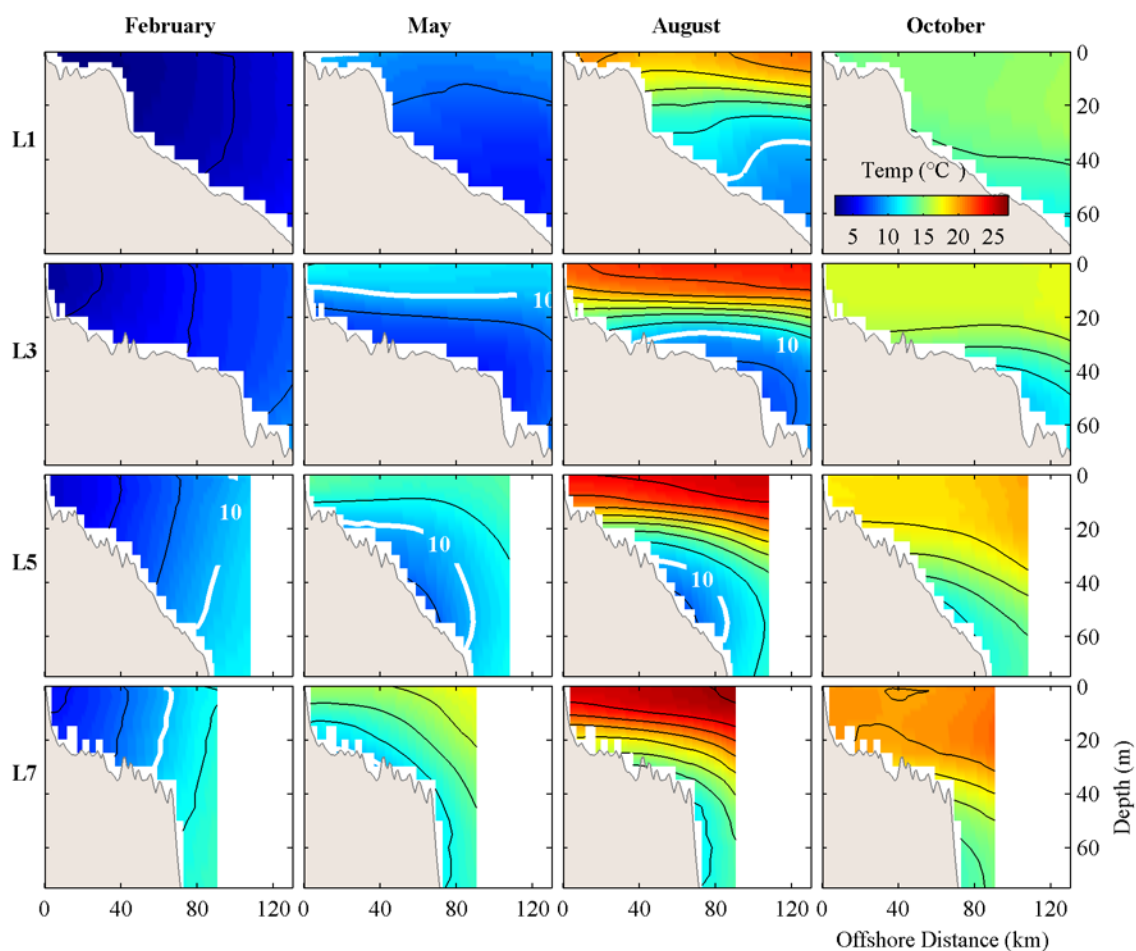
Figure 8-6: Cross-shelf transects of temperature for February, May, August and October at four transects through the MAB from Cape Cod (L1) to the southern MAB (L7).

gradient warming to the south, but with little variation in the nearly-vertically-

stratified structure.
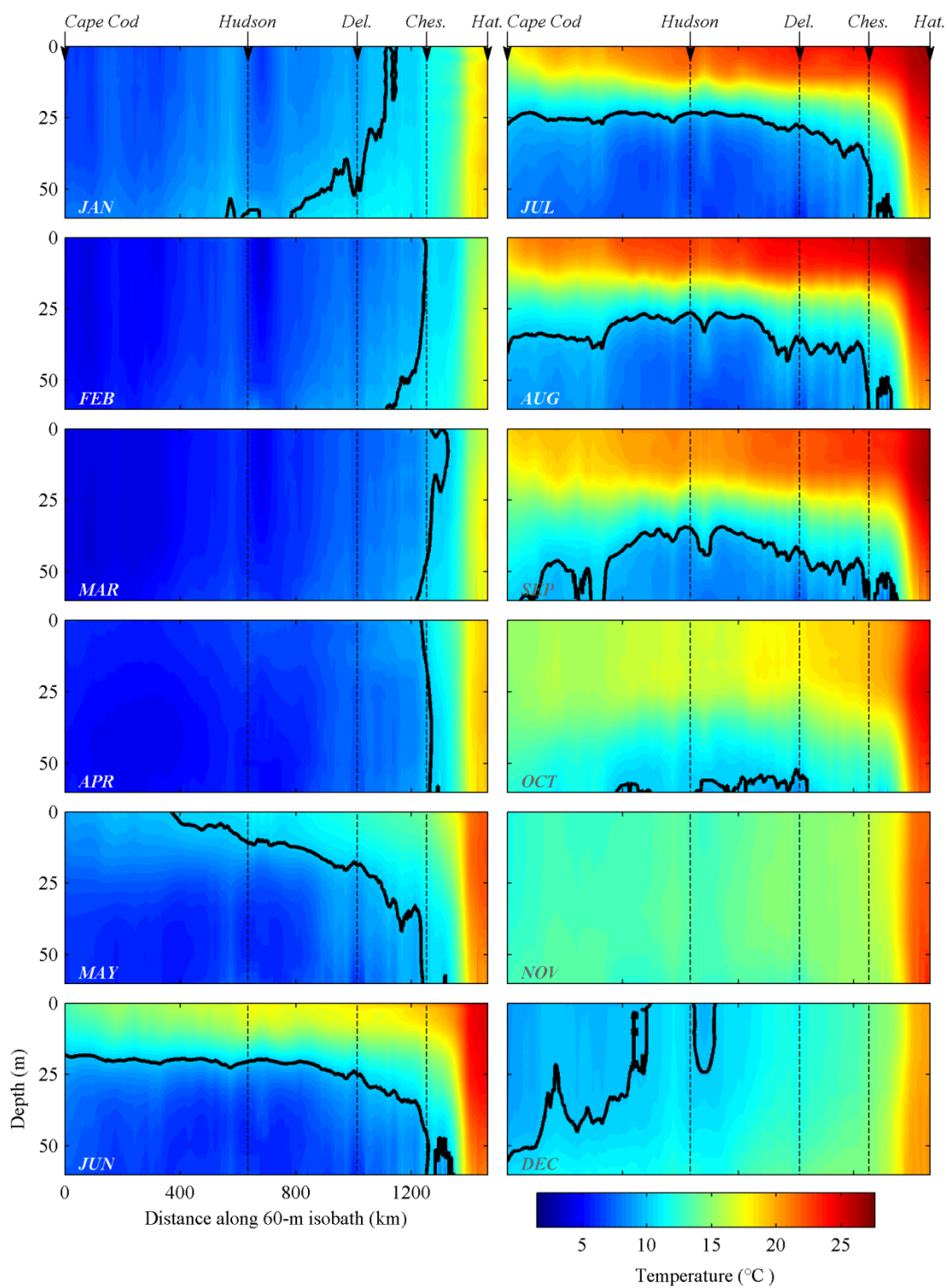
Figure 8-7: Monthly temperatures along the 60-m isobath, from Cape Cod (0 km) to Cape Hatteras (1460 km). Dashed lines indicate major freshwater inputs along the coast: Hudson River, Delaware River and Chesapeake Bay.

8.5 Along-shore Patterns in Salinity

A general pattern of fresher water to the north and saltier water to the south is evident along the 60-m isobath (Figure 8-8). Near-shore waters are fresher than offshore throughout the year, other than at Cape Hatteras due to the influence of the Gulf Stream. The greatest contrast from North to South occurs in February and March.

Evidence of the freshwater input (from the major rivers) is apparent, particularly from the Hudson River. In the summer months, a fresher layer overlies saltier water throughout the MAB. At mid-depths, the freshwater input from the Hudson is even more apparent (Figure 8-9). A fresher-to-saltier alongshore gradient exists from north to south throughout the winter months, disappearing in summer as the fresher water extends south past Chesapeake Bay, with a fresher layer on the surface also apparent. A similar alongshore and seasonal pattern exists at the outer shelf, but with higher overall salinity.
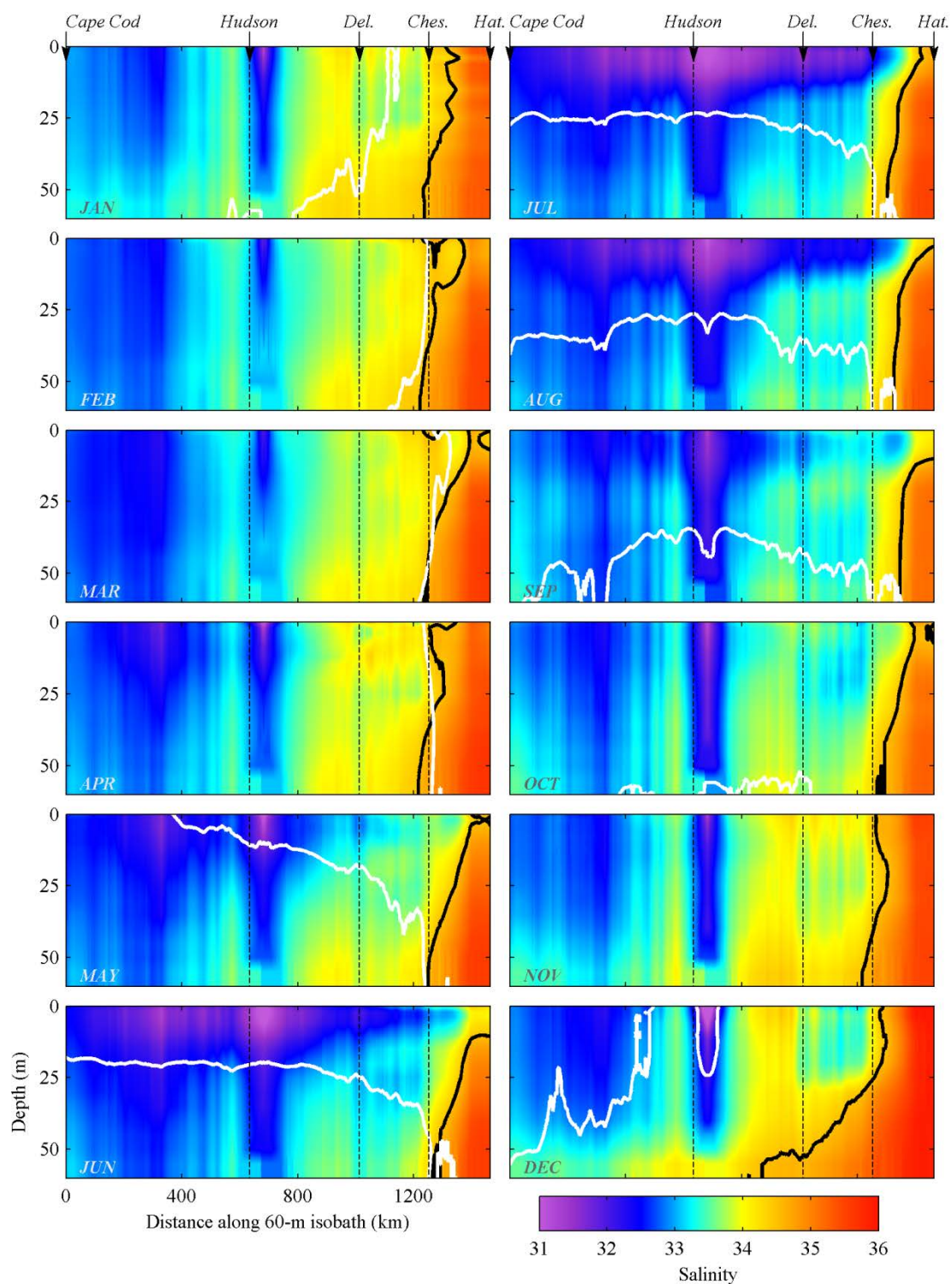
Figure 8-8: Salinity along the 60-m isobath for each month of the year. Distance is measured from L1 at Cape Cod. Dashed lines indicate location of major freshwater inputs: Hudson River Estuary, Delaware Bay and Chesapeake Bay.
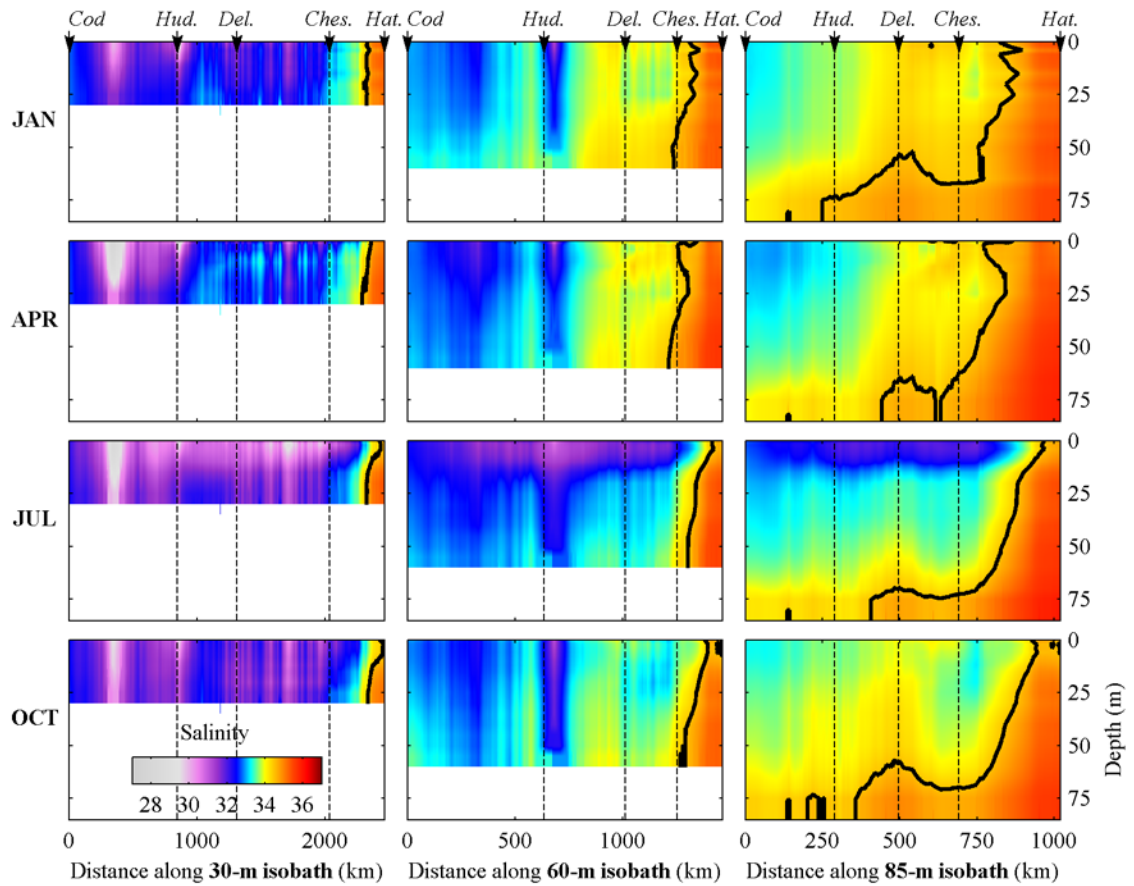
Figure 8-9: Salinity along 30-, 60- and 85-m isobaths (from Cape Cod to Cape Hatteras), during January, April, July and October. Dashed lines indicate location of major freshwater inputs: Hudson River Estuary, Delaware Bay and Chesapeake Bay.

8.6 Defining the Cold Pool

If one defines the cold pool as the parcel of water trapped beneath the summer thermocline, it is not easy to choose a single isotherm to define its edges. Depending on the season, the alongshore position, and the cross-shore position, one could come up with quite different numbers. In published literature, the cold pool has been

taken variously as water less than 8°C, 10°C, or 11°C (§2.3.5). Using MOCHA values from early summer at mid-depths, the cold pool could be defined as waters less than 7–8ºC, but as the water column warms and the thermocline deepens this value could increase to 12ºC by September (Figure 8-10). A typical measure of the mid-summer mid-depth mid-MAB cold pool boundary is the 10ºC isotherm, and is therefore used here in this work to illustrate the approximate location of the cold pool, rather than to define it.
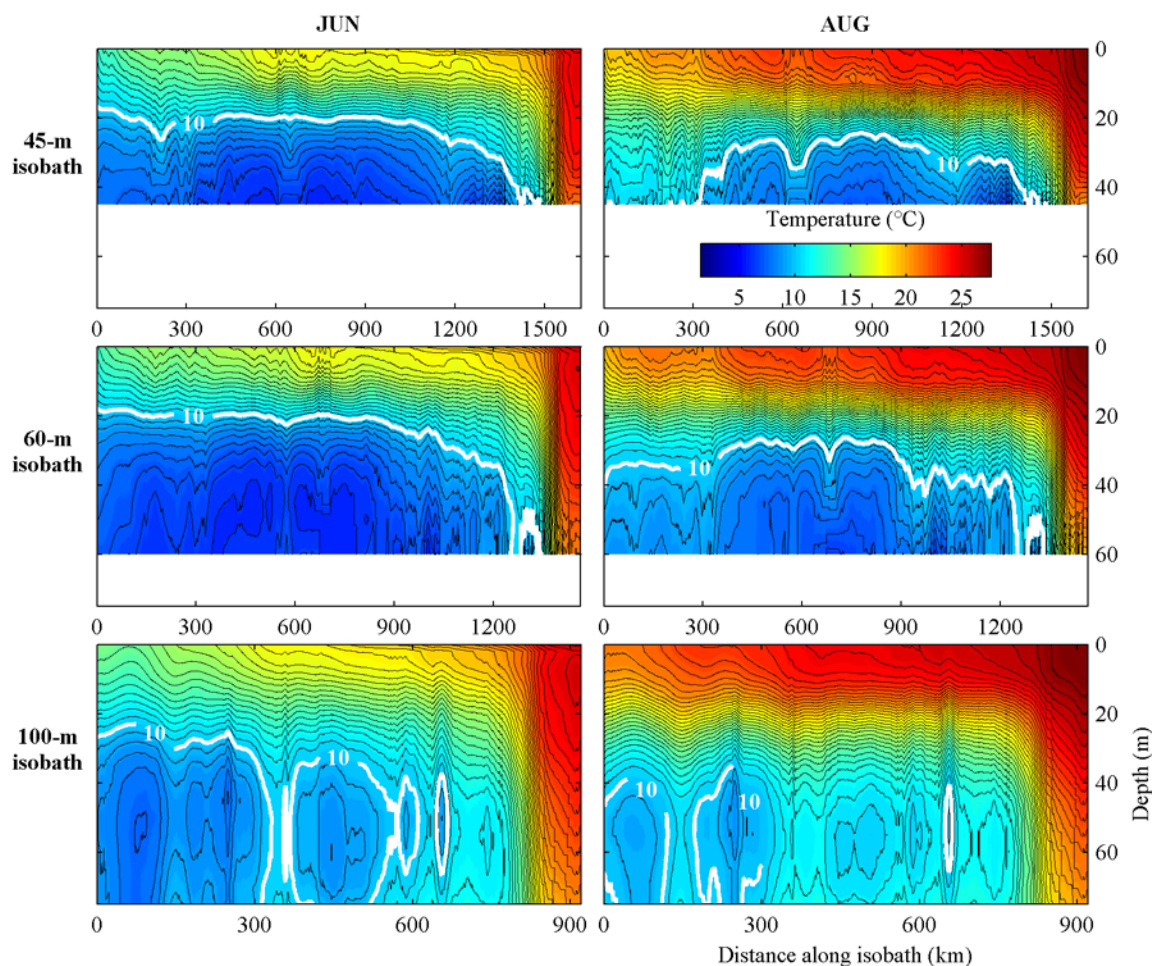
Figure 8-10: Defining the cold pool: the 10ºC isotherm provides a good measure of the outer boundary of the cold pool for the northern and mid MAB regions in June.

8.7 The Cold Pool: A Summary in Four Dimensions

Cold water resides throughout the length of the MAB during January through April, and as solar warming beings in the spring, this cool water is trapped beneath the thermocline, forming the cold pool. This "cold pool" is surrounded by warmer water on both inner-shelf and outer-shelf, and to the south, beyond Chesapeake Bay (see Figure 8-7 & Figure 8-11). The cold pool is pushed progressively deeper as the thermocline strengthens over the summer, and is generally found over the 35–75 m isobaths, since in areas shallower than 35 m summer warming reaches to the ocean floor.

The area of the cold pool on the shelf shrinks as waters warm, however a core parcel of cold pool water remains until September, as indicated by bottom temperatures below 10ºC (Figure 8-11). Remnants of cooler water are still trapped in October at mid-depths over the northern half of the MAB shelf, but are completely depleted by November. Waters do not cool again to winter temperatures until January, and the cycle begins once more.

The cold pool is visualized in 3-D using the 8 ºC and 10ºC iso-surfaces (Figure 8-12): In December and January the 10ºC isotherm borders cooler waters inshore, extending from top to bottom, and moving further offshore with time. During February to April, waters cooler than 10ºC fill most of the MAB shelf. In April, the first surface warming is apparent in the south, as the isotherm now covers inshore
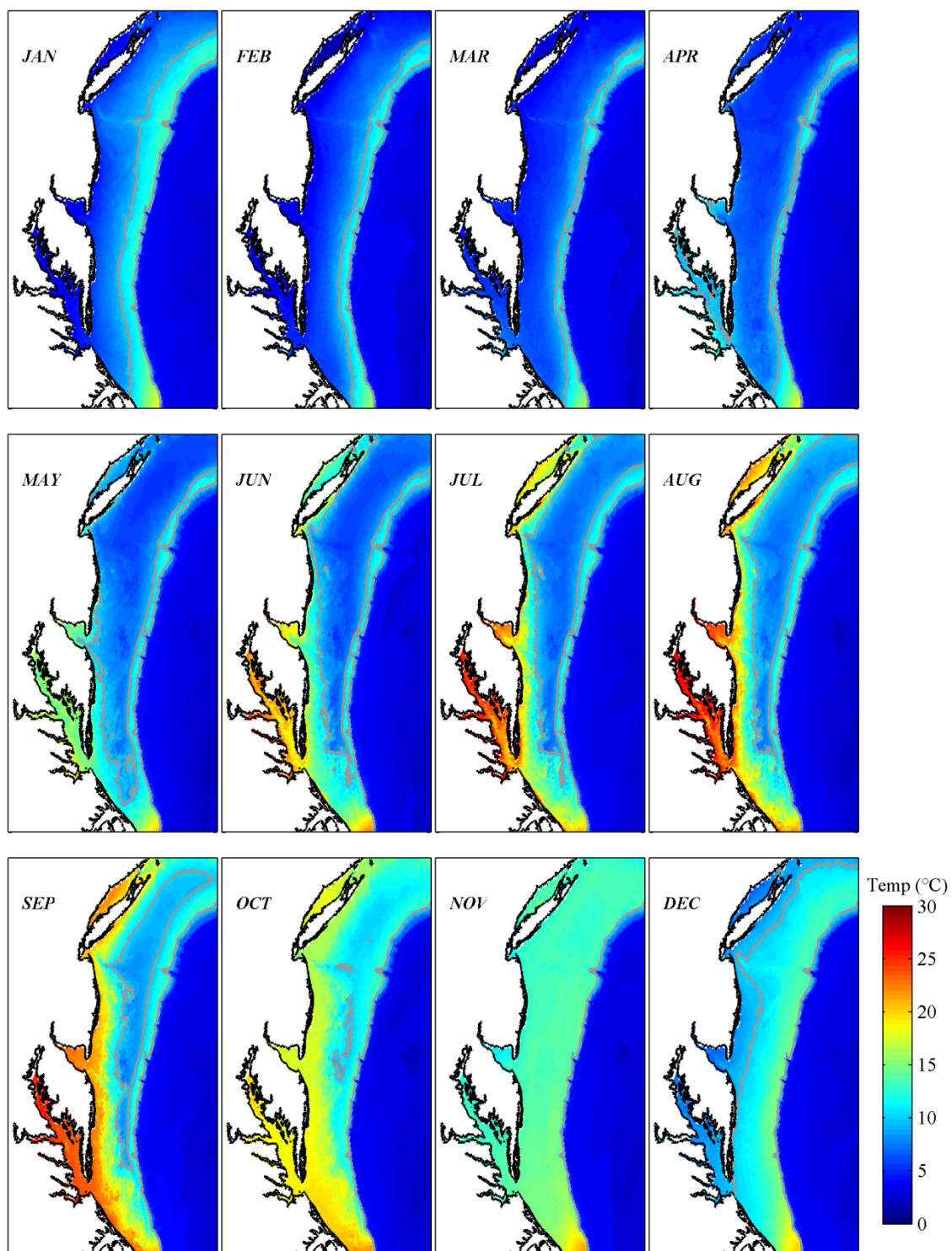
Figure 8-11: MAB bottom temperature for each month of the year. The 10ºC isotherm is marked in grey.

waters below the surface. The cold pool develops fully by June, as the 10°C isotherm overlays water over nearly the whole extent of the MAB. The bulge of cold pool water diminishes slowly in July through August as convection mixes away the stratification, and it remains only in the mid-MAB at mid-depths in September. The shelf is well mixed by October and November, and waters warmer than 10°C now exist throughout the entire MAB shelf region.

A Hovmöller diagram (Figure 8-13) illustrates the progression in time of the cold pool, as illustrated by bottom temperature along the 60-m isobath over time. Between January and March, cold pool waters move further south, with isotherms travelling at a rate of about 0.15 m s^{-1} (excepting the influence of the Hudson Canyon and the Hudson River discharge). The cold pool waters are bounded during the summer by Chesapeake Bay, until September when the cold pool disappears in the north and in the south. Warmer waters over the Hudson Canyon, and to a lesser extent offshore of Delaware Bay, split the cold pool in August and September. Remnants of the cold pool remain the longest in the mid-MAB, from north of Long Island to Delaware Bay. By October all cold pool water is gone.
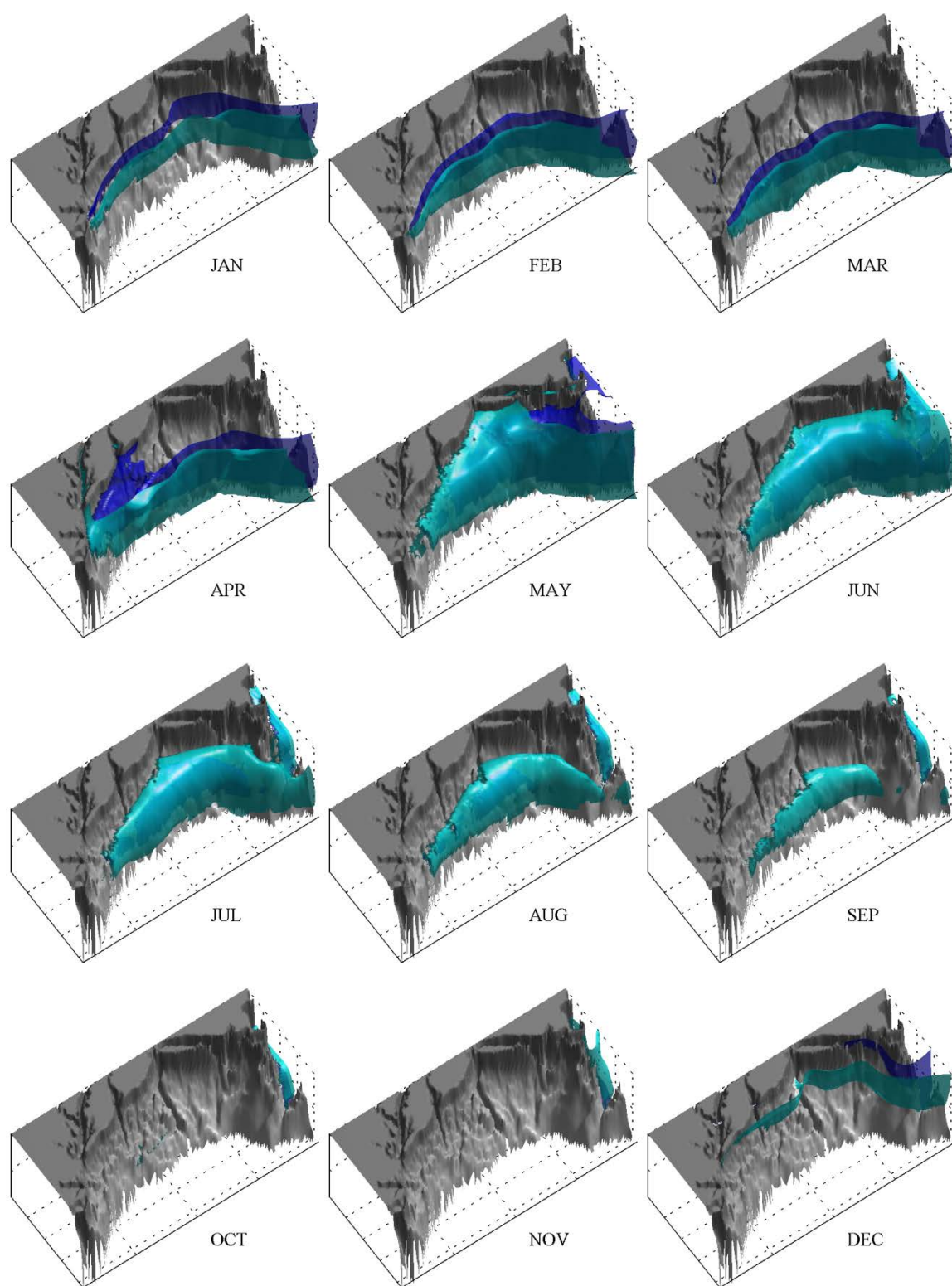
Figure 8-12: Illustrating the cold pool in 4-D for each month of the year: the 10ºC isotherm is illustrated in cyan, and the 8ºC isotherm in blue.
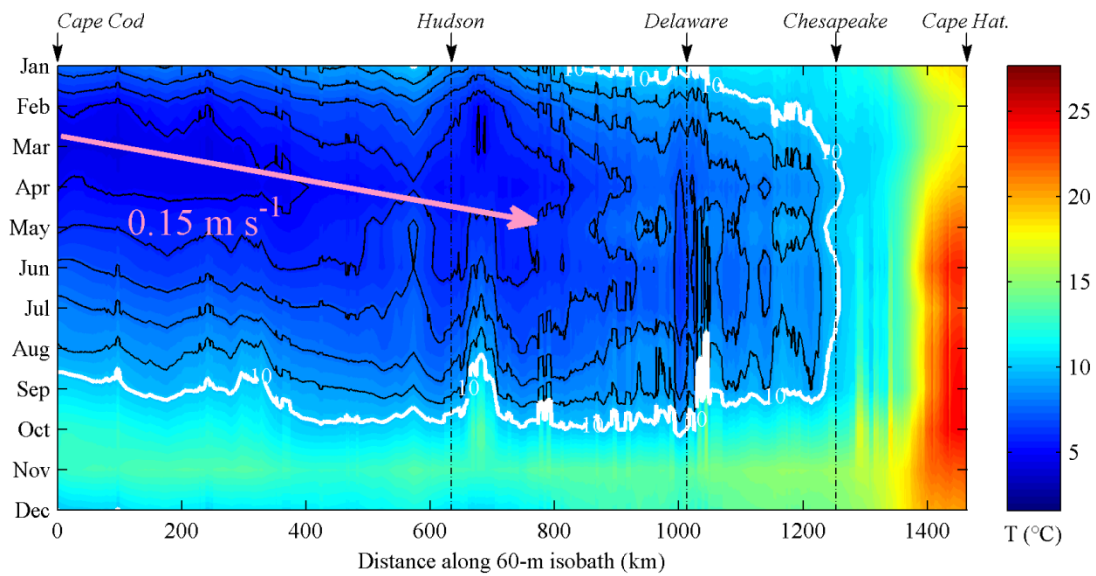
Figure 8-13: Hovmöller Diagram showing bottom temperature along the 60-m isobath over time. Distances are measured along-isobath from Cape Cod. Dashed lines indicate significant freshwater inputs along the MAB coast. The 10ºC isotherm is highlighted in white; black isotherms are at 1ºC intervals.

Another way to visualize the evolution of the cold pool is by examining a single temperature profile changing in time. Figure 8-14 illustrates three single vertical profiles; taken in 25 m, 57.3 m and 80 m deep waters along L4 (off the mid-New Jersey coast): coldest water exists inshore in the winter months; surface heating begins by May; cold pool water has disappeared by June; and waters become vertically stratified by September. Figure 8-14b illustrates the typical mid-depth development of the cold pool, and Figure 8-14c the weaker cold pool signal that exists on the outer shelf.
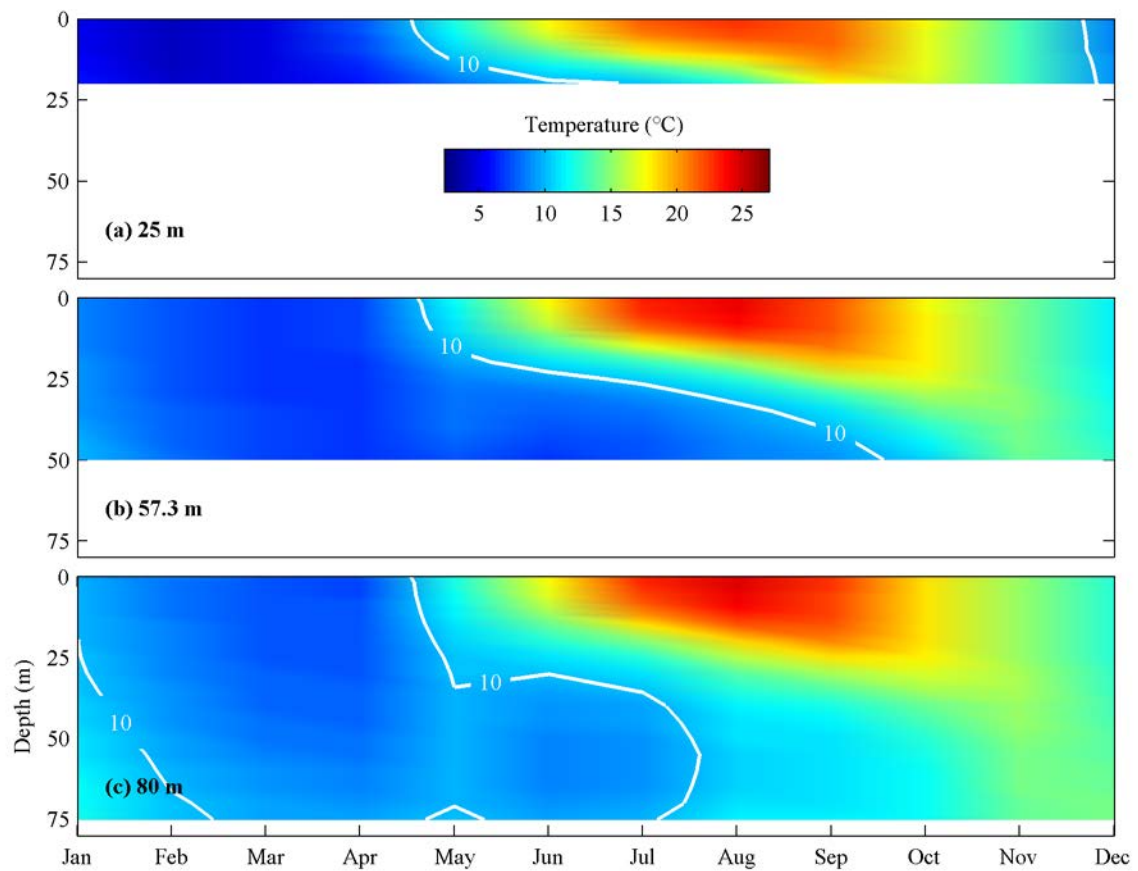
Figure 8-14: Hovmöller Diagrams illustrating the temperature of three individual profiles progressing in time, in (a) 25 m, (b) 57.3 m and (c) 80 m depth of water along the cross-shelf transect L4 (mid-NJ). The cold pool is illustrated using the 10ºC isotherm (in white).

8.8 Volume of the Cold Pool

The volume of cold pool water in the MAB during each month is estimated by calculating the volume of all grid cells containing water $\leq 10^\circ$C. An annual cycle is clearly evident with maximum volume in spring and minimum volume in autumn (Figure 8-15).
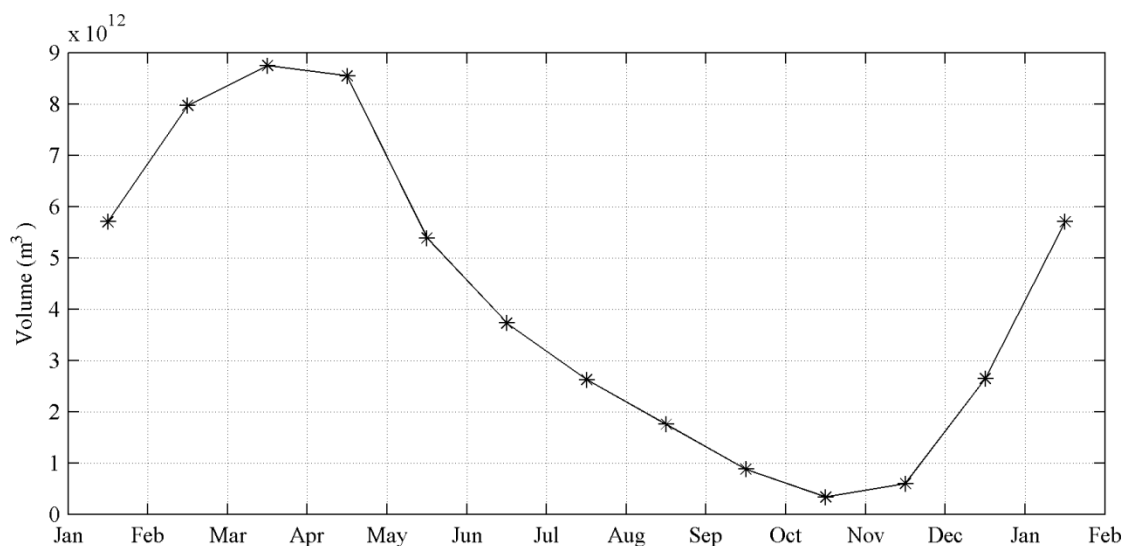
Figure 8-15: The annual cycle of cold pool volume, as estimated by the volume of MOCHA grid cells on the MAB shelf containing water $\leq 10^{\circ}$C.

Cold pool water volume can be used to visualize the depth-extent of the cold pool, as well as the geographical extent, which is illustrated by the bottom temperature "foot-print" (Figure 8-11). The cold pool thickness at each grid cell is shown for each month of the year (Figure 8-16). The shrinking of the cold pool from both coastal and seaward sides is once again clearly evident, and here the vertical reduction in the cold pool volume is also shown by decreased thicknesses through the summer and fall. Cold pool temperatures are re-established in December from the coast and migrate across the shelf in January, which is consistent with local air-sea fluxes driving cooling to the seafloor in progressively deeper water.
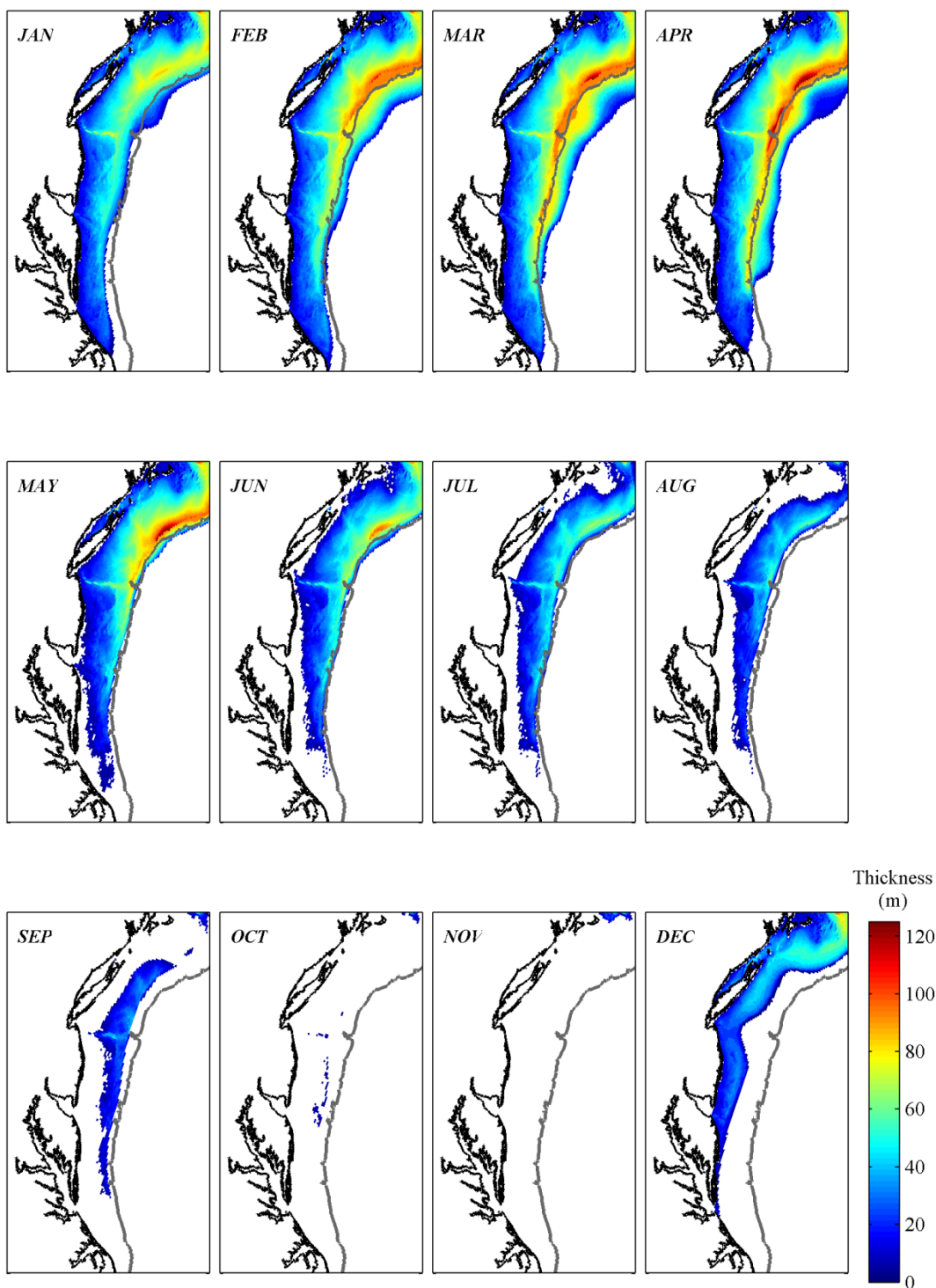
Figure 8-16: Thickness of the cold pool (m) in the MAB for each month of the year. The cold pool is defined here by water of temperatures ≤ 10ºC.

8.9 Summary

The distinct annual cycle of temperature in the MAB can be investigated from multiple viewpoints using the MOCHA dataset. The well-known cycle of the warming of a summer mixed layer with a strong thermocline, and the development and shrinking of the cold pool are clearly visible, and in much greater detail than has previously been published. In contrast to many previous studies that simply analyze a single transect (or a region averaged onto a single transect), alongshore patterns are also discernable: MAB waters are generally cooler and fresher to the north and warmer and saltier to the south (despite coastal inputs of freshwater). Significant variations in along-shore salinity are identified, while temperature is observed to increase smoothly in the alongshore direction to the southeast.

The MOCHA dataset provides a unique three-dimensional spatial view of the MAB shelf and patterns in salinity and temperature. Calculating monthly maps, rather than seasonal, allows the observation of the annual cycle (the fourth dimension) in greater detail than in previous studies.

9 MAB Budgets and Circulation

9.1 Introduction

Where does the MAB water exit the shelf? This has long been a question for physical oceanographers studying the region. The waters entering the MAB from the north through Georges Bank flow equatorward along the continental shelf until they reach Cape Hatteras. At this point, the greater part of the current turns offshore and merges with the northwestward flowing Gulf Stream (e.g. Bumpus 1973; Ford et al. 1952; Lillibridge et al. 1990; Kupferman and Garfield 1977), while only a small percentage of MAB water volume continues through the South Atlantic Bight (SAB) (e.g. Bumpus and Pierce 1955; Townsend et al. 2006; Bignami and Hopkins 2003; Pietrafesa et al. 1994). However, it has long been postulated that a substantial proportion of the water volume entering the MAB is lost to the ocean before it reaches Cape Hatteras (e.g. Biscaye et al. 1994; Bignami and Hopkins 2003). The "leaky current" theory is commonly held: that is, the volume of water is lost at an approximately uniform rate along the length of the MAB (e.g. Mountain 1991; Lozier and Gawarkiewicz 2001). Most studies caution, however, that cross-shore currents are very small and thus it is difficult to measure them accurately (or to infer cross-shore transport from them) (e.g. Chen and He 2010). Rasmussen et al. (2005) take that caution even further, and state "little concrete evidence exists for the inferred cross-shelf export of large quantities of shelf water".

In this work, the leaky current theory is investigated. Is cross-shore flow uniform along the length of the MAB, or are there preferential sites for cross-shore transport? What are the corresponding fluxes of heat, salt and freshwater?

The majority of models and climatologies of current flow in the MAB assume that conditions are similar along-shelf. Many are entirely two dimensional: cross-shore density gradients, along-shelf sea surface slope and wind stress are all assumed constant throughout the MAB; the alongshore density gradient is assumed to be zero; and depth-averaged flow is assumed to follow isobaths (or the coordinate system is rotated to align with the depth-averaged flow), and thus a boundary condition of zero depth-averaged cross-shore is applied ($\int_{-h}^{0} u\, dz = 0$). A preponderance of studies are located on the New England shelf, nearby to the Woods Hole Oceanographic Institution, and most make the assumption that the conditions in that region apply to the entire MAB shelf (i.e. no along-shore variability in properties) (e.g. Csanady 1976; Lentz 2008a; Wright 1976).

In this work the MAB is divided into eight regions (or "boxes") for which volume, heat, salt and freshwater budgets are modelled for each month. The boxes are bounded by "lines" that are drawn perpendicular to local isobaths, and extend out to the 85-m isobath, which forms the offshore boundary. Currents along these lines, and along the 85-m isobath, are calculated using fully 3-D fields of density and 2-D fields of wind-stress. No assumption is made regarding the direction of the flow, since this is under investigation. River inputs from the seven largest rivers in the regions are also included in the budgets.

Three-dimensional fields of temperature and salinity from MOCHA are used in conjunction with air-sea heat and salt flux reanalyzes to estimate the heat, salt and freshwater balance within in each box.

9.2 Conservative Seawater Properties

In this chapter MOCHA temperature and salinity are converted into the International Thermodynamic Equations of Seawater 2010 (TEOS–10) variables using the Gibbs-SeaWater (GSW) Oceanographic Toolbox (McDougall and Barker 2011) for MATLAB[i]. Practical salinity (which is unit less) is converted into Absolute Salinity (S_A), and Preformed Salinity (S_*), both of which have units of g kg^{-1}; while *in situ* temperature is converted into Conservative Temperature (Θ). All thermodynamic properties are functions of Absolute Salinity, so this is needed to calculate the *in situ* density, whereas Conservative Temperature and Preformed Salinity are the conservative variables required for use in conservation equations. Further details of these variables and their conversion can be found in the TEOS–10 Manual (IOC et al. 2010), the TEOS–10 Primer (Pawlowicz 2010).

The "heat content" of seawater is represented under TEOS–10 by the Potential Enthalpy h and the Conservative temperature Θ is defined to be proportional to that:

$$\Theta \equiv \frac{h^0}{C_p^{\ 0}} \qquad\qquad 9\text{-}1$$

where $C_p^{\,0}$ = 3991.867 957 119 63 J kg^{-1} K^{-1} is the fixed heat capacity where Θ is given in kelvins (K) (IOC, 2010). The units of potential enthalpy are joules per kilogram (J kg^{-1}). In the past, potential energy has been used as the conservative temperature variable, however the error in assuming Potential enthalpy is conservative is less than 100 times the error in assuming potential energy is conservative (McDougall 2003; Graham and McDougall 2013).

9.3 The Equations of Motion

9.3.1 Governing Equations

A simplified set of the equations of motion (Eqs. 9-2–9-4), commonly applied to coastal oceanographic regions, is derived from the Navier-Stokes equations by assuming a steady state, hydrostatic and incompressible fluid and applying the Boussinesq approximation. The vertical flow is assumed to be much smaller than horizontal motion, and the nonlinear advective terms are also neglected. The details of these assumptions can be found in most physical oceanography texts (e.g. Csanady 1982; Pond and Pickard 1983; Bowden 1983; Vallis 2006). Under the Boussinesq approximation, the mass conservation equation reduces to volume conservation, and in this form it is termed the *continuity equation* (Eq. 9-5).

$$-fv = -\frac{1}{\rho_0}\frac{\partial p}{\partial x} + \frac{1}{\rho_0}\frac{\partial \tau^x}{\partial z} \qquad \text{9-2}$$

$$fu = -\frac{1}{\rho_0}\frac{\partial p}{\partial y} + \frac{1}{\rho_0}\frac{\partial \tau^y}{\partial z} \qquad \text{9-3}$$

$$\frac{\partial p}{\partial z} + \rho g = 0 \qquad\qquad\qquad 9\text{-}4$$

$$\frac{\partial u}{\partial x} + \frac{\partial v}{\partial y} + \frac{\partial w}{\partial z} = 0 \qquad\qquad\qquad 9\text{-}5$$

Here u, v and w are the velocities in the cross-shore (x), alongshore (y) and vertical (z)

directions; p is the pressure, τ^x is the stress term, f is the Coriolis parameter and g

is the gravitational acceleration.

Equations 9-2 and 9-3 describe a balance in the horizontal momentum between the

Coriolis force on the left-hand side (lhs) and the pressure gradient force and

frictional shear stresses: the first and second terms, respectively, on the right-hand

side (rhs).

Note the different symbols used for density: the Boussinesq approximation leads to

the use of a constant reference density ρ_0 in all terms other than the buoyancy term

which retains the fully varying 3-D density field which is depicted by ρ.

9.3.2   Deriving the Buoyancy Term

Pressure gradients are very difficult to measure accurately in the ocean, so it is

usual to replace the pressure gradient term with one derived from the hydrostatic

equation in its differential form: $dp = -\rho g \; dz$.

Integrating the hydrostatic equation over depth from the bottom -h to the (sloping) surface η leads to

$$\int_{-h}^{\eta} dp = -g \int_{-h}^{\eta} \rho dz$$

$$= -g \int_{-h}^{0} \rho dz - g\rho_0 \int_{0}^{\eta} dz \qquad \text{9-6}$$

where the density is assumed to vary throughout the water column in the first term on the rhs; but is assumed constant at the surface, and set equal to the reference density in the second term, both in keeping with the Boussinesq approximation.

Integration by parts is now applied to solve for pressure, yielding

$$p\big|_{-h}^{\eta} = -g \left[\left(\rho z \right)\big|_{-h}^{0} - \int_{-h}^{0} z d\rho \right] - g\rho_0 \eta$$

$$\underbrace{p\big|_{\eta}}_{p_{\text{atm}}} - \underbrace{p\big|_{-h}}_{p_{\text{bot}}} = -\rho g h - g \int_{-h}^{0} z d\rho - g\rho_0 \eta \qquad \text{9-7}$$

where the first term on the lhs is the atmospheric pressure at the surface, p_{atm}, and the second term on the lhs is the bottom pressure, $p_{\text{bot.}}$ Rearranging for the bottom pressure, and once again integrating by parts leads to

$$p_{\text{bot}} = p_{\text{atm}} + \rho_0 g \eta + g \rho h + g \int_{-h}^{0} z \, d\rho$$

$$= p_{\text{atm}} + \rho_0 g \eta + g \rho h - \left(g \left. \rho \right|_{-h}^{0} - g \int_{-h}^{0} \rho \, dz \right)$$

$$= p_{\text{atm}} + \rho_0 g \eta + g \int_{-h}^{0} \rho \, dz \qquad\qquad 9\text{-}8$$

This states that the pressure at the ocean floor ($z = -h$) is the sum of the pressure of the atmosphere, the pressure due to the sloping sea surface, and the pressure due to the density of the accumulated water column below: a simple and logical result.

One can similarly derive equivalent statements for any depth, $z \in [0, -h]$, hence the general expression for pressure as a function of depth is

$$p(z) = p_{\text{atm}} + \rho_0 g \eta + g \int_{z}^{0} \rho \, dz' \qquad\qquad 9\text{-}9$$

where dz' is a dummy variable of integration.

Having derived a term for the pressure, the next step is to derive a term for the horizontal density gradients, as they appear in the momentum equations (Eqs. 9-2 and 9-3). Differentiating Eq. 9-9, and using the fundamental theorem of calculus to differentiate the integral on the rhs, the horizontal pressure gradient terms are

$$\frac{\partial p}{\partial x} = \frac{\partial}{\partial x}\left(p_{\text{atm}} + \rho_0 g\eta + g\int_z^0 \rho dz' \right)$$

$$= 0 + \rho_0 g\frac{\partial \eta}{\partial x} + \frac{\partial}{\partial x}\left(g\int_z^0 \rho dz' \right)$$

$$= \rho_0 g\frac{\partial \eta}{\partial x} + g\int_z^0 \frac{\partial \rho}{\partial x} dz' \qquad \text{9-10}$$

where p_{atm} is assumed to be constant of the domain of interest. Similarly,

$$\frac{\partial p}{\partial y} = \rho_0 g\frac{\partial \eta}{\partial y} + g\int_z^0 \frac{\partial \rho}{\partial y} dz' \qquad \text{9-11}$$

The pressure gradient terms in Eqs. 9-2 and 9-3 can now be eliminated, replaced by

terms containing the density gradients, and the sea-surface slope:

$$-fv = -g\frac{\partial \eta}{\partial x} - \frac{g}{\rho_0}\int_z^0 \frac{\partial \rho}{\partial x} dz' + \frac{1}{\rho_0}\frac{\partial \tau^x}{\partial z} \qquad \text{9-12}$$

$$fu = -g\frac{\partial \eta}{\partial y} - \frac{g}{\rho_0}\int_z^0 \frac{\partial \rho}{\partial y} dz' + \frac{1}{\rho_0}\frac{\partial \tau^y}{\partial z}$$

then dividing through by f, the expressions for velocity become

$$v = \frac{g}{f}\frac{\partial \eta}{\partial x} + \frac{g}{\rho_0 f}\int_z^0 \frac{\partial \rho}{\partial x} dz' - \frac{1}{\rho_0 f}\frac{\partial \tau^x}{\partial z}$$

$$u = -\frac{g}{f}\frac{\partial \eta}{\partial y} - \frac{g}{\rho_0 f}\int_z^0 \frac{\partial \rho}{\partial y} dz' + \frac{1}{\rho_0 f}\frac{\partial \tau^y}{\partial z} \qquad \text{9-13}$$

$$\underbrace{}_{\substack{\text{barotropic}\\\text{pressure}\\\text{gradient}\\\text{terms}}} \qquad \underbrace{}_{\substack{\text{baroclinic}\\\text{pressure}\\\text{gradient}\\\text{terms}}} \qquad \underbrace{}_{\substack{\text{friction}\\\text{terms}}}$$

where the first term on the rhs is the barotropic pressure gradient: a result of the sea-level slope, it is constant with depth; the second term on the rhs is the baroclinic pressure gradient due to the varying density field $\rho = \rho(x, y, z)$, which does vary with depth. Note that the term "baroclinic" is used in differing ways by oceanographers: here it refers to the density-driven portion of the pressure gradient term.

9.3.3 Along-shore Flow

The across-shore momentum balance in the MAB is assumed to be geostrophic (a balance between only the Coriolis force and the pressure-gradient force), which is justified from many observations over the years (e.g. Noble et al. (1983); Brown et al. (1985); and Shearman and Lentz (2003), to name a few), and including the observations reported in §3.5. Thus the stress terms can be neglected, and the along-shore velocity of Eq. 9-13 reduces to

$$v = \underbrace{\frac{g}{f}\frac{\partial \eta}{\partial x}}_{\text{barotropic}} + \underbrace{\frac{g}{\rho_0 f}\int_z^0 \frac{\partial \rho}{\partial x}dz'}_{\text{baroclinic}}$$

9-14

Since density is readily calculated from MOCHA, the across-shore sea-surface slope is the only unknown. The cross-shore sea-surface gradient is very small, and difficult to measure. It can be eliminated by assuming a linear drag law for the bottom stress, and relating it to the near-bottom velocity:

$$\tau^{by} = \rho_0 r v_{\text{bot}}$$

9-15

where v_{bot} is the alongshore bottom velocity and r is a linear drag coefficient. Thus

$$v_{\text{bot}} = \frac{\tau^{by}}{\rho_0 r} \qquad \text{9-16}$$

The aim is now to extract the bottom alongshore velocity from Eq. 9-14. Using the

integral rules $\int_a^b f(x)\,dx = \int_a^c f(x)\,dx + \int_c^b f(x)\,dx$ and $\int_a^b f(x)\,dx = -\int_b^a f(x)\,dx$, the

integral in the baroclinic term of Eq. 9-13 can be split into depth-varying and depth-

independent components:

$$\int_z^0 \frac{\partial \rho}{\partial x}\,dz' = \int_z^{-h} \frac{\partial \rho}{\partial x}\,dz' + \int_{-h}^0 \frac{\partial \rho}{\partial x}\,dz'$$

$$= -\underbrace{\int_{-h}^z \frac{\partial \rho}{\partial x}\,dz'}_{\substack{\text{depth-}\\ \text{varying}}} + \underbrace{\int_{-h}^0 \frac{\partial \rho}{\partial x}\,dz'}_{\substack{\text{depth}\\ \text{independent}}} \qquad \text{9-17}$$

Further, the depth varying part can be split into its bottom value, and the

remainder, giving us separate expressions for the bottom velocity and the depth-

varying component of the baroclinic flow, as desired.

$$v = \underbrace{\frac{g}{f}\frac{\partial \eta}{\partial x}}_{\substack{\text{barotropic}\\ \text{bottom}\\ \text{velocity}}} + \underbrace{\frac{g}{\rho_0 f}\int_{-h}^0 \frac{\partial \rho}{\partial x}\,dz'}_{\substack{\text{baroclinic}\\ \text{bottom}\\ \text{velocity}}} - \underbrace{\frac{g}{\rho_0 f}\int_{-h}^z \frac{\partial \rho}{\partial x}\,dz'}_{\substack{\text{baroclinic}\\ \text{depth-varying}\\ \text{velocity}}}$$

$$= v_{\text{bot}} - \frac{g}{\rho_0 f}\int_{-h}^z \frac{\partial \rho}{\partial x}\,dz' \qquad \text{9-18}$$

By substituting Eq. 9-14 into his 2-D model, Lentz (2008) found a relationship between the depth averaged velocity v_{da} and water depth h:

$$v_{da} = -1.8 - 0.07h \quad \left[\text{cm s}^{-1}\right]$$ 9-19

that compared well to observations in the MAB in water depths above 30 m (below this, his model is not valid).

Here, the general form of this relation

$$v_{da} = a + bh$$ 9-20

will be used at all water depths to derive an expression for v_{bot} (and hence τ^{by}). While this is not ideal, some relation must be set to close the equations, and it is left to a further study to find a more appropriate relation for the shallower regions.

The depth average velocity is defined as

$$v_{da} \equiv \frac{1}{h} \int_{-h}^{0} v\, dz$$

$$= \frac{1}{h} \int_{-h}^{0} (v_{bot} + v_{dv})\, dz$$ 9-21

$$= v_{bot} + \frac{1}{h} \int_{-h}^{0} v_{dv}\, dz$$

thus, after substituting Eq. 9-20 and rearranging, an expression for the bottom velocity is

$$v_{\text{bot}} = a + bh - \frac{1}{h} \int_{-h}^{0} v_{\text{dv}} \, dz = \frac{\tau^{by}}{\rho_0 r} \qquad \text{9-22}$$

Substituting this into Eq. 9-18, the across-shore sea-surface slope is eliminated, and the final expression for alongshore velocity in terms of a and b, becomes

$$v = \underbrace{a + bh - \frac{1}{h} \int_{-h}^{0} v_{\text{dv}} \, dz}_{v_{\text{bot}}} \underbrace{- \frac{g}{\rho_0 f} \int_{-h}^{z} \frac{\partial \rho}{\partial x} \, dz'}_{v_{\text{dv}}} \qquad \text{9-23}$$

<div align="center">bottom velocity   baroclinic depth-varying velocity</div>

or, in terms of the bottom stress,

$$v = \frac{\tau^{by}}{\rho_0 r} - \frac{g}{\rho_0 f} \int_{-h}^{z} \frac{\partial \rho}{\partial x} \, dz' \qquad \text{9-24}$$

The unknown is now the bottom stress, or the values a and b, if using Eq. 9-20, where

$$\tau^{by} = \rho_0 r \left(a + bh - \frac{1}{h} \int_{-h}^{0} v_{\text{dv}} \, dz \right) \qquad \text{9-25}$$

9.3.4 Across-shore Flow

A layered depth regime (as used by Csanady (1976), Janowitz and Pietrafesa (1980), Dever (1997), and Lentz (2008)) is used to solve the Ekman stress terms in the across-shore velocity of Eq. 9-13. Surface and bottom layers are assumed to be a constant depth and the stress is constant (with depth) within each layer (Figure 9-1).
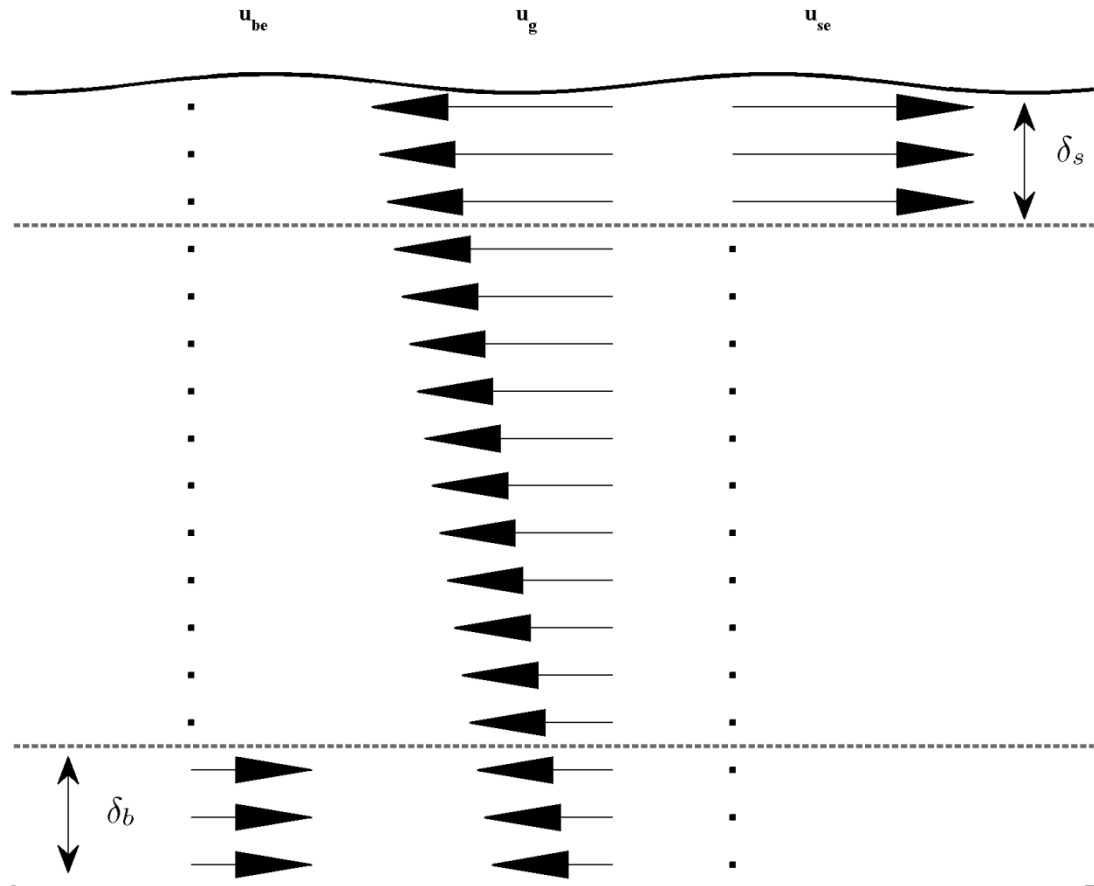
Figure 9-1: Scheme used to calculate across-shore velocity along the 85-m isobaths, comprising of a fixed surface layer of depth, δ_s , and a fixed bottom layer, δ_b. The stress-driven flows in these layers are added to the geostrophic flow which exists throughout the entire water column. The direction and relative size of the arrows are for illustrative purposes only.

Within the surface layer, the stress term is

$$\left.\frac{\partial \tau^y}{\partial z}\right|_{0 \le z \le -\delta_s} = \frac{\tau^{sy}}{\delta_s}$$

9-26

where τ^{sy} is the surface Ekman wind stress.

Similarly, within the bottom layer

$$\left.\frac{\partial \tau^y}{\partial z}\right|_{-\delta_b \le z \le -h} = \frac{\tau^{by}}{\delta_b}$$

9-27

where τ^{by} is the bottom Ekman stress.

The components of the across-shore flow are thus

$$u_g = \underbrace{-\frac{g}{f}\frac{\partial \eta}{\partial y}}_{\substack{\text{alongshore} \\ \text{sea-surface slope} \\ \text{(barotropic)}}} \underbrace{-\frac{g}{\rho_0 f}\int_z^0 \frac{\partial \rho}{\partial y}dz'}_{\substack{\text{alongshore} \\ \text{buoyancy gradient} \\ \text{(baroclinic)}}}$$

$$u_{se} = \underbrace{\frac{\tau^{sy}}{\rho_0 f \delta_s}}_{\substack{\text{alongshore} \\ \text{wind stress}}}$$

9-28

$$u_{be} = \underbrace{-\frac{\tau^{by}}{\rho_0 f \delta_b}}_{\substack{\text{alongshore} \\ \text{bottom stress}}}$$

where u_g is the across-shore geostrophic flow which acts throughout the water column, u_{se} is the across-shore surface Ekman flow in the surface layer, and u_{be} is the across-shore bottom Ekman flow in the bottom layer; and with labels indicating the forcing for each term.

Thus, the total cross-shore velocity can be summarized by the expression

$$
\left.
\begin{aligned}
u_g + u_{se} \quad & z \geq -\delta_s \\
u_g \quad & z \in (-h + \delta_b, -\delta_s) \\
u_g + u_{be} \quad & z \leq -h + \delta_b
\end{aligned}
\right\}
\qquad \text{9-29}
$$

noting that the stress term is zero in the (fully) geostrophic interior.

9.4 Transports and Volume Budget

9.4.1 Overview

The circulation in the MAB is calculated using a model which extends that of Lentz (2008) which in turn is based on the models presented by Csanady (1976), and Dever (1997). This work extends Lentz' 2-D annual-mean depth-averaged velocity model into three dimensions: varying fields are used for surface wind-stress and density gradients; it allows along-shore variation in properties; and it does not impose the "coastal condition", $\int_{-h}^{0} u \, dz = 0$, instead it allows for a non-zero cross-shore transport.

The model inputs include a 3-D density field, a 2-D surface wind stress field, river input, and solves for an along-shore sea-surface slope that varies with month and along-shore region. Volume and heat (or salt, or freshwater) budgets are used to close the model, with the additional input of air-sea heat, (or salt, or freshwater) fluxes.

9.4.2   Box Volume Budgets

The MAB shelf is divided into eight regions (hereafter referred to as *boxes*) which are bounded off-shore by the 85-m isobath (Figure 9-2). Each box extends approximately 90–100 km along the 85-m isobaths (with the exception of Box 1 which is only 51 km long), with cross-shore lines lying perpendicular to local isobaths, giving rise to curved across-shore lines. The boxes do not extend into river and bays: they are cropped in line with the local coastline. Care was taken so that rivers and estuaries each lie well within a single box.

Table 9-1: MAB box specifications.

Box	Location	Along-isobath length (km)	Surface Area (km²)	Volume (km³)
1	New England	51	9,700	415
2	Long Island	98	12,400	642
3	Hudson	91	14,800	655
4	Mid NJ	94	10,500	460
5	Delaware	93	11,900	444
6	Maryland	92	8,800	310
7	Chesapeake	95	10,100	297
8	Cape Hatteras	91	8,500	266
TOTAL	MAB	705 km	86,700	3489
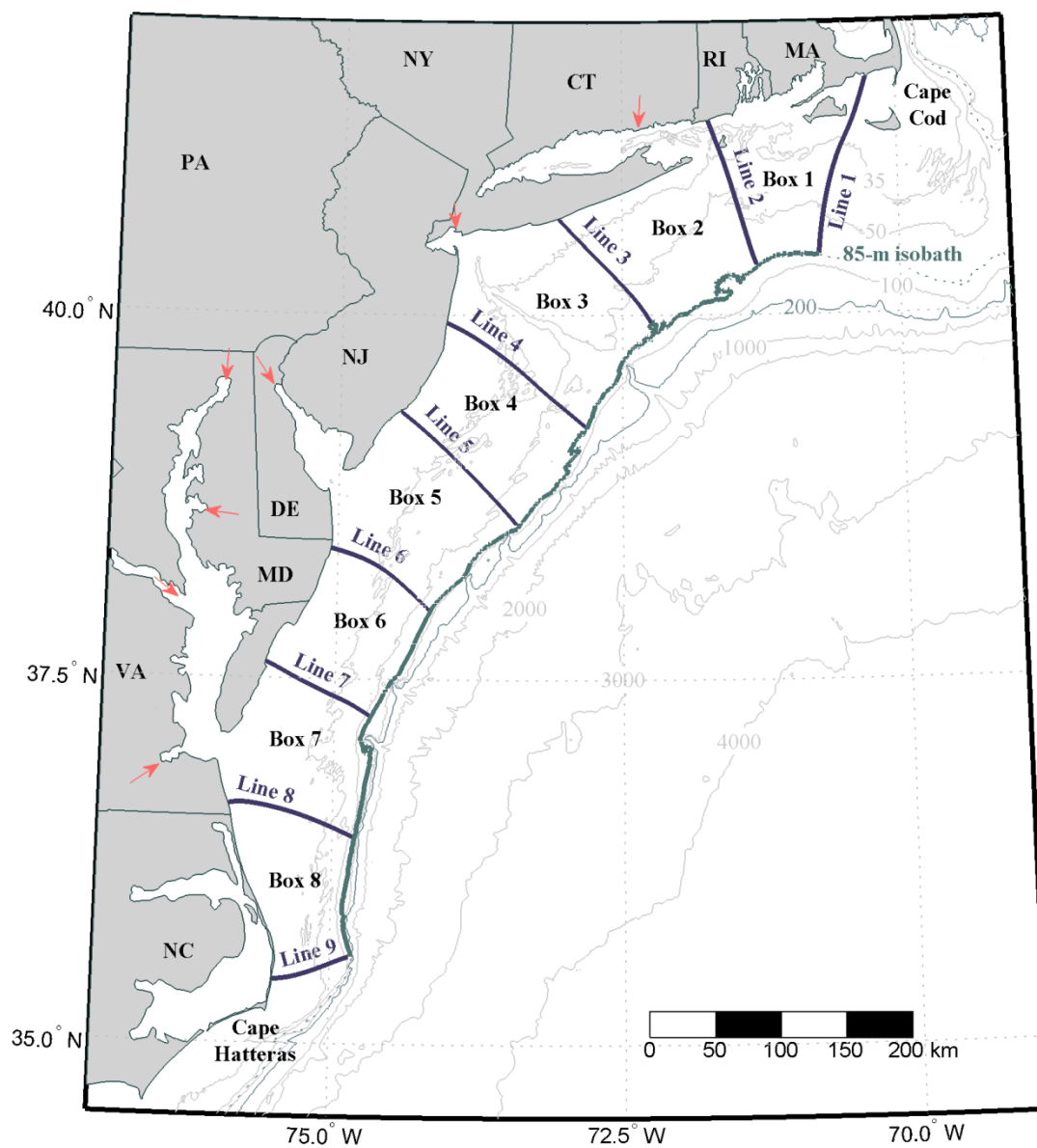
Figure 9-2: The MAB shelf "boxes" used for calculating budgets. Along-shore currents are estimated at the navy lines, and across-shore currents along the 85-m isobath (teal line). Discharge from seven major rivers in the region (red arrows) are included in the budgets.
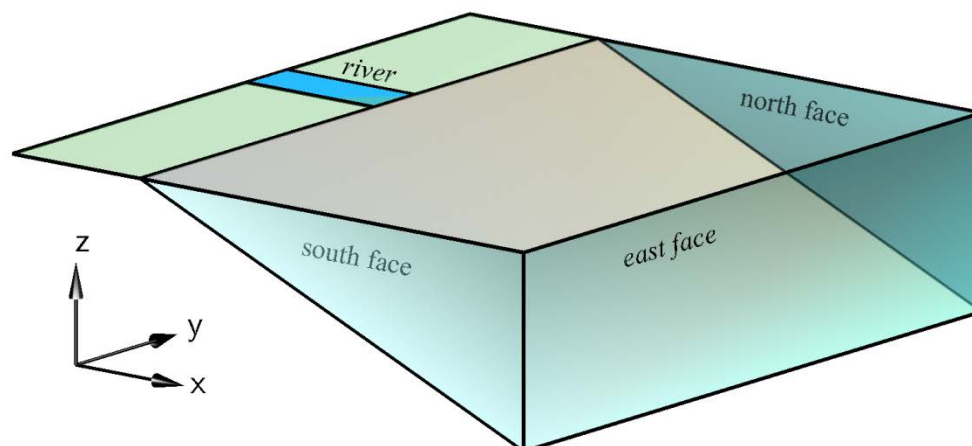
Figure 9-3: A representative MAB box used to calculate volume budgets: the east face lies along the 85-m isobath; the north and south faces lie perpendicular to local isobaths, and a river (or rivers) may flow into the box at the coastline.

Fluxes of volume, heat, salt and freshwater are calculated at the faces each box. For simplicity, the cross-shore faces of the boxes are referred to as the *north* (poleward) and *south* (equatorward) faces, and the area along the 85-m isobath is referred to as the *east* face (Figure 9-3). Air-sea fluxes are calculated through the surface, and the river input is included for the seven largest rivers in the region (see §9.8.5). The coordinate system is x: positive offshore, y: positive upshore (poleward), and z: positive upward. Transports are assumed negligible at the bottom, and along the coastline apart from at the rivers.

9.4.3 Defining Flux and Transport

The terms and symbols for *velocity*, *flux* and *transport* are not used consistently in oceanography, and thus require definition here. In this study, the across shore velocity and alongshore velocity are u and v, respectively; while the across shore and alongshore *volume* transport are U and V. The depth-integrated velocity (often also referred to as transport, or as volume transport per unit area) is not assigned a symbol, to avoid confusion. These terms and definitions are summarized in Table 9-2.

Table 9-2: Defining velocity and transports.

Flow through a …	Name	Mathematical expression	Units	Symbol (in this work)	Symbol (in literature)
point	velocity	v	m s^{-1}	u,v	u,v; U,V
line	depth-integrated velocity[a] (or transport)	$\displaystyle\int_{z_1}^{z_2} v\,dz$	m^2 s^{-1}	-	U, V; Q_x, Q_y M_x, M_y[b]; S_x, S_y
area	volume transport	$\displaystyle\int_{x_1}^{x_2}\int_{z_1}^{z_2} v\,dz\,dx$	m^3 s^{-1}	U,V	S_x, S_y; Q_x, Q_y q, T

[a] The depth-integrated velocity should not be confused with the depth-averaged, or depth-mean, velocity: $\bar{v} = \left(\int_{z_1}^{z_2} v\,dz\right)\big/\left(z_2 - z_1\right)$

[b] M_x, M_y are also (and more commonly) used to symbolize *mass* transport: $\int_{z_1}^{z_2} \rho\,v\,dz$

A flux q is defined as the amount of a substance that passes through a cross-section, per unit area and per time. The *amount* of the substance is usually taken as its mass, so for water, the mass flux q_m has units of kilograms, and the units of the mass flux of water are kilograms per meters squared per second (kg m^{-2} s^{-1}). This is calculated by multiplying the velocity times the concentration of the substance (where the concentration is the amount per unit volume):

$$q_m = \rho v \quad \left[\frac{\text{kg}}{\text{m}^3}\frac{\text{m}}{\text{s}}\right] = \left[\text{kg m}^{-2}\text{ s}^{-1}\right] \qquad 9\text{-}30$$

where the square brackets indicate the units of the expression.

The transport of a substance is the total flux of the substance through a cross-section, (i.e. the flux is the transport per unit area). Units of transport are the amount of the substance per second, e.g.

$$\oint q_m \, dA = \oint \rho v \, dA \quad \left[\frac{\text{kg}}{\text{m}^3}\frac{\text{m}}{\text{s}}\text{m}^2\right] = \left[\text{kg s}^{-1}\right] \qquad 9\text{-}31$$

The *process* described by flux and transport, that is of a substance being passively moved by the flow, is termed "advection".

Confusion may arise due to the multiple usages of the term transport: it is commonly used to refer to the depth-integrated velocity (transport per unit length), as well as for volume transport. The definitions used in this work are given in Table 9-3.

Table 9-3: Defining flux and transport.

Variable	Mass		Heat		Salt	
	Expression	Unit	Expression	Unit	Expression	Unit
Concen-tration	ρ	kg m^{-3}	$\rho C_p T$	J m^{-3}	ρS	kg m^{-3}
Content	$\iiint\limits_{vol} \rho\, dx dy dz$	kg	$\iiint\limits_{vol} \rho C_p T\, dx dy dz$	J	$\iiint\limits_{vol} \rho S\, dx dy dz$	kg
Flux	ρv	kg m^{-2} s^{-1}	$\rho C_P T v$	J m^{-2} s^{-1} (W m^{-2})	$\rho S v$	kg m^{-2} s^{-1}
Transport	$\oiint\limits_{\substack{cross-\\section}} \rho v\, dx dz$	kg s^{-1}	$\oiint\limits_{\substack{cross-\\section}} \rho C_p T v dx dz$	J s^{-1} (W)	$\oiint\limits_{\substack{cross-\\section}} \rho S v dx dz$	kg s^{-1}

9.4.4 Calculating Volume Transport

The velocity equations can be simplified by setting the buoyancy terms to

$$B_y = \frac{g}{\rho_0} \int\limits_z^0 \frac{\partial \rho}{\partial y} dz', \quad R_x = \frac{g}{\rho_0} \int\limits_{-h}^z \frac{\partial \rho}{\partial x} dz' \qquad \text{9-32}$$

where B_y is the full alongshore-shore baroclinic term, and R_x is the across-shore baroclinic term *minus* the baroclinic bottom velocity (and hence the different limits of the integral).

The cross-shore volume transport is calculated by integrating the total velocity over each face:

$$U = -\int_{y_S}^{y_N}\int_{-h}^{0}\frac{g}{f}\frac{\partial\eta}{\partial y}\,dz\,dy - \int_{y_S}^{y_N}\int_{-h}^{0}\frac{B_y}{f}\,dz\,dy$$

$$+\int_{y_S}^{y_N}\int_{-\delta_s}^{0}\frac{\tau^{sy}}{\rho_0 f \delta_s}\,dz\,dy - \int_{y_S}^{y_N}\int_{-h}^{-h+\delta_b}\frac{\tau^{by}}{\rho_0 f \delta_b}\,dz\,dy$$

$$= -\frac{gh_E\Delta y}{f}\frac{\partial\eta}{\partial y} - \frac{1}{f}\int_{y_S}^{y_N}\int_{-h}^{0}B_y\,dz\,dy + \frac{1}{\rho_0 f}\int_{y_S}^{y_N}\tau^{sy}\,dy - \frac{1}{\rho_0 f}\int_{y_S}^{y_N}\tau^{by}\,dy$$

<div align="right">9-33</div>

Similarly, the alongshore volume transport is given by

$$V = \int_{0}^{x_E}\int_{-h}^{0}\frac{\tau^{by}}{\rho_0 r}\,dz\,dx - \int_{0}^{x_E}\int_{-h}^{0}\frac{R_x}{f}\,dz\,dx$$

$$= \frac{1}{\rho_0 r}\int_{0}^{x_E}\tau^{by}h\,dx - \frac{1}{f}\int_{0}^{x_E}\int_{-h}^{0}R_x\,dz\,dx$$

<div align="right">9-34</div>

where y_S and y_N refer to the southern and northern y coordinates of each box, x_E is the offshore coordinate of the east face (i.e. along the 85-m isobath); h is the varying water depth along the cross-shore faces; h_E is the fixed depth of 85 m along the east face; $\delta_b = \delta_s = 15$ m is the depth of the surface and bottom Ekman layers; and Δy is the length along the 85-m isobath on the eastern face of the box.

9.4.5   Closing the Volume Budget

The conservation of volume (via the continuity equation) implies that the volume transport through the faces of a closed volume must equal zero. Assuming no flow through the sea-floor and negligible flow at the surface (since (*E–P*) is typically very small: see §9.8.8), the flow into any box through the south face, plus river discharge, must equal (given our coordinate frame) the flow through the north and east faces:

$$V_S + V_R - V_N - U = 0$$
$$\left(V_{\text{bot}\langle S\rangle} + V_{\text{dv}\langle S\rangle}\right) + V_R - \left(V_{\text{bot}\langle N\rangle} + V_{\text{dv}\langle N\rangle}\right) - \left(U_{\text{se}} + U_{\text{be}} + U_{\text{bt}} + U_{\text{bc}}\right) = 0 \qquad 9\text{-}35$$
$$V_{\text{bot}\langle S\rangle} + V_{\text{dv}\langle S\rangle} + V_R - V_{\text{bot}\langle N\rangle} - V_{\text{dv}\langle N\rangle} - U_{\text{se}} - U_{\text{be}} - U_{\text{bt}} - U_{\text{bc}} = 0$$

where the subscripts $\langle S\rangle$ and $\langle N\rangle$ refer to the southern and northern faces, respectively, and symbols are defined in Table 9-4.

The unknown variables in this budget are the constants *a* and *b* from the expression containing τ^{by} (Eq. 9-25), and the sea surface slope $\partial\eta/\partial y$, which is assumed to be constant for each box. The unknown constant *b* is given a set value, leaving two unknown values: *a* and $\partial\eta/\partial y$. To solve for two unknowns, two equations are needed: first the volume budget will be used to find an expression for $\partial\eta/\partial y$ in terms of *a* and *b*, and then the heat (or salt, or freshwater) budget will be used to solve for *a*.

In summary: starting with the northern-most box (Box 1), each individual term in the volume budget (Eq. 9-35) is calculated, then manipulated to obtain an expression

for the sea-surface slope in terms of the bottom stress (and hence a and b). For subsequent boxes, the terms for the northern volume transport are taken from the results of the previous box's values. Thus, while b is held constant for all boxes, and $\partial\eta/\partial y$ will be constant for each box, a will not be constant for the entire box, except for the first: a different value of a will be found (and used to calculate τ^{by}) for the south and east lines, from that found for the northern line in the previous calculation.

Table 9-4: Summary of alongshore and across-shore velocity and transport terms.

Axis	Term	Velocity (m s⁻¹)		Volume Transport (m³ s⁻¹)	
		Symbol	Equation	Symbol	Equation
y	Along-shore sea-level slope	u_{bt}	$-\dfrac{g}{f}\dfrac{\partial\eta}{\partial y}$	U_{bt}	$-\dfrac{gh_E\Delta y}{f}\dfrac{\partial\eta}{\partial y}$
	Alongshore density gradient	u_{bc}	$-\dfrac{B_y}{f}$	U_{bc}	$-\dfrac{1}{f}\displaystyle\int_{y_S}^{y_N}\int_{-h}^{0}B_y\,dz\,dy$
	Surface Ekman	u_{se}	$+\dfrac{\tau^{sy}}{\rho_0 f\delta_s}$	U_{se}	$+\dfrac{1}{\rho_0 f}\displaystyle\int_{y_S}^{y_N}\tau^{sy}\,dy$
	Bottom Ekman	u_{be}	$-\dfrac{\tau^{by}}{\rho_0 f\delta_b}$	U_{be}	$-\dfrac{1}{\rho_0 f}\displaystyle\int_{y_S}^{y_N}\tau^{by}\,dy$
x	Bottom	v_{bot}	$+\dfrac{\tau^{by}}{\rho_0 r}$	V_{bot}	$+\dfrac{1}{\rho_0 r}\displaystyle\int_{0}^{x_E}\tau^{by}h\,dx$
	Depth-Varying	v_{dv}	$-\dfrac{R_x}{f}$	V_{dv}	$-\dfrac{1}{f}\displaystyle\int_{0}^{x_E}\int_{-h}^{0}R_x\,dz\,dx$

9.4.6 Solution for Box 1

The volume budget for Box 1 is

$$V_{\text{bot}\langle S\rangle} - V_{\text{bot}\langle N\rangle} - U_{\text{be}} - U_{\text{bt}} = V_{\text{dv}\langle N\rangle} - V_{\text{dv}\langle S\rangle} - V_R + U_{\text{se}} + U_{\text{bc}}$$

9-36

Those terms that contain τ^{by} or $\partial\eta/\partial y$ are written out in full:

$$\int_0^{x_{E\langle S\rangle}} \frac{\tau^{by}}{\rho_0 r} h_S \, dx - \int_0^{x_{E\langle N\rangle}} \frac{\tau^{by}}{\rho_0 r} h_N \, dx + \int_{y_S}^{y_N} \frac{\tau^{by}}{\rho_0 f} dy + \frac{g h_E \Delta y}{f} \frac{\partial\eta}{\partial y}$$

$$= V_{\text{dv}\langle N\rangle} - V_{\text{dv}\langle S\rangle} - V_R + U_{\text{se}} + U_{\text{bc}}$$

9-37

and then using Eq. 9-22:

$$\int_0^{x_{E\langle S\rangle}} \left(a + b h_S - \frac{1}{h_S} \int_{-h}^0 v_{\text{dv}\langle S\rangle} \, dz \right) h_S \, dx - \int_0^{x_{E\langle N\rangle}} \left(a + b h_N - \frac{1}{h_N} \int_{-h}^0 v_{\text{dv}\langle N\rangle} \, dz \right) h_N \, dx$$

$$+ \frac{1}{f} \int_{y_S}^{y_N} \left(ra + rbh_E - \frac{r}{h_E} \int_{-h}^0 v_{\text{dv}\langle E\rangle} \, dz \right) dy + \frac{g h_E \Delta y}{f} \frac{\partial\eta}{\partial y}$$

$$= V_{\text{dv}\langle N\rangle} - V_{\text{dv}\langle S\rangle} - V_R + U_{\text{se}} + U_{\text{bc}}$$

9-38

noting that $\int_{-h}^0 v_{\text{dv}\langle E\rangle} \, dz$ cannot be calculated exactly, since v_{dv} is only calculated at the cross-shore lines (i.e. at only each end of the eastern face). It is therefore estimated by averaging those two values, and that estimate is thus a constant:

$$\int_{-h}^0 v_{\text{dv}\langle E\rangle} \, dz \cong \frac{1}{2} \left(\int_{-h}^0 v_{\text{dv}\langle EN\rangle} \, dz + \int_{-h}^0 v_{\text{dv}\langle ES\rangle} \, dz \right) = \varepsilon$$

9-39

Rearranging, and grouping terms that contain a and b:

$$a\left(\int_0^{x_{E\langle S\rangle}} h_S\, dx - \int_0^{x_{E\langle N\rangle}} h_N\, dx + \frac{r\Delta y}{f}\right) + b\left(\int_0^{x_{E\langle S\rangle}} h_S{}^2 dx - \int_0^{x_{E\langle N\rangle}} h_N{}^2 dx + \frac{rh_E\Delta y}{f}\right)$$

$$-\frac{r\varepsilon\Delta y}{f\,h_E} + \frac{gh_E\Delta y}{f}\frac{\partial\eta}{\partial y} - V_{dv\langle S\rangle} + V_{dv\langle N\rangle} = V_{dv\langle N\rangle} - V_{dv\langle S\rangle} - V_R + U_{se} + U_{bc}$$

9-40

noting that the alongshore transport terms cancel out. Finally, solving for the sea-surface slope, the result is

$$\frac{\partial\eta}{\partial y}\bigg|_{\text{Box 1}} = \frac{U_{se} + U_{bc} - V_R + \dfrac{r\varepsilon\Delta y}{f\,h_E} + a\zeta_1 + b\zeta_2}{\dfrac{gh_E\Delta y}{f}}$$

9-41

where

$$\zeta_1 = \int_0^{x_{E\langle N\rangle}} h_N\, dx - \int_0^{x_{E\langle S\rangle}} h_S\, dx - \frac{r\Delta y}{f}$$

9-42

$$\zeta_2 = \int_0^{x_{E\langle N\rangle}} h_N{}^2 dx - \int_0^{x_{E\langle S\rangle}} h_S{}^2 dx - \frac{rh_E\Delta y}{f}$$

9.4.7   Solution for the Southern Boxes

The volume budget for additional boxes (to the south) is evaluated after the final result for Box 1 is found (e.g. by applying the heat budget; §9.5). Thus, with the set value b, calculated values a and $\partial\eta/\partial y$, all components of the velocity and transport (Table 9-4) can be calculated. The V_S of Box 1 is, of course, the V_N of Box 2, and so on.

Thus for all boxes south of Box 1, the volume budget can be expressed as:

$$V_{\text{bot}\langle S\rangle} - U_{\text{be}} - U_{\text{bt}} = V_N - V_{\text{dv}\langle S\rangle} - V_R + U_{\text{se}} + U_{\text{bc}} \qquad 9\text{-}43$$

since V_N is now a known quantity.

In this case, the expression for the sea surface slope (after following the same steps as above) becomes

$$\left.\frac{\partial \eta}{\partial y}\right|_{\text{Box 2+}} = \frac{U_{\text{se}} + U_{\text{bc}} + V_N - V_R + \dfrac{r\varepsilon\Delta y}{f\,h_E} + a\zeta_3 + b\zeta_4}{\dfrac{gh_E\Delta y}{f}} \qquad 9\text{-}44$$

where

$$\zeta_3 = -\int_0^{x_{E\langle S\rangle}} h_S\,dx - \frac{r\Delta y}{f}$$

$$\zeta_4 = -\int_0^{x_{E\langle N\rangle}} h_S{}^2\,dx - \frac{rh_E\Delta y}{f}$$

$$9\text{-}45$$

9.5   Heat Budget

9.5.1   Overview

The heat budget is applied to each box, for each month: the rate of change of heat content in the box is balanced by the air-sea heat exchange through the surface and the advective heat transport through the north, south and east faces, plus any river input (Figure 9-4).
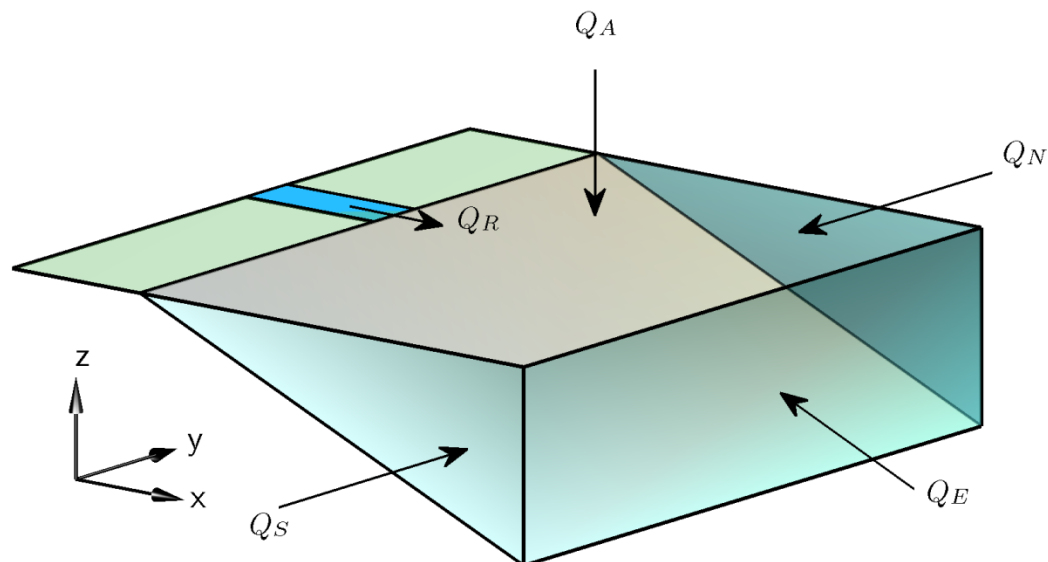
Figure 9-4: Direction of heat flux into a MAB "box". Q_A is the air-sea flux, Q_R is river input, and the subscripts N, S and E refer to advection through the "north", "south", and "east" faces of the box, respectively. The coordinate system is positive to the north (poleward), east (offshore) and upward.

The variable being used in this study for 'heat" is potential enthalpy (see §9.2) which has units of Joules per unit mass (J kg⁻¹). For conservation under a Boussinesq system of equations, the potential enthalpy is divided by density to give a measure of heat content per unit volume instead:

$$\frac{h^0}{\rho} = C_p^0 \rho \Theta \quad \left[\text{J m}^{-3}\right]$$

9-46

The heat balance for any box is then

$$\underbrace{\iiint_{vol} C_p^0 \frac{d(\rho\Theta)}{dt} dV}_{\substack{\text{rate of change of} \\ \text{heat content}}} = \underbrace{\oiint Q_A\, dA}_{\substack{\text{air-sea} \\ \text{heat transport}}} + \underbrace{\oiint \rho C_p^0 \Theta v\, dA}_{\substack{\text{advective} \\ \text{heat transport}}}$$

9-47

where terms have units of Joules per second (J s^{-1} or Watts, W). That is, the rate of change of heat content is the sum of the air-sea heat transport and the advective heat transport.

A monthly mean heat budget is approximated by

$$\underbrace{\frac{1}{\Delta t}\iiint_{vol}\rho\, C_p^0\Theta\, dV}_{\substack{\text{rate of change of}\\\text{heat content}}} = \underbrace{\oiint Q_A\, dA}_{\substack{\text{air-sea}\\\text{heat transport}}} + \underbrace{\oiint \rho\, C_p^0\Theta\, v\, dA}_{\substack{\text{advective}\\\text{heat transport}}}$$

9-48

where Δt is the number of seconds in one month.

Multiplying Eq. 9-48 by Δt leads to an equation for the change in heat content of a box over one month (now in units of Joules, J):

$$\underbrace{\iiint_{vol}\Delta(\rho\Theta)\, C_p^0\, dV}_{\substack{\text{change in}\\\text{heat content}}} = \underbrace{\Delta t\oiint Q_A\, dA}_{\substack{\text{heat change due to}\\\text{air-sea exchange}}} + \underbrace{\Delta t\oiint \rho\, C_p^0\Theta\, v\, dA}_{\substack{\text{heat change due to}\\\text{advection}}}$$

9-49

Breaking up the advection term into its components:

$$\underbrace{\iiint\Delta(\rho\Theta)\, C_p^0\, dV}_{\substack{\text{box}\\\text{heat content (H}_C)}} = \underbrace{\Delta t\oiint Q_A\, dA}_{\substack{\text{surface}\\\text{air-sea exchange (H}_A)}} + \underbrace{\Delta t\, C_p^0\rho_R\Theta_R V_R}_{\text{advection from rivers (H}_R)}$$

$$+\ \underbrace{\Delta t\, C_p^0\oiint \rho_S\Theta_S v_S\, dA}_{\substack{\text{south face}\\\text{advection through south face}}} -\ \underbrace{\Delta t\, C_p^0\oiint \rho_N\Theta_N v_N\, dA}_{\substack{\text{north face}\\\text{advection through north face}}}$$

9-50

$$-\ \underbrace{\Delta t\, C_p^0\oiint \rho_E\Theta_E u\, dA}_{\substack{\text{east face}\\\text{advection through east face}}}$$

A positive heat content change indicates an increase in heat in the box; Q_A is positive downward (i.e. also indicating an increase in heat in the box), and the signs of the advection terms depend on the choice of coordination system: here the river flow and flow through the south face are positive into the box, while flow through the north and east faces is negative.

Dividing Eq. 9-50 through by the constant values of Δt and $C_p^{\,0}$ leads to

$$\underbrace{\oiint_{\substack{\text{south}\\\text{face}}} \rho_S \Theta_S v_S \, dA}_{q_S} - \underbrace{\oiint_{\substack{\text{north}\\\text{face}}} \rho_N \Theta_N v_N \, dA}_{q_N} - \underbrace{\oiint_{\substack{\text{east}\\\text{face}}} \rho_E \Theta_E u \, dA}_{q_E} = \frac{H_C - H_A - H_R}{\Delta t \, C_p^{\,0}}$$

9-51

The velocity in each of the advection terms on the lhs are expanded out into their component parts, and terms containing $\partial\eta/\partial y$ or τ^{by} are written out in full. For the south face,

$$q_S = \oiint_{\substack{\text{south}\\\text{face}}} \rho_S \Theta_S v_S \, dA$$

$$= \int_0^{x_{E\langle S\rangle}} \int_{-h}^{0} \rho_S \Theta_S v_S \, dz \, dx$$

$$= \int_0^{x_{E\langle S\rangle}} \int_{-h}^{0} \rho_S \Theta_S \left(\frac{\tau^{by}}{\rho_0 r} + v_{dv\langle S\rangle} \right) dz \, dx$$

9-52

$$= \int_0^{x_{E\langle S\rangle}} \frac{\tau^{by}}{\rho_0 r} \int_{-h}^{0} \rho_S \Theta_S \, dz \, dx + \int_0^{x_{E\langle S\rangle}} \int_{-h}^{0} \rho_S \Theta_S v_{dv\langle S\rangle} \, dz \, dx$$

and similarly for the north face,

$$q_{\mathrm{N}} = \oiint_{\substack{\text{north}\\\text{face}}} \rho_{\mathrm{N}} \Theta_{\mathrm{N}} v_{\mathrm{N}} \, dA$$

$$\vdots$$

$$= \int_0^{x_{E\langle N\rangle}} \frac{\tau^{by}}{\rho_0 r} \int_{-h}^0 \rho_{\mathrm{N}} \Theta_{\mathrm{N}} \, dz \, dx \;+\; \int_0^{x_{E\langle N\rangle}} \int_{-h}^0 \rho_{\mathrm{N}} \Theta_{\mathrm{N}} v_{dv\langle \mathrm{N}\rangle} \, dz \, dx \qquad \text{9-53}$$

At the east face,

$$q_{\mathrm{E}} = \oiint_{\substack{\text{east}\\\text{face}}} \rho_{\mathrm{E}} \Theta_{\mathrm{E}} u \, dA$$

$$= \int_{y_S}^{y_N} \int_{-h}^0 \rho_{\mathrm{E}} \Theta_{\mathrm{E}} u \, dz \, dy$$

$$= \int_{y_S}^{y_N} \int_{-h}^0 \rho_{\mathrm{E}} \Theta_{\mathrm{E}} u_{bt} \, dz \, dy + \int_{y_S}^{y_N} \int_{-h}^0 \rho_{\mathrm{E}} \Theta_{\mathrm{E}} u_{bc} \, dz \, dy + \int_{y_S}^{y_N} \int_{-\delta_s}^0 \rho_{\mathrm{E}} \Theta_{\mathrm{E}} u_{se} \, dz \, dy$$

$$+ \int_{y_S}^{y_N} \int_{-h}^{-h+\delta_b} \rho_{\mathrm{E}} \Theta_{\mathrm{E}} u_{be} \, dz \, dy$$

$$= -\frac{g}{f} \frac{\partial \eta}{\partial y} \int_{y_S}^{y_N} \int_{-h}^0 \rho_{\mathrm{E}} \Theta_{\mathrm{E}} \, dz \, dy \;+\; \int_{y_S}^{y_N} \int_{-h}^0 \rho_{\mathrm{E}} \Theta_{\mathrm{E}} u_{bc} \, dz \, dy$$

$$+ \int_{y_S}^{y_N} \int_{-\delta_s}^0 \rho_{\mathrm{E}} \Theta_{\mathrm{E}} u_{se} \, dz \, dy - \frac{\tau^{by}}{\rho_0 f \delta_b} \int_{y_S}^{y_N} \int_{-h}^0 \rho_{\mathrm{E}} \Theta_{\mathrm{E}} \, dz \, dy$$

$$= -\frac{g}{f} \frac{\partial \eta}{\partial y} \int_{y_S}^{y_N} \int_{-h}^0 \rho_{\mathrm{E}} \Theta_{\mathrm{E}} \, dz \, dy - \frac{\tau^{by}}{\rho_0 f \delta_b} \int_{y_S}^{y_N} \int_{-h}^{-h+\delta_b} \rho_{\mathrm{E}} \Theta_{\mathrm{E}} \, dz \, dy$$

$$+ \int_{y_S}^{y_N} \int_{-h}^0 \rho_{\mathrm{E}} \Theta_{\mathrm{E}} u_{bc} \, dz \, dy + \int_{y_S}^{y_N} u_{se} \int_{-\delta_s}^0 \rho_{\mathrm{E}} \Theta_{\mathrm{E}} \, dz \, dy$$

9-54

Note that τ^{by} is a constant along the east face, and so can be taken out from under

the integral in Eq. 9-54. This is true from Eq. 9-22, as both height, $h = h_E$ (= 85 m),

and the estimated $\int_{-h}^0 v_{dvE} \, dz \, (\cong \varepsilon)$, are constant along the east face.

9.5.2 Solution for Box 1

After substituting in each of the advective face terms from Eqs. 9-52–9-54, Eq. 9-51 becomes

$$
\int_0^{x_{E\langle S\rangle}} \frac{\tau^{by}}{\rho_0 r} \int_{-h}^0 \rho_S \Theta_S \, dz \, dx + \int_0^{x_{E\langle S\rangle}} \int_{-h}^0 \rho_S \Theta_S v_{dv\langle S\rangle} \, dz \, dx - \int_0^{x_{E\langle N\rangle}} \frac{\tau^{by}}{\rho_0 r} \int_{-h}^0 \rho_N \Theta_N \, dz \, dx
$$

$$
- \int_0^{x_{E\langle N\rangle}} \int_{-h}^0 \rho_N \Theta_N v_{dv\langle N\rangle} \, dz \, dx + \frac{g}{f} \frac{\partial \eta}{\partial y} \int_{y_S}^{y_N} \int_{-h}^0 \rho_E \Theta_E \, dz \, dy
$$

$$
+ \frac{\tau^{by}}{\rho_0 f \delta_b} \int_{y_S}^{y_N} \int_{-h}^{-h+\delta_b} \rho_E \Theta_E \, dz \, dy - \int_{y_S}^{y_N} \int_{-h}^0 \rho_E \Theta_E u_{bc} \, dz \, dy
$$

$$
- \int_{y_S}^{y_N} u_{se} \int_{-\delta_s}^0 \rho_E \Theta_E \, dz \, dy = \frac{H_C - H_A - H_R}{\Delta t \, C_p^0}
$$

9-55

To simplify further derivations, the following expressions are defined:

$$
\Psi_{dvN} = \int_0^{x_{E\langle N\rangle}} \int_{-h}^0 \rho_N \Theta_N v_{dv\langle N\rangle} dz \, dx, \qquad \Psi_{dvS} = \int_0^{x_{E\langle S\rangle}} \int_{-h}^0 \rho_S \Theta_S v_{dv\langle S\rangle} \, dz \, dx
$$

$$
\Psi_{ubc} = \int_{y_S}^{y_N} \int_{-h}^0 \rho_E \Theta_E u_{bc} dz \, dy \qquad \Psi_{use} = \int_{y_S}^{y_N} u_{se} \int_{-\delta_s}^0 \rho_E \Theta_E \, dz \, dy
$$

$$
\Upsilon_E = \int_{y_S}^{y_N} \int_{-h}^0 \rho_E \Theta_E \, dz \, dy, \qquad \Upsilon_{Eb} = \int_{y_S}^{y_N} \int_{-h}^{-h+\delta_b} \rho_E \Theta_E \, dz \, dy
$$

$$
\gamma_S = \int_{-h}^0 \rho_S \Theta_S \, dz \,, \qquad \gamma_N = \int_{-h}^0 \rho_N \Theta_N dz
$$

9-56

thus Eq. 9-55 can be re-written as

$$
\int_0^{x_{E\langle S\rangle}} \frac{\tau^{by}}{\rho_0 r} \gamma_S \, dx + \Psi_{vdv\langle S\rangle} - \int_0^{x_{E\langle N\rangle}} \frac{\tau^{by}}{\rho_0 r} \gamma_N \, dx - \Psi_{vdv\langle N\rangle} + \frac{g}{f} \frac{\partial \eta}{\partial y} \Upsilon_E
$$

$$
+ \frac{\tau^{by}}{\rho_0 f \delta_b} \Upsilon_{Eb} - \Psi_{ubc} - \Psi_{use} = \frac{H_C - H_A - H_R}{\Delta t \, C_p^0}
$$

9-57

Rearranging to place terms containing the unknown values τ^{by} and $\partial\eta/\partial y$ on the lhs,

$$
\int_0^{x_{E\langle S\rangle}} \frac{\tau^{by}}{\rho_0 r}\gamma_S dx - \int_0^{x_{E\langle N\rangle}} \frac{\tau^{by}}{\rho_0 r}\gamma_N dx + \frac{g}{f}\frac{\partial\eta}{\partial y}\Upsilon_E + \frac{\tau^{by}}{\rho_0 f \delta_b}\Upsilon_{Eb}
$$

$$
= \frac{H_C - H_A - H_R}{\Delta t\; C_p^0} + \Psi_{vdv\langle N\rangle} - \Psi_{vdv\langle S\rangle} + \Psi_{ubc} + \Psi_{use}
$$

9-58

Next, a temporary value is assigned to simplify further manipulation, with the rhs being set to

$$
\Re = \frac{H_C - H_A - H_R}{\Delta t\; C_p^0} + \Psi_{vdv\langle N\rangle} - \Psi_{vdv\langle S\rangle} + \Psi_{ubc} + \Psi_{use}
$$

9-59

The bottom stress relation (Eq. 9-22) is now inserted:

$$
\int_0^{x_{E\langle S\rangle}}\left(a + bh_S - \frac{1}{h_S}\int_{-h}^0 v_{dv\langle S\rangle}dz \right)\gamma_S dx
$$

$$
- \int_0^{x_{E\langle N\rangle}}\left(a + bh_N - \frac{1}{h_N}\int_{-h}^0 v_{dv\langle N\rangle}dz \right)\gamma_N dx
$$

$$
+ \frac{\left(ra + rbh_E - \dfrac{\varepsilon r}{h_E} \right)\Upsilon_{Eb}}{f\delta_b} + \frac{g}{f}\frac{\partial\eta}{\partial y}\Upsilon_E = \Re
$$

9-60

$$
a\int_0^{x_{E\langle S\rangle}}\gamma_S\, dx + b\int_0^{x_{E\langle S\rangle}} h_S\gamma_S\, dx - \int_0^{x_{E\langle S\rangle}}\left(\frac{\gamma_S}{h_S}\int_{-h}^0 v_{dv\langle S\rangle}dz \right)dx - a\int_0^{x_{E\langle N\rangle}}\gamma_N\, dx
$$

$$
- b\int_0^{x_{E\langle N\rangle}} h_N\gamma_N\, dx + \int_0^{x_{E\langle N\rangle}}\left(\frac{\gamma_N}{h_N}\int_{-h}^0 v_{dv\langle N\rangle}dz \right)dx + \frac{ra\Upsilon_{Eb}}{f\delta_b} + \frac{rbh_E\Upsilon_{Eb}}{f\delta_b} - \frac{r\varepsilon\Upsilon_{Eb}}{h_E f\delta_b}
$$

$$
+ \frac{g}{f}\frac{\partial\eta}{\partial y}\Upsilon_E = \Re
$$

and the following expressions are set:

$$\Upsilon_S = \int_0^{x_{E\langle S\rangle}} \gamma_S \, dx \left(= \int_0^{x_{E\langle S\rangle}} \int_{-h}^0 \rho_S \Theta_S \, dz \, dx \right), \quad \Upsilon_N = \int_0^{x_{E\langle N\rangle}} \gamma_N \, dx \left(= \int_0^{x_{E\langle N\rangle}} \int_{-h}^0 \rho_N \Theta_N \, dz \, dx \right)$$

$$\chi_S = \int_0^{x_{E\langle S\rangle}} h_S \gamma_S \, dx, \qquad\qquad \chi_N = \int_0^{x_{E\langle N\rangle}} h_N \gamma_N \, dx \qquad\qquad \text{9-61}$$

$$\Gamma_S = \int_0^{x_{E\langle S\rangle}} \left(\frac{\gamma_S}{h_S} \int_{-h}^0 v_{dv\langle S\rangle} \, dz \right) dx, \qquad \Gamma_N = -\int_0^{x_{E\langle N\rangle}} \left(\frac{\gamma_N}{h_N} \int_{-h}^0 v_{dv\langle N\rangle} \, dz \right) dx$$

Thus Eq. 9-60 can be re-written as

$$a\Upsilon_S + b\chi_S - \Gamma_S - a\Upsilon_N - b\chi_N + \Gamma_N \; + \frac{ra\Upsilon_{Eb}}{f\delta_b} + \frac{rbh_E \Upsilon_{Eb}}{f\delta_b} - \frac{r\varepsilon\Upsilon_{Eb}}{h_E f\delta_b}$$

$$+ \frac{g}{f}\frac{\partial\eta}{\partial y}\,\Upsilon_E = \Re \qquad\qquad \text{9-62}$$

Once again, the equation is rearranged so that terms containing the unknown

values (now a, b and $\partial\eta/\partial y$) are on the lhs:

$$a\left(\Upsilon_S - \Upsilon_N + \frac{r\Upsilon_{Eb}}{f\delta_b} \right) + b\left(\chi_S - \chi_N + \frac{rh_E \Upsilon_{Eb}}{f\delta_b} \right) + \frac{g}{f}\frac{\partial\eta}{\partial y}\,\Upsilon_E$$

$$= \Gamma_S - \Gamma_N + \frac{r\varepsilon\Upsilon_{Eb}}{h_E f\delta_b} + \Re \qquad\qquad \text{9-63}$$

and once again, the rhs is assigned to a temporary variable:

$$\Re_2 = \Gamma_S - \Gamma_N + \frac{r\varepsilon\Upsilon_{Eb}}{h_E f\delta_b} + \Re$$

$$= \Gamma_S - \Gamma_N + \frac{r\varepsilon\Upsilon_{Eb}}{h_E f\delta_b} + \frac{H_C - H_A - H_R}{\Delta t\, C_p^0} + \Psi_{vdv\langle N\rangle} - \Psi_{vdv\langle S\rangle} + \Psi_{ubc} + \Psi_{use} \qquad\qquad \text{9-64}$$

so that Eq. 9-63 can be rewritten as

$$a\left(\Upsilon_S - \Upsilon_N + \frac{r\Upsilon_{EB}}{f\delta_b}\right) + b\left(\chi_S - \chi_N + \frac{rh_E\Upsilon_{EB}}{f\delta_b}\right) + \frac{g}{f}\frac{\partial\eta}{\partial y}\Upsilon_E = \Re_2 \qquad 9\text{-}65$$

The expression for the sea-surface slope (Eq. 9-41) from the volume budget is now

substituted in, with the third term on the lhs becoming

$$\frac{g}{f}\frac{\partial\eta}{\partial y}\Upsilon_E = \frac{\Upsilon_E}{h_E\Delta y}\left(U_{se} + U_{bc} - V_R + \frac{r\varepsilon\Delta y}{fh_E} + a\zeta_1 + b\zeta_2\right)$$

$$= \frac{\Upsilon_E}{h_E\Delta y}\left(U_{se} + U_{bc} - V_R + \frac{r\varepsilon\Delta y}{fh_E}\right) + a\frac{\Upsilon_E\zeta_1}{h_E\Delta y} + b\frac{\Upsilon_E\zeta_2}{h_E\Delta y} \qquad 9\text{-}66$$

thus Eq. 9-65 becomes

$$a\left(\Upsilon_S - \Upsilon_N + \frac{r\Upsilon_{Eb}}{f\delta_b} + \frac{\zeta_1\Upsilon_E}{h_E\Delta y}\right) + b\left(\chi_S - \chi_N + \frac{rh_E\Upsilon_{Eb}}{f\delta_b} + \frac{\zeta_2\Upsilon_E}{h_E\Delta y}\right)$$

$$= \Re_2 - \frac{\Upsilon_E}{h_E\Delta y}\left(U_{se} + U_{bc} - V_R + \frac{r\varepsilon\Delta y}{fh_E}\right) \qquad 9\text{-}67$$

and solving for the unknown constant, a:

$$a = \frac{\Re_2 - \dfrac{\Upsilon_E}{h_E\Delta y}\left(U_{se} + U_{bc} - V_R + \dfrac{r\varepsilon\Delta y}{fh_E}\right) + b\left(\chi_N - \chi_S - \dfrac{rh_E\Upsilon_{Eb}}{f\delta_b} - \dfrac{\zeta_2\Upsilon_E}{h_E\Delta y}\right)}{\left(\Upsilon_S - \Upsilon_N + \dfrac{r\Upsilon_{Eb}}{f\delta_b} + \dfrac{\zeta_1\Upsilon_E}{h_E\Delta y}\right)} \qquad 9\text{-}68$$

Removing the temporary value $\mathfrak{R}_2$ (and $\mathfrak{R}$), and setting

$$a_{\text{num}} = \Gamma_S - \Gamma_N + \frac{r\varepsilon\Upsilon_{Eb}}{h_E f \delta_b} + \frac{H_C - H_A - H_R}{\Delta t\ C_p^0} + \Psi_{vdv\langle N\rangle} - \Psi_{vdv\langle S\rangle} + \Psi_{ubc} + \Psi_{use}$$

$$- \frac{\Upsilon_E}{h_E \Delta y}\left(U_{se} + U_{bc} - V_R + \frac{r\varepsilon\Delta y}{fh_E} \right) + b\left(\chi_N - \chi_S - \frac{rh_E\Upsilon_{Eb}}{f\delta_b} - \frac{\zeta_2\Upsilon_E}{h_E\Delta y} \right) \qquad \text{9-69}$$

$$a_{\text{denom}} = \Upsilon_S - \Upsilon_N + \frac{r\Upsilon_{Eb}}{f\delta_b} + \frac{\zeta_1\Upsilon_E}{h_E\Delta y}$$

then

$$a_{\text{Box 1}} = \frac{a_{\text{num}}}{a_{\text{denom}}} \qquad\qquad \text{9-70}$$

Finally, the bottom stress is now calculated from Eq. 9-25.

9.5.3   Solution for Other Boxes

For boxes to the south of Box 1, the equations simplify somewhat, since the total velocity at the north line is now a known value, so there is no need to break v_N into its component parts. Equation 9-51 becomes

$$\frac{1}{\rho_0 r} \int_0^{x_{E\langle S\rangle}} \tau^{by} \int_{-h}^0 \rho_S\Theta_S\, dz\, dx + \int_0^{x_{E\langle S\rangle}} \int_{-h}^0 \rho_S\Theta_S v_{dv\langle S\rangle}\, dz\, dx - \int_0^{x_{E\langle N\rangle}} \int_{-h}^0 \rho_N\Theta_N v_N\ dz\ dx$$

$$+ \frac{g}{f}\frac{\partial\eta}{\partial y} \int_{y_S}^{y_N} \int_{-h}^0 \rho_E\Theta_E dz\, dy + \frac{\tau^{by}}{\rho_0 f\delta_b} \int_{y_S}^{y_N} \int_{-h}^{-h+\delta_b} \rho_E\Theta_E dz\, dy \qquad \text{9-71}$$

$$- \int_{y_S}^{y_N} \int_{-h}^0 \rho_E\Theta_E u_{bc} dz\, dy - \int_{y_S}^{y_N} u_{se} \int_{-\delta_s}^0 \rho_E\Theta_E\, dz\, dy = \frac{H_C - H_A - H_R}{\Delta t\ C_p^0}$$

and an additional expression is defined as

$$\Psi_N = \int_0^{x_{E\langle N \rangle}} \int_{-h}^{0} \rho_N \Theta_N v_N \ dz \ dx \qquad \text{9-72}$$

Equation 9-71 reduces to

$$\frac{1}{\rho_0 r} \int_0^{x_{E\langle S \rangle}} \tau^{by} \gamma_S \ + \frac{g}{f} \frac{\partial \eta}{\partial y} \ \Upsilon_E + \frac{\tau^{by}}{\rho_0 f \delta_b} \ \Upsilon_{Eb}$$

$$= \frac{H_C - H_A - H_R}{\Delta t \ C_P^0} + \Psi_N - \Psi_{vdv\langle S \rangle} + \Psi_{ubc} + \Psi_{use} \qquad \text{9-73}$$

Following the same steps as for Box 1, after substituting in the bottom stress the

balance is

$$a \left(\Upsilon_S + \frac{r \Upsilon_{Eb}}{f \delta_b} \right) + b \left(\chi_S + \frac{r h_E \Upsilon_{Eb}}{f \delta_b} \right) + \frac{g}{f} \frac{\partial \eta}{\partial y} \ \Upsilon_E$$

$$= \Gamma_S + \frac{r \varepsilon \Upsilon_{Eb}}{h_E f \delta_b} + \frac{H_C - H_A - H_R}{\Delta t \ C_P^0} + \Psi_N - \Psi_{vdv\langle S \rangle} + \Psi_{ubc} + \Psi_{use} \qquad \text{9-74}$$

and after substituting the sea-surface slope from the volume budget for the southern

boxes (Eq. 9-44), the value of a is found to be

$$a_{\text{num (2)}} = \Gamma_S + \frac{r \varepsilon \Upsilon_{Eb}}{h_E f \delta_b} + \frac{H_C - H_A - H_R}{\Delta t \ C_P^0} + \Psi_N - \Psi_{vdv\langle S \rangle} + \Psi_{ubc} + \Psi_{use}$$

$$- \frac{\Upsilon_E}{h_E \Delta y} \left(U_{se} + U_{bc} + V_N - V_R + \frac{r \varepsilon \Delta y}{f h_E} \right) + b \left(-\chi_S - \frac{r h_E \Upsilon_{Eb}}{f \delta_b} - \frac{\zeta_4 \Upsilon_E}{h_E \Delta y} \right) \qquad \text{9-75}$$

$$a_{\text{denom (2)}} = \Upsilon_S + \frac{r \Upsilon_{Eb}}{f \delta_b} + \frac{\zeta_3 \Upsilon_E}{h_E \Delta y}$$

so that

$$a_{\text{Box 2+}} = \frac{a_{\text{num (2)}}}{a_{\text{denom(2)}}} \qquad \text{9-76}$$

9.5.4   Summary of Heat Budget Calculations

1) Set a value for the constant b.

2) Calculate the unknown constant a for Box 1 from Eq. 9-70.

3) Calculate τ^{by} from Eq. 9-22 along each face.

4) Calculate $\partial\eta/\partial y$ for Box 1 from Eq. 9-41.

5) Calculate velocities and transports for Box 1 (from Table 9-4) using these values of τ^{by} and $\partial\eta/\partial y$.

6) Calculate a for the next box (to the south) from Eq. 9-76, using V_N and v_N calculated (as V_S and v_S) for the previous box.

7) Calculate τ^{by} from Eq. 9-25 along the south and east faces using the new value of a.

8) Calculate $\partial\eta/\partial y$ for this box from Eq. 9-44.

9) Calculate velocities and transports (from Table 9-4) along the south and east faces using the new values τ^{by} and $\partial\eta/\partial y$.

10) Repeat steps (6)–(9) for all subsequent boxes.

11) Calculate the heat budget terms for all boxes from Eq. 9-50.

9.6 Salt and Freshwater Budgets

A salt budget can be approached in an identical manner as the heat budget. Since the salt is only a small fraction (typically about 3.5% by mass) of a parcel of seawater, it is common to instead derive a freshwater budget (i.e. the other 96.5% of the parcel). Since the *changes* in either salt or freshwater have the same value, errors and uncertainties can be a significant proportion of the salt content, but have much less impact on the freshwater budget.

9.6.1 Salt Budget

The salt budget is expressed in terms of the conservative value Preformed Salinity S_* (see §9.2):

$$\underbrace{\iiint_V \frac{d\left(\rho\left(S_*/1000\right)\right)}{dt}\, dV}_{\substack{\text{rate of change in}\\ \text{salt content}}} = +\underbrace{\oiint \frac{d\left(E-P\right)\left(S_*/1000\right)}{dt}\, dA}_{\substack{\text{air-sea}\\ \text{salt transport}}} + \underbrace{\oiint \rho\left(S_*/1000\right)v\; dA}_{\substack{\text{advective}\\ \text{salt transport}}} \qquad \text{9-77}$$

where terms have units of salt transport (kg s^{-1}), and where E is the evaporation and P is the precipitation (both in units of kg m^{-2}). Preformed Salinity has units of *grams* of salt per kilogram of seawater (g kg^{-1}), so the divisor of 1000 is required to convert it to *kilograms* of salt per kilograms of seawater (kg$_{(salt)}$/kg).

The change in salt content (in kg$_{\text{(salt)}}$) over a month is therefore

$$\underbrace{\iiint_V \Delta(\rho S_*)/1000 \; dV}_{\substack{\text{change in} \\ \text{salt content}}} = \underbrace{\oiint (E-P)(S_*/1000) \; dA}_{\substack{\text{change due to} \\ \text{air-sea exchange}}} + \underbrace{\Delta t \oiint \rho(S_*/1000) v \; dA}_{\substack{\text{change due to} \\ \text{advection}}}$$

9-78

Expanding out the velocity in the advection term,

$$\underbrace{\iiint_V \Delta(\rho S_*)/1000 \; dV}_{\substack{\text{change in} \\ \text{salt content } (S_C)}} = \underbrace{\oiint_{\text{surface}} (E-P)(S_*/1000) \; dA}_{\substack{\text{salt change due to} \\ \text{air-sea exchange } (S_A)}}$$

$$+ \underbrace{\Delta t (S_*/1000) \rho_R V_R}_{\substack{\text{salt advection} \\ \text{from river discharge } (S_R)}} + \underbrace{\Delta t \oiint_{\text{south face}} \rho_S (S_*/1000) v_S \; dA}_{\substack{\text{salt advection through the} \\ \text{south face}}}$$

9-79

$$- \underbrace{\Delta t \oiint_{\text{north face}} \rho_N (S_*/1000) v_N \; dA}_{\substack{\text{salt advection through} \\ \text{north face}}} - \underbrace{\Delta t \oiint_{\text{east face}} \rho_E (S_*/1000) u \; dA}_{\substack{\text{salt advection through} \\ \text{east face}}}$$

and dividing through by Δt, and rearranging,

$$\frac{S_C - S_A - S_R}{\Delta t} = \oiint_{\substack{\text{south} \\ \text{face}}} \rho_S (S_*/1000) v_S \; dA - \oiint_{\substack{\text{north} \\ \text{face}}} \rho_N (S_*/1000) v_N \; dA$$

$$- \oiint_{\substack{\text{east} \\ \text{face}}} \rho_E (S_*/1000) u \; dA$$

9-80

which can be combined with the bottom stress relation (Eq. 9-22) and the volume

budget solutions (Eq. 9-41 or Eq. 9-44) to obtain values for velocity and transport in

the same manner as the heat budget method. Once those are obtained, each term in

the salt budget (Eq. 9-79) can then be calculated.

9.6.2 Freshwater Budget

Freshwater is expressed as the mass of freshwater per kilogram of seawater $(kg_{(fw)}/kg)$, its relation to Preformed Salinity being:

$$F_W = 1 - (S_*/1000) \qquad\qquad 9\text{-}81$$

The monthly mean freshwater budget corresponding to Eq. 9-50 for heat, and Eq. 9-79 for salt, is

$$\underbrace{\iiint_{\text{box}} \Delta\{\rho[1-(S_*/1000)]\}\, dV}_{\substack{\text{change in} \\ \text{freshwater content } (F_C)}} = \underbrace{\oiint_{\text{surface}} (P-E)[1-(S_*/1000)]\, dA}_{\substack{\text{freshwater change due to} \\ \text{air-sea exchange } (F_A)}}$$

$$+ \underbrace{\Delta t[1-(S_*/1000)]\rho_R V_R}_{\substack{\text{freshwater advection from} \\ \text{river discharge } (F_R)}} \quad + \quad \underbrace{\Delta t \oiint_{\text{south face}} \rho_S[1-(S_*/1000)]v_S\, dA}_{\substack{\text{freshwater advection through} \\ \text{south face}}} \qquad 9\text{-}82$$

$$- \underbrace{\Delta t \oiint_{\text{north face}} \rho_N[1-(S_*/1000)]v_N\, dA}_{\substack{\text{freshwater advection through} \\ \text{north face}}} - \underbrace{\Delta t \oiint_{\text{east face}} \rho_E[1-(S_*/1000)]u\, dA}_{\substack{\text{freshwater advection through} \\ \text{east face}}}$$

in units of kilograms of freshwater.

Dividing through by Δt,

$$\frac{F_C - F_A - F_R}{\Delta t} = \oiint_{\substack{\text{south} \\ \text{face}}} \rho_S[1-(S_*/1000)]v_S\, dA - \oiint_{\substack{\text{north} \\ \text{face}}} \rho_N[1-(S_*/1000)]v_N\, dA$$

$$- \oiint_{\substack{\text{east} \\ \text{face}}} \rho_E[1-(S_*/1000)]u\, dA$$

$$9\text{-}83$$

which can also be combined with the volume budget to obtain solutions for velocity and transport along with the freshwater budget terms.

9.6.3   Summary of Budget Terms

Table 9-5: Heat, salt and freshwater budget terms.

Quantity	Heat	Salt	Freshwater
Content	$\rho C_p{}^0 \Theta$	$\rho\left(\dfrac{S_*}{1000}\right)$	$\rho\left(1 - \dfrac{S_*}{1000}\right)$
	$\left[\text{J m}^{-3}\right]$	$\left[\text{kg m}^{-3}\right]$	$\left[\text{kg m}^{-3}\right]$
Advective Flux	$\rho C_p{}^0 \Theta\, v$	$\rho\left(\dfrac{S_*}{1000}\right)v$	$\rho\left(1 - \dfrac{S_*}{1000}\right)v$
	$\left[\text{W m}^{-2}\right]$	$\left[\text{kg m}^{-2}\ \text{s}^{-1}\right]$	$\left[\text{kg m}^{-2}\ \text{s}^{-1}\right]$
Air-sea flux	Q_{net}	$\dfrac{1}{\Delta t}(E - P)\left(\dfrac{S_*}{1000}\right)$	$\dfrac{1}{\Delta t}(P - E)\left(1 - \dfrac{S_*}{1000}\right)$
	$\left[\text{W m}^{-2}\right]$	$\left[\text{kg m}^{-2}\text{s}^{-1}\right]$	$\left[\text{kg m}^{-2}\text{s}^{-1}\right]$

9.7 Air-sea Heat Fluxes

9.7.1 Introduction

The net air-sea heat flux at the ocean surface Q_A is

$$Q_A = Q_{SW} + Q_{LW} + Q_S + Q_L$$
$$= (Q_{SW\text{-down}} - Q_{SW\text{-up}}) + (Q_{LW\text{-down}} - Q_{LW\text{-up}}) + Q_S + Q_L \qquad \text{9-84}$$

where Q_{SW} is the net shortwave radiation, Q_{LW} is the net long-wave (infra-red)
radiation, Q_S is the sensible heat flux (due to conduction), and Q_L is the latent heat
flux (due to evaporation). Positive values indicate heat gain by the ocean (i.e.
positive downward). Q_{SW} is always positive: it is the incoming solar radiation from
the sun; Q_{LW} is almost always negative (i.e. representing a heat loss): it is the back
radiation from the ocean surface; Q_L is also almost always negative whereas Q_S
can be either positive or negative, depending on the sign of the temperature
difference between the ocean and the atmosphere.

Two different estimates of the net surface heat flux are used in this study. Flux and
radiation estimates produced by the National Centers for Environmental
Prediction–North American Regional Reanalysis (NCEP–NARR; Mesinger et al.
2006) from 1979–2000 are combined to give the net air-sea heat flux. NCEP–NARR
data were provided by the NOAA/ESRL PSD, Boulder, Colorado, USA, from their
website at http://www.esrl.noaa.gov/psd/. A second estimate of the net surface air-
sea flux is obtained from the Woods Hole Oceanographic Institution (WHOI)
Objectively Analyzed air-sea Fluxes (OAFlux; Yu and Weller 2007 & Yu et al. 2008)

project (http://oaflux.whoi.edu) funded by the NOAA Climate Observations and
Monitoring (COM) program. The OAFlux project provides estimates of the turbulent
air-sea fluxes (latent and sensible heat), and a net surface heat flux estimate is also
available by combining with radiative fluxes (shortwave and long-wave radiation)
from the International Satellite Cloud Climatology Project (ISCCP; Zhang et al.
2004). The OAFlux estimates used in this work span the years 1983–2009.

The NCEP–NARR has a resolution of approximately 0.3º (around 32 km) and 83 grid
points lie with the eight MAB boxes, while the OAFlux has a 1º resolution, with 8
points within the region of interest (Figure 9-5).
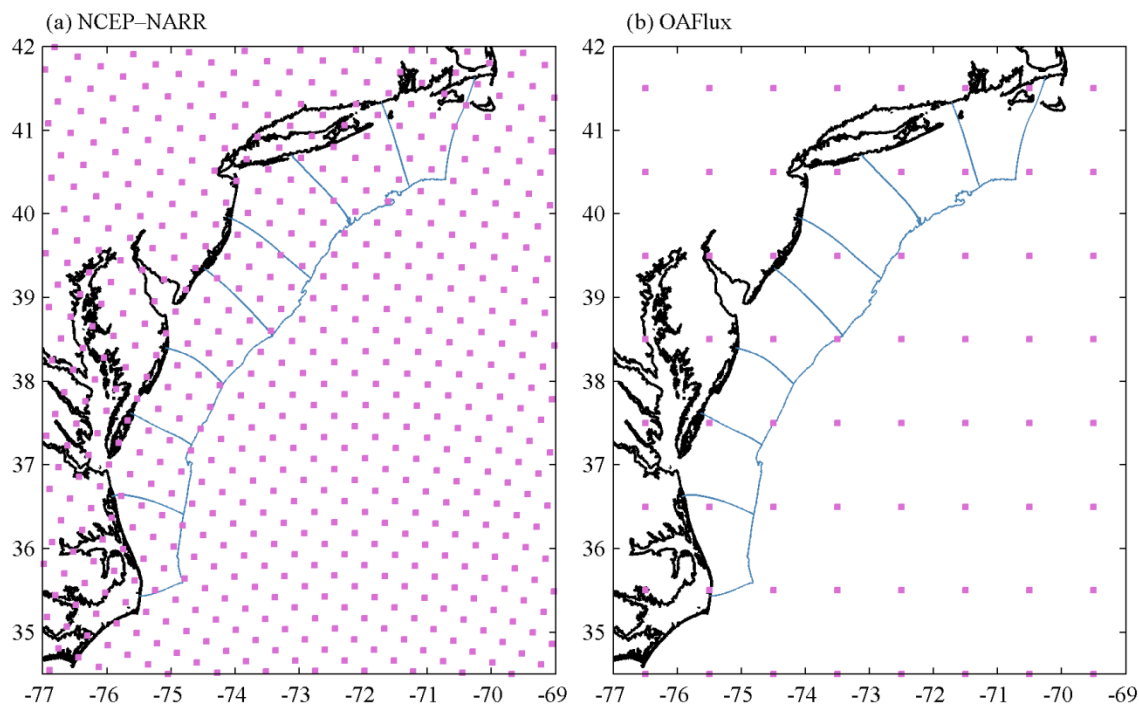
Figure 9-5: Air-sea heat flux coverage: (a) NCEP–NARR with 83 grid points lying within the
eight MAB boxes and (b) OAFlux with eight grid points.

9.7.2   NCEP-NARR Surface Heat Fluxes

The NCEP–NARR is a long-term, high resolution meteorological reanalysis of North America, with 45 vertical layers in the atmosphere, and a horizontal resolution of approximately 0.3º (32 km). Here, the long term monthly mean data from the period 1979–2010 is used.

The NCEP–NARR is a new high resolution regional version of the global reanalyzes NCEP–NCAR (NCEP–R1; Kalnay et al. 1996) and the NCEP–Department of Energy (DOE) reanalysis (NCEP–R2; Kanamitsu et al. 2002). Systematic biases were identified in the latent and sensible heat flux estimates of the NCEP–R1 (of overestimating losses), which are particularly apparent during strong winds, due to an inappropriate heat roughness length in the bulk aerodynamic formulas (e.g. Zeng et al. 1998; Josey 2001; Renfrew et al. 2002; Vivier et al. 2002; Sun et al. 2003). Josey (2001) also uncovered an underestimate in the shortwave gain. The NCEP–R2 improved on the net radiation budget (Kanamitsu et al. 2002), and the sensible heat flux, but not the latent (Sun et al. 2003). However, Szeto et al. (2008) found that NCEP–R2 surface heat fluxes still compared unfavorably to data, and advised caution on relying on them.

While the R2 is considered a corrected and updated version of the NCEP–R1, the NCEP–NARR is a new model, and is a major improvement on both those earlier reanalyzes (Mesinger et al. 2006): notably, it utilizes the NCEP Eta model with a convective parameterization as described by Janjic (1994), and does not assimilate precipitation observations. Note that the next NCEP *global* reanalysis product is

termed the Climate Forecast System Reanalysis (CFSR; Saha et al. 2010 & Xue et al. 2011).

While the NCEP–NARR has been evaluated extensively over land, few studies have evaluated the surface heat fluxes over the ocean. Moore et al. (2008) compares air temperature, specific humidity and SST around Cape Farewell, Greenland, and concludes that they are in generally good agreement with buoy observations. Renfrew et al. (2009) compares both the NCEP–R1 and NCEP–NARR along with six other analyses or hind casts in the Denmark Strait and Irminger Sea, and finds that overall NCEP–NCAR compares poorly with data, while NCEP–NARR comparisons are generally good. However, the NCEP–NARR surface heat fluxes do not compare well, with both latent and sensible heat fluxes biased high. Renfrew et al. (2009) infers that once again the bulk flux algorithm is the issue. Moore (2014) uses NCEP–NARR to capture the mesoscale structure of jets around Cape Farewell, but after citing Renfrew et al. (2009) uses an alternative "well-established" bulk algorithm (COARE 3.0; see §9.7.3 for further details) for the heat fluxes, instead of the NCEP–NARR calculation. Wang et al. (2012) identified a year-round overestimation (> 20%) in NCEP–NARR values of incoming short-wave radiation near Delaware Bay, when compared with values from a local observation system.

9.7.3   OAFlux Net Surface Heat Flux

The OAFlux is an objectively analyzed synthesis of satellite data and reanalysis products, including NCEP–R1 and NCEP–R2 (Yu et al. 2008). It was created to

address the known issues with previous air-sea flux products, and to provide an improved estimate of latent and sensible heat fluxes . A net surface heat flux estimate made by combining radiation data from the ISCCP. The third version covering 1958–present, and described by Yu et al. (2008) is used in this work.

OAFlux uses the Coupled Ocean-Atmosphere Response Experiment (COARE) algorithm: the first version implemented COARE 2.6a (Fairall et al. 1996; Bradley et al. 2000), while the second and third use COARE 3.0 (Fairall et al. 2003). Brunke et al. (2003) evaluates 12 bulk algorithms in common use, and finds the COARE 3.0 algorithm to be the top performing, while the algorithm used by NCEP–R1 is among the worst.

9.7.4   Which Estimate Is More Accurate?

Yu et al. (2004a) compares OAFlux (version 1) with both the NCEP–R2 output fluxes and the fluxes calculated from NCEP–R2 variables using the COARE 2.6a algorithm and finds, as with earlier investigations, that the NCEP–R2 overestimates latent and sensible heat fluxes. The recalculated values are reduced. But they noted that the recalculated values are not the same as the OAFlux values, and concluded that OAFlux input variables are improved by the objective analysis, and not only the by the improved bulk flux algorithm. The companion paper (Yu et al. 2004bb) compares OAFlux (version 1) to in situ buoy and ship measurements, and concludes that OAFlux values are an improvement over NCEP–R2 values at all locations. Yu et al. (2006) compares OAFlux (plus ISCCP) to NCEP–R1 and concludes that the new

combination is a better estimate of net surface heat flux than NCEP–R1. Lentz 2010a) finds that OAFlux estimates of latent and sensible heat loss in the winter are larger than NCEP–R1, noting that it was not possible to determine which estimate was more accurate, and goes on to use and compare both estimates in his analysis.

The author is unaware of any studies providing an evaluation of the two estimates together: that is directly comparing both NCEP–NARR air-sea fluxes and OAFlux with observations. Dong et al. (2007) did find that combining radiation from NCEP-NARR and computing latent and sensible heat fluxes using the COARE 2.5b algorithm (Fairall et al. 1996) gave the same result as OAFlux implying that NCEP–NARR turbulent heat fluxes were not as accurate as those calculated with the COARE (as OAFlux are).

In conclusion, without any study comparing both the models to observations, it is unknown which is more accurate. The OAFlux has been shown to compare well to observations, and to other models including the earlier NCEP models, however the NCEP–NARR has much higher resolution (over 10 times the number of grid points on the MAB shelf) so it is of interest to compare results using both air-sea flux estimates.

9.8 Data and Methods

9.8.1 Constants

The f-plane approximation is applied over each box, so that the Coriolis parameter f becomes a constant ($f \simeq f_0 = 2\Omega \sin\theta_0$), where Ω is the rotation rate of the earth, and θ_0 is a fixed latitude: in this case, the mid-point of the box. The reference density ρ_0 is assigned the value of the mean annual density throughout all the boxes: 1025.1, and the gravitational acceleration g is 9.806,65 m s^{-2}.

Following Lentz (2008) the Ekman layer depths at both surface and bottom (δ_s and δ_b) are set to a constant 15 m, and the linear resistance coefficient r is set to 2.5 × 10^{-4} m s^{-1}. The constant b is set to −0.0001.

9.8.2 MOCHA Seawater Values

The MOCHA climatology of monthly temperature and salinity is summed over all grid cells within each MAB box for volume integrals in the heat budget, and is interpolated along all box boundaries and then summed, for current flow calculations. To capture the entire volume (or area), an additional depth level equal to the depth of the water column is added to each profile in both cases, and the value at the bottom is obtained from linear extrapolation. Integrals are calculated numerically using the trapezoidal method.

9.8.3 Cross-shore Density Gradients

Cross-shore density gradients for each month at each line are calculated from MOCHA in situ density slices. The gradients are generally higher near the coast (where salinity is lower), and higher in wintertime when waters are vertically mixed, than during the summertime when waters are typically horizontally stratified (Figure 9-6). Values are generally higher than the 4×10^{-6} (kg m^{-3}) m^{-1} average found by Lentz (2008), however his estimate was from an annual mean value with the seasonal cycle removed. Here, considerable variation is seen both cross-shore and alongshore, as well as some variation throughout the months, so the full gradient fields are kept, rather than using a single mean value. The cross-shore gradients generally increase from north to south until Line 9, which clearly extends beyond the MAB shelf into the less dense waters of the Gulf Stream.

9.8.4 Alongshore Density Gradients

Alongshore density gradients are calculated from a moving average over 100 data points (which roughly corresponds to 20–30 km distance) along the 85-m isobath. A longer section of the isobath is used to avoid missing sections at each end. Values are typically small: between -5×10^{-6} and 5×10^{-6}, with higher values of up to 1.5×10^{-5} near Cape Hatteras. A positive density gradient means higher density waters to the north. The along-shore distance is labelled in Figure 9-7 as negative from Line 1, as a reminder that the coordinate system is positive to the north, even though the budget calculations begin in the northernmost box.
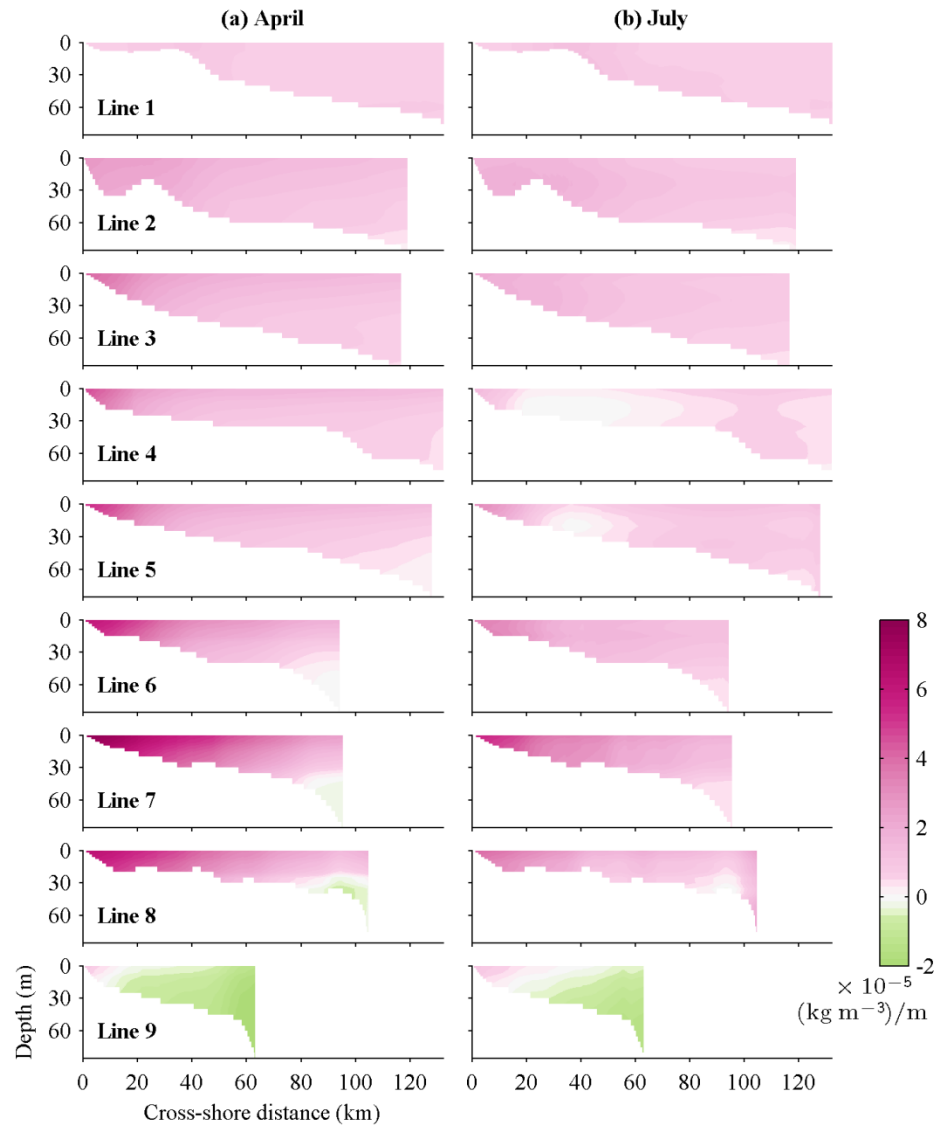
Figure 9-6: Cross-shore density gradients ((kg m^{-3}) m^{-1}) calculated from MOCHA at each line during (a) April and (b) October.

Through Boxes 1–7, density gradients follow salinity patterns: low salinity water in Box 1 increases to the south to a peak around Line 5, leading to a negative density gradient in the first four boxes, and to a positive gradient in Box 5 and the north of Box 6. Salinity increases markedly after the Chesapeake Bay, leading to another region of negative density gradient in Box 6 and Box 7. In Box 8 the large increase in
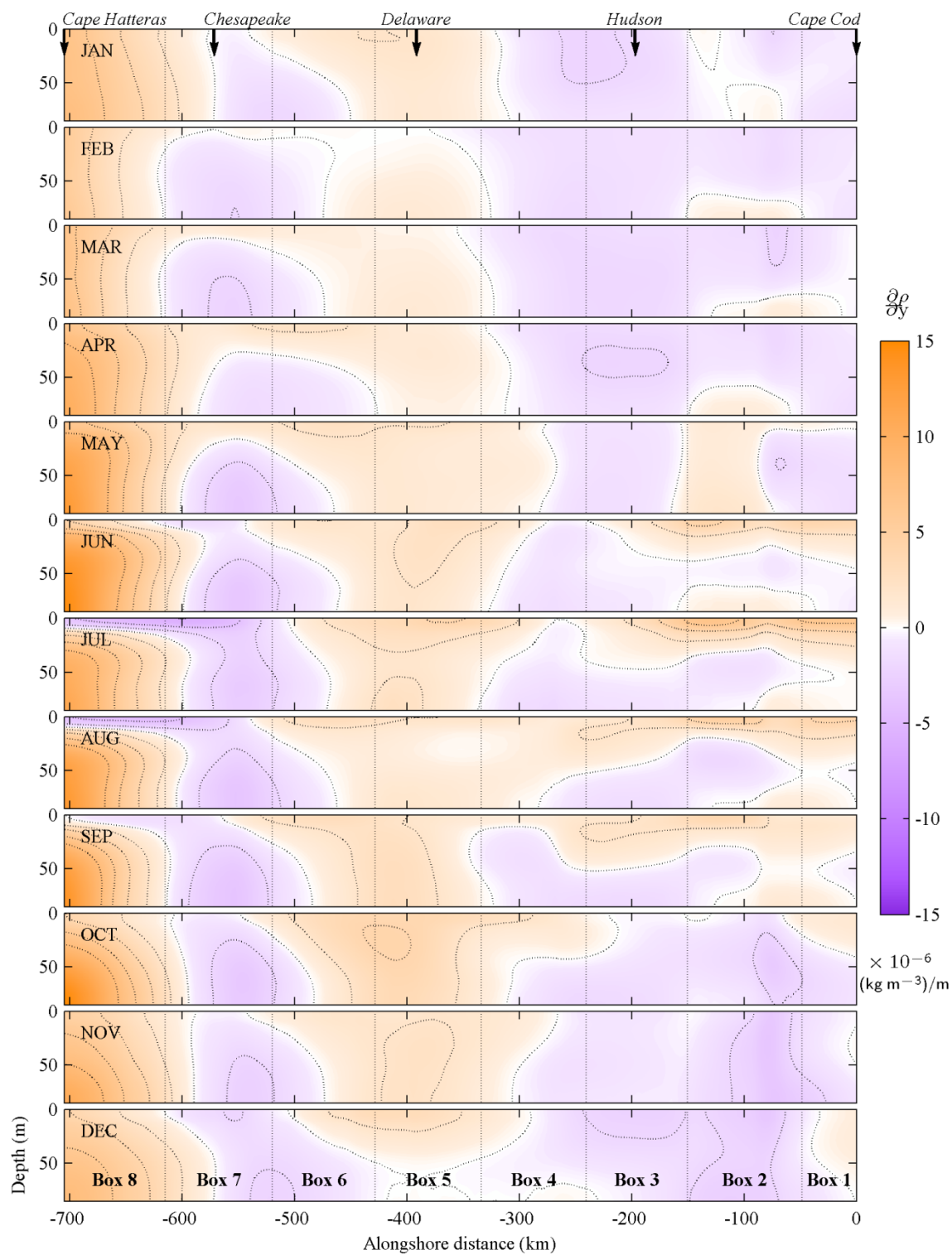
Figure 9-7: Alongshore density gradients ((kg m⁻³) m⁻¹) calculated from MOCHA. Contour lines are 2×10^{-6} apart.

temperature of the warmer slope waters overtakes the influence of salinity on the density gradient, and the water becomes less dense, leading to a positive density gradient that is more pronounced with depth. Thus the zero-density gradient line represents the point at which temperature effects on density overtake the salinity effects. During the summer months the surface layer of positive density gradient is evident. Although salinity is higher in the northern boxes, the temperature pattern dominates here, and the cooler temperatures in the north lead to higher densities.

In summary, the along-shore density gradient follows salinity gradients throughout most of the MAB, and throughout most of the year, except in areas (or months) where very high temperature gradients exist: namely the summer thermocline in the northern boxes, and at the shelf break near Cape Hatteras.

9.8.5   River Discharge

Volume transport from the seven major rivers in the region are obtained from those used in the ESPreSSO model (see §7.7). The Connecticut river flows into Box 2; the Hudson river flows out from the Hudson River Estuary just south of Long Island in Box 3; and the Delaware river flows through Delaware Bay into Box 5. The Susquehanna, Potomac, Choptank and James rivers all flow into Chesapeake Bay which is located within Box 7.

All the rivers exhibit a similar annual cycle with peak volume transport in the spring and lowest volume transport during summertime (Figure 9-8). The river

water volume entering Box 7 from Chesapeake Bay is generally 3–4 times that from each of the other three rivers.
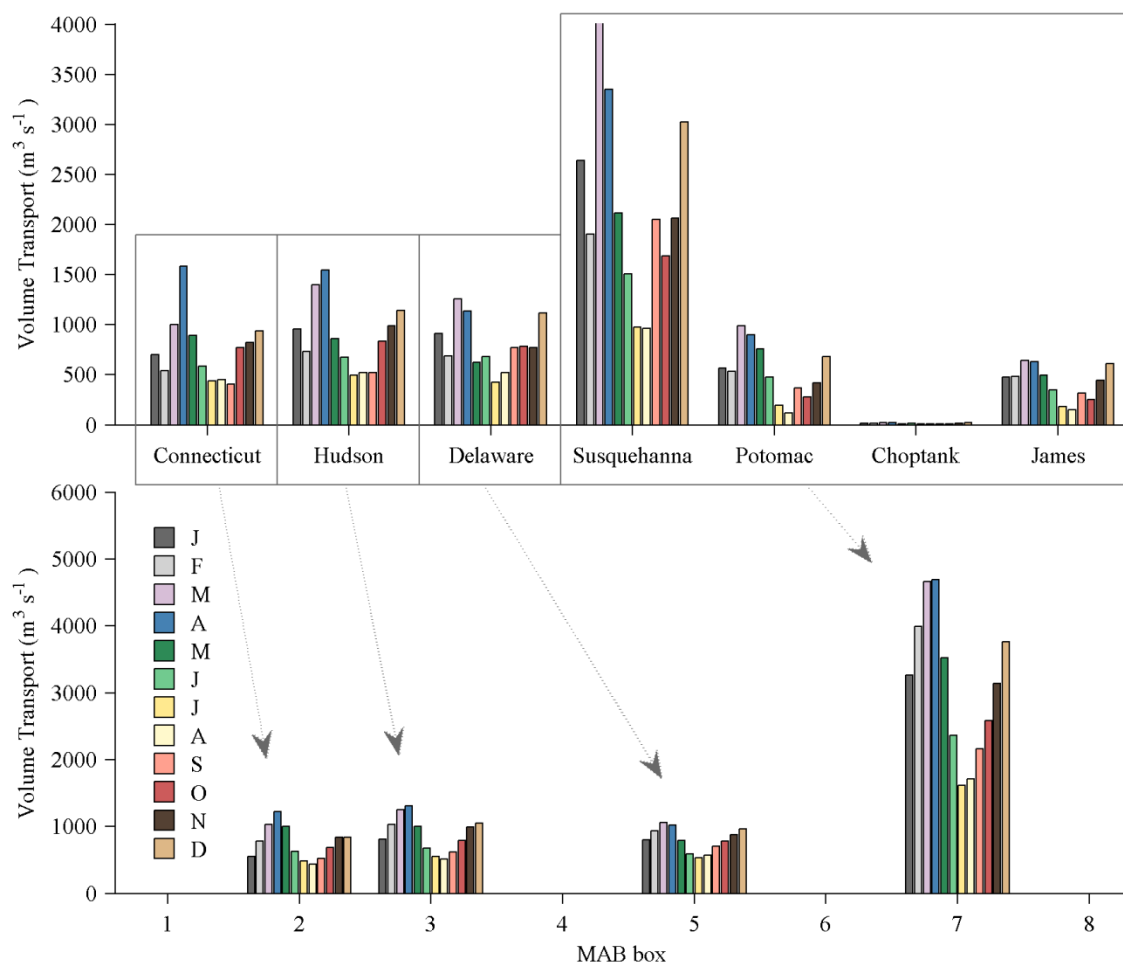
Figure 9-8: Monthly river discharge as volume transport (m^3 s^{-1}) by (a) river , and by (b) MAB box.

9.8.6 Wind stress

Wind stress values are calculated from NCEP–NARR wind speed data estimates. The wind speed data are rotated to obtain the components perpendicular and parallel to each cross-shore line and to the 85-isboath (i.e. the north, south and off-shore faces of each box), and averaged to give monthly values at each location. This average monthly value (of wind speed at 10 m) is converted into wind stress (Figure 9-9) using the formula described by Large and Pond (1981). A summary of seasonal wind patterns in the MAB is found in §2.5.1.

9.8.7 Air-sea Heat Flux

The air-sea temperature flux for a box during a particular month is calculated using:

$$\text{Air-sea flux} = \int_{y_1}^{y_2} \int_{x_1}^{x_2} Q_A \, dx \, dy \quad [\text{W}]=[\text{Js}^{-1}] \qquad \text{9-85}$$

This flux is multiplied by the number of seconds in that month, to give the total heat content change due to air-sea flux, during that month, in Joules:

$$H_A = \Delta t \int_{y_1}^{y_2} \int_{x_1}^{x_2} Q_A \, dx \, dy \quad [\text{J}] \qquad \text{9-86}$$

Monthly mean values (in units of W m^{-2}) for each of the components in Eq. 9-84 are obtained from NCEP–NARR and combined to give the net surface heat flux Q_A. A net surface heat flux output is directly available from OAFlux (which combines the OAFlux latent and heat fluxes with radiation values from ISCCP).
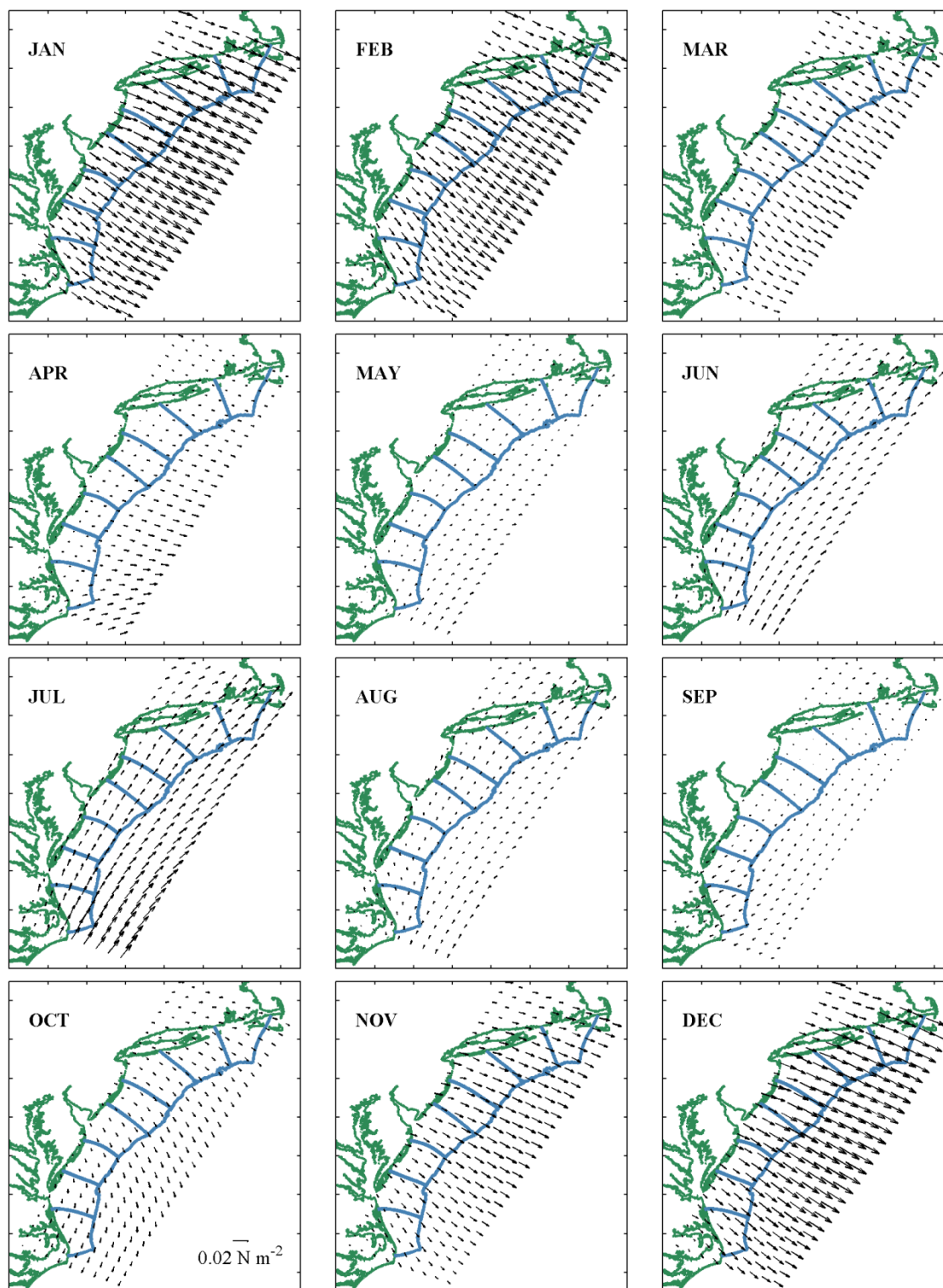
Figure 9-9: Monthly mean wind stress (N m^{-2}) over the Middle Atlantic Bight. Data source: NCEP–NARR provided by the NOAA/ESRL PSD, Boulder Colorado, USA, from their website at http://www.esrl.noaa.gov/psd/
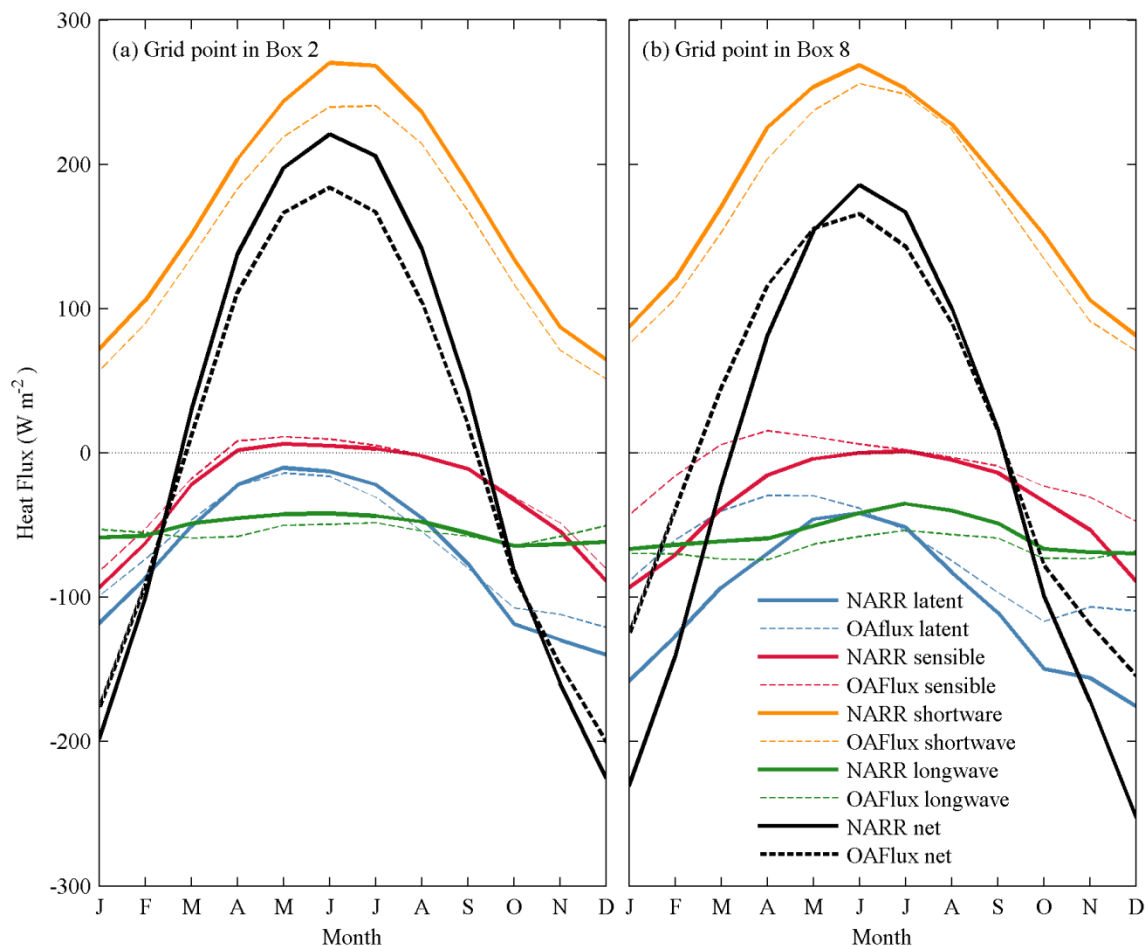
Figure 9-10: NCEP–NARR (solid) and OAFlux (dashed) air-sea flux components (W m^{-2}) for the grid point at (a) -72.5°E, 40.5°N (within Box 2), and (b) -75.5°E, 40.5°N (within Box 8). Month tick marks are at the mid-point of the month.

For both datasets, all grid cells that contain land are deleted, and gaps are filled by interpolation and extrapolation from ocean-only grid cells. Then the set surface heat flux is interpolated onto the MOCHA grid points within the MAB boxes (Figure 9-11).

A strong annual cycle of net surface heat flux is apparent due to the dominance of the annual incoming solar shortwave radiation (Figure 9-10), peaking in June, and

with a low in December and January. Long wave radiation is fairly steady year-round, while both latent and sensible heat fluxes are weak in summer and stronger (more negative) in winter. The net surface heat flux peaks in mid-June, and remains positive from mid-March through early October. Net heat loss occurs during the fall and winter months.

The most obvious spatial pattern in the heat flux (e.g. NCEP–NARR: Figure 9-11) is the broad region of heat loss over the Gulf Stream during the fall and winter months, where latent and sensible heat losses are larger.

The NCEP–NARR estimates of each surface heat flux component are interpolated to the eight OAFlux grid points inside the MAB boxes. Both estimates at these points, one in Box 2 and one in Box 8, are displayed in Figure 9-10. The NCEP–NARR estimate of shortwave radiation is persistently larger than the OAFlux estimate (on average around 14% greater), in keeping with the findings by Wang et al. (2012). NCEP–NARR estimates of shortwave, latent and sensible heat loss are all larger (more negative) during the winter. The difference in the wintertime turbulent heat losses is largest in the southern-most boxes, near the Gulf Stream region. These effects combine to result in NCEP–NARR net surface heat flux estimate being generally higher than OAFlux during the spring and summer, and lower in fall and winter; while the OAFlux fields show less influence of the Gulf Stream region impinging on the southern boxes, than NCEP–NARR fields do (Figure 9-12). This could simply be due to the much lower resolution of the OAFlux grid.
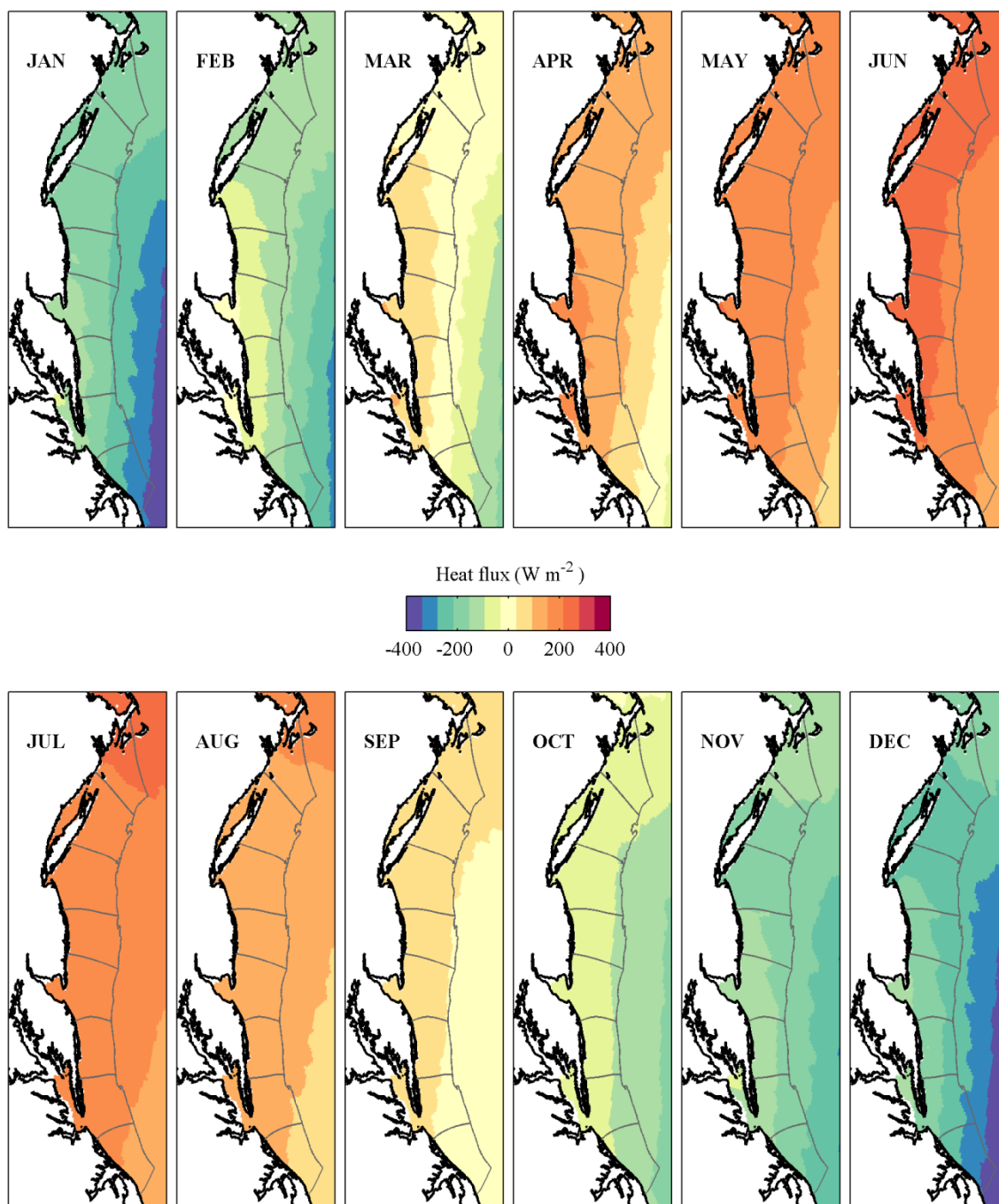
Figure 9-11: Air-sea net surface heat flux (W m^{-2}) from NCEP–NARR for each month of the year.
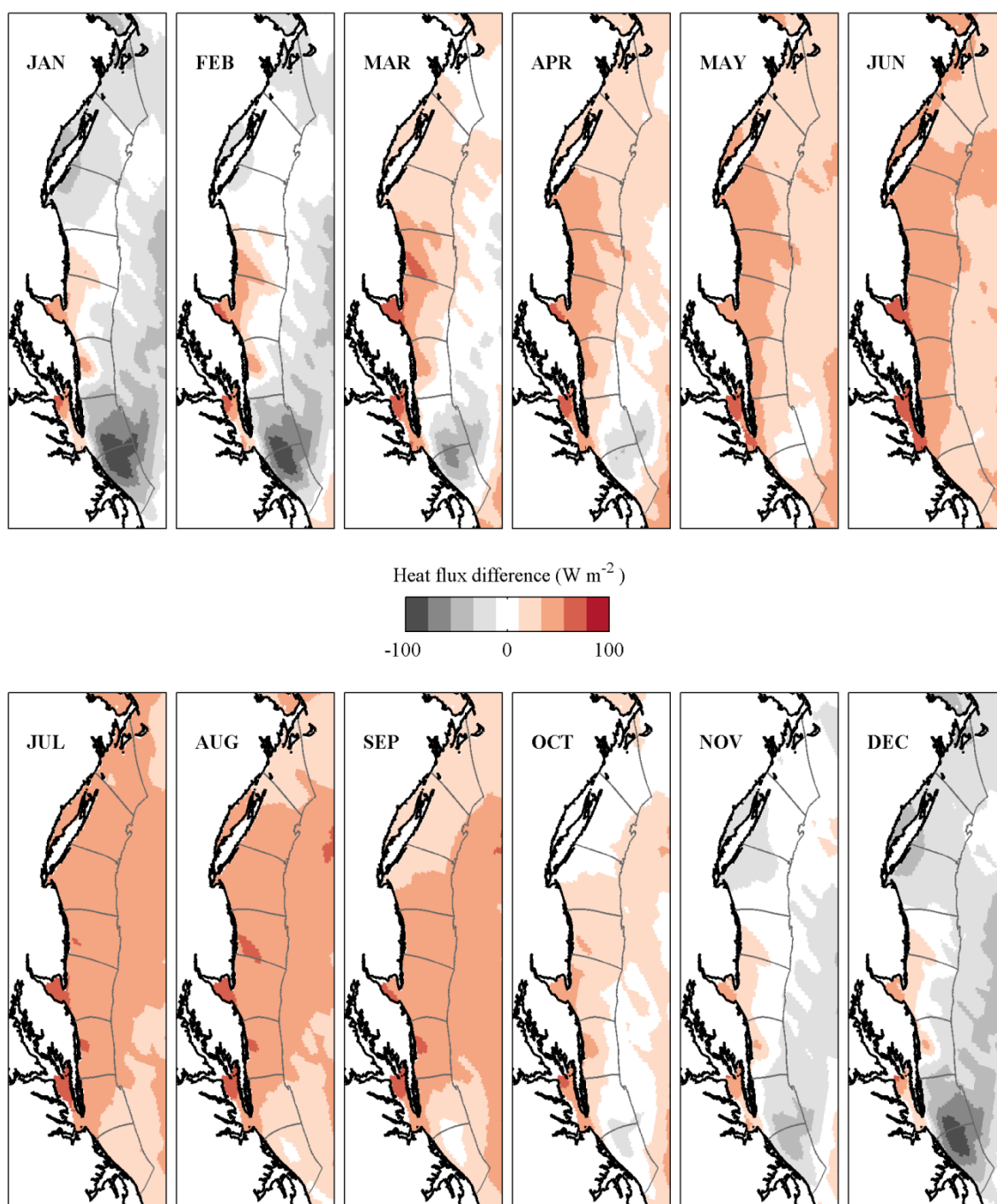
Figure 9-12: The difference in airsea heat flux estimates (W m⁻²) from NCEP–NARR and OAFlux–ISCPP for each month of the year. Positive values indicate that NCEP–NARR estimates are higher.

9.8.8   Air-sea Salt and Freshwater Flux

Total accumulated precipitation P and evaporation E estimates for each month are

obtained from the NCEP–NARR reanalysis, in units of $\mathrm{kg\,m^{-2}}$ (equivalent to mm).

The accumulation gain from precipitation is larger than the loss by evaporation (e.g.

Figure 9-13), so there is a net gain of freshwater by the ocean all year round

throughout the MAB (Figure 9-14).
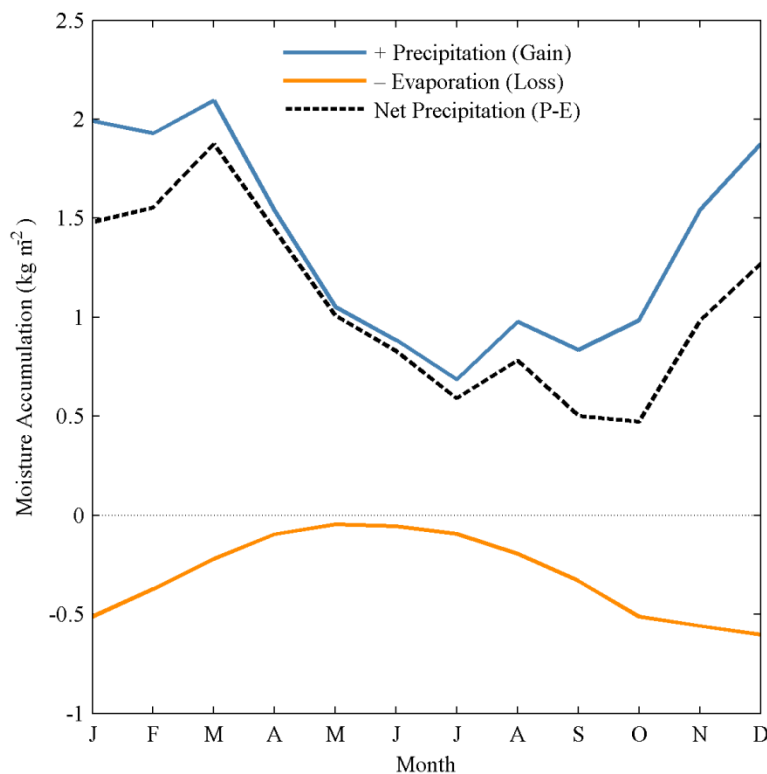
Figure 9-13: NCEP–NARR precipitation and evaporation ($\mathrm{kg\,m^{-2}}$) estimates for the grid point at $-72.5°\mathrm{E}$, $40.5°\mathrm{N}$ (within Box 2), and the net precipitation ($P-E$). Month tick marks are at the mid-point of the month.
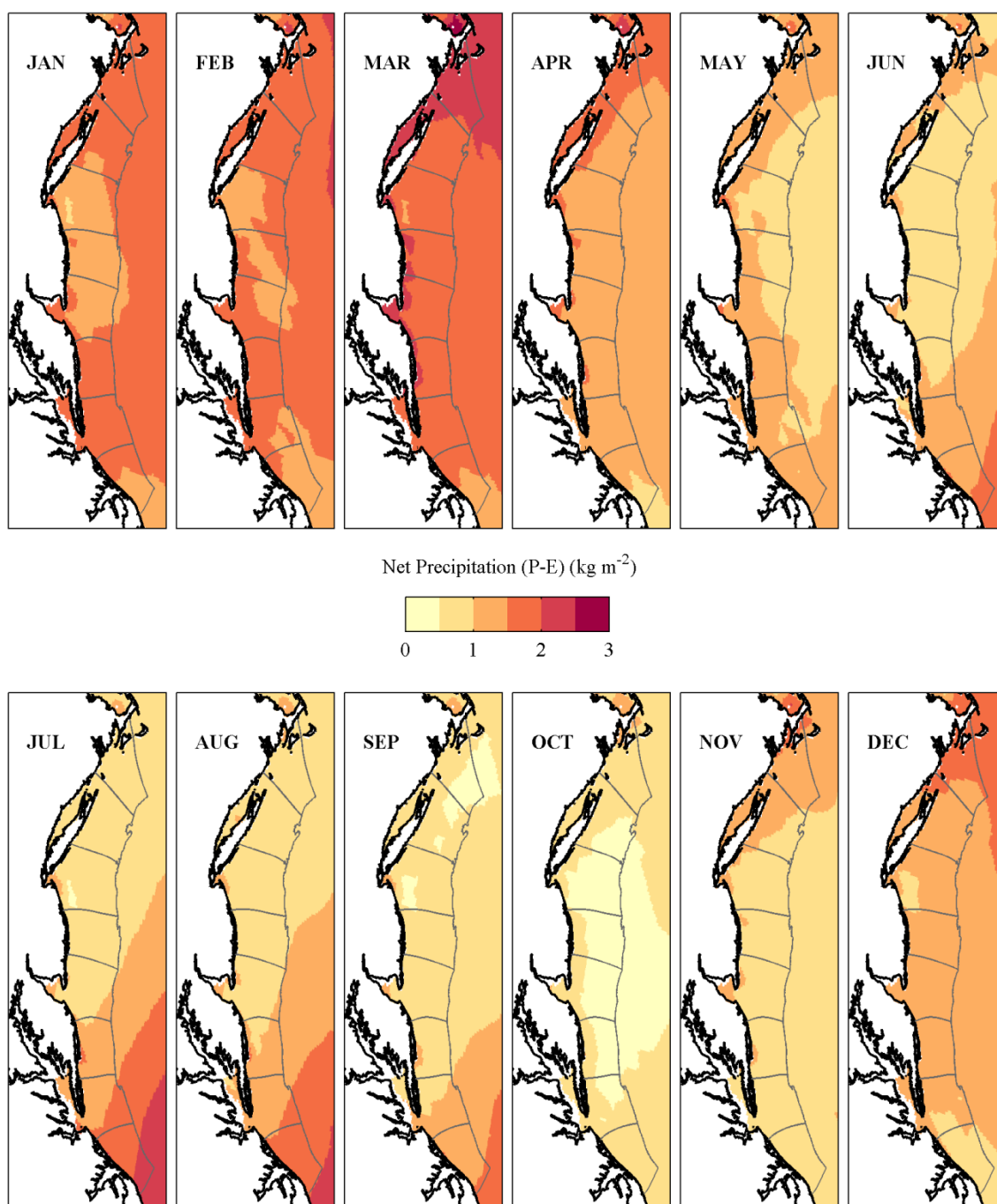
Figure 9-14: NCEP–NARR long term monthly means of net accumulated precipitation ($P{-}E$), displayed in units of kg m^{-2} (or, mm).

Precipitation and evaporation are both larger in summer, but the range of precipitation is larger than for evaporation, which leads to a net precipitation that is higher in winter and lower in summer (Figure 9-13). In winter, P and E are both fairly uniform throughout the MAB box (Figure 9-14), so the net value is also fairly uniform, except to the south where high evaporation reduces the net value. During the summer higher precipitation to the south, along with greater evaporation offshore in the southern boxes, leads to higher net values in the south. High evaporation rates have been reported (e.g. Joyce 1987) over a large swath of ocean surrounding the Gulf Stream, explains the higher evaporation rates in the southern boxes.

The salt flux is derived by multiplying (*P–E*) by the salinity, and dividing through by the seconds in one month:

$$\text{salt flux} = \frac{1}{\Delta t} \oiint (E - P)(S_* / 1000) \ dA \quad \left[\text{kg}_{(salt)} \text{m}^{-2} \text{s}^{-1} \right]$$

9-87

 The freshwater flux is obtained by multiplying (*E-P)* by the freshwater content:

$$\text{freshwater flux} = \frac{1}{\Delta t} \oiint (P - E)\left[1 - (S_* / 1000)\right] \ dA \quad \left[\text{kg}_{(fw)} \text{m}^{-2} \text{s}^{-1} \right]$$

9-88

The surface freshwater flux (Figure 9-15) displays a broadly similar pattern to the net precipitation. Although a distinct cross-shore gradient exists in surface salinity (typically from around 28 near the coast to about 34 at the 85-m isobath), the variations in salinity term of the freshwater flux (Eq. 9-88) are typically less than 2% of the variation in the net precipitation.
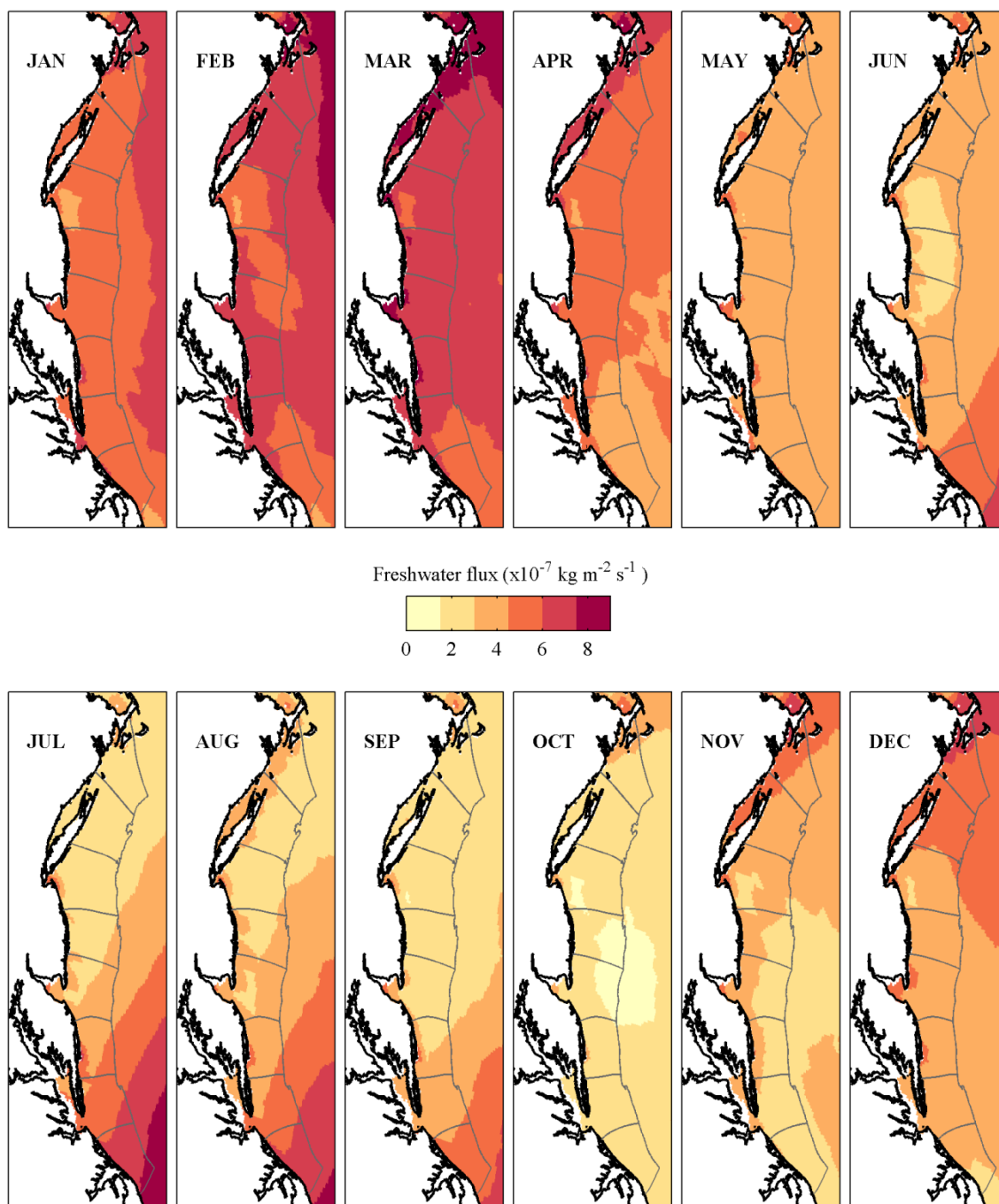
Figure 9-15: Monthly mean freshwater fluxes (kg m⁻² s⁻¹) in the MAB boxes. Positive values are into the ocean.

9.8.9   Advective Heat Flux

Great care needs to be taken when calculating the terms in the advective heat flux.
The monthly heat content advected through the north and south faces of any box is a
very large number (of the order of 10^{20} J). The difference of these (i.e. the net
alongshore advection) is an order of magnitude smaller, and is very close to the
advection through the east face. The difference of these (which is the total advection)
is an order of magnitude smaller again (see Figure 9-16). Thus, tiny rounding or
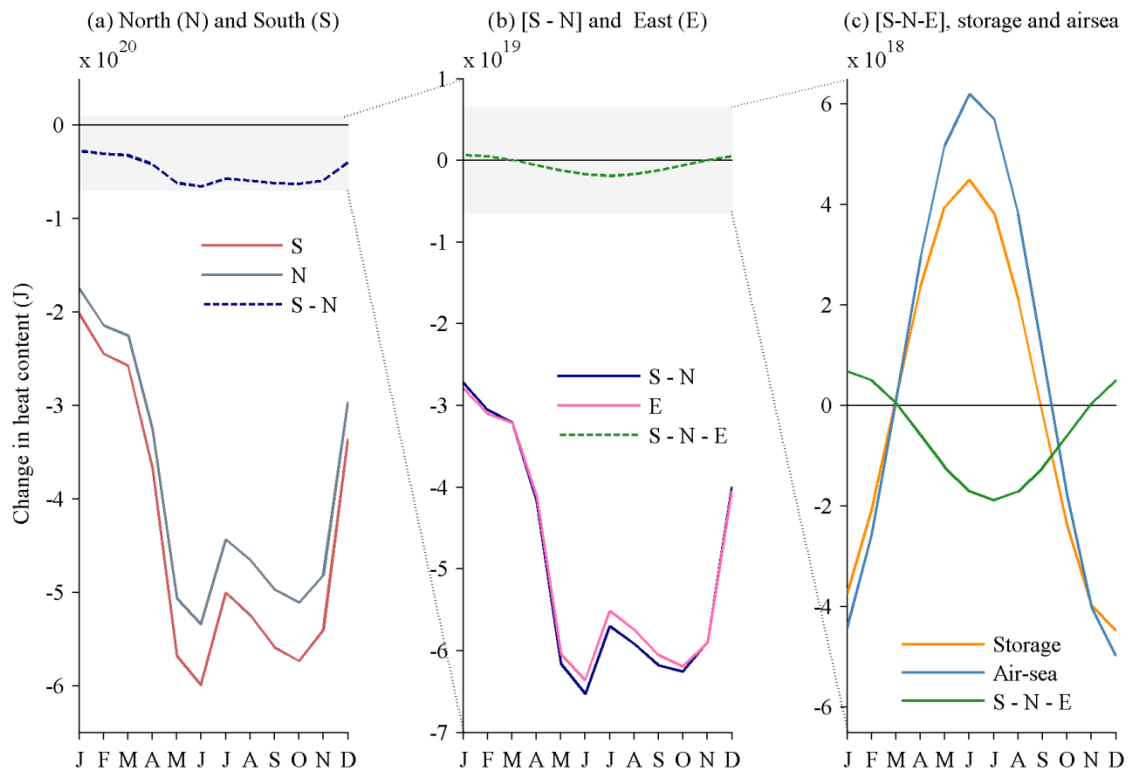
Figure 9-16: Advective change in heat content (ΔJ) for Box 1 (no river) firstly showing (a)
north face (N) and south face (S) terms, and their difference (S−N). The shaded region
indicates the axis used in the next panel; (b) the difference (S-N), the east face (E), and their
difference (S−N−E). The shaded region indicates the axis used in the final panel; (c) the final
advection term (S−N−E) along with the storage and air-sea terms. Ticks refer to midpoint of
month. Note the differing y axis scales.

truncation errors in the original north and south transports can be significant in the final value of the net advection.

 Such errors were apparent in MATLAB before care was taken to avoid them. The errors disappeared once the following procedures were followed: grouping terms with brackets even when numerically unnecessary; performing longer calculations on one line instead of breaking the equation up into multiple steps; and performing all calculations within one script instead of saving large variables and calculating their differences in a later script.

9.9 Results and Discussion

9.9.1 Overview

The Lentz (2008) value of $b = -0.07$ (cm s^{-1}) m^{-1} produced alongshore velocities that were very weak, due to the corresponding positive values of the intercept a which resulted in mean depth averaged velocities at the coast that were northward: typically about 4 cm s^{-1} . In this study a smaller slope of $b = -0.01$ (cm s^{-1}) m^{-1} was chosen as it produced more realistic results with annual mean velocities of around 3 cm s^{-1}. This is in keeping with historical observations of 3–12 cm s^{-1} for the entire MAB shelf (§2.4.1), remembering that velocities increase off-shore and a strong jet occurs at the shelf-break front; thus a mean of 3 cm s^{-1} for the region of only out to 85-m isobath is reasonable. Currents calculated from a climatology may also be

weaker than those observed in real time, due to the smoothing of density gradients during the mapping procedure.

Lentz (2008) fitted a single line to current observations out to depths of 140 m (which includes the shelfbreak jet) throughout the whole MAB, for the whole year (Lentz 2008; his Figure 3), to obtain his value of $b = -0.07$ (cm s^{-1}) m^{-1}. It is entirely reasonable to suppose that the currents in one localized region during one particular month have less cross-shore variation (and hence a lower value of b) than is observed when looking at the entire dataset, and since here the value of the intercept a is allowed to vary with each region and month. A useful follow-on project would be to develop a climatology of current measurements, and use these to choose the most appropriate values of a and b (or to uncover a new nonlinear relationship between the depth-averaged velocity (or bottom velocity) and the water depth). Alternatively, one would need measurements or reliable estimates of either bottom stress or bottom velocity everywhere in the MAB for each month of the year.

Thus a heuristic approach is used in selecting the slope b to obtain a plausible solution for MAB currents and transports. Emphasis is therefore placed on the seasonal and alongshore patterns and differences in the results rather than on their absolute values.

Four different solutions for the sea surface slope and bottom stress are obtained using (1) a heat budget with NCEP–NARR air-sea fluxes, (2) a heat budget with OAFlux estimates (3) a salt budget and (4) a freshwater budget. The two heat budgets and the freshwater fluxes produce very similar results which differ

generally by only a few percent: the heat budgets differ mostly by 2–3%, while the

freshwater budget differs from each of those 4–5%. The NCEP–NARR air-sea fluxes

in general give slightly larger values for the sea surface slope than the OAFlux

estimates, and the freshwater budget gives slightly smaller values for the sea

surface slope than for either heat budget.

The freshwater budget results are closer to the results of the NCEP–NARR version

of the heat budget than the OAFlux version of the budget. The salt budget differs by

a much larger amount: the percentage differences are generally between 15–20%.

Values for the salt content are about 30 times smaller than the freshwater content,

but their monthly *difference* is the same order of magnitude, leading to much more

noise in the annual salt budget signal (Figure 9-17). Therefore, only results for the

heat budget using NCEP–NARR air-sea fluxes and the freshwater budget are

presented here.

It is possible that any errors within the model will amplify from box to box, leading

to values further and further from reality as one moves southwards. To test this

theory, the model was also reconfigured to allow any box to be the starting position,

and if at neither end, values are calculated outwards. Thus one would assume that

starting in either Box 4 or Box 5 would produce the smallest overall error, as the

errors can only propagate for four or five boxes, not 8. However, only minor

differences in the output values (sea surface slope and bottom stress) occur for any

start box, (except for Box 8 which is clearly a different regime from the typical MAB

scenario). Varying other parameters (r, δ_s, δ_b, ρ_0) did not produce startlingly different results.

No attempt is made here to calculate error bars for output results. The long list of assumptions and simplifications that go into the calculations make any realistic attempt impossible. The climatology itself, while having error estimates in the form of RMS values, is a smoothed, mean field, and is intended to be a first guess at the ocean conditions, rather than a realistic snapshot in any point in time.
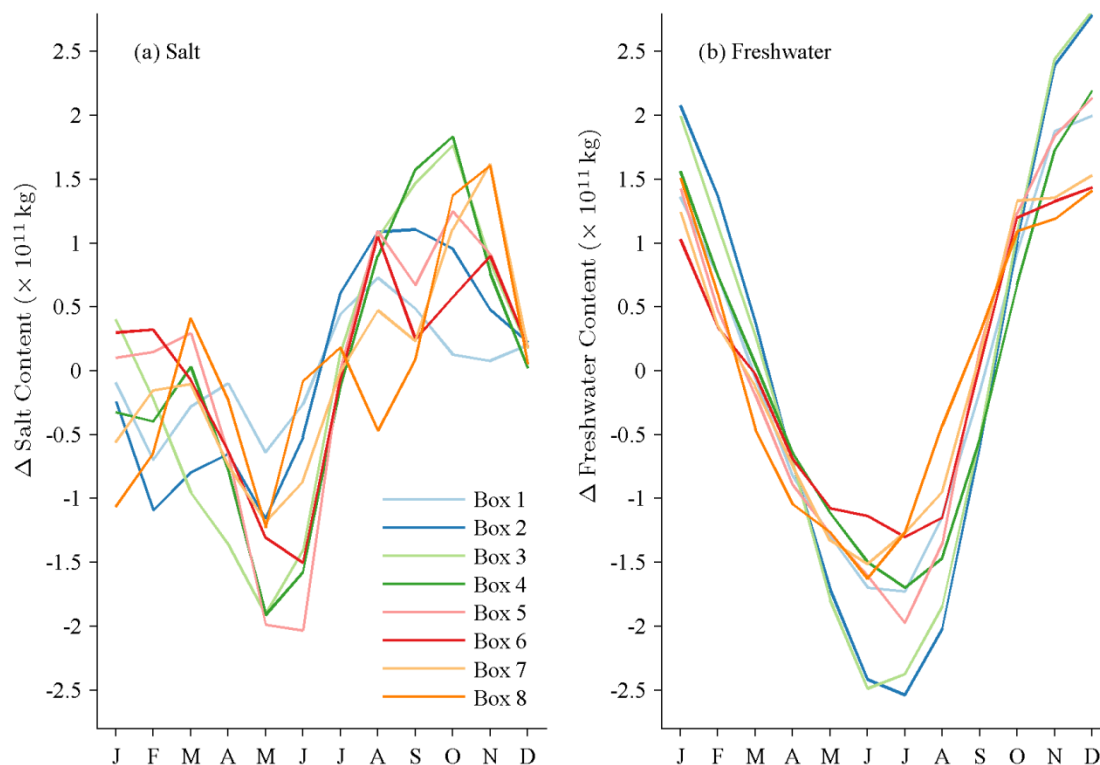
Figure 9-17: The change in (a) salt content and (b) freshwater for each box (in units of 10^{11} kg). Month ticks refer to the mid-point of the month.

9.9.2 Alongshore Sea Surface Slope

In this study, the alongshore sea-surface slope is allowed to vary with each box, and with each month, unlike most previous studies which use a single constant value. Results range from -4.3×10^{-7} to $+1.5 \times 10^{-7}$ (Table 9-6), with the following general trends: a positive gradient (sloping upward toward the north) in the northern MAB during the cooler half of the year; a negative gradient in the summer months; a negative gradient in the central MAB; and a large negative gradient approaching Cape Hatteras (Figure 9-18). In the cooler months, a minimum in sea-level appears around Line 5 (north of Delaware Bay), where sea-level is up to 2.2 cm lower than at Line 1 (Cape Cod).

The strong slope in the Box 8 is consistent with the cross-isobath flow known to occur in this region, as the MAB waters turn offshore to merge with slope and Gulf Stream waters. Considering the MAB north of Line 8, the overall change in sea-level height from Cape Cod is negative (sloping down to the south by up to 2 cm) during December–March; no overall slope in November; and larger increases to the south during rest of the year (of up to 2.5 cm) (Figure 9-19).

Historically, the sea-surface slope throughout the MAB has been estimated to be of the order of 10^{-8} to 10^{-7} (i.e. 0.1–1 cm in 100 km). These numbers are generally based on two-dimensional models located in the northern MAB, and using temporally and spatially uniform values for variables such as the wind stress components and density gradients. However, the wind stress is not constant (Figure

9-9), and neither is the orientation of the coastline; nor are the alongshore or across shore density gradients. Thus it is not surprising that the results presented here show seasonal and alongshore variation.
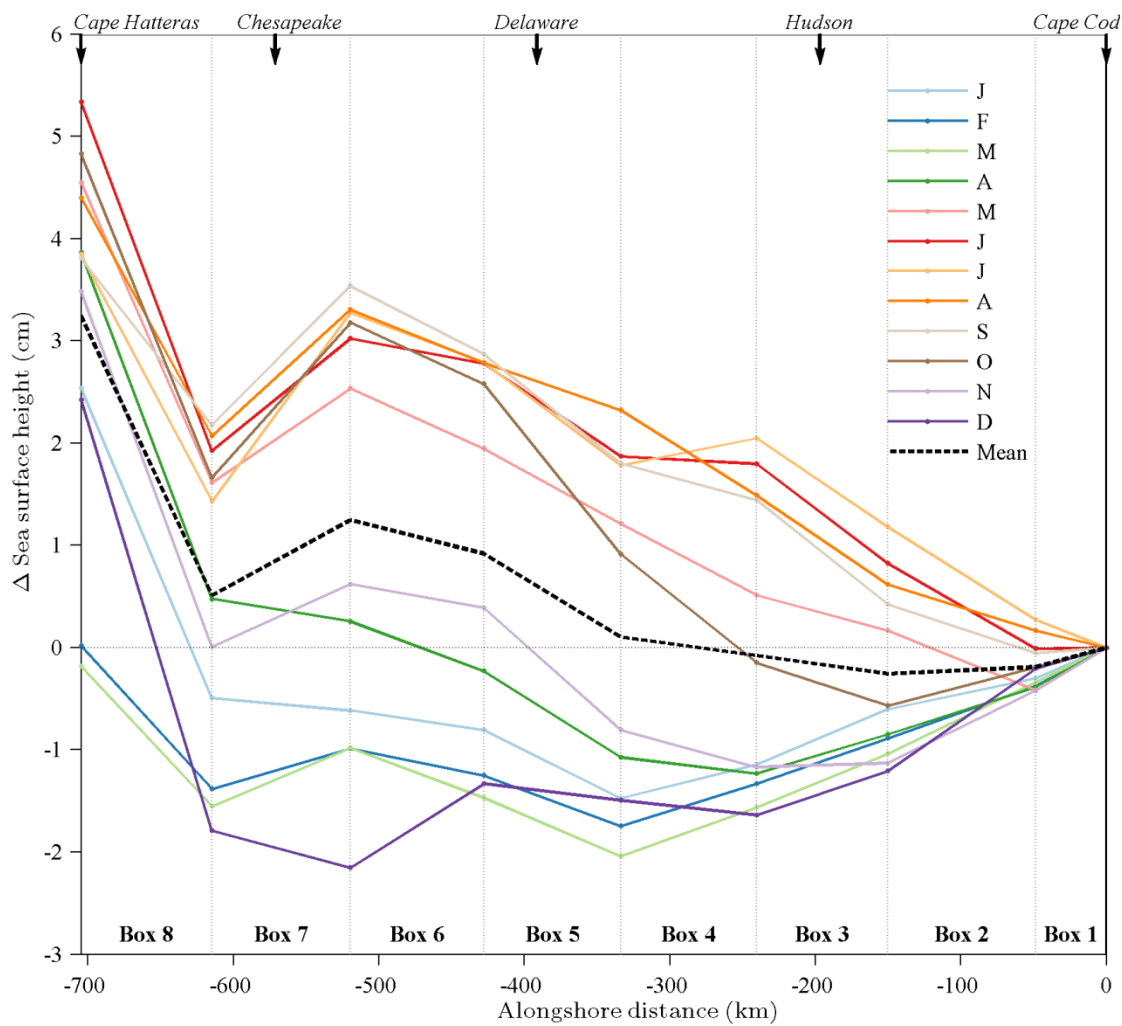
Figure 9-18: Alongshore sea-surface height (cm) at the 85-m isobath displayed as change in height (cm) from Line 1. (Inferred from the heat budget).

Csanady (1979) estimates of sea level height in spring and summer reaching from the Grand Banks to Cape Hatteras. An overall negative gradient is apparent in his figures between Nova Scotia/Gulf of Maine region and the MAB/Cape Hatteras
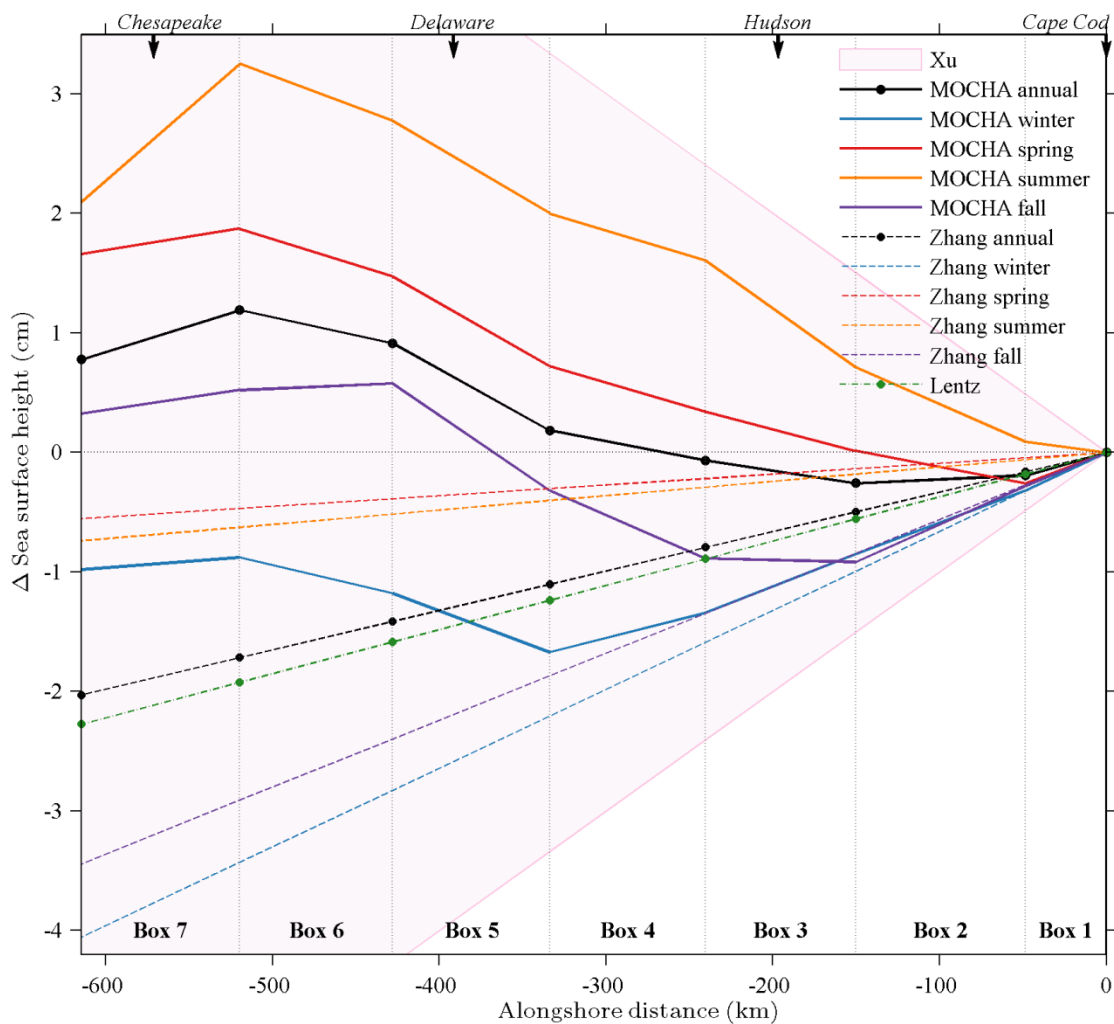
Figure 9-19: Alongshore sea-surface height (cm) at the 85-m isobaths plotted with previous estimates displayed as change in height (cm) from Line 1 (at Cape Cod). Monthly MOCHA results (inferred from the heat budget) are averaged into seasons (solid lines), the annual mean is plotted in black. Seasonal values from Zhang et al. (2011), are plotted in dashed lines with color corresponding to the MOHCA season, (data kindly provided by Gordon Zhang, WHOI); The Lentz (2008) value representing a slope of 3.7×10^{-8} is depicted by the green dashed line. Xu and Oey (2011)'s range of $\pm 1 \times 10^{-7}$ is shaded in pink.

region, however the surface heights *within* the MAB shelf display a similar pattern
to the results presented here. An increase in sea level height from Cape Cod to Cape
Hatteras of about 3 cm is evident in both spring and summer, with a local minimum
in SSH occurring in the central MAB, and a marked increase in height just north of
Cape Hatteras. The local minimum is less pronounced in summer than it is in
spring. All of this is in keeping with the results estimated from MOCHA.

The often quoted value of 1.44×10^{-7} from Scott and Csanady (1976) is based on
observations taken south of Long Island during 25 days in September 1975 in 32 m
of water. Our September value in this region (Box 2) is -0.4×10^{-8}, although the
slope is positive here from October through April (Table 9-6). Scott and Csanady
(1976) compare their value to measurements from geodetic levelling that cites a 7-
cm level difference between Boston and Atlantic City, which happens to be the same
as theirs. They do note however, that they feel the agreement is fortuitous, given the
low level of accuracy in geodesic measurements. It is worth noting, however that
such a difference is apparent in Csanady (1979)'s figures; however the majority of
this drop occurs between Boston and Cape Cod: it is not a constant gradient. It is
also worth noting that offshore of Atlantic City is the location of the local minimum
seen both in Csanady (1979) and in the cooler half of the year in this work (Figure
9-18), so any results measuring the slope from Boston to Atlantic City are not going
to be representative of the MAB shelf (i.e. from just Cape Cod to Cape Hatteras).

Hopkins (1982) finds a summer value of 0.227×10^{-7} in summer, and a value of -0.038×10^{-7} in winter, these signs in keeping with the results found here. Lentz (2008) calculates a value of 3.7×10^{-8}, noting that this is from the region north of Chesapeake Bay.

More recent estimates that have looked at the seasonal variation in the sea-surface slope show a similar pattern to the results found here: Zhang et al. (2011) conduct a 2-D study a region of the New England shelf break (see §7.8.2 for further details) and find that fall and winter sea-surface slopes are considerably more positive than those in spring and summer (they do not observe negative gradients). Xu and Oey (2011), on the other hand, show a consistent switch over the years between a positive gradient of about 1×10^{-7} in the winter, and -1×10^{-7} in the winter.

Seasonal averages of MOCHA sea-surface slope are calculated and converted to change in sea-surface height (from Line 1). These values are compared to those of Zhang et al. (2011), Xu and Oey (2011), and Lentz (2008). All MOCHA values lie within the Xu and Oey (2011) envelope (-1×10^{-7} to 1×10^{-7}), and wintertime values in the northernmost boxes are similar to the other estimates (Figure 9-19). The annual mean MOCHA estimate diverges from other estimates in that it predicts an increase in sea-surface height from Cape Cod to Chesapeake Bay.

The negative gradient in the northern boxes during summertime is due mostly U_{bc} term in Eqs. 9-41 and 9-44. During the summer when the thermocline is present, cooler waters to the north results in a positive along-shore density gradient (Figure

9-7), whereas during the rest of the year, the salinity dominates the density

gradient, and saltier waters in the south produce a negative along-shore density

gradient.

Table 9-6: Along-shore sea surface slope from the MOCHA heat budget (using NCEP–NARR air-sea fluxes). Values are $\times 10^{-8}$.

| Box | Month | | | | | | | | | | | | Annual |
	Jan	Feb	Mar	Apr	May	Jun	Jul	Aug	Sep	Oct	Nov	Dec	Mean
1	7	7	5	7	8	1	−5	−2	2	4	9	4	4
2	3	5	7	5	−5	−8	−9	−5	−4	3	6	9	1
3	6	5	6	4	−5	−10	−9	−9	−11	−6	0	4	−2
4	3	4	4	−2	−7	−2	1	−9	−5	−12	−5	−2	−3
5	−6	−5	−5	−8	−8	−8	−10	−5	−10	−16	−12	−1	−8
6	−2	−3	−5	−5	−5	−3	−4	−4	−7	−6	−2	9	−3
7	−4	3	4	−5	5	6	15	9	12	11	2	−8	4
8	−31	−16	−16	−35	−29	−32	−24	−23	−18	−32	−35	−43	−28

9.9.3 Bottom Stress

Bottom stress is calculated from the intercept a (Table 9-7) and the slope b from Eq. 9-25. Lentz (2008a) found a value of -1.8 cm s^{-1} for a, using a slope of $b = -0.07$ (cm s^{-1}) m^{-1}. Here, b was set to -0.01 (cm s^{-1}) m^{-1}, and a allowed to vary in each box and month (Table 9-7). Values are typically negative and tend to lie within -3 and 1 cm s^{-1}.

Table 9-7: The unknown intercept a (cm s^{-1}), rounded to 1 decimal place.

Box	Month											
	Jan	Feb	Mar	Apr	May	Jun	Jul	Aug	Sep	Oct	Nov	Dec
1	−0.5	−0.8	−0.8	−1.4	−2.3	−2.6	−1.9	−2.0	−2.3	−2.3	−2.2	−1.1
2	−0.6	−1.1	−1.2	−1.7	−2.0	−2.2	−1.7	−2.1	−2.6	−2.3	−2.1	−1.2
3	−0.5	−1.2	−1.2	−1.4	−1.0	−1.0	−1.0	−1.4	−1.8	−1.4	−1.9	−0.8
4	−0.3	−1.3	−1.2	−0.6	−0.1	−0.6	−1.4	−0.6	−1.3	−0.2	−1.5	−0.3
5	−0.6	−1.3	−1.3	0.0	0.1	−1.1	−2.0	−1.0	−1.5	0.3	−1.5	−1.9
6	−1.0	−0.8	−0.5	0.6	0.2	−1.3	−1.6	−0.8	−1.7	−0.7	−2.2	−5.1
7	−0.4	−1.5	−1.7	1.1	−1.8	−2.9	−3.7	−2.0	−4.4	−3.5	−2.8	−2.6
8	3.8	0.0	−1.6	6.4	−1.5	−1.7	0.8	1.7	−3.9	0.5	2.9	7.5

Bottom stress values (Table 9-8) range from -9.3×10^{-4} to 5.3×10^{-4} N m^{-2}, with a tendency for positive values during spring and summer, and negative values in winter. The most extreme values occur within Box 8.

Bottom stress estimates from the different solutions are more variable that the sea-surface slope estimates: differences are typically 50–150%, and up to 3.7×10^{-4}, occur between NCEP–NARR and OAFlux heat budget estimates of bottom stress.

However, the same patterns exist: NCEP–NARR and OAFlux results are more

similar than either are with the freshwater budget, with the NCEP–NARR results

being more similar to freshwater than OAFlux.

Table 9-8: Bottom stress ($\times$ 10^{-4} N m^{-2}).

Box	Month											
	Jan	Feb	Mar	Apr	May	Jun	Jul	Aug	Sep	Oct	Nov	Dec
1	−2.8	−3.3	−0.2	3.1	0.9	−3.0	−5.9	−5.8	−5.2	−2.1	−2.8	−2.8
2	−1.4	−1.4	−0.6	0.9	2.0	3.0	1.4	2.6	0.0	0.1	−1.5	−2.0
3	−3.4	−2.2	−0.9	0.4	2.2	4.1	4.4	3.7	2.1	0.0	−4.3	−4.9
4	−2.8	−1.7	−0.7	0.2	1.6	2.8	−0.2	0.1	−0.5	−1.6	−3.4	−3.9
5	−1.6	−2.3	−0.4	1.3	3.0	2.2	−0.4	0.7	1.1	−1.0	−1.7	−0.4
6	−1.3	−2.5	−1.5	0.6	1.7	0.7	0.8	1.4	−1.0	−1.7	−1.3	0.2
7	−5.1	−3.8	−1.6	0.2	1.5	1.6	1.1	2.8	−1.8	−2.3	−3.1	−7.9
8	−5.4	−9.3	−7.4	5.3	−3.3	−4.1	4.0	4.8	−3.5	−1.7	−5.2	−9.0

9.9.4   Along-shore Currents

Alongshore currents (Figure 9-20 through Figure 9-22) are consistent with those historically reported, although at the lower end of historical estimates (which are generally 3−10 cm s^{-1}). Depth-averaged MOCHA values on the mid shelf ($h > 30$ m) range from 1–6 cm s^{-1}, with the exception of Line 9, just north of Cape Hatteras, where currents flow pole-ward during some months of the year. Clearly the presence of the Gulf Stream is felt at this line, and pole-ward flow is also evident at depth at the off-shore portions of Lines 7 and 8. Lower values for alongshore flow will be partly due to historical estimates including the shelf/slope front region, which typically contains the strongest currents, but is not usually located within the 85-m isobath.

Alongshore currents have a similar structure throughout the year, and with alongshore position, with the exception of Line 9. Nearshore surface currents are generally the highest: currents decrease with depth, and with alongshore distance. The highest equatorward currents (of 15–16 cm s^{-1}) are observed at Lines 7 and 8, while the highest poleward currents are seen in the Gulf Stream region in Line 9 in April and December. Currents are generally weaker in winter, with the exception of Line 6. The larger currents in December at Line 7 appear to be anomalous. The bottom velocity at this location and month is the highest.
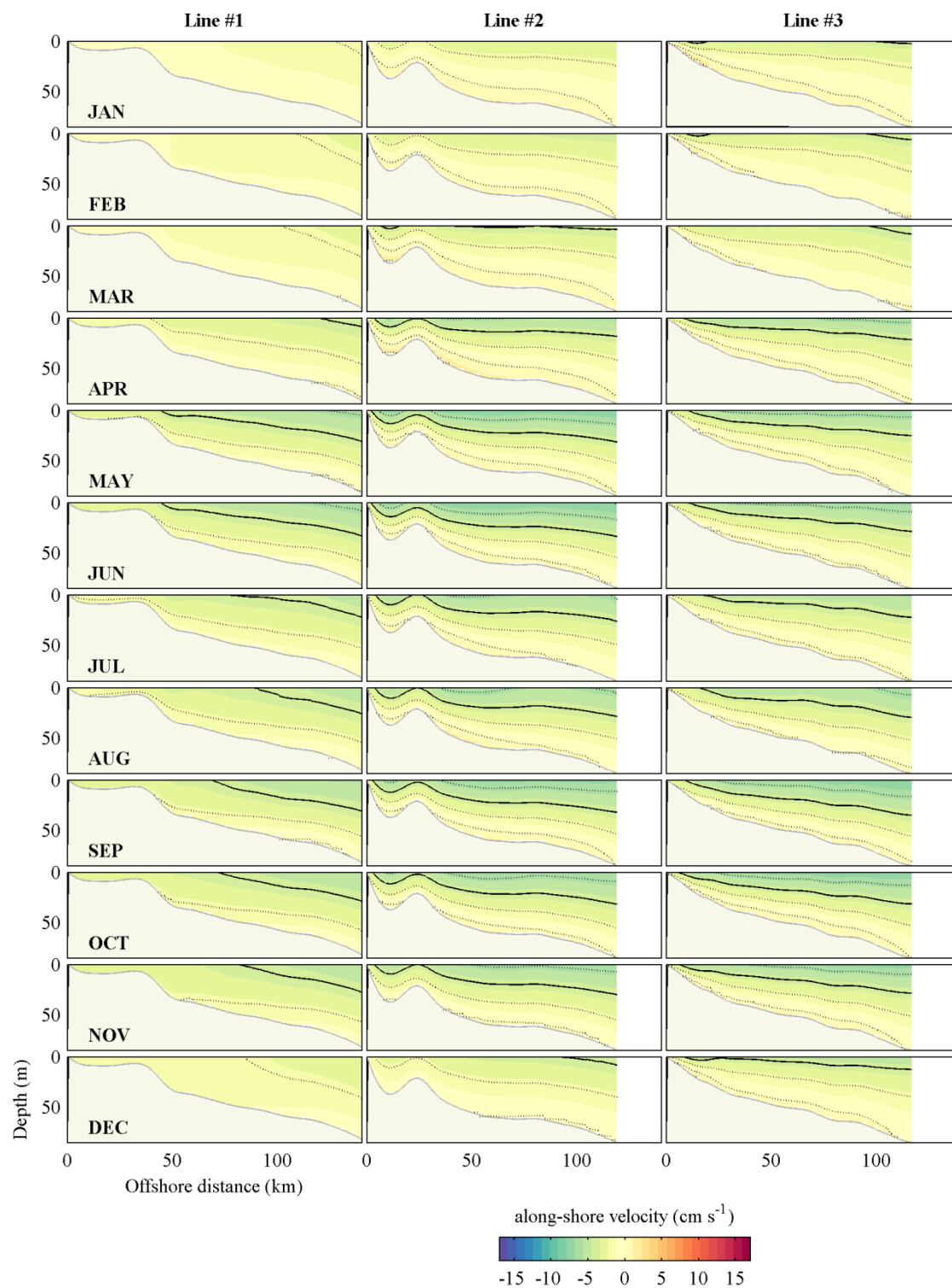
Figure 9-20: Monthly average along-shore velocity at Lines1–3 (cm s^{-1}). Contour intervals are 2 cm s^{-1}, with −4 cm s^{-1} in bold. Negative values are equatorward.
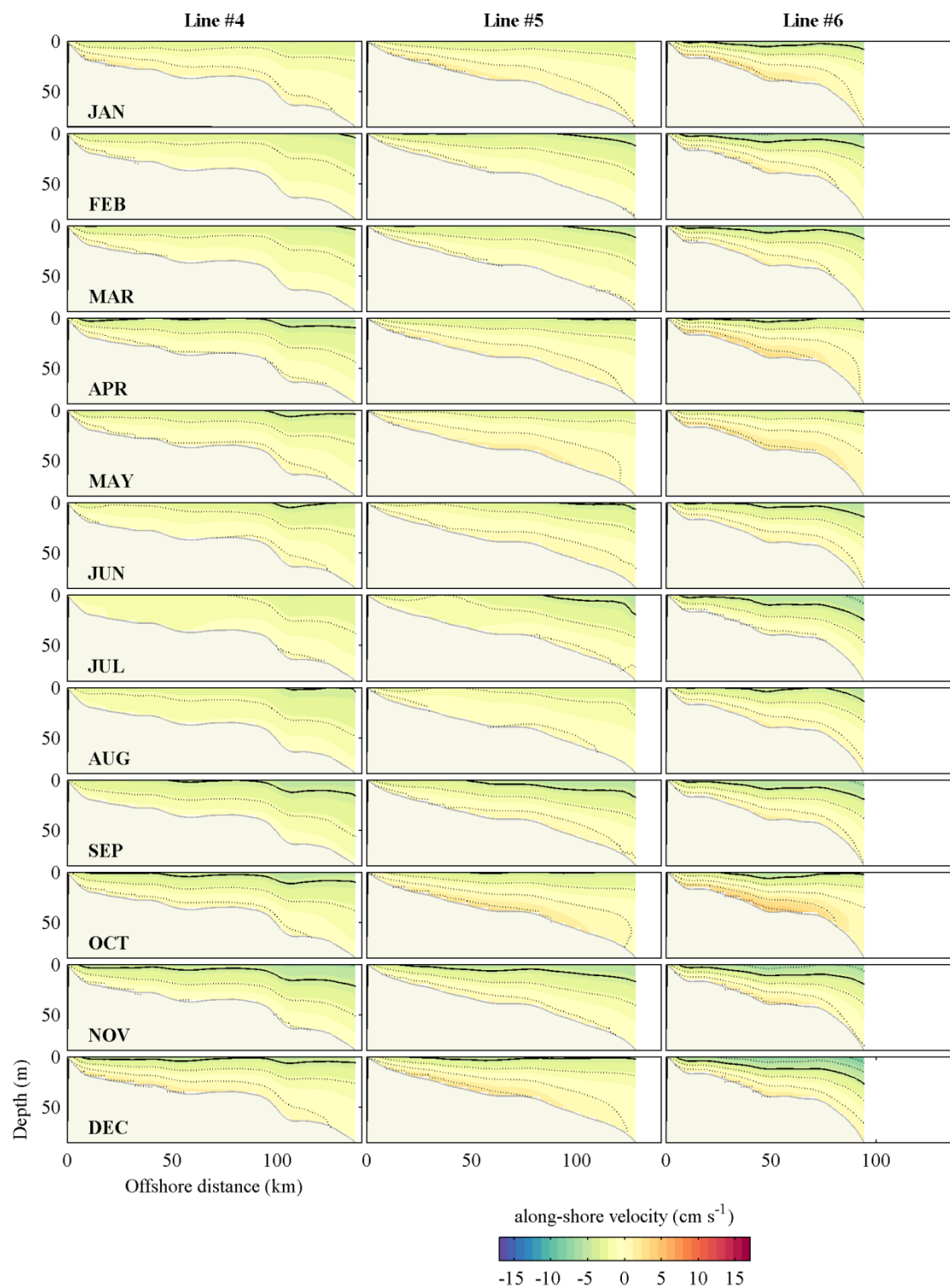
Figure 9-21: As for Figure 9-20, except for Lines 4–6.
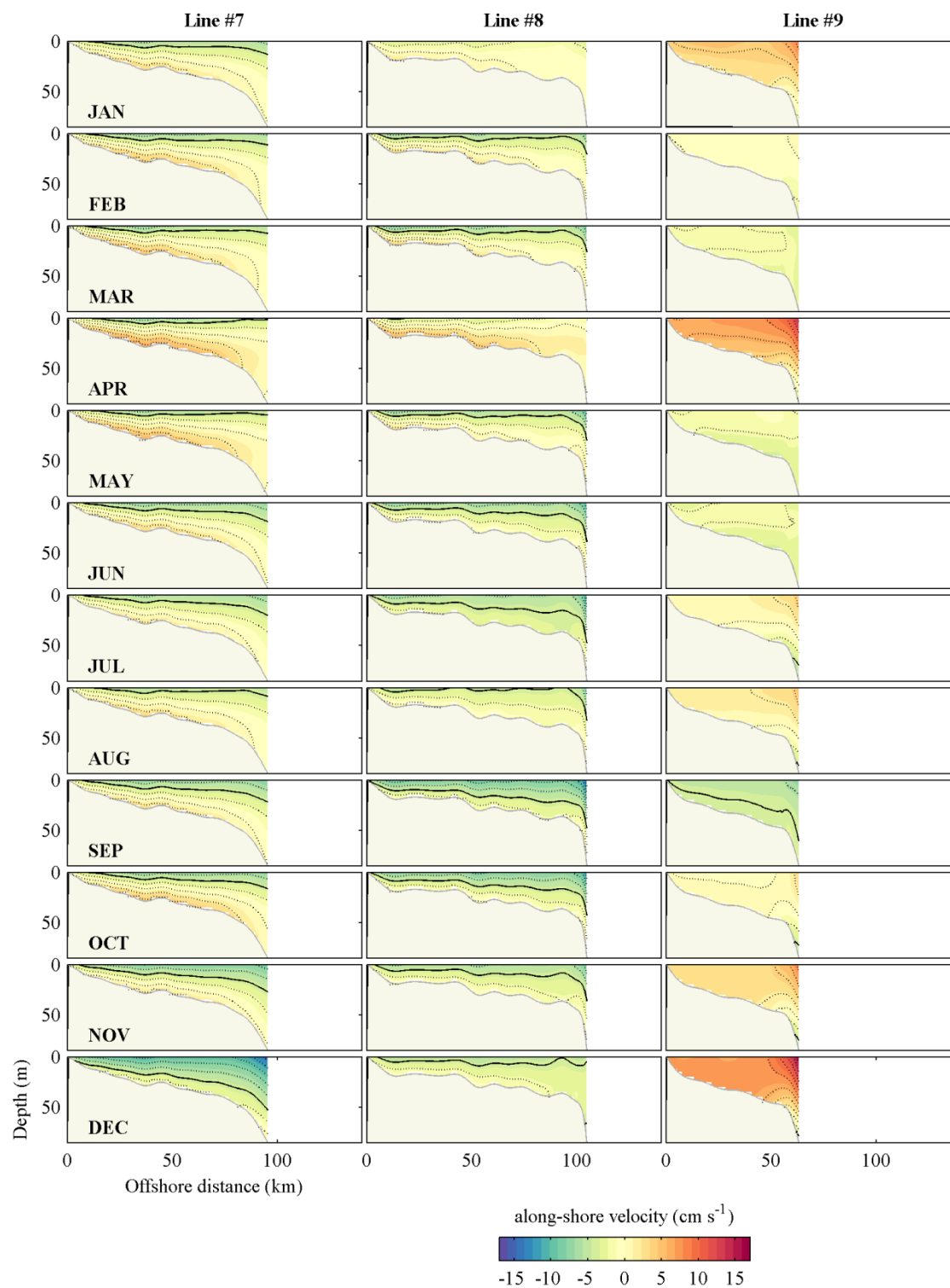
Figure 9-22: As for Figure 9-20, except for Lines 7–9.

9.9.5 Cross-shore Currents

Cross-shore currents are generally small: mostly (84%) between -1–1 cm s^{-1} (Figure 9-23), and nearly all (96%) are between -2–2 cm s^{-1}. Larger offshore currents (of up to 4.5 cm s^{-1}) are seen in Box 8, with strong onshore flow (nearly 8 cm s^{-1}) seen below the surface layer at the southern end of the box. This southernmost box is an area of strong alongshore density gradients due to the influence of the saltier, but also much warmer, waters from the SAB and from the neighboring Gulf Stream.

Bottom Ekman currents (Figure 9-24) are close to zero. Surface Ekman currents are small, but tend to be larger in winter, and their influence changes alongshore as the orientation of the coast changes, highlighting the non-uniformity of wind stress components along the MAB.

The surface geostrophic flow is determined from the barotropic flow which comes from the sea surface slope (Figure 9-18), while the alongshore baroclinic density gradient (Figure 9-7) tells us how the currents changes with depth. Thus the large alongshore sea surface slope in Box 8 generates strong surface currents, while the strong alongshore density gradients create large vertical shear in the flow. The large offshore flow in the northern half of the section, and in the surface waters of the southern half, agree well with many previous observations that the MAB waters turn offshore north of Cape Hatteras (see §2.3.7).
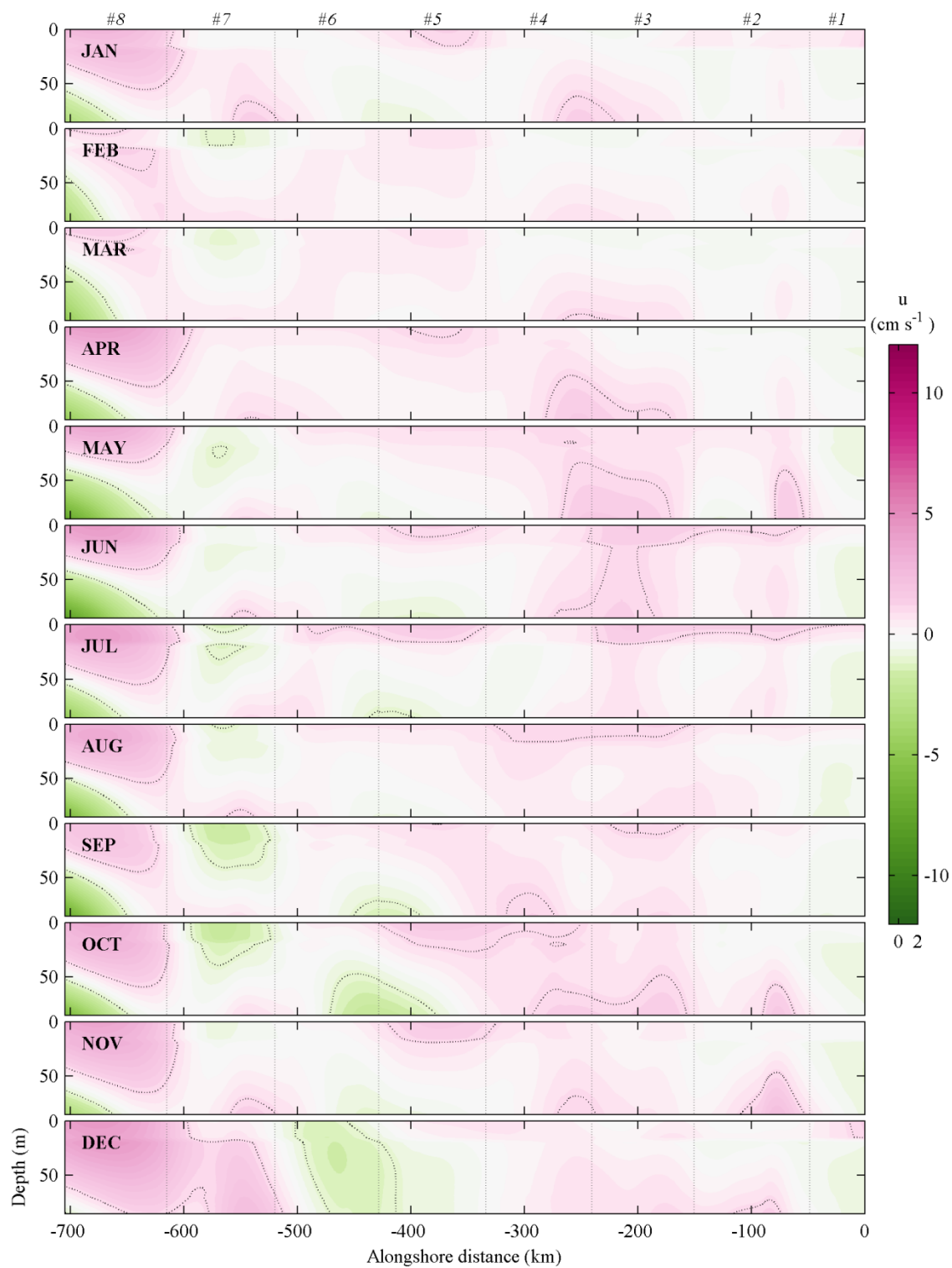
Figure 9-23: Total cross-shelf velocities (cm s^{-1}) along 85-m isobaths, with u_{bt} smoothed. Contour lines (dotted) are at 1 cm s^{-1} intervals.
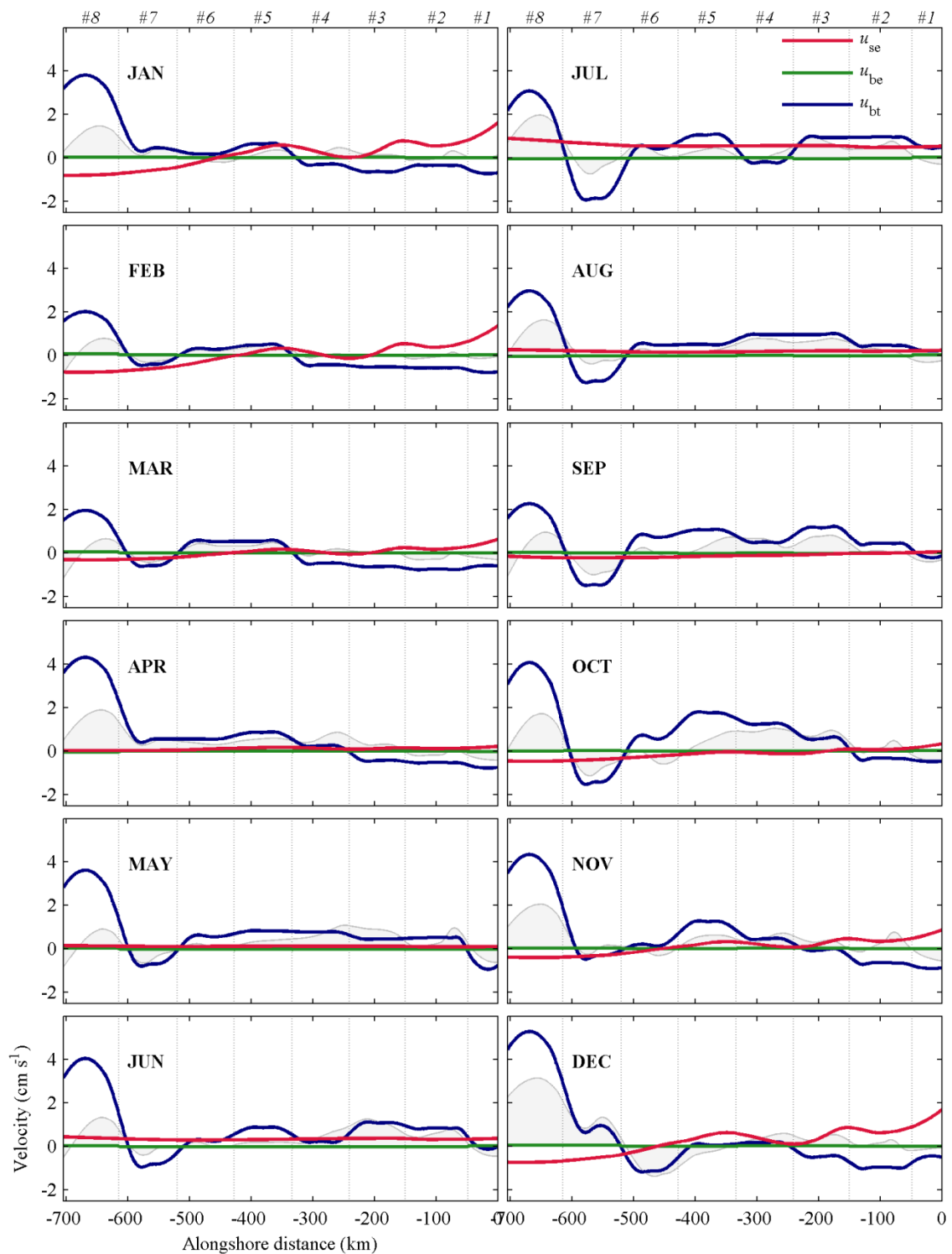
Figure 9-24: Cross-shore velocity components (cm s^{-1}): surface Ekman velocity (u_{se}), barotropic velocity (u_{bt}), and bottom ekman velocity (u_{be}). The shaded region is the depth-mean (total) velocity, plotted for comparison.
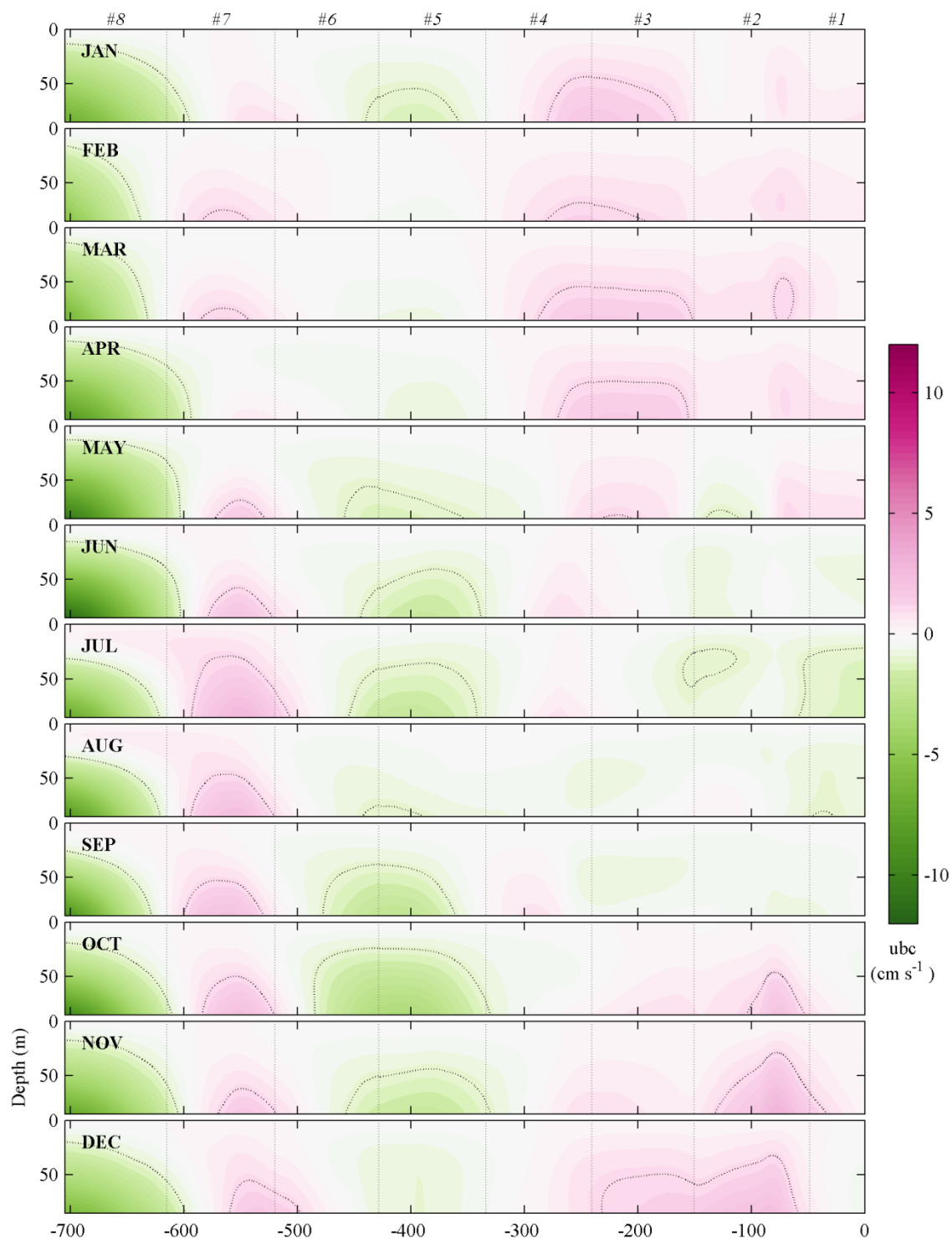
Figure 9-25: The cross-shore baroclinic (density driven) term (cm s^{-1}) that gives the vertical shear in the geostrophic velocity, relative to zero at the sea surface.

Regional patterns are evident in the baroclinic (density driven) currents (Figure 9-25). In the north, currents become more negative with depth during the summer, and more positive with depth throughout the rest of the year. Through Boxes 5 and 6, the currents become more negative with depth, while in Box 7 the opposite pattern in seen. In Box 8 the density gradient in the southern end of the MAB is larger, with vertical shear in the flow being strongly negative.

9.9.6   Transports

A question of particular interest is where the MAB water leaves the shelf: how much of the MAB volume of water exits south through Line 9 into the SAB; how much turns offshore north of Cape Hatteras; and how much "leaks" out across the shelf along the whole length of the MAB? While this study cannot definitively answer questions about transport across the shelf *break* (which generally occurs at around the 100–200-m isobath in the northern and central MAB), an assumption can be made that the transport across the 85-m isobath is an indication of the transport that would be seen at the shelf break. The results also allow investigation of the assumption that flow follows isobaths.

The volume of MAB shelf water extends considerably beyond the 85-m isobath. MAB waters extend to the shelf-break, and the shelfbreak front generally extends out, sloping up gradually, to some distance offshore (see §2.3.3). Thus the volume transports calculated here cannot be equated directly to existing estimates of total MAB water volume. The farther extant of the shelf-break front and the existence of

the shelf-break jet means that a large portion of the MAB transport is not included in these estimates.

Volume transport estimates are very sensitive to velocity measurements: small increases or decreases in the flow magnify when integrated twice to obtain volume transport. Once again, the emphasis will be on highlighting differences between seasons and spatial regions, rather than on magnitudes. River transports are included for completeness, although they contribute little to the total flow.

Even a quick glance at the volume transports displayed in Figure 9-26 shows that any assumption of fixed along-shelf transport is not supported by this model. Cross-shelf transports are very small in Box 1, which supports existing models based in this region, however the amount of off-shore volume transport varies considerably along the length of the MAB, with substantial on-shore transport occurring in Box 7 before the large off-shore flow north of Cape Hatteras (in Box 8).

Simplifying Figure 9-26 to show only the transport through the outer edge of the domain, Figure 9-27 highlights the fate of MAB shelf waters (onshore of the 85-m isobath). Outgoing flow is divided into the net flow out of the east faces of Boxes 1–7 combined (i.e. the "leaky" component), the flow through the east face of Box 8 (the offshore turning of the current to join the Gulf Stream), and the flow through Line 9 into the SAB. Each of these components is labeled with its value as a percentage of the incoming volume transport (flowing into the MAB through Line 1).

Significant variation is seen throughout the year. Incoming volume is higher during May–November, than in winter and early spring. During some months of the year, flow through Line 9 is in fact northwards, indicating that Line 9 is in a transition zone, rather than in the MAB proper, at least during those months of the year. When the transport through Line 9 is directed to the south, the percentage varies between 13% and 58% of the water coming in to the north. The onshore flow seen in several boxes in several months of the year (Figure 9-28) complicates these numbers. Clearly, the volume transport is not static, and is not bounded by isobaths: both off- and on-shore transport influence the along-shelf transport throughout the MAB.

When examining only the transport through the east faces (Figure 9-28), the tendency for MAB water to turn offshore north of Cape Hatteras is again prominently displayed. However, it is interesting to note that offshore (and onshore) transports at other boxes, while generally smaller, are still significant; and in individual cases the offshore transport in another box can be larger than that in Box 8. The months in which this occurs (February, March, May, June and September), are the months when flow is southward (rather than northward) through Line 9. This indicates that the southern edge of the MAB could be farther south than Line 9 during these months (i.e. the flow may turn offshore farther south, so the off-shore flow does not appear in our results). However, without further information, it could equally indicate that during these months larger volumes of MAB water make their way into the SAB. A further study would extend the MAB domain to the south, and include smaller boxes to build a more detailed picture of the flow in this region.

Annual mean alongshore transports decrease from 0.13–0.14 Sv equatorward, at the northern three lines down to 0.05–0.07 at Lines 6–8, while the annual mean at Line 9 is 0.02 Sv to the north. These values are lower than previous estimates (Table 9-9). This is partly due to most estimates being from cross-sections that extend out to the shelfbreak (usually the 100–200 m isobath) and thus include both a much larger cross-sectional area and the enhanced transport region of the shelfbreak jet. However, MOCHA transports are low even compared to those taken across similar cross-sectional areas: once again leading to the conclusion that MOCHA current estimates are on the low side. Notwithstanding this discrepancy, a general trend of decreasing transport along the length of the MAB is clear.

Table 9-9: Historical values for alongshore transports (Sv) within the MAB. The nearest line to each measurement is also listed.

Reference	Transport (Sv)	Cross-section	Near Line:
Beardsley and Flagg (1976)	0.17	0–100 m	2
Beardsley and Flagg (1976)	0.28	0–100 m	3
Beardsley and Flagg (1976)	0.26	0–100 m	8
Flagg (1977)	0.4	20−100 m	2
Beardsley et al. (1985)	0.38	46−120 m	1
Mountain (1991)	0.4	0−shelf/slope front	1
Biscaye et al. (1994)	0.10	0−90 m	8
Pietrafesa et al. (1994)	0.025	leaving MAB to SAB	9
Bignami and Hopkins (2003)	0.025	leaving MAB to SAB	9
Gawarkiewicz et al. (2008)	0.61	0−40 km	9
Lentz (2008)	0.64	0−125 m	1
Lentz (2008)	0.41	0−90 m	3
Lentz (2008)	0.27	0−85 m	4/5
Lentz (2008)	0.19	0−75 m	7
Lentz (2008)	0.09	0−45 m	9
Chen and He (2015)	0.52	0−200 m	1
Chen and He (2015)	0.22	0−200 m	9
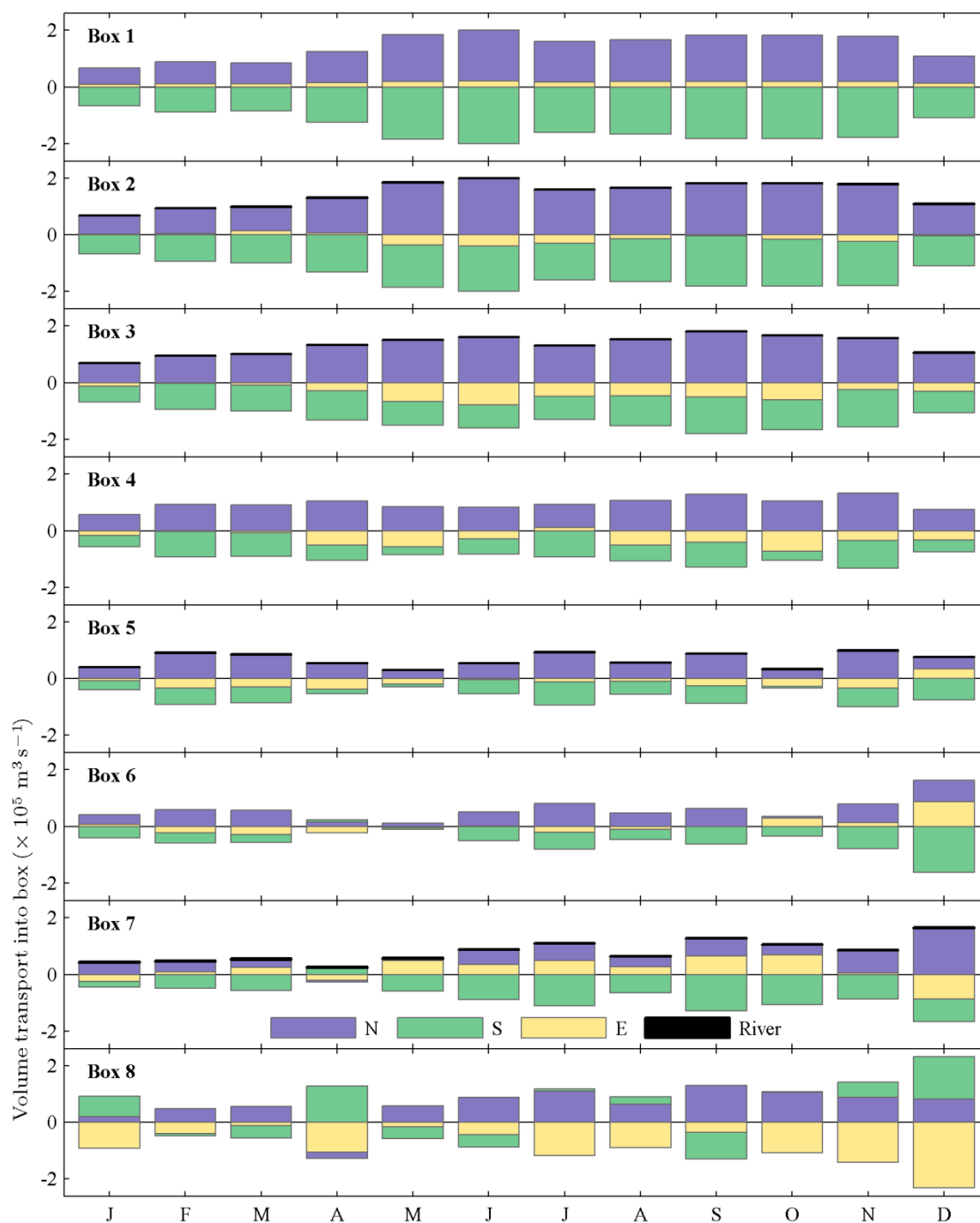
Figure 9-26: Volume transports (m³ s⁻¹) in the MAB for each box and month. Positive values indicate poleward transport. Transport through the "northern" face of each box is depicted in purple, transport through the "southern" face of each box is in green, transport through the offshore ("eastern") face is in yellow, and river input is in black. Thus going down the figure for a single month, the southern transport (green) for a box will be equal to the northern transport (purple) of the next box. The sum of the four transports within a box and month equals zero.
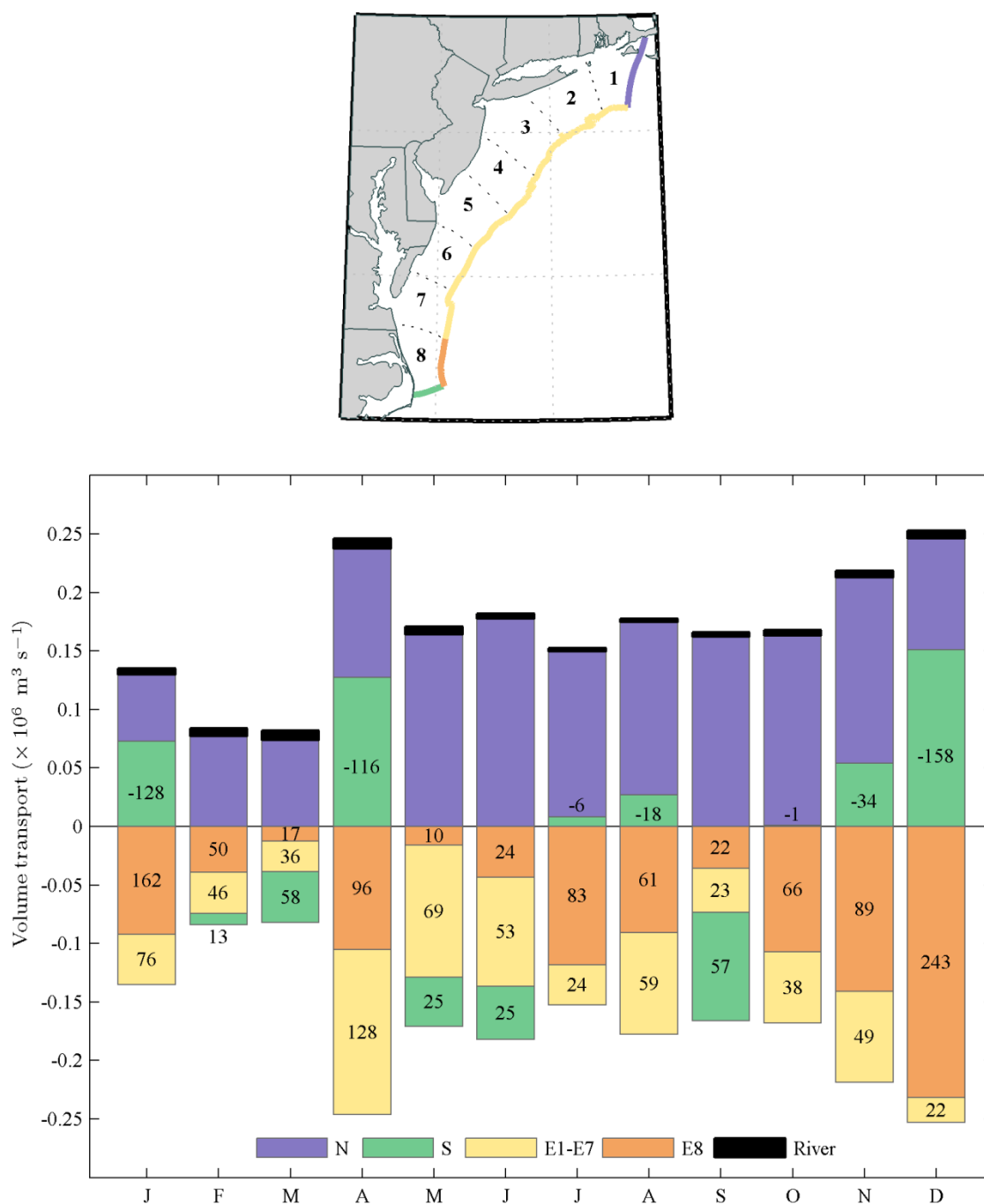
Figure 9-27: Volume transport (m³ s⁻¹) around the entire MAB. A simplified version of Figure 9-26: here only the outer faces of the entire MAB region are shown. Transport into the northern MAB through Line 1 in the north is depicted in purple, the transport out of the southern MAB through Line 9 is in green, with the transport through the offshore face of the MAB split into Box 1−8 (yellow) and Box 9 (terracotta). River transport is in black. Bars are labeled with their percentage of the incoming transport (purple). For each month, the total volume transport sums to zero.
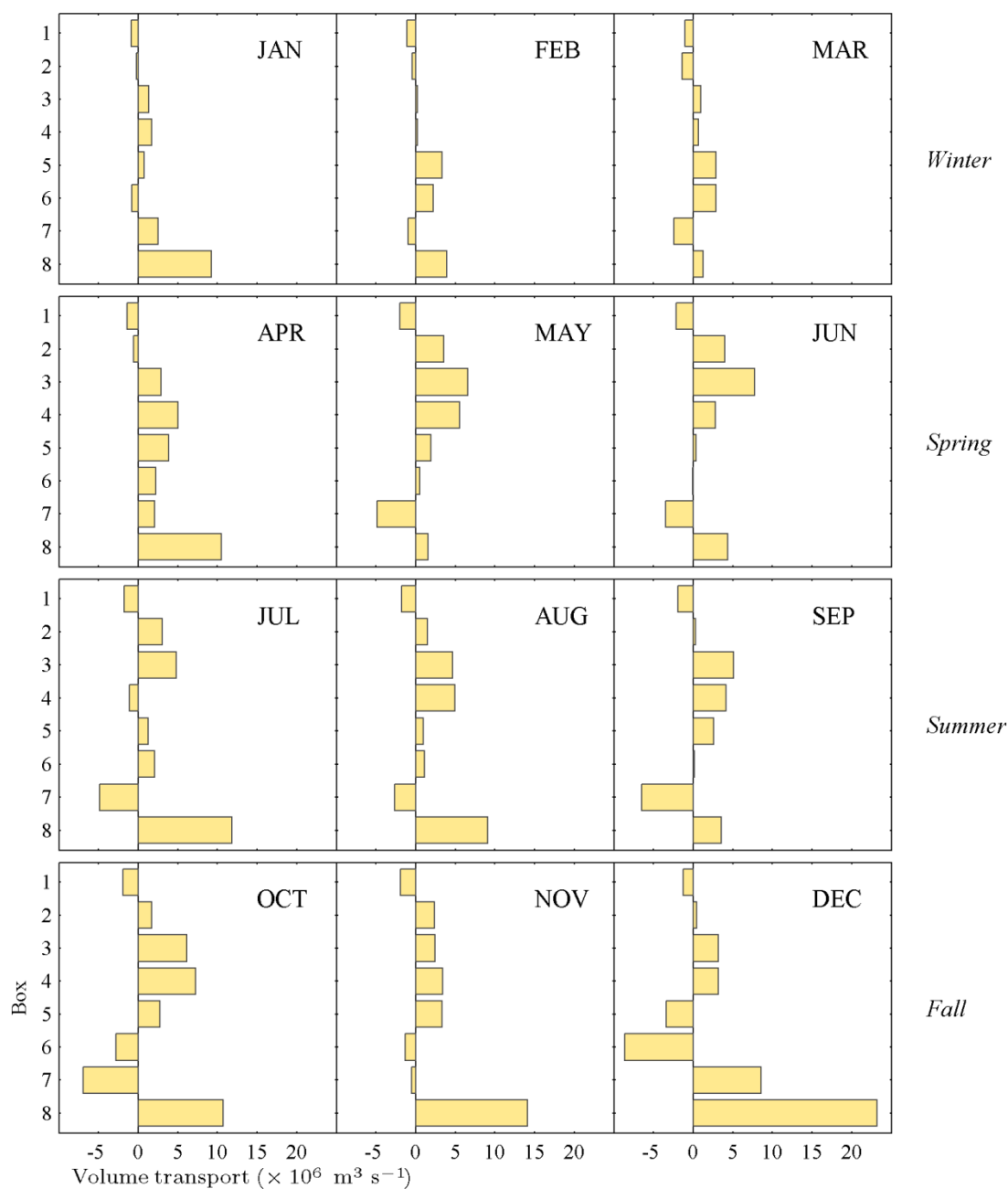
Figure 9-28: Volume transport through eastern boundary (m³ s⁻¹) for each box and month. Positive values are out of the box (offshore).

9.9.7   Heat Budget

The heat budget for each MAB box (Figure 9-29) follows the expected pattern: the change in heat storage is at a maximum during summertime (June–July) and is at a minimum during winter (December–January). The change in heat storage is nearly balanced by the OAFlux air-sea fluxes in all MAB boxes except the southernmost (Box 8), whereas the NCEP–NARR fluxes are larger, especially in winter, and thus result in a larger advective flux. The overall pattern of the advective flux is the same whether using OAFlux or NCEP–NARR air-sea fluxes: there is a negative heat content change (heat leaving the box) during summer, and a positive change (heat entering the box) during winter. For the northernmost six boxes, the advective heat change is only a small percentage of the heat storage change, however in Box 7 it increases, and in Box 8 during winter, it has a similar magnitude to both the air-sea flux and heat storage terms.

Figure 9-29 shows the total heat content change throughout the volume of each box, the heat change induced by air-sea surface flux of each box, and the total advective flux through all faces of the box (including river input). In order to compare results between boxes, each of these terms is normalized by the surface area of the box, to give heat flux in units of W m^{-1} (Figure 9-30). This clearly shows that the heat storage rate is fairly uniform throughout the MAB, and that it is the air-sea heat flux and advective heat flux that are anomalous during the wintertime in Box 8. The air-sea heat flux is more negative during the winter, and the advective heat flux is more positive. Throughout the rest of the MAB, the advective heat flux is positive for
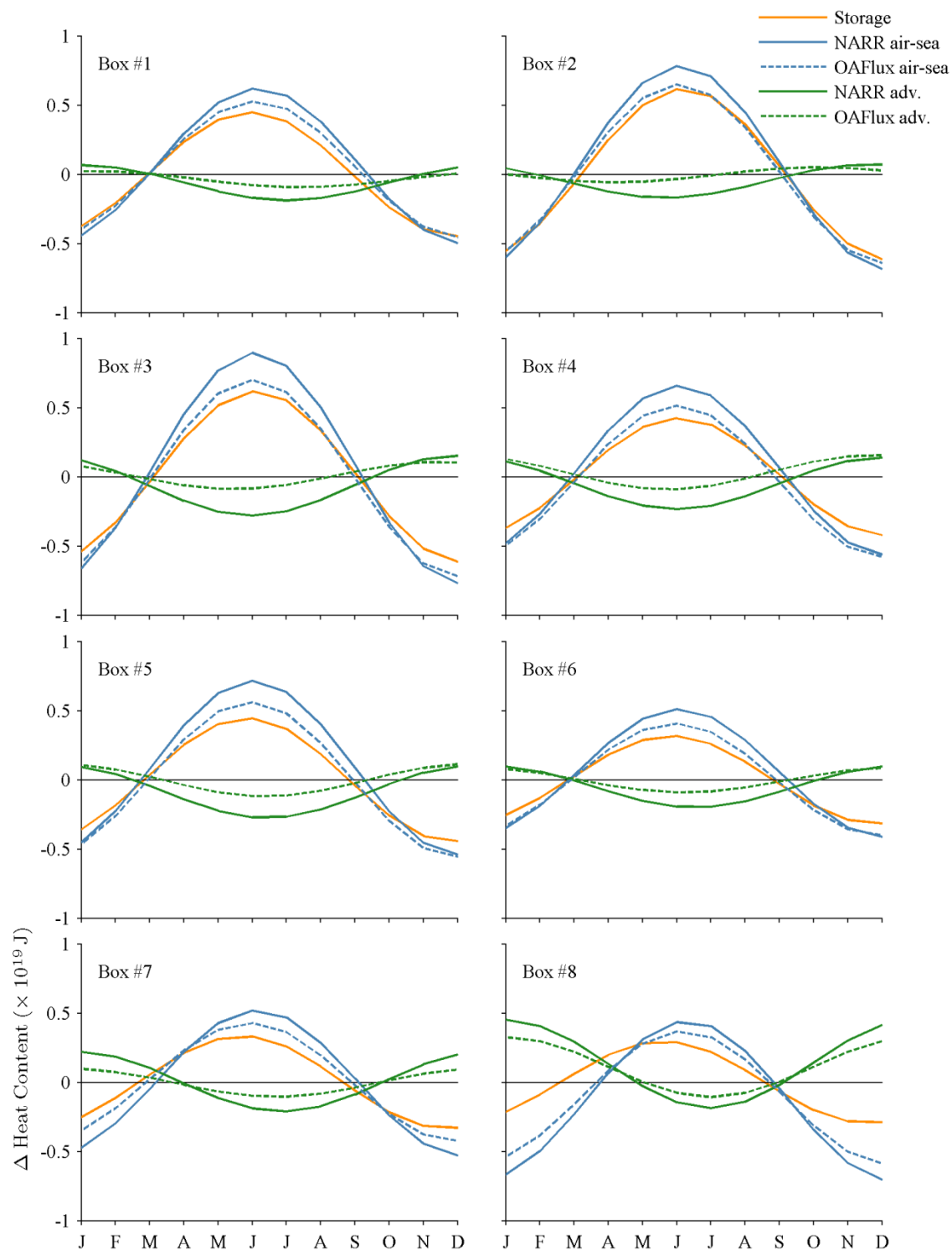
Figure 9-29: Annual MAB heat budget for each box (J): heat storage (orange), air-sea flux (blue) and advection (green). Terms calculated using NCEP−NARR air-sea fluxes are plotted with solid lines, and those using OAFlux are dashed. Month ticks refer to the mid-point of the month.

seven or eight months during the warmer part of the year (between March/April to Sep/Oct), while in Box 8, there is a positive advective heat flux only for five months (between May and September).
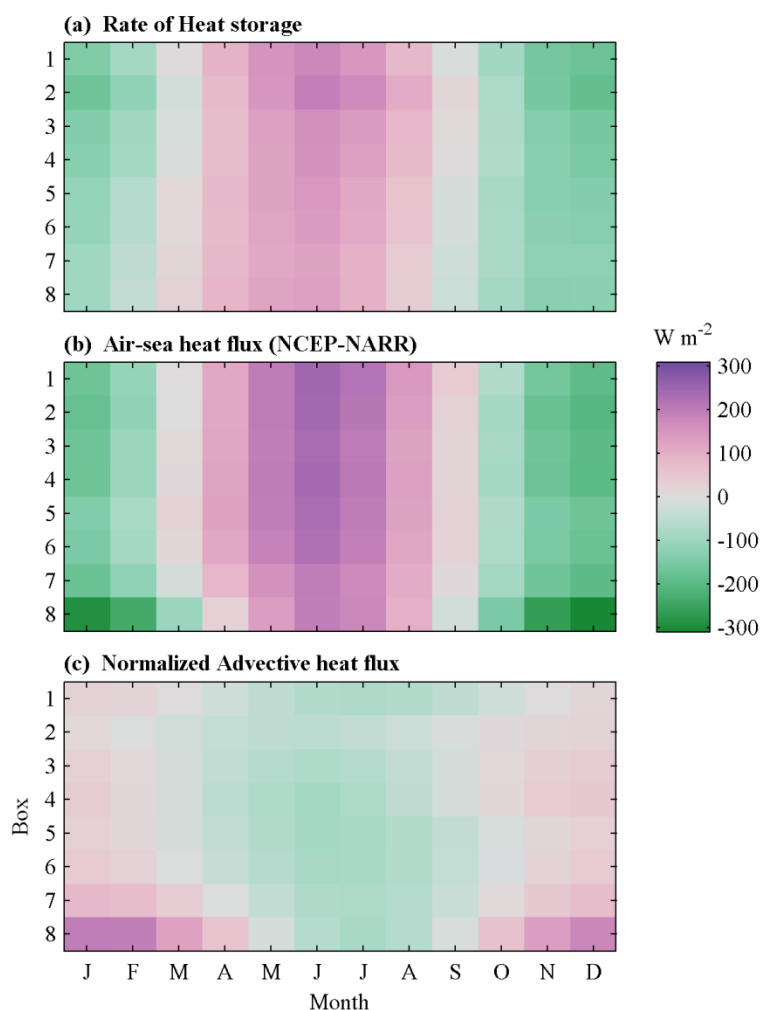
Figure 9-30: Heat budget components normalized by the box surface area (W m⁻²): (a) rate of heat storage in the volume of the box, (b) the NCEP−NARR air-sea heat flux and (c) the total advective heat flux (through all faces).

The difference between NCEP–NARR and OAFlux air-sea fluxes are larger in the summer throughout the MAB, and during winter in the southern two boxes (Box 7 and Box 8) (Figure 9-31). NCEP–NARR values tend to be more extreme: they are higher in the summer by up to 53 W m^{-2}, and more negative during winter in the southern boxes, by up to -56 W m^{-2}. The difference in advective heat flux from using the two different air-sea flux estimates, is simply the inverse of Figure 9-31, since the heat storage rate is the same in both cases.
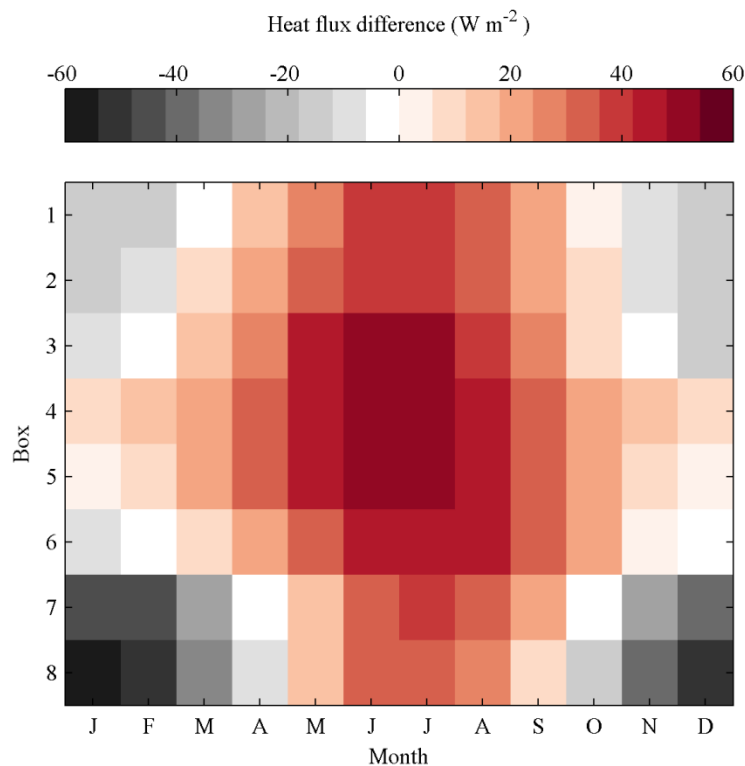
Figure 9-31: The difference in airsea heat flux estimates (W m^{-2}): (NCEP–NARR minus OAFlux). Positive values indicate a higher NCEP–NARR estimate.

The advective heat transport into and out of the box is summarized in Figure 9-32. The pattern is similar to that of volume transport (Figure 9-27). Incoming heat transports to the MAB through Line 9 are up to 2×10^{14} W. The largest heat loss through the southern end of the MAB occurs in the transition months (March and September): both lose approximately 60% of the incoming heat, across Line 9. Otherwise, the trend is for a greater percentage of the heat to be lost out of the east face of Box 8 than through all seven northern boxes during the wintertime, with more variable results throughout the rest of the year.
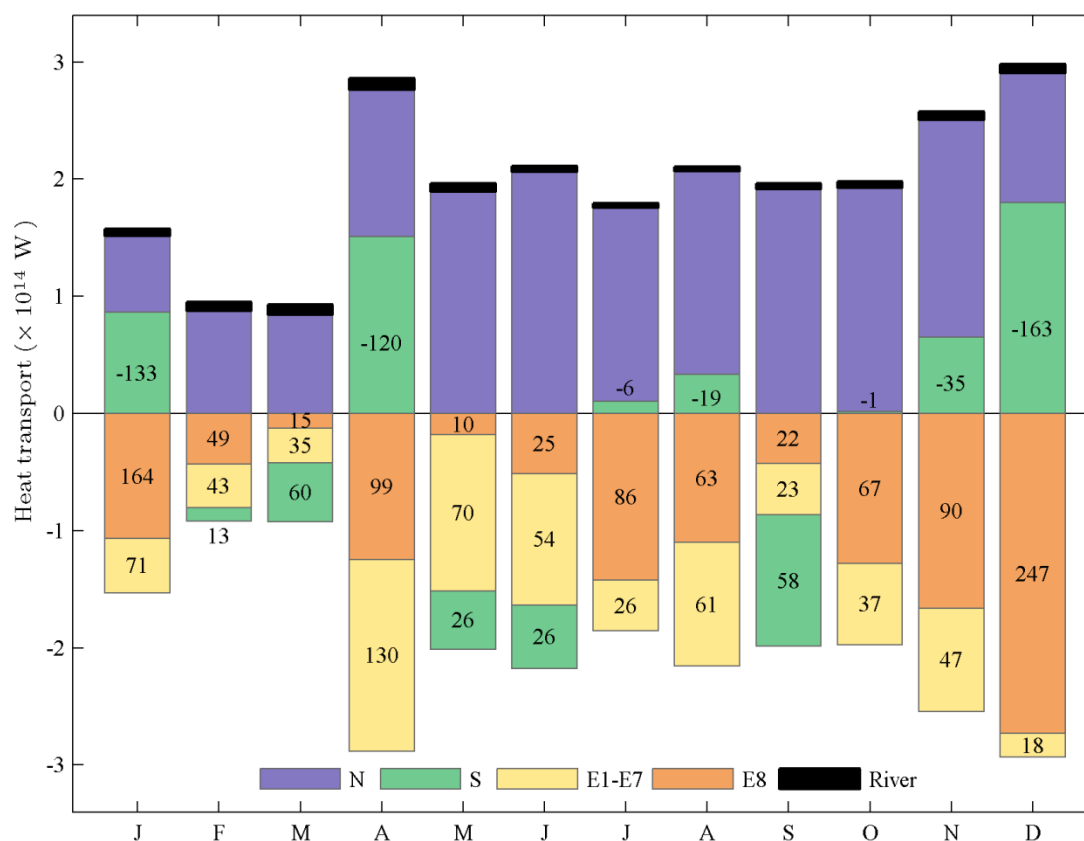
Figure 9-32: As for Figure 9-27, except for heat transport (W).

The heat transport through the east face of each individual box has the same pattern as volume transport (Figure 9-28), with values ranging from -101×10^{12} to 273×10^{12} W. The differences in the east advective heat transport depend on which air-sea flux is used, ranging from $-3.7 \times 10^{12} - 4.5 \times 10^{12}$ W (Figure 9-33). Generally speaking, transports calculated using OAFlux values are larger than those using NCEP–NARR values during spring and summer (except for in Box 3), and are variable throughout the rest of the year.
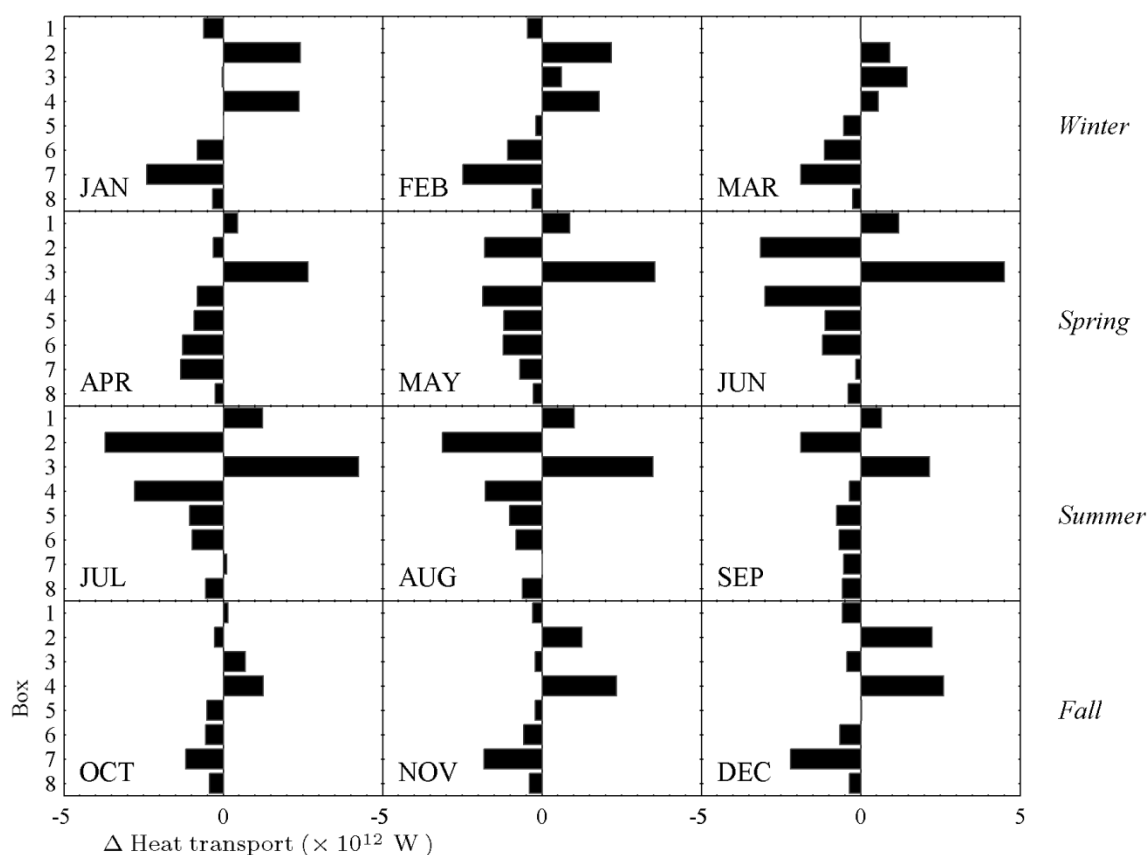
Figure 9-33: Difference between east face heat advection estimates (W): (NCEP−NARR minus OAFlux). Positive values indicate greater NCEP−NARR values.

9.9.8 Freshwater Budget

The freshwater budget exhibits a distinct annual cycle with a minimum (freshwater out of the box) in summer and a maximum (freshwater into the box) in winter (Figure 9-34). Freshwater storage is balanced almost entirely advection—the change in freshwater due to air-sea fluxes is very small: values of the order of 10^{-9}–10^{-8}, and generally no more than 1–2% of the storage and advective terms.

When values are normalized by the surface area of each box (Figure 9-35), the seasonal cycle dominates, with no consistent alongshore pattern evident. The freshwater flux throughout the MAB ranges from -7.7×10^{-6} kg m^{-2} s^{-1} in summer to $+8.5 \times 10^{-6}$ kg m^{-2} s^{-1} in winter.

The freshwater transport through each face (Figure 9-36) follows that same pattern as volume transport (Figure 9-26): offshore freshwater transport is small in the northernmost regions, larger in Boxes 3 and 4, is small in Boxes 5 and 6. It increases in Box 7, before increasing considerably in Box 8. The freshwater transport into and out of the entire MAB (keeping Box 8 separate) (Figure 9-37) displays a similar pattern as for heat transport (Figure 9-32). Incoming freshwater transport through Line 1 at the northern end of the MAB ranges from 5–17×10^{7} kg s^{-1}, and the offshore freshwater transport in Box 8 ranges from -2 to -23×10^{7} kg s^{-1}. The offshore and onshore transports of freshwater follow the same pattern as both volume (Figure 9-28) and heat.
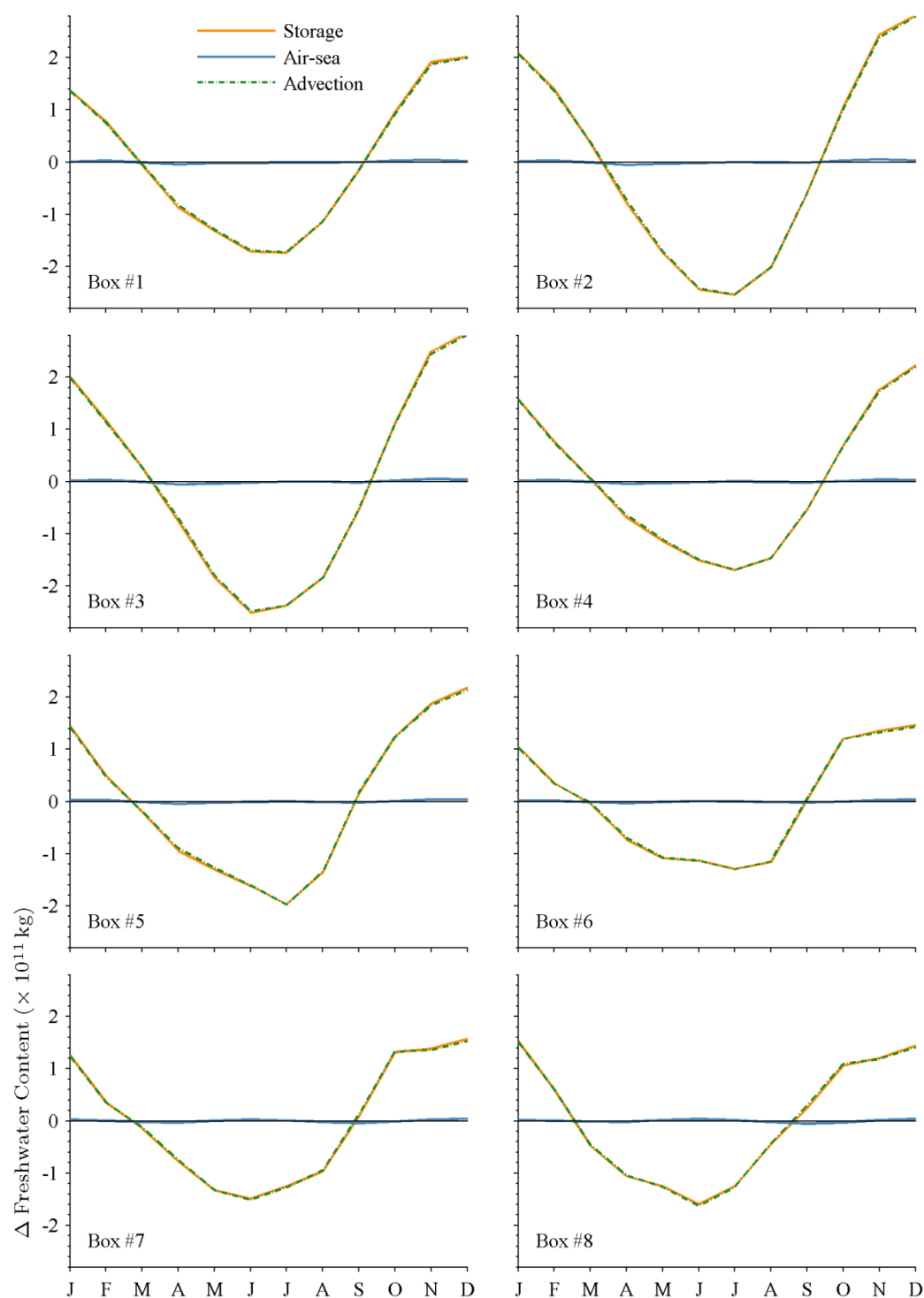
Figure 9-34: The annual freshwater budget for each MAB box (kg). The air-sea freshwater flux is plotted in blue, and is close to zero. The freshwater storage in each box volume is plotted in orange, and is very close to the total freshwater advection through all sides, plotted in a dash-dot green line. Month tick labels depict the midpoint of the month.
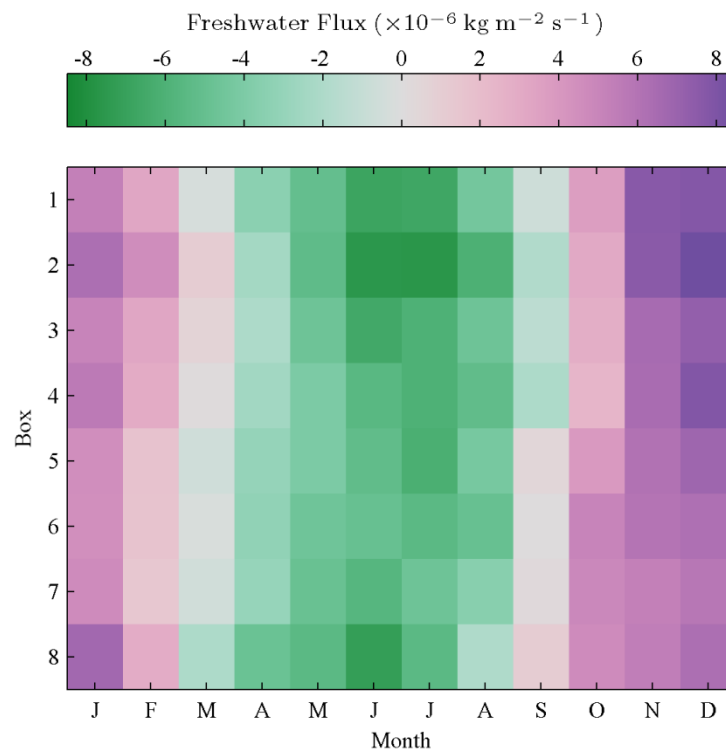
Figure 9-35: MAB freshwater flux (kg m⁻² s⁻¹) for each box and month: that is, the freshwater content change within the volume, per second, and normalized by the surface area of the box.
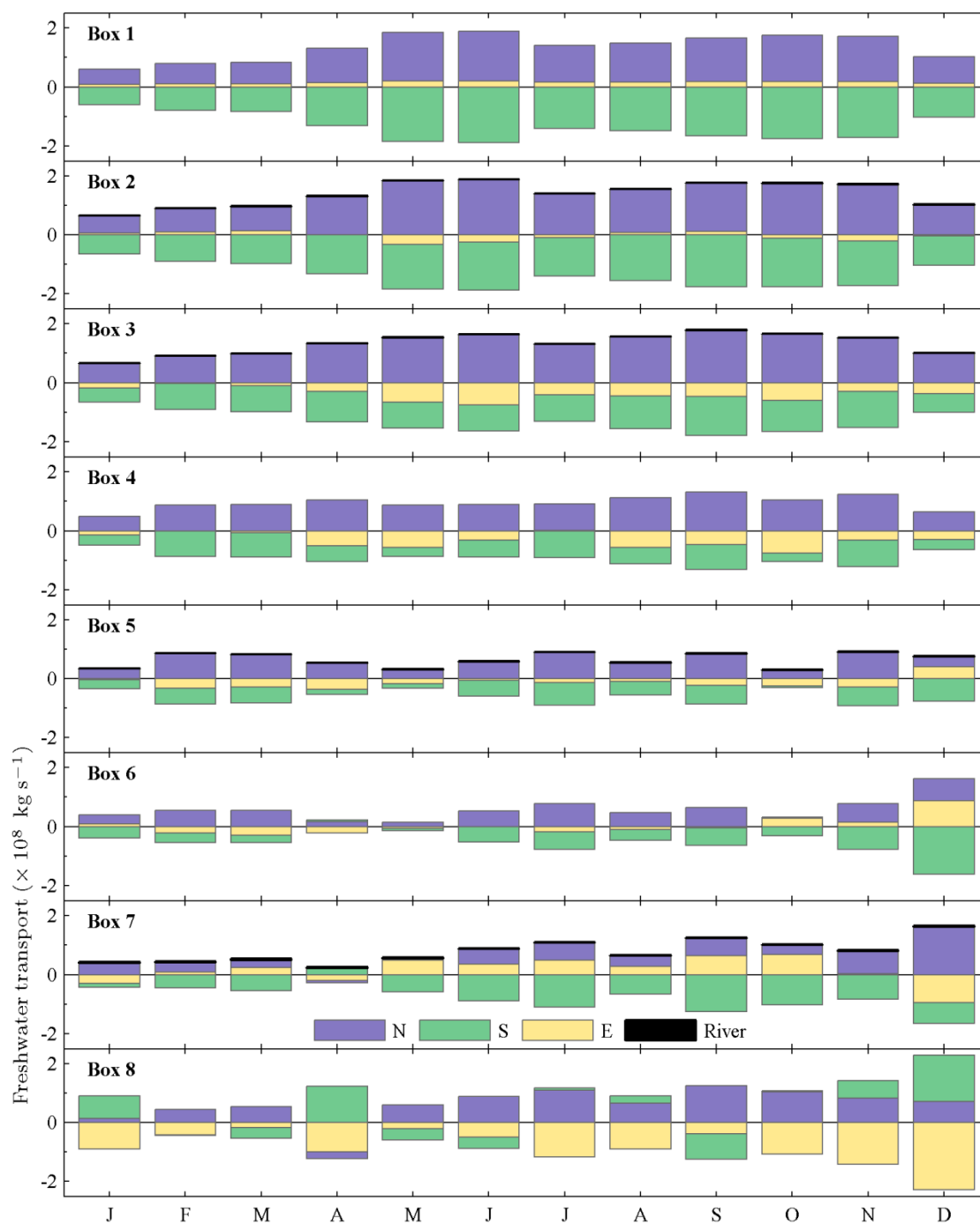
Figure 9-36: As for Figure 9-26, except for freshwater transport (kg s⁻¹).
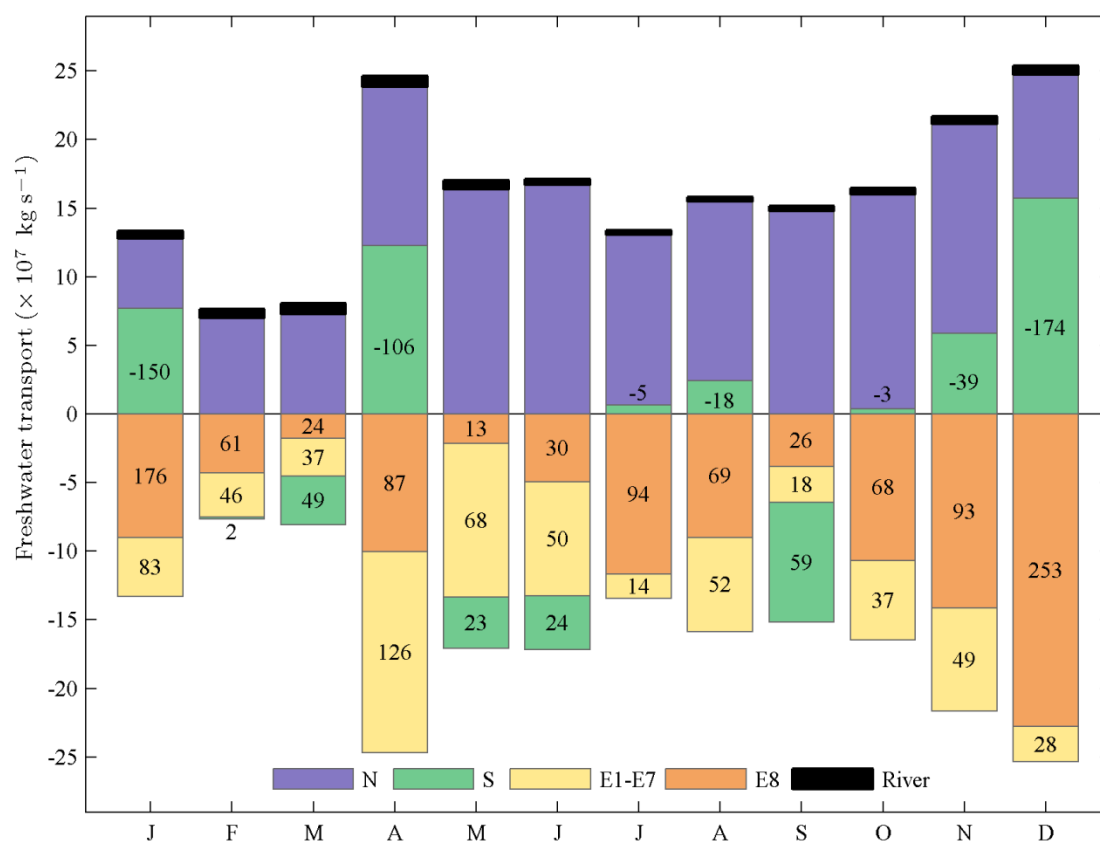
Figure 9-37: As for Figure 9-27, except for freshwater transport (kg s^{-1}).
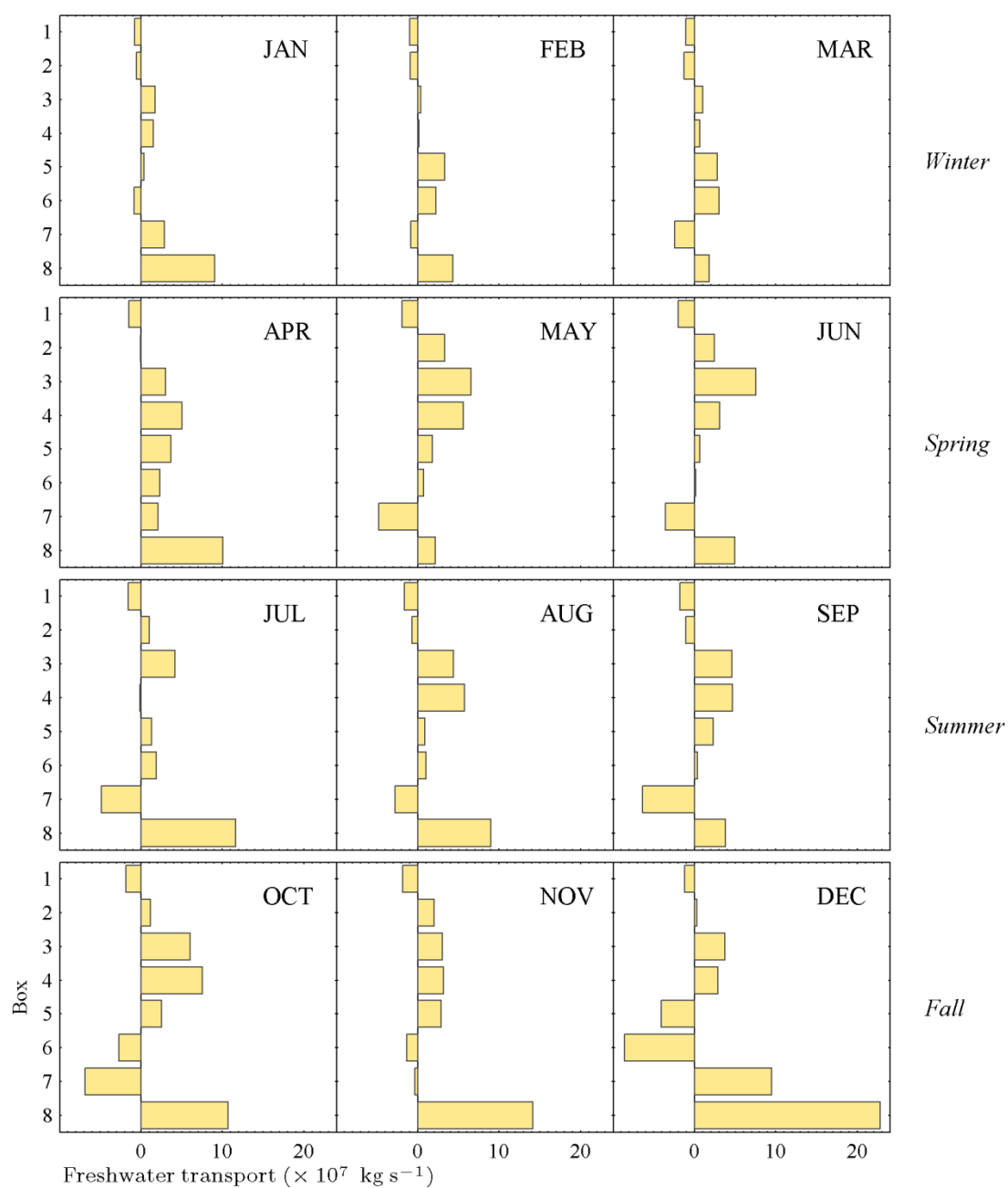
Figure 9-38: Freshwater transport through the east face of each box (kg s^{-1}). Negative values indicate transport out of the box.

9.10 Conclusions

The well-established equatorward alongshore flow is clearly observed in MOCHA circulation values. Volume transport decreases toward the south, until a large portion of MAB water turns offshore north of Cape Hatteras. Only small volumes of water (if any) are seen to travel through to the SAB. Cross-shore currents are small and variable with no well-established pattern, except for the large offshore currents north of Cape Hatteras. Heat and freshwater budgets exhibit a strong seasonal cycle, and advective transports follow volume transport patterns. Clearly, volume, heat and freshwater are both lost and gained offshore along the length of the MAB, not just at the southern tip. Since the cross-shore lines were carefully placed to be perpendicular to isobaths, the oft-used assumption that flow follows isobaths exactly is clearly not the case.

The alongshore sea-surface slope is seen to vary with both region and month. The slope in the northern MAB tends to be positive in winter, and negative in summer, a distinct improvement over previous estimates of a single uniform value. The sea level rises sharply travelling south from Chesapeake Bay, which is in keeping with the offshore flow in that region.

This analysis should be considered a first approach rather than a definitive result. The primary reason for this is the lack of information regarding both the bottom stress and the along-shore sea surface slope in the MAB. Secondary reasons include the simplifications and assumptions made in deriving the equations, and in that the

analysis is not for the entire MAB shelf, but only out to the 85-m isobath. It should also be remembered that these results are based on the mean circulation only: whereas the fluctuating (eddy) portion of the current can also generate significant transports.

Currents and transports observed here are weaker and smaller, respectively, than in previous observations. This could be due to a number of reasons: the uncertainties mentioned above, the smoothing effect a climatology has on density gradients, and the fact that the sections here do not include the shelfbreak jet (except in the very south of the MAB where the shelf narrows).

On the other hand, significant improvements have been made beyond previous two-dimensional models. MOCHA provides much better estimate of density gradients and the alongshelf variation of other properties. The budget analysis clearly shows that a non-uniform sea-surface slope exists in the MAB, and provides a new methodology for computing along and cross-shore transports.

Further work would examine the cross-shore budgets along different isobaths, or attempt to outline MAB waters precisely, along varying isobaths. Further insight could be gained by analyzing the transport from different components of the flow (e.g. geostrophic vs Ekman), and wind-stress could be included in the cross-shelf momentum balance. An independent dataset could be used to determine whether the OA Flux of the NCEP−NARR air-sea fluxes are closer to observations (or a combination of the two). The Ekman depth could be based on observations and allowed to vary with region and/or wind speed. A larger project would be to compile

a climatology of velocity or transport observations, and especially bottom velocity observations. This would facilitate finding a more accurate relation for the bottom stress, and identify the best choice of the constant b (or an alternate constant in a new relation), and allow verification of results. Data collected by the new Pioneer Array operated by the Ocean Obervatories Initiative and located at the shelf break within Box 1 will provide useful and interesting comparisons for the cross-shelf flux estimates calculated here.

10 Concluding Remarks

In this thesis, a four-dimensional climatology of the temperature and salinity of the Middle Atlantic Bight is developed. The MAB is shown to be a region of both strong seasonal variability, and also containing alongshore gradients and variability that is often ignored in the literature. MOCHA is a thus a very useful tool in studying the physical oceanography of the region.

MOCHA has been shown to be a good representation of its input data, and it compares well to independent datasets, and other models. It is of particular note that MOCHA performs well even in comparison to sophisticated real-time ocean models. MOCHA is thus useful for model input and boundary conditions, for nudging and for data assimilation, and it may also be used on its own as a good first predictor of the ocean conditions during any particular month.

The MAB seasonal cycle is clearly portrayed in MOCHA, which gives a unique three-dimensional spatial view of the MAB shelf, and patterns in salinity and temperature. Monthly, rather than annual mean or seasonal, fields provide the fourth dimension (time) in greater detail than in most previous studies.

The well-known cycles of the warming of a summer mixed layer with a strong thermocline, and the development and shrinking of the cold pool, are clearly evident

in MOCHA fields. In contrast to many previous studies that simply analyze a single transect, alongshore patterns are also discernable, with MAB waters being generally cooler and fresher to the north, and warmer and saltier to the south. Significant variations in along-shore salinity are also identified.

For the first time, box volume budgets for the entire MAB are calculated using detailed three-dimensional spatial data (rather than using box averages), and for each month of the year. Unlike most previous studies, no assumptions are made regarding alongshore variability: the density field, wind stress, and other parameters are allowed to vary in the alongshore direction. No assumption is made regarding the depth-averaged transport on the outer edge of the MAB (in this work taken as the 85-m isobath). Instead, cross-shore lines are carefully chosen to lie parallel to local isobaths, and the components of the flow are calculated as they are found in relation to them.

Results show the now well-established pattern of alongshore mean currents flowing equatorward throughout the MAB, until north of Cape Hatteras, when the majority (or all) of the MAB water volume turns offshore. On- and off-shore flow is also seen along the entire 85-m isobath throughout the MAB, with volume transport decreasing southwards, supporting the "leaky current" theory that some MAB water is lost to the ocean prior to the turning at Cape Hatteras.

The alongshore sea-surface slope varies with both alongshore region and month, in contrast to many previous studies which assume a value both constant in time, and

uniform throughout the MAB. Instead, the slope in the northern MAB tends to be positive in winter, and negative in summer, with sea level rising sharply between Chesapeake Bay and Cape Hatteras (which is in keeping with the offshore flow in that region). Heat and freshwater budgets exhibit a strong seasonal cycle, and advective transport patterns follow the volume transport. Volume, heat and freshwater are both lost and gained offshore along the entire length of the MAB, not just at the southern end.

Once again MOCHA provides a much more detailed view of the MAB, and indicates that there is considerable along-shore variation that should be taken into account in future studies. Assumptions of two-dimensionality, uniform properties, and that flow always follows isobaths, do not provide the wealth of detail that MOCHA does. Analyses of transports, and the import and export fluxes of properties such as nutrient and carbon need to include the entire MAB shelf, not just the turning point north of Cape Hatteras. The Middle Atlantic Bight is a complex and varying region, with many details of its physical oceanography still to be uncovered.

Bibliography

Abood, K. A. (1977). Evaluation of Circulation in Partially Stratified Estuaries as Typified by the Hudson River. Ph.D. dissertation, Rutgers University.

Argo. (2014). "Argo - part of the integrated global observation strategy." from http://www.argo.ucsd.edu.

Baird, D. and R. E. Ulanowicz (1989). "The seasonal dynamics of the Chesapeake Bay ecosystem." Ecological Monographs **59**(4): 329-364.

Beardsley, R. C., W. C. Boicourt and D. V. Hansen (1976). "Physical oceanography of the Middle Atlantic Bight." Limnology and Oceanography Special Symposium **2**: 20-34.

Beardsley, R. C., D. C. Chapman, K. H. Brink, S. Ramp and R. Schlitz (1985). "The Nantucket Shoals Flux Experiment: Part I. A basic description of the current and temperature variability." Journal of Physical Oceanography **15**: 713-748.

Beardsley, R. C. and C. N. Flagg (1976). "The water structure, mean currents, and shelf-water/slope-water front on the New England continental shelf." Mem. Soc. Roy. Sci. Liege **6**: 209-225.

Becker, J. J., D. T. Sandwell, W. H. F. Smith, J. Braud, B. Binder, J. Depner, . . . P. Weatherall (2009). "Global bathymetry and elevation data at 30 arc seconds resolution: SRTM30_PLUS." Marine Geodesy **32**(4): 355-371

Bigelow, H. B. (1933). "Studies of the waters on the continental shelf, Cape Cod to Chesapeake Bay. I. The cycle of temperature." Papers in Physical Oceanography and Meteorology **2**(4): 1-135.

Bignami, F. and T. S. Hopkins (2003). "Salt and heat trends in the shelf waters of the southern Middle-Atlantic Bight." Continental Shelf Research **23**(6): 647-667.

Biscaye, P. E., C. N. Flagg and P. G. Falkowski (1994). "The shelf edge exchange processes experiment, SEEP-II: an introduction to hypotheses, results and conclusions." Deep-Sea Research, Part II (Topical Studies in Oceanography) **41**(2-3): 231-252.

Bowden, K. F. (1983). Physical oceanography of coastal waters. Chichester, England, Ellis Horwood Ltd.

Boyer, T., S. Levitus, H. Garcia, R. A. Locarnini, C. Stephens and J. Antonov (2005). "Objective analyses of annual, seasonal, and monthly temperature and salinity for

the World Ocean on a 0.25 grid." <u>International Journal of Climatology</u> **25**(7): 931-945.

Boyer, T. P., J. I. Antonov, O. K. Baranova, H. E. Garcia, D. R. Johnson, R. A. Locarnini, . . . M. M. Zweng (2009). World Ocean Database 2009 <u>NOAA Atlas NESDIS 66</u>. S. Levitus. Washington, DC, US Gov. Printing Office**:** 216.

Bradley, E., C. Fairall, J. Hare and A. Grachev (2000). <u>An old and improved bulk algorithm for air-sea fluxes: COARE 2.6a</u>. AMS 14th Symposium on Boundary Layers and Turbulence.

Brown, W. S., N. R. Pettigrew and J. D. Irish (1985). "The Nantucket Shoals Flux Experiment (NSFE79). II. The structure and variability of across-shelf pressure gradients." <u>Journal of Physical Oceanography</u> **15**(6): 749-771.

Brunke, M. A., C. W. Fairall, X. Zeng, L. Eymard and J. A. Curry (2003). "Which bulk aerodynamic algorithms are least problematic in computing ocean surface turbulent fluxes?" <u>Journal of Climate</u> **16**(4): 619-635.

Bumpus, D. F. (1973). "A description of the circulation on the continental shelf of the east coast of the United States." <u>Progress in Oceanography</u> **6**: 111-157.

Bumpus, D. F. and E. L. Pierce (1955). "The hydrography and the distribution of chaetognaths over the continental shelf off North Carolina." <u>Deep-Sea Research</u> **3**: 92-109.

Burrage, D. M. and R. W. Garvine (1988). "Summertime hydrography at the shelfbreak front in the Middle Atlantic Bight." <u>Journal of Physical Oceanography</u> **18**(10): 1309-1319.

Butman, B., R. C. Beardsley, B. Magnell, D. Frye, J. A. Vermersch, R. Schlitz, . . . M. A. Noble (1982). "Recent observations of the mean circulation on Georges Bank." <u>Journal of Physical Oceanography</u> **12**(6): 569-591.

Butman, B., D. C. Twichell, P. A. Rona, B. E. Tucholke, T. J. Middleton and J. M. Robb (2006). Sea floor topography and backscatter intensity of the Hudson Canyon region offshore of New York and New Jersey. <u>U.S. Geological Survey Open-File Report 2004-1441</u>.

Castelao, R., S. Glenn and O. Schofield (2010). "Temperature, salinity, and density variability in the central Middle Atlantic Bight." <u>Journal of Geophysical Research: Oceans</u> **115**(C10005): doi:10.1029/2009JC006082.

Castelao, R., S. Glenn, O. Schofield, R. Chant, J. Wilkin and J. Kohut (2008). "Seasonal evolution of hydrographic fields in the central Middle Atlantic Bight from glider observations." <u>Geophysical Research Letters</u> **35**(3).

Chang, G. C., T.D. Dickey, O. Schofield, A.D. Weidemann, E. Boss, W.S. Pegau, M.A. Moline, S.M. Glenn (2002). "Nearshore physical processes and bio-optical properties in the New York Bight." Journal of Geophysical Research **107**(C9): 1-16.

Chant, R. J., S. Glenn and J. Kohut (2004). "Flow reversals during upwelling conditions on the New Jersey inner shelf." Journal of Geophysical Research **109**(C12S03): doi:10.1029/2003JC001941.

Chant, R. J., S. M. Glenn, E. Hunter, J. Kohut, R. F. Chen, R. W. Houghton, . . . O. Schofield (2008). "Bulge formation of a buoyant river outflow." Journal of Geophysical Research: Oceans **113**(C01017): doi:10.1029/2007JC004100.

Chapman, D. C. (1986). "A simple model of the formation and maintenance of the shelf/slope front in the Middle Atlantic Bight." Journal of Physical Oceanography **16**(7): 1273-1279.

Chapman, D. C. and R. C. Beardsley (1989). "On the origin of shelf water in the Middle Atlantic Bight." Journal of Physical Oceanography **19**(3): 384-391.

Chapman, D. C. and G. Gawarkiewicz (1993). "On the establishment of the seasonal pycnocline in the Middle Atlantic Bight." Journal of Physical Oceanography **23**(11): 2487-2492.

Chen, K. and R. He (2010). "Numerical Investigation of the Middle Atlantic Bight Shelfbreak Frontal Circulation Using a High-Resolution Ocean Hindcast Model." Journal of Physical Oceanography **40**(5): 949-964.

Chen, K. and R. He (2015). "Mean circulation in the coastal ocean off northeastern North America from a regional-scale ocean model." Ocean Science **11**(4): 503-517.

Chu, P. C. and C. Fan (2010). "A conserved minimal adjustment scheme for stabilization of hydrographic profiles." Journal of Atmospheric and Oceanic Technology **27**(6): 1072-1083.

Churchill, J. H. and T. J. Berger (1998). "Transport of Middle Atlantic Bight shelf water to the Gulf Stream near Cape Hatteras." Journal of Geophysical Research **103**(C13): 30605-30621.

Churchill, J. H. and P. C. Cornillon (1991). "Gulf stream water on the shelf and upper slope north of Cape Hatteras." Continental Shelf Research **11**(5): 409-431.

Churchill, J. H. and G. Gawarkiewicz (2009). "Shelfbreak frontal eddies over the continental slope north of Cape Hatteras." Journal of Geophysical Research **114**(C02017): doi:10.1029/2007JC004642.

Churchill, J. H., E. R. Levine, D. N. Connors and P. C. Cornillon (1993). "Mixing of shelf, slope and Gulf Stream water over the continental slope of the Middle Atlantic

Bight." <u>Deep-Sea Research, Part I (Oceanographic Research Papers)</u> **40**(5): 1063-1085.

Cleveland, W. S. (1979). "Robust locally weighted regression and smoothing scatterplots." <u>Journal of the American Statistical Association</u> **74**(368): 829-836.

Cleveland, W. S. and S. J. Devlin (1988). "Locally weighted regression: an approach to regression analysis by local fitting " <u>Journal of the American Statistical Association</u> **83**(403): 596-610.

Cooper, J. C., F. R. Cantelmo and C. E. Newton (1988). Overview of the Hudson River Estuary. <u>Science, Law and Hudson River Power Plants: A Case Study in Environmental Impact Assessment</u>. L. W. Barnthouse, R. J. Klauda, D. S. Vaughn and R. L. Kendall. Bethesda, Maryland, American Fisheries Society**:** 11-24.

Csanady, G. (1976). "Mean circulation in shallow seas." <u>Journal of Geophysical Research</u> **81**(30): 5389-5399.

Csanady, G. T. (1979). "The pressure field along the western margin of the North Atlantic." <u>Journal of Geophysical Research</u> **84**(C8): 4905-4915.

Csanady, G. T. (1982). <u>Circulation in the Coastal Ocean</u>, Springer Netherlands.

Curry, R. (2001). HydroBase2 - A database of hydrographic profiles and tools for climotological analysis, Woods Hole Oceanographic Institution**:** 81.

Dever, E. (1997). "Wind-forced cross-shelf circulation on the Northern California shelf." <u>Journal of Physical Oceanography</u> **27**(8): 1566-1580.

Dong, S., S. L. Hautala and K. A. Kelly (2007). "Interannual variations in upper-ocean heat content and heat transport convergence in the western North Atlantic." <u>Journal of Physical Oceanography</u> **37**(11): 2682-2697.

Dunn, J. R. and K. R. Ridgway (2002). "Mapping ocean properties in regions of complex topography." <u>Deep Sea Research Part I: Oceanographic Research Papers</u> **49**(3): 591-604.

Fairall, C., E. F. Bradley, J. Hare, A. Grachev and J. Edson (2003). "Bulk parameterization of air-sea fluxes: updates and verification for the COARE algorithm." <u>Journal of Climate</u> **16**(4): 571-591.

Fairall, C. W., E. F. Bradley, D. P. Rogers, J. B. Edson and G. S. Young (1996). "Bulk parameterization of air-sea fluxes for tropical ocean-global atmosphere coupled-ocean atmosphere response experiment." <u>Journal of Geophysical Research: Oceans</u> **101**(C2): 3747-3764.

Flagg, C. N. (1977). The kinematics and dynamics of the New England continental shelf and shelf/slope front. Ph.D. dissertation, Massachusetts Institute of Technology and Woods Hole Oceanographic Institution.

Flagg, C. N., M. Dunn, D. P. Wang, H. T. Rossby and R. L. Benway (2006). "A study of the currents of the outer shelf and upper slope from a decade of shipboard ADCP observations in the Middle Atlantic Bight." Journal of Geophysical Research: Oceans **111**(C06003): doi:10.1029/2005JC003116.

Flagg, C. N., L. J. Pietrafesa and G. L. Weatherly (2002). "Springtime hydrography of the southern Middle Atlantic Bight and the onset of seasonal stratification." Deep Sea Research Part II: Topical Studies in Oceanography **49**(20): 4297-4329.

Fong, D. A. and W. R. Geyer (2001). "Response of a river plume during an upwelling favorable wind event." Journal of Geophysical Research **106**(C1): 1067-1084.

Ford, W., J. Longard and R. Banks (1952). "On the nature, occurrence and origin of cold low salinity water along the edge of the Gulf Stream." Journal of Marine Research **11**(3): 281-293.

Forsyth, J. S. T., M. Andres and G. G. Gawarkiewicz (2015). "Recent accelerated warming of the continental shelf off New Jersey: Observations from the CMV Oleander expendable bathythermograph line." Journal of Geophysical Research: Oceans **120**(3): 2370-2384.

Fratantoni, P. S. and R. S. Pickart (2007). "The western North Atlantic shelfbreak current system in summer." Journal of Physical Oceanography **37**(10): 2509-2533.

Garvine, R. W. (2004). "The vertical structure and subtidal dynamics of the inner shelf off New Jersey." Journal of Marine Research **62**(3): 337-371.

Gawarkiewicz, G., F. Bahr, R. C. Beardsley and E. H. Brink (2001). "Interaction of a slope eddy with the shelfbreak front in the Middle Atlantic Bight." Journal of Physical Oceanography **31**(9): 2783-2796.

Gawarkiewicz, G., K. H. Brink, F. Bahr, R. C. Beardsley, M. Caruso, J. F. Lynch and C. Ching-Sang (2004). "A large-amplitude meander of the shelfbreak front during summer south of New England: observations from the Shelfbreak PRIMER experiment." Journal of Geophysical Research **109**(C03006): doi:10.1029/2002JC001468.

Gawarkiewicz, G., T. M. Church, G. W. Luther, III, T. G. Ferdelman and M. Caruso (1992). "Large-scale penetration of Gulf Stream water onto the continental shelf north of Cape Hatteras." Geophysical Research Letters **19**(4): 373-376.

Gawarkiewicz, G., J. Churchill, F. Bahr, C. Linder and C. Marquette (2008). "Shelfbreak frontal structure and processes north of Cape Hatteras in winter." Journal of Marine Research **66**(6): 775-799.

Gawarkiewicz, G., R. K. McCarthy, K. Barton, A. K. Masse and T. M. Church (1990). "A Gulf Stream-derived pycnocline intrusion on the Middle Atlantic Bight shelf." Journal of Geophysical Research **95**(C12): 22305-22313.

Geyer, W. R., J. H. Trowbridge and M. M. Bowen (2000). "The dynamics of a partially mixed estuary." Journal of Physical Oceanography **30**(8): 2035-2048.

Glenn, S., R. A. Arnone, T. Bergmann, W. P. Bissett, M. Crowley, J. Cullen, . . . O. Schofield (2004). "Biogeochemical impact of summertime coastal upwelling on the New Jersey shelf." Journal of Geophysical Research **109**(C12S02): doi:10.1029/2003JC002265.

Glenn, S. M., M. F. Crowley, D. B. Haidvogel and Y. T. Song (1996). "Underwater observatory captures coastal upwelling events off New Jersey." EOS Transactions **77**: 233-236.

Glenn, S. M., D. B. Haidvogel, O. M. Schofield, C. von Alt and E. R. Levine (1998). "Coastal predictive skill experiments." Sea Technology **39**(4): 63-69.

Gong, D., J. T. Kohut and S. M. Glenn (2010). "Seasonal climatology of wind-driven circulation on the New Jersey shelf." Journal of Geophysical Research **115**(C4): C04006.

Gordon, A. L. and F. Aikman, III (1981). "Salinity maximum in the pycnocline of the Middle Atlantic Bight " Limnology and Oceanography **26**(1): 123-130.

Graham, F. S. and T. J. McDougall (2013). "Quantifying the nonconservative production of conservative temperature, potential temperature, and entropy." Journal of Physical Oceanography **43**(5): 838-862.

Hickey, B. M., L. J. Pietrafesa, D. A. Jay and W. C. Boicourt (1998). "The Columbia River plume study: Subtidal variability in the velocity and salinity fields." Journal of Geophysical Research: Oceans (1978–2012) **103**(C5): 10339-10368.

Hofmann, E., J. N. Druon, K. Fennel, M. Friedrichs, D. Haidvogel, C. Lee, . . . J. O'Reilly (2008). "Eastern US continental shelf carbon budget: integrating models, data assimilation, and analysis." Oceanography **21**(1): 86–104.

Hopkins, T. (1982). "On the sea level forcing of the Mid-Atlantic Bight." Journal of Geophysical Research: Oceans **87**(C3): 1997-2006.

Houghton, R. W., C. N. Flagg and L. J. Pietrafesa (1994). "Shelf-slope water frontal structure, motion and eddy heat flux in the southern Middle Atlantic Bight." Deep-Sea Research, Part II (Topical Studies in Oceanography) **41**(2-3): 273-306.

Houghton, R. W., R. Schlitz, R. C. Beardsley, B. Butman and J. Lockwood Chamberlin (1982). "The Middle Atlantic Bight cold pool: evolution of the

temperature structure during summer 1979." Journal of Physical Oceanography **12**(10): 1019-1029.

Howells, G. P. (1972). "The estuary of the Hudson River, USA." Proceedings of the Royal Society of London. Series B. Biological Sciences **180**(1061): 521-534.

Hunkins, K. (1981). "Salt dispersion in the Hudson Estuary." Journal of Physical Oceanography **11**(5): 729-738.

IOC, SCOR and IAPSO (2010). The international thermodynamic equation of seawater-2010: calculation and use of thermodynamic properties, . Manual and Guides No. 56. I. O. Commission, UNESCO (English)**:** 196.

Janjic, Z. I. (1994). "The step-mountain eta coordinate model: further developments of the convection, viscous sublayer, and turbulence closure schemes." Monthly Weather Review **122**(5): 927-945.

Janowitz, G. and L. Pietrafesa (1980). "A model and observations of time-dependent upwelling over the mid-shelf and slope." Journal of Physical Oceanography **10**(10): 1574-1583.

Johnson, D. R., T. P. Boyer, H. E. Garcia, R. A. Locarnini, O. K. Baranova and M. M. Zweng (2009). World Ocean Database 2009 documentation. NODC Internal Report. S. Levitus. Silver Spring, MD, NOAA Printing Office**:** 175.

Johnson, D. R., J. Miller and O. Schofield (2003). "Dynamics and optics of the Hudson River outflow plume." Journal of Geophysical Research **108**(C10): doi:10.1029/2002JC001485.

Jolliff, J. K., J. C. Kindle, I. Shulman, B. Penta, M. A. M. Friedrichs, R. Helber and R. A. Arnone (2009). "Summary diagrams for coupled hydrodynamic-ecosystem model skill assessment." Journal of Marine Systems **76**(1-2): 64-82.

Josey, S. (2001). "A comparison of ECMWF, NCEP-NCAR, and SOC surface heat fluxes with moored buoy measurements in the subduction region of the northeast Atlantic." Journal of Climate **14**(8): 1780-1789.

Joyce, T. (1987). "Meteorology and air-sea interactions." The Marine Environment of the US Atlantic Continental Slope and Rise: 5-26.

Kalnay, E., M. Kanamitsu, R. Kistler, W. Collins, D. Deaven, L. Gandin, . . . J. Woollen (1996). "The NCEP/NCAR 40-year reanalysis project." Bulletin of the American Meteorological Society **77**(3): 437-471.

Kanamitsu, M., W. Ebisuzaki, J. Woollen, S. Yang, J. Hnilo, M. Fiorino and G. Potter (2002). "NCEP-DEO AMIP-II Reanalysis (R-2)." Bulletin of the American Meteorological Society **83**(2): 1631–1643.

Keller, G. H., D. Lambert, G. Rowe and N. Startesinic (1973). "Bottom Currents in the Hudson Canyon." Science **180**(4082): 181-183.

Ketchum, B. H., A. C. Redfield and J. C. Ayers (1951). "The oceanography of the New York Bight." Papers in Physical Oceanography and Meteorology **12**(1): 4-46.

Kohut, J. T., S. M. Glenn and R. J. Chant (2004). "Seasonal current variability on the New Jersey inner shelf." Journal of Geophysical Research **109**(C7).

Kupferman, S. L. and N. Garfield (1977). "Transport of low-salinity water at the slope water-Gulf Stream boundary." Journal of Geophysical Research **82**(24): 3481-3486.

Large, W. G. and S. Pond (1981). "Open ocean momentum flux measurements in moderate to strong winds." Jounal of Physical Oceanography **11**: 1603-1611.

Lentz, S. (2004). "The response of buoyant coastal plumes to upwelling-favorable winds." Journal of Physical Oceanography **34**(11): 2458-2469.

Lentz, S., K. Shearman, S. Anderson, A. Plueddemann and J. Edson (2003). "Evolution of stratification over the New England shelf during the Coastal Mixing and Optics study, August 1996 - June 1997." Journal of Geophysical Research **107**(C1): 8-1.

Lentz, S. J. (2008). "Observations and a model of the mean circulation over the Middle Atlantic Bight continental shelf." Journal of Physical Oceanography **38**(6): 1203-1221.

Lentz, S. J. (2010). "The mean along-isobath heat and salt balances over the Middle Atlantic Bight continental shelf." Journal of Physical Oceanography **40**(5): 934-948.

Lillibridge, J., G. Hitchcock, T. Rossby, E. Lessard, M. Mork and L. Golmen (1990). "Entrainment and mixing of shelf/slope waters in the near-surface Gulf Stream." Journal of Geophysical Research: Oceans **95**(C8): 13065-13087.

Linder, C. A. and G. Gawarkiewicz (1998). "A climatology of the shelfbreak front in the Middle Atlantic Bight." Journal of Geophysical Research **103**(C9): 18405-18423.

Linder, C. A., G. G. Gawarkiewicz and M. Taylor (2006). "Climatological estimation of environmental uncertainty over the Middle Atlantic Bight shelf and slope." IEEE Journal of Oceanic Engineering **31**(2): 308-324.

Loder, J. W., B. Petrie and G. Gawarkiewicz (1998). "The coastal ocean off northeastern North America: a large-scale view." The Sea **11**: 105-133.

Lozier, M. S. and G. Gawarkiewicz (2001). "Cross-frontal exchange in the Middle Atlantic Bight as evidenced by surface drifters." Journal of Physical Oceanography **31**(8): 2498-2510.

Lozier, M. S., M. S. C. Reed and G. G. Gawarkiewicz (2002). "Instability of a shelfbreak front." Journal of Physical Oceanography **32**(3): 924-944.

Mann, K. H. and J. R. N. Lazier (1996). Dynamics of marine ecosystems: biological-physical interactions in the oceans, Wiley-Blackwell.

Manning, J. P., D. J. McGillicuddy Jr, N. R. Pettigrew, J. H. Churchill and L. S. Incze (2009). "Drifter observations of the Gulf of Maine coastal current." Continental Shelf Research **29**(7): 835-845.

Mannino, A., M. E. Russ and S. B. Hooker (2008). "Algorithm development and validation for satellite-derived distributions of DOC and CDOM in the US Middle Atlantic Bight." Journal of Geophysical Research **113**(C07051): doi:10.1029/2007JC004493.

McDougall, T. J. (2003). "Potential enthalpy: A conservative oceanic variable for evaluating heat content and heat fluxes." Journal of Physical Oceanography **33**(5): 945-963.

McDougall, T. J. and P. M. Barker (2011). Getting started with TEOS-10 and the Gibbs Seawater (GSW) Oceanographic Toolbox. S. I. WG127. **127:** 28.

Mesinger, F., G. DiMego, E. Kalnay, K. Mitchell, P. C. Shafran, W. Ebisuzaki, . . . E. H. Berbery (2006). "North American regional reanalysis." Bulletin of the American Meteorological Society **87**(3).

Moody, J. A. (1984). Atlas of tidal elevation and current observations on the northeast American continental shelf and slope, Dept. of the Interior, US Geological Survey.

Moore, G. (2014). "Mesoscale structure of Cape Farewell tip jets." Journal of Climate **27**(23): 8956-8965.

Moore, G., R. S. Pickart and I. A. Renfrew (2008). "Buoy observations from the windiest location in the world ocean, Cape Farewell, Greenland." Geophysical Research Letters **35**(18).

Mountain, D. G. (1991). "The volume of Shelf Water in the Middle Atlantic Bight: seasonal and interannual variability, 1977-87." Continental Shelf Research **11**(3): 251-267.

Mountain, D. G. (2003). "Variability in the properties of Shelf Water in the Middle Atlantic Bight, 1977-1999." Journal of Geophysical Research **107**(C1): 14-11.

Mountain, D. G. and M. H. Taylor (1998). "Spatial coherence of interannual variability in water properties on the U.S. northeast shelf." Journal of Geophysical Research **103**(C2): 3083-3092.

Münchow, A. (1992). The formation of a buoyancy driven coastal current,. Ph.D. dissertation, University of Delaware.

Münchow, A. and R. J. Chant (2000). "Kinematics of inner shelf motions during the summer stratified season off New Jersey." Journal of Physical Oceanography **30**(2): 247-268.

NEFSC. (2014). "Oceanography at the Northeast Fisheries Science Center." 2007, from http://www.nefsc.noaa.gov/epd/ocean/MainPage/index.html.

Noble, M., B. Butman and E. Williams (1983). "On the longshelf structure and dynamics of subtidal currents on the eastern United States continental shelf." Journal of Physical Oceanography **13**(12): 2125-2147.

Ou, H. W. (1983). "Some two-layer models of the shelf-slope front: geostrophic adjustment and its maintenance." Journal of Physical Oceanography **13**(10): 1798-1808.

Parker, C. E. (1971). "Gulf stream rings in the Sargasso Sea." Deep Sea Research **18**(10): 981-993.

Pawlowicz, R. (2010). What every oceanographer needs to know about TEOS-10 (The TEOS-10 Primer), unpublished manuscript, available from www.TEOS-10.org 10.

Pawlowicz, R., B. Beardsley and S. Lentz (2002). "Classical tidal harmonic analysis including error estimates in MATLAB using T-TIDE." Computers & Geosciences **28**(8): 929-937.

Pickart, R. S., D. J. Torres, T. K. McKee, M. J. Caruso and J. E. Przystup (1999). "Diagnosing a meander of the shelf break current in the Middle Atlantic Bight." Journal of Geophysical Research **104**(C2): 3121-3132.

Pietrafesa, L. J., J. M. Morrison, M. P. McCann, J. Churchill, E. Bohm and R. W. Houghton (1994). "Water mass linkages between the Middle and South Atlantic Bights." Deep-Sea Research, Part II (Topical Studies in Oceanography) **41**(2-3): 365-389.

Pond, S. and G. L. Pickard (1983). Introductory dynamical oceanography, Butterworth-Heinemann.

Posmentier, E. S. and J. W. Rachlin (1976). "Distribution of salinity and temperature in the Hudson Estuary." Journal of Physical Oceanography **6**(5): 775-777.

Rasmussen, L. L., G. Gawarkiewicz, W. B. Owens and M. S. Lozier (2005). "Slope water, Gulf Stream, and seasonal influences on southern Mid-Atlantic Bight circulation during the fall-winter transition." Journal of Geophysical Research **110**(C02009): doi:10.1029/2004JC002311.

Rattray Jr, M. (1962). "Interpolation errors and oceanographic sampling." <u>Deep Sea Research</u> **9**: 25-37.

Reiniger, R. F. and C. K. Ross (1968). "A method of interpolation with application to oceanographic data." <u>Deep-Sea Research</u> **15**(2): 185-193.

Renfrew, I. A., G. Moore, P. S. Guest and K. Bumke (2002). "A comparison of surface layer and surface turbulent flux observations over the Labrador Sea with ECMWF analyses and NCEP reanalyses." <u>Journal of Physical Oceanography</u> **32**(2): 383-400.

Renfrew, I. A., G. Petersen, D. Sproson, G. Moore, H. Adiwidjaja, S. Zhang and R. North (2009). "A comparison of aircraft-based surface-layer observations over Denmark Strait and the Irminger Sea with meteorological analyses and QuikSCAT winds." <u>Quarterly Journal of the Royal Meteorological Society</u> **135**(645): 2046-2066.

Rennie, S. E., J. L. Largier and S. J. Lentz (1999). "Observations of a pulsed buoyancy current downstream of Chesapeake Bay." <u>Journal of Geophysical Research</u> **104**(C8): 18227-18240.

Richardson, P. L., R. Cheney and L. Worthington (1978). "A census of Gulf Stream rings, Spring 1975." <u>Journal of Geophysical Research: Oceans (1978–2012)</u> **83**(C12): 6136-6144.

Ridgway, K. R., J. R. Dunn and J. L. Wilkin (2002). "Ocean interpolation by four-dimensional weighted least squares - application to the waters around Australasia." <u>Journal of Atmospheric and Oceanic Technology</u> **19**(9): 1357-1375.

Saha, S., S. Moorthi, H.-L. Pan, X. Wu, J. Wang, S. Nadiga, . . . D. Behringer (2010). "The NCEP climate forecast system reanalysis." <u>Bulletin of the American Meteorological Society</u> **91**(8): 1015-1057.

Saunders, P. M. (1977). "Wind stress on the ocean over the eastern continental shelf of North America." <u>Journal of Physical Oceanography</u> **7**(4): 555-566.

Savidge, D. K., J. A. Austin and B. O. Blanton (2013). "Variation in the Hatteras front density and velocity structure Part 1: High resolution transects from three seasons in 2004–2005." <u>Continental Shelf Research</u> **54**: 93-105.

Schofield, O., T. Bergmann, P. Bissett, J. F. Grassle, D. B. Haidvogel, J. Kohut, . . . S. M. Glenn (2002). "The Long-term Ecosystem Observatory: an integrated coastal observatory." <u>IEEE Journal of Oceanic Engineering</u> **27**(2): 146-154.

Scott, J. and G. Csanady (1976). "Nearshore currents off Long Island." <u>Journal of Geophysical Research</u> **81**(30): 5401-5409.

Sharp, J. H. (2009). "Sharp's Delaware Estuary Database." 2009, from http://www.ceoe.udel.edu/cms/jsharp/CruiseDatabase.htm.

Shearman, R. K. and S. J. Lentz (2003). "Dynamics of mean and subtidal flow on the New England shelf." Journal of Geophysical Research **108**(C8): 37-31.

Shearman, R. K. and S. J. Lentz (2004). "Observations of tidal variability on the New England shelf." Journal of Geophysical Research **109**(C6).

Signel, R. (2005). "Historic coastline extractor." 2009, from http://www.ngdc.noaa.gov/mgg/coast/.

Simpson, H. J., R. Bopp and D. Thurber (1973). "Salt movement patterns in the lower Hudson." Third Symposium on Hudson River Ecology: 39-111.

Stow, C. A., J. Jolliff, D. J. McGillicuddy Jr, S. C. Doney, J. Allen, M. A. Friedrichs, . . . P. Wallhead (2009). "Skill assessment for coupled biological/physical models of marine systems." Journal of Marine Systems **76**(1): 4-15.

Sun, B., L. Yu and R. A. Weller (2003). "Comparisons of surface meteorology and turbulent heat fluxes over the Atlantic: NWP model analyses versus moored buoy observations." Journal of Climate **16**(4): 679-695.

Szeto, K., H. Tran, M. MacKay, R. Crawford and R. Stewart (2008). "The MAGS water and energy budget study." Journal of Hydrometeorology **9**(1): 96-115.

Tang, D., J. N. Moum, J. F. Lynch, P. A. Abbot, R. Chapman, P. H. Dahl, . . . J. A. Goff (2007). "Shallow Water '06: A joint acoustic propagation/nonlinear internal wave physics experiment." Oceanography **20**(4): 156-167.

Taylor, K. E. (2001). "Summarizing multiple aspects of model performance in a single diagram." Journal of Geophysical Research: Atmospheres (1984–2012) **106**(D7): 7183-7192.

Townsend, D. W., A. C. Thomas, L. M. Mayer, M. A. Thomas and J. A. Quinlan (2006). "Oceanography of the northwest Atlantic continental shelf." The Sea: The Global Coastal Ocean: Interdisciplinary Regional Studies and Syntheses **14A**: 119-168.

Uchupi, E., N. Driscoll and R. D. Ballard (2001). "Drainage of late Wisconsin glacial lakes and the morphology and late quaternary stratigraphy of the New Jersey-southern New England continental shelf and slope." Marine Geology **172**: 117-145.

Vallis, G. K. (2006). Atmospheric and oceanic fluid dynamics: fundamentals and large-scale circulation, Cambridge University Press.

Vivier, F., K. A. Kelly and L. A. Thompson (2002). "Heat budget in the Kuroshio Extension region: 1993-99." Journal of Physical Oceanography **32**(12): 3436-3454.

Wang, X., Y. Chao, D. R. Thompson, S. A. Chien, J. Farrara, P. Li, . . . A. Gangopadhyay (2013). "Multi-model ensemble forecasting and glider path planning in the Mid-Atlantic Bight." <u>Continental Shelf Research</u> **63**(Supplement): S223-S234.

Wang, Z., D. B. Haidvogel, D. Bushek, S. E. Ford, E. E. Hofmann, E. N. Powell and J. Wilkin (2012). "Circulation and water properties and their relationship to the oyster disease MSX in Delaware Bay." <u>Journal of Marine Research</u> **70**(2-3): 279-308.

Whitney, M. M. and R. W. Garvine (2006). "Simulating the Delaware Bay buoyant outflow: comparison with observations." <u>Journal of Physical Oceanography</u> **36**(1): 3-21.

Wilk, S. J. and B. E. Brown (1980). <u>A description of those fisheries, which take place in the western North Atlantic beween the U.S.-Canadian border and North Carolina, that presently have or potentially could have user group allocation conflicts.</u> Technical Consultation on Allocation of Fishery Resources, Vichy (France).

Wilkin, J. L. and E. J. Hunter (2013). "An assessment of the skill of real-time models of Mid-Atlantic Bight continental shelf circulation." <u>Journal of Geophysical Research: Oceans</u> **118**(6): 2919-2933.

Wright, W. (1976). "Limits of shelf water south of Cape-Cod, 1941 to 1972." <u>Journal of Marine Research</u> **34**(1): 1-14.

Wright, W. R. and C. E. Parker (1976). "A volumetric temperature/salinity census for the Middle Atlantic Bight." <u>Limnology and Oceanography</u> **21**(4): 563-571.

Xu, F. H. and L. Y. Oey (2011). "The origin of along-shelf pressure gradient in the Middle Atlantic Bight." <u>Journal of Physical Oceanography</u> **41**(9): 1720-1740.

Xue, Y., B. Huang, Z.-Z. Hu, A. Kumar, C. Wen, D. Behringer and S. Nadiga (2011). "An assessment of oceanic variability in the NCEP climate forecast system reanalysis." <u>Climate Dynamics</u> **37**(11-12): 2511-2539.

Yankovsky, A. E. and R. W. Garvine (1998). "Subinertial dynamics on the inner New Jersey shelf during the upwelling season." <u>Journal of Physical Oceanography</u> **28**(12): 2444-2458.

Yankovsky, A. E., R. W. Garvine and A. Munchow (2000). "Mesoscale currents on the inner New Jersey shelf driven by the interaction of buoyancy and wind forcing." <u>Journal of Physical Oceanography</u> **30**(9): 2214-2230.

Yu, L., X. Jin and R. Weller (2008). Multidecade global flux datasets from the objectively analyzed air-sea fluxes (OAFlux) project: latent and sensible heat fluxes, ocean evaporation, and related surface meteorological variables. <u>OAFlux Project Technical Report</u>**:** 64.

Yu, L., X. Jin and R. A. Weller (2006). "Role of net surface heat flux in seasonal variations of sea surface temperature in the tropical Atlantic Ocean." Journal of Climate **19**(23): 6153-6169.

Yu, L. and R. A. Weller (2007). "Objectively analyzed air-sea heat fluxes for the global ice-free oceans (1981-2005)." Bulletin of the American Meteorological Society **88**(4): 527-539.

Yu, L., R. A. Weller and B. Sun (2004a). "Improving latent and sensible heat flux estimates for the Atlantic Ocean (1988-99) by a synthesis approach." Journal of Climate **17**(2): 373-393.

Yu, L., R. A. Weller and B. Sun (2004b). "Mean and variability of the WHOI daily latent and sensible heat fluxes at in situ flux measurement sites in the Atlantic Ocean*." Journal of Climate **17**(11): 2096-2118.

Zeng, X., M. Zhao and R. E. Dickinson (1998). "Intercomparison of bulk aerodynamic algorithms for the computation of sea surface fluxes using TOGA COARE and TAO data." Journal of Climate **11**(10): 2628-2644.

Zhang, W. G., G. G. Gawarkiewicz, D. J. McGillicuddy and J. L. Wilkin (2011). "Climatological mean circulation at the New England shelf break." Journal of Physical Oceanography **41**(10): 1874-1893.

Zhang, W. G., D. J. McGillicuddy and G. G. Gawarkiewicz (2013). "Is biological productivity enhanced at the New England shelfbreak front?" Journal of Geophysical Research: Oceans **118**(1): 517-535.

Zhang, X., D. Haidvogel, D. Munroe, E. N. Powell, J. Klinck, R. Mann and F. S. Castruccio (2015). "Modeling larval connectivity of the Atlantic surfclams within the Middle Atlantic Bight: model development, larval dispersal and metapopulation connectivity." Estuarine, Coastal and Shelf Science **153**: 38-53.

Zhang, Y., W. B. Rossow, A. A. Lacis, V. Oinas and M. I. Mishchenko (2004). "Calculation of radiative fluxes from the surface to top of atmosphere based on ISCCP and other global data sets: refinements of the radiative transfer model and the input data." Journal of Geophysical Research: Atmospheres **109**(D19105): doi:10.1029/2003JD004457.